PROGRESS IN RESEARCH

April 1, 2012 - March 31, 2013

CYCLOTRON INSTITUTE

Texas A&M University

College Station, Texas

PROGRESS IN RESEARCH

APRIL 1, 2012- MARCH 31, 2013

Prepared By

The Cyclotron Institute Staff

Texas A&M University

College Station, TX 77843-3366

Phone: (979) 845-1411
Fax: (979) 845-1899

Web: http://cyclotron.tamu.edu

July 2013

TABLE OF CONTENTS

Introduction ..... **ix**
R.E. Tribble, Director

SECTION I: NUCLEAR STRUCTURE, FUNDAMENTAL INTERACTIONS AND ASTROPHYSICS

Superallowed beta decay **I-1**
J. C. Hardy, I. S. Towner, V. E. Iacob, H. I. Park, L. Chen, V. Horvat, N. Nica, M. Bencomo and R. E. Tribble

Tests of internal-conversion theory with precise γ- and x-ray spectroscopy: the case of $^{119}Sn^{m}$ **I-5**
N. Nica, J. C. Hardy, V. E. Iacob, M. Maguire, and M. B. Trzhaskovskaya

United States nuclear structure data program (USNDP) and evaluated nuclear structure data file (ENSDF) at Texas A&M University **I-9**
N. Nica and J. C. Hardy

Measurement of branching-ratios in the β decay of ^{38}Ca **I-11**
H.I. Park, J.C. Hardy, V.E. Iacob, M. Bencomo, L. Chen, V. Horvat, N. Nica, B.T. Roeder, E. Simmons and R.E. Tribble

Optical pumping model of the polarization for the TRINAT experiment **I-13**
R. S. Behling, B. Fenker, M. Mehlman, D. Melconian and P. D. Shidling

Update on the progress of the ^{37}K β asymmetry experiment **I-16**
R. S. Behling, B. Fenker, M. Mehlman, D. Melconian and P. D. Shidling

Current status of the TAMUTRAP measurement Penning trap **I-18**
R. S. Behling, Y. Boran, B. Fenker, M. Mehlman, D. Melconian and P. D. Shidling

Update on the study of the $^{14}C+n \leftrightarrow {}^{15}C$ system **I-20**
M. McCleskey, A.M. Mukhamedzhanov, V. Goldberg, and R.E. Tribble

Status of AstroBox and analysis of ^{23}Al β-delayed proton decay data **I-25**
L.Trache, E. Simmons, A. Spiridon, M. McCleskey, B. T. Roeder, A. Saastamoinen, R. E. Tribble, E. Pollacco, M. Kebbiri, J. P. Mols, M. Raillot, G. Pascovici

Progress in the analysis of the delayed proton and gamma decay of ^{27}P for nuclear astrophysics..... I-28
E. Simmons, L. Trache, A. Banu, A. Saastamoinen, M. McCleskey, B. Roeder, A. Spiridon, R. E. Tribble, T. Davinson, P. J. Woods, G. J. Lotay, J. Wallace, and D. Doherty

Feasibility study of time-inverse measurement of the stellar reaction ^{22}Mg(α,p)^{25}Al..... I-30
A. Banu, D. Votaw, B. T. Roeder, G. G. Rapisarda, M. McCleskey, A. Saastamoinen, E. Simmons, A. Spiridon, L. Trache, R. E. Tribble and C. A. Gagliardi

Level Structure of ^{10}C..... I-34
V. Z. Goldberg and G. V. Rogachev

Investigation of ^{27}P with the AstroBox prototype detector I-40
E. Simmons, L. Trache, M. McCleskey, A. Saastamoinen, R. G. Pizzone, G. G. Rapisarda, B. Roeder, A. Spiridon, R.E. Tribble, E. Pollacco, G. Pascovici, M. Riallot, J. P. Mols, and M. Kebbiri

Spin physics with STAR at RHIC I-42
Z. Chang, P. Djawotho, C. A. Gagliardi, M. M. Mondal, R. E. Tribble and the STAR Collaboration

SECTION II: HEAVY ION REACTIONS

Factors influencing residue cross section in ^{48}Ca-induced reactions.....II-1
D. A. Mayorov, T. A. Werke, M. C. Alfonso, M. E. Bennett, and C. M. Folden III

Characterization of a gas stopper for heavy element chemistry studies.....II-6
M. C. Alfonso, D. A. Mayorov, T. A. Werke, and C. M. Folden III

Fabrication of lanthanide targets for nuclear reaction studies.....II-7
D. A. Mayorov, T. A. Werke, M. E. Bennett, and C. M. Folden III

Excitation functions of ^{45}Sc-induced reactions: towards future superheavy element synthesis II-9
T. A. Werke, D. A. Mayorov, M. C. Alfonso, M. E. Bennett, and C. M. Folden III

Ionization chamber development for super heavy elements search.....II-15
S. K. Wuenschel, E. J. Kim, M. Barbui, J. B. Natowitz, H. Zheng, N. Blando, and K. Hagel

Probing custerization in ^{40}Ca ^{40}Ca reaction at 35 MeV/A.....II-17
K. Schmidt, K. Hagel, M. Barbui, S. Wuenschel, G. Giuliani, H. Zheng, E. Kim,

N. Blando, A. Bonasera and J. B. Natowitz

Investigating the experimental capabilities of the quadrupole thermometer.....II-21
S. Wuenschel, J. B. Natowitz, M. Barbui, N. Blando, A. Bonasera, G. Guilani,
K. Hagel, E. J. Kim, K. Schmidt, and H. Zheng

Exploring the alpha cluster structure of nuclei using the thick target inverse kinematics technique for multiple alpha decays.....II-26
M. Barbui, K. Hagel, V.Z. Goldberg, J.B. Natowitz, H. Zheng, G. Giuliani,
G.Rapisarda, S. Wuenschel and X.Q. Lin

Alternative reaction paths to heavy elements.....II-30
K. Hagel, M. Barbui, S. Wuenschel, K. Schmidt, G. Giuliani , H. Zheng, N. Blando,
Z. Majka, A.Wieloch, Z. Sosin, S. Kowalski and J. B. Natowitz

Using break-up mechanisms in heavy ion collisions at low energies to constrain the asymmetry energy at Low Nuclear Density II-33
Paul J. Cammarata, Lauren A. Heilborn, Justin Mabiala, Larry W. May,
Alan B. McIntosh, Andrew Raphelt, Andrew Zarrella, and Sherry J. Yennello

Experimental and simulation results for isoscailng of a reconstructed quasi-projectile.....II-37
A. Raphelt, P. J. Cammarata, L. Heilborn, J. Mabiala, L. May,
A. B. McIntosh, A. Zarrella, and S. J. Yennello

Using light charged particles to probe the asymmetry dependence of the caloric curve II-40
A. B. McIntosh, A. Bonasera, Z. Kohley, P. J. Cammarata, K. Hagel,
L. Heilborn, J. Mabiala, L. W. May, P. Marini, A. Raphelt, G. A. Souliotis,
S. Wuenschel, A. Zarrella, and S. J. Yennello

Experimental correlation function using FAUST upgrade.....II-43
L. Heilborn, P. J. Cammarata, J. Mabiala, A.B. McIntosh, L.W. May, A. Raphelt,
A. Zarrella, and S. J. Yennello

Determination of QP mass with measured neutrons II-46
Andrew Zarrella, Paola Marini, Alan McIntosh, Paul Cammarata,
Lauren Heilborn, Justin Mabiala, Larry W. May, Andrew Raphelt, Sherry Yennello

Critical scaling of excited nuclear systems from quantum fluctuations II-49
J. Mabiala, A. Bonasera, H. Zheng, A. B. McIntosh, P. Cammarata, K. Hagel,
L. Heilborn, Z. Kohley, L. W. May, A. Raphelt, G.A. Souliotis, A. Zarrella,
and S.J. Yennello

Toward understanding relativistic heavy-ion collisions with the STAR detector at RHIC.....II-52
M. Cervantes, S. Mioduszewski, and the STAR Collaboration

SECTION III: NUCLEAR THEORY

Coulomb renormalization and ratio of proton and neutron asymptotic normalization coefficients for mirror nuclei III-1
A. M. Mukhamedzhanov

Electron- and photon-impact atomic ionisation III-2
I. Bray, D. V. Fursa, A. S. Kadyrov, A. T. Stelbovics, A. S. Kheifets, and A. M. Mukhamedzhanov

Generalized Faddeev equations in the Alt-Grassberger-Sandhas form for deuteron stripping with explicit inclusion of target excitations and Coulomb interaction III-3
A. M. Mukhamedzhanov, V. Eremenko, and A. I. Sattarov

Measurement of the -3 keV resonance in the reaction $^{13}C(\alpha,n)^{16}O$ of importance in the s-process III-4
M. La Cognata, C. Spitaleri, O. Trippella, G. G. Kiss, G.V. Rogachev, A. M. Mukhamedzhanov, M. Avila G. L. Guardo, E. Koshchiy, A. Kuchera, L. Lamia, S. M. R. Puglia, S. Romano, D. Santiago, and R. Sparta

Density and temperature of fermions and bosons from quantum fluctuations..... III-5
Hua Zheng, Gianluca Giuliani, Matteo Barbarino, and Aldo Bonasera

Effects of initial fluctuations on bottomonium suppression in relativistic heavy ion collsions III-16
T. Song, K. C. Han and C. M. Ko

Subthreshold cascade production in heavy ion collisions..... III-18
L. Feng, L.W. Chen, C.M. Ko, and S.H. Lee

Charmonium production from nonequilibrium charm and anticharm quarks in Quark –gluon plasma III-20
T. Song, K. C. Han and C. M. Ko

Heavy quark potential at finite temperature..... III-22
S.H. Lee, K. Morita, T. Song, and C. M. Ko

Dilepton production in heavy ion collisions at LHC III-23
O. Linnyk, W. Cassing, J. Manninen, E.L. Bratkovskaya, P.B. Gossiaux, J. Aichelin, T. Song, and C.M. Ko

Quarkonium formation time in quark-gluon plasma III-25
T. Song, C. M. Ko, and S. H. Lee

Jet fragmentaton via recombination of parton showers **III-27**
K. C. Han, R. J. Fries, and C. M. Ko

Partonic mean-field effects on matter and antimatter elliptic flow **III-28**
T. Song, S. Plumari, V Greco, C. M. Ko, and F. Li

Energy dependence of pion in-medium effects on π^+/π^- ratio in heavy-ion collisions **III-30**
J. Xu, L. W. Chen, C. M. Ko, B. A. Li, and Y. G. Ma

Effects of initial fluctuations on jet-energy loss **III-32**
H. Zhang, T. Song, and C. M. Ko

Isoscalar and isovector giant resonances in ^{208}Pb **III-34**
M. R. Anders and S. Shlomo

Correlations among nuclear matter properties of Skyrme interactions **III-36**
M. R. Anders and S. Shlomo

Giant resonances in ^{208}Pb and the nuclear matter equation of state **III-38**
M. R. Anders and S. Shlomo

Density determinations in heavy ion collisions **III-40**
G. Roepke, S. Shlomo, A. Bonasera, J. B. Natowitz, S. J. Yennello, A. B. McIntosh,
J. Mabiala, L. Qin, S. Kowalski, K. Hagel, M. Barbui, K. Schmidt, G. Giulani,
H. Zheng, and S. Wuenschel

A T-matrix calculation for heavy-quark gluon scattering **III-42**
K. Huggins and R. Rapp

Sum rule analysis of vector and axial-vector spectral functions with excited states in vacuum **III-44**
P. M. Hohler and R. Rapp

Quantitative sum rule analysis of low-temperature spectral functions **III-46**
Nathan P. M. Holt, Paul M. Hohler, and Ralf Rapp

Predictions for direct photons for the p+Pb run at LHC **III-48**
R. J. Fries and S. De

The D_s Meson as a quantitative probe of diffusion and hadronization in heavy ion collisions **III-49**
M. He, R. J. Fries and R. Rapp

Directed flow from color glass condensate **III-51**
R. J. Fries and G. Chen

Skyrme-Hartree-Fock calculations of the isospin-symmetry breaking correction in superallowed beta decay III-53
I. S. Towner and J. C. Hardy

Beta-neutrino angular-correlation coefficient in ^{21}Na III-57
I. S. Towner and J. C. Hardy

SECTION IV: SUPERCONDUCTING CYCLOTRON, INSTRUMENTATION AND RIB UPGRADE

K500 operations and development IV-1
D. P. May, G. J. Kim, H. L. Clark, and F. P. Abegglen

ECR2 development IV-3
D. P. May, B. T. Roeder, F. P. Abegglen, and H. Peeler

Texas A&M cyclotron radiation effects facility April 1, 2012 – March 31, 2013 ..... IV-5
H. L. Clark, J. Brinkley, L. Chen, G. Chubarian, V. Horvat, B. Hyman, B. Roeder and G. Tabacaru

Cyclotron computing IV-7
R. Burch and K. Hagel

Cyclotron Institute upgrade project IV-8
H. L. Clark, F. Abegglen, G. Chubarian, G. Derrig, G. Kim, D. May, B. Roeder and G. Tabacaru

Progress on the charge breeding ECR ion source IV-23
G. Tabacaru, J. Arje, and D. P. May

Attenuation length in strip scintillators IV-26
Jonathan Button, William McGrew, Y.-W. Lui, D. H. Youngblood

Automatic degrader changer IV-31
M. Bencomo and J. C. Hardy

High-precision nuclear beta decay half-life measurement of ^{26}Al^{m} by a digital beta counting method IV-33
L. Chen, J. C. Hardy, M. Bencomo, V. Horvat, N. Nica, and H. I. Park

Time-interval analysis of β decay IV-38
V. Horvat and J. C. Hardy

Tests of the system to measure branching ratios..... IV-43
V. E. Iacob, H. I. Park and J. C. Hardy

TAMUTRAP facility annual report IV-46
R. S. Behling, Y. Boran, B. Fenker, M. Mehlman, D. Melconian and P. D. Shidling

Upgrade plan for the Oxford detector IV-50
A. Spiridon, R. Chyzh, M. Dag, M. McCleskey, and R. E. Tribble

A reliable, low-cost automated LN_2 filling system for the STARLiTe clover array IV-52
M. McCleskey

Detector tests for SAMURAI silicon tracker..... IV-55
A. Saastamoinen, M. McCleskey, B. T. Roeder, L. Trache, R. E. Tribble,
L. G. Sobotka, J. Elison, J. C. Blackmon, C. Rasco, M. Kurokawa, H. Baba,
H. Otsu, K. Yoneda, and J. Zenihiro

Status of STARLiTe beamline at Texas A&M Cyclotron Institute..... IV-58
J. T. Burke, R. Casperson, M. McCleskey and the STARLiTe collaboration

SECTION V: PUBLICATIONS

Papers published V-1

SECTION VI: APPENDIX

Talks presented VI-1

Research personnel and engineering staff VI-9

Students..... VI-10

Organizational chart..... VI-11

Graduate degree students..... VI-12

Institute colloquia and seminars..... VI-13

Introduction
April 1, 2012 – March 31, 2013

Progress in research and operations at the Texas A&M Cyclotron Institute is summarized in this report for the period April, 1, 2012 through March 31, 2013. The format follows that of previous years. Sections I through III contain reports from individual research projects. Operation and technical developments are given in Section IV. Section V lists the publications with Cyclotron Institute authors and the Appendix gives additional information including talks presented by members of the Institute during the past year. Once again, the full volume of this year's Progress in Research is available only on our web site (http://cyclotron.tamu.edu). *Since most of the contributions presented here are truly reports on progress in research, results and conclusions should not be quoted from the report without the consent of the authors.*

We have now completed 8 1/2 years of the Upgrade Project, which will give us accelerated radioactive beams at intermediate energies. The K150 cyclotron is fully operational and has been used for a number of experiments with both positive-ion and negative-ion stable beams. Recently, commissioning work on the light-ion guide system has begun with a K150 beam. The full transport system for radioactive ions and charge breeding from the charge-breeding ECR source have been tested with a 1^+ ion source. Test results show that the efficiency of accelerated beam in the K500 cyclotron exceeds that used in RIB yield estimates. The high-power beam dump was completed during this last year and is being installed for production of Light Ion Guide beams. A cryopanel for the K150 cyclotron was built and recently installed. In July, it will be tested with LN_2 cooling. Also the heavy-ion guide system was recently transported to TAMU from Argonne National Laboratory and is now being installed in the ion-guide cave.

We completed a search for a new faculty member to join the Department of Physics & Astronomy with joint appointments in the Cyclotron Institute and the Nuclear Solutions Institute when Professor Grigory Rogachev, currently at Florida State University, accepted a position with us to begin in September, 2013.

We have had a major disruption in Institute activities this past year with the on-going construction of an additional floor of offices at the Institute. The construction project was completed in mid-May, 2013. Faculty, staff, and students who had been displaced during the construction were moved back into the upgraded office building by the end of May.

As in previous reports, I include here some highlights of work carried out over the past year.

- Recent experiments show evidence for an N/Z dependence of the nuclear caloric curve.
- After many years of incremental improvements, the group studying superallowed beta decay has successfully reached its goal of determining the branching-ratio for a superallowed beta-transition to a precision of 0.1% in the presence of other strong branches. Their proof of principle was the case of ^{38}Ca decay but this accomplishment is crucial for the characterization of all T_z = -1 parent decays,

which—unlike $T_z = 0$ decays—exhibit a number of strong Gamow-Teller branches that compete with the superallowed Fermi branch.

- A number of theoretical astrophysical EOS models have been experimentally tested by measuring cluster yields in low density nuclear matter. These new experimental data for cluster equilibrium constants provide important constraints on low density equations of state. The data strongly indicate that accounting for in-medium effects, as in the semi-empirical excluded volume approximation or a more sophisticated Quantum Statistical Model approach is required.
- Calculations based on a new theoretical approach show sensitivity to spectroscopic factors that are determined in ^{14}C+n when the asymptotic normalization coefficient is used in constraining the calculations.
- In recent work, the excitation function of the ^{154}Gd(^{48}Ca,4n)^{198}Po reaction has been measured. The results clearly demonstrate the influence on the compound nucleus survival probability of the difference in fission barrier height and neutron binding energy.
- Preliminary STAR inclusive jet A_{LL} results from 2009 were included in a global analysis of polarized parton distributions for the first time. They provide the first indication of non-zero gluon polarization within the momentum range that is sampled at RHIC.
- Based on the NJL model for the baryon-rich quark-gluon plasma produced in relativistic heavy ion collisions, we have demonstrated that the experimentally observed splitting of particle and antiparticle elliptic flows can help constrain the quark vector interaction and thus the equation of state of the baryon-rich quark-gluon plasma.
- Hartree-Fock based random-phase-approximation results for the energies of isoscalar and isovector giant resonances of multipolarities L=0-3 in ^{208}Pb, obtained for over 35 commonly used Skyrme interactions, were compared with experimental data to pin down the values of nuclear matter properties that are needed to improve the predictive power of our successful KDE0v1 energy density functional.
- A new theory of deuteron stripping reactions populating bound states and resonances based on the surface integral formalism, R matrix and CDCC was developed. A new generalized Faddeev formalism, which takes into account target excitations and explicitly includes the Coulomb interaction for deuteron stripping reactions, was developed.
- We have used multiplicity and quadrupole fluctuations from heavy ion collisions (both theory and experiment) to determine the density and temperature in fragmentation. Those quantities were determined for fermions (protons and neutrons) as well as bosons (deuterons and alpha particles). We showed that the energy density vs T scales for different particle types once Coulomb corrections are included.
- Theoretical predictions for the excitation function of low-mass dilepton spectra turn out to be in good agreement with STAR data from the RHIC beam-energy scan, from top RHIC energy down to SPS energies.
- Recent theoretical work suggests using Ds mesons (charm-strange bound states) as a unique probe of heavy-flavor dynamics in ultra-relativsitic heavy ion collisions. Comparison of Ds- to D-meson

observables can discriminate effects of heavy-quark hadronization and hadronic diffusion on transport coefficients. Preliminary data from the ALICE experiment confirm the validity of this idea.

- Commissioning has begun on the gas-filled RFQ in the Penning Trap beam line, and though no optimization has occurred yet, the efficiency is ~60%. This is already close to that obtained at other facilities now in operation.
- The characterization of the efficiency of a new gas stopper as a function of ion energy, gas flow rate, and electric field strength has been carried out.
- A forward array-quadrupole triplet spectrometer system for studying the asymmetry dependence of heavy ion breakup mechanisms in Xe and Sn + Ni reactions below the Fermi energy has been commissioned.

Institute scientists remain active in a number of collaborative research efforts around the world. Major programs include: mass measurements using the Penning Trap at the University of Jyväskylä; continued work with the STAR collaboration at RHIC; measurements of beta decays with the TRINAT collaboration at TRIUMF; and participation in the SAMURAI collaboration at RIBF in Tokyo, Japan.

Once again, I am indebted to Dr. Y.-W. Lui for assembling this report.

R.E. Tribble
June 30, 2013

SECTION I

NUCLEAR STRUCTURE, FUNDAMENTAL INTERACTIONS AND ASTROPHYSICS

Superallowed beta decay

J. C. Hardy, I. S. Towner, V. E. Iacob, H. I. Park, L. Chen, V. Horvat, N. Nica,
M. Bencomo and R. E. Tribble

Superallowed $0^+ \rightarrow 0^+$ beta decay between T=1 analogue states has been a subject of continuous and often intense study for five decades. The *ft* values of such transitions are nearly independent of nuclear-structure ambiguities and depend uniquely on the vector part of the weak interaction. Their measurement gives us access to clean tests of some of the fundamental precepts of weak-interaction theory, and, over the years, this strong motivation has led to very high precision being achieved in both the experiments and the theory used to interpret them. We have a major program at the Cyclotron Institute to study superallowed beta decay.

To obtain the *ft* value for any transition, three quantities must be measured: the half-life of the parent, the Q_{EC} value for the transition of interest, and the branching ratio for that transition. Our most recent complete survey of existing data on these superallowed decays, published in 2009 [1], provided a critical evaluation of all the experimental data and obtained final *ft* values from the averaged results, to which improved radiative and isospin-symmetry-breaking corrections [2] were applied in order to derive a final set of "corrected ft values", denoted $\mathcal{F}t$ (see Fig. 1). One of the new features added at that time was that we calculated the radial-overlap correction, δ_{C2}, with Hartree-Fock radial wave functions as well as the Saxon-Woods wave functions we have used before. The differences in the results from these two methods are used as a measure of the systematic uncertainty to be applied to the theoretical corrections. These differences also offer the possibility that measured *ft* values with the highest precision could actually distinguish between the two methods and thereby reduce the systematic uncertainty.

With the updated world data and improved corrections the $\mathcal{F}t$ values were seen to be completely consistent with one another, thus demonstrating the constancy of G_V to 1.3 parts in 10^4. Not only is this an important confirmation of the Conserved Vector Current (CVC) hypothesis but it sets the stage for using the average value of G_V to test a fundamental principle of the electroweak standard model: the unitarity of the Cabibbo-Kobayashi-Maskawa (CKM) matrix. The up-down quark mixing element of that matrix, V_{ud}, is given by $V_{ud} = G_V / G_F$, where G_F is the weak interaction constant for the purely leptonic muon decay. The value of V_{ud} is a key component of the most demanding test available for the unitarity of the CKM matrix, the sum of squares of its top-row elements [1]. As elaborated in our 2010 review article on the evaluation of V_{ud} [3], superallowed nuclear beta decays provide by far the most precise and reliable value for V_{ud} and, in fact, that element is also the most precisely known one in the CKM matrix – by an order of magnitude! Its current value [1,3,4] is 0.97425(22), a result that yields the most up-to-date CKM unitarity sum of 1.0008(56) [4], in full agreement with the standard-model expectation, and carrying the smallest uncertainty yet obtained.

This result is not only a significant verification of the standard model but the uncertainty quoted on the sum provides a tight limit on any possible new physics beyond the standard model, such as right-hand currents, extra *Z* bosons or supersymmetric models. In short, superallowed $0^+ \rightarrow 0^+$ beta

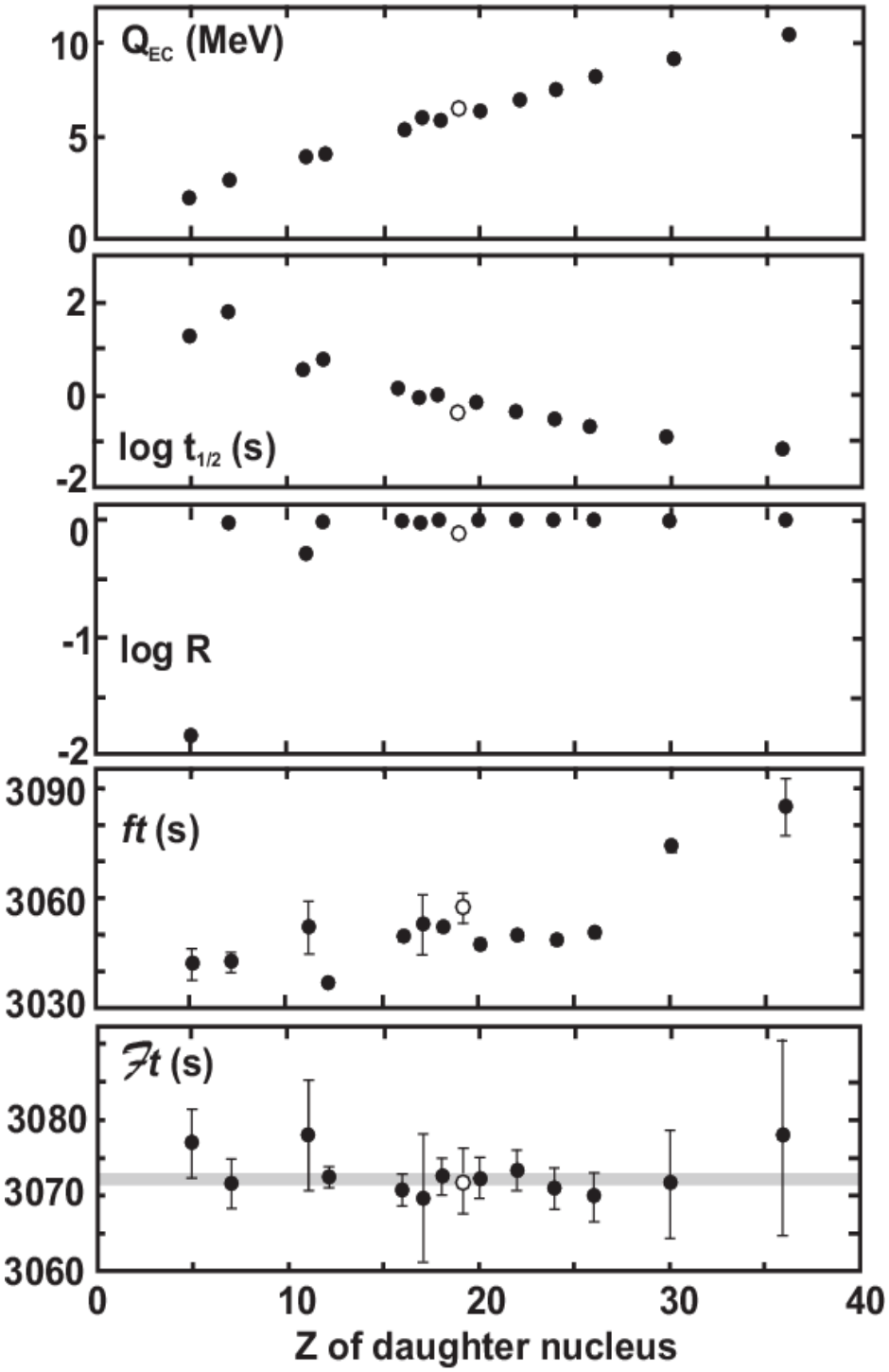

FIG. 1. Results from the most recent survey of 13 precisely measured superallowed $0^+ \rightarrow 0^+$ β transitions appear as solid black circles. The parents of these transitions, from left to right, are ^{10}C, ^{14}O, ^{22}Mg, ^{26}Al^m, ^{34}Cl, ^{34}Ar, ^{38}K^m, ^{42}Sc, ^{46}V, ^{50}Mn, ^{54}Co, ^{62}Ga and ^{74}Rb. The top three panels present the average of measured Q_{EC}, log $t_{1/2}$ and log R (branching ratio) values for each transition. The bottom two panels give the corresponding *ft* and $\mathcal{F}t$ values. The shaded horizontal line in the bottom panel represents the overall average $\mathcal{F}t$ value for all transitions. All error bars are shown: in the cases where none are visible, they are smaller than the data point. Recent results for ^{38}Ca are shown as open circles.

decay

provides a high-profile application of nuclear-physics measurements to the study of fundamental symmetries, a subject of vital interest to both nuclear and particle physicists. Although much has already been achieved in this field by nuclear physicists, improvements are still possible. Reducing the uncertainty on the unitarity sum – and, with it, the scope for new physics – remains the primary goal of our research program.

Our approach follows from the observation [1,3,4] that the second largest contributor to the uncertainty in V_{ud} is the theoretical uncertainty in the nuclear-structure-dependent corrections, δ_{NS} and δ_C, used in the derivation of the $\mathcal{F}t$ values. Though these corrections are only of order 1%, their effect is very significant: The bottom two panels of Fig. 1 show the result of applying δ_{NS} and δ_C (together with δ'_R, which is nearly independent of *Z*). Obviously they act very well to remove the considerable "scatter" in *ft* values apparent in the second panel from the bottom, replacing it with the consistent set of corrected $\mathcal{F}t$ values appearing in the bottom panel. Since these corrections were determined [2] completely independently of the superallowed decay data, this consistency in $\mathcal{F}t$ values is already a powerful validation of these calculated corrections, but obviously the remaining uncertainty still influences the final result for V_{ud}.

Even though the 2009 survey [1] included more than 145 individual measurements relating to 13 precisely known *ft* values, it is still possible for well selected experiments to make real improvements in the validation tests of the nuclear-structure-dependent correction terms. At TAMU we are currently focusing on adding to the *ft*-value list new superallowed transitions, selected from amongst those with *large* calculated corrections. If the *ft* values measured for cases with large calculated corrections also turn into corrected $\mathcal{F}t$ values that are consistent with the others, then this must verify the calculations' reliability for the existing cases, which have smaller corrections. We are studying decays from T_z = -1 parent nuclei, which consistently have higher predicted structure-dependent correction terms than the well known T_z = 0 cases.

In that context, we believe that we have achieved a major milestone this past year: After many years of incremental improvements we have finally reached our goal of determining the branching-ratio for a superallowed β-branch to a precision of 0.1% in the presence of other strong branches. This is crucial for the characterization of T_z = -1 parent decays, which – unlike T_Z = 0 decays – exhibit a number of strong Gamow-Teller branches that compete with the superallowed Fermi branch. After making considerable improvements to our electronics and data-acquisition system [5] using off-line sources to generate β-γ coincidences, in September 2012 we made an on-line measurement of the decay of ^{38}Ca ($t_{1/2}$ = 444 ms), the analysis of which is now nearly complete [6].

We expect that we will be able to quote the branching ratio for the Gamow-Teller branches from ^{38}Ca to a relative precision of about 0.3%. Since these branches represent ~23% of the decays from ^{38}Ca, the relative precision on the superallowed Fermi branch, which is determined by subtraction from 100%, will be at or below 0.1%. It thus would be the first measurement of a T_Z = -1 emitter with significant non-superallowed branches to be measured with a precision of 0.1%, and will complete all the data required for a precise *ft*-value result for ^{38}Ca.

To our knowledge, this promises to be the most precise branching-ratio measurement ever made for short-lived beta emitter. It will also provide the first mirror pair of $0^+ \rightarrow 0^+$ superallowed emitters (^{38}Ca and $^{38}K^m$) and will make possible a more demanding test of the isospin symmetry-breaking correction, δ_C, used to extract V_{ud} from the measured *ft* values. By improving our ability to discriminate among the different calculations of δ_C, measurements of $T_Z = -1$ emitters like ^{26}Si, ^{34}Ar and ^{38}Ca, can potentially lead to reduced uncertainties on δ_C and ultimately to reduced uncertainties on V_{ud} as well as the unitary sum for the Cabibbo-Kobayashi-Maskawa matrix. This approach to testing δ_C calculations was first proposed by us and has been discussed in detail in Ref. [7] and in this progress report [8].

We are also endeavoring to improve our data acquisition techniques for half-life measurements by a variety of means, including a new TDC-based data-acquisition system, which allows us to determine half-lives by time-interval analysis [9], and a digital-pulse-analysis system for the signals from our 4π proportional gas counter, with which we have now measured a new more precise value for the half-life of $^{26}Al^m$ [10]. We have worked to eliminate spurious pulses and to reduce, or improve our handling of our system dead time. We have achieved some modest success towards this goal, as evidenced by the improved $^{26}Al^m$ result, but have had to conclude that our count-rate will now be limited, not by our electronics, but by the inherent properties of our gas counter.

[1] J.C. Hardy and I.S. Towner, Phys. Rev. C **79**, 055502 (2009).

[2] I.S. Towner and J.C. Hardy, Phys. Rev. C **77**, 025501 (2008).

[3] I.S. Towner and J.C. Hardy, Rep. Prog. Phys. **73**, 046301 (2010).

[4] J.C. Hardy and I.S. Towner, Ann. Phys. (Berlin), 1-9 (2013)/DOI 10.1002/ andp. 201300004.

[5] V.E. Iacob, H.I. Park and J.C. Hardy, *Progress in Research,* Cyclotron Institute, Texas A&M University (2011-2012), p. V-21; and V.E. Iacob, H.I. Park and J.C. Hardy, *Progress in Research,* Cyclotron Institute, Texas A&M University (2012-2013), p. IV-43.

[6] H.I. Park, J.C. Hardy, V.E. Iacob, M. Bencomo, L. Chan, V. Horvat, N. Nica, B.T. Roeder, E. Simmons and R.E. Tribble, *Progress in Research,* Cyclotron Institute, Texas A&M University (2012-2013), p. I-11.

[7] I.S. Towner and J.C. Hardy, Phys. Rev. C **82**, 065501 (2010).

[8] I.S. Towner and J.C. Hardy, *Progress in Research,* Cyclotron Institute, Texas A&M University (2012-2013), p. III-53.

[9] V. Horvat and J.C. Hardy, *Progress in Research,* Cyclotron Institute, Texas A&M University (2012-2013), p. IV-38; and Nucl. Instrum. Methods Phys Res. **A713**, 19 (2013).

[10] L. Chen, J.C. Hardy, M. Bencomo, V. Horvat, N. Nica and H.I. Park, *Progress in Research,* Cyclotron Institute, Texas A&M University (2012-2013), p. IV-33; and Nucl. Instrum. Methods Phys Res. A. (submitted).

Tests of internal-conversion theory with precise γ- and x-ray spectroscopy: the case of $^{119}Sn^{m}$

N. Nica, J. C. Hardy, V. E. Iacob, M. Maguire, and M. B. Trzhaskovskaya[1]
[1]*Petersburg Nuclear Physics Institute, Gatchina RU-188300, Russia*

Internal conversion is an important component of most nuclear decay schemes. In order to balance decay schemes correctly, one needs to know the internal conversion contribution to each transition as expressed by its internal conversion coefficient (ICC). Nevertheless, ICCs are only rarely measured; instead they are taken from tabulations. As a result, calculated ICCs are essential input to every decay scheme, except those for the lightest nuclei. Unfortunately, over the decades, tabulated ICC values have differed significantly from one calculation to another by a few percent. Although for many applications such differences can be tolerated, transitions used in critical calibrations require very precise and accurate ICC values, precision that has simply been impossible to guarantee at the one-percent level or below.

In order to correct for this deficiency one can only seek guidance from measured ICCs that have sufficient precision to distinguish among the various calculations. However, as recently as ten years ago, when a survey of measured ICCs was made by Raman et al. [1], there were only five published ICC values with precision of the order of ±1%, not enough to make any definitive conclusion possible. At that time, one aspect of the ICC calculations remained a particular concern. The final-state electron wave function must be calculated in a field that adequately represents the remaining atom. But should that representation include the atomic vacancy created by the conversion process? Some calculations included it and some did not.

Thus the problem of measuring ICCs at the ±1% precision level became critical and, with our very precisely efficiency-calibrated HPGe detector [2], we found ourselves in a position to be able to address it. Consequently, over the past decade we have been measuring a series of ICCs [3,4] covering a wide range of atomic numbers. So far, all these results have indicated that the atomic vacancy should be taken into account in the calculations. The new case reported here, a 65.7-keV M4 transition in ^{119}Sn, extends our measurements to lower Z than any case we have yet studied.

For an isolated electromagnetic transition that converts in the atomic *K* shell, the observation of a *K* x ray is a signal that an electron conversion has taken place; whereas a γ ray indicates that no conversion has taken place. If both x rays and γ rays are recorded in a measurement, then the value of α_K is given by

$$\alpha_K \omega_K = \frac{N_K}{N_\gamma} \cdot \frac{\varepsilon_\gamma}{\varepsilon_K} \quad , \qquad (1)$$

where ω_K is the fluorescence yield that we take from Ref. [5]; N_K and N_γ are the respective peak areas of the K x rays and the γ ray; and ε_K and ε_γ are the corresponding detector absolute efficiencies. As described

in Ref. [2] ε_γ for a 65.7-keV γ ray in our detector is known to ±0.15% relative precision; however a special investigation was required in order to get a precise value for ε_K at the ~25-keV energy of the Sn K x rays.

As described in our previous progress report [6], two impurities in the source affected the 65.7-keV γ ray: ^{182}Ta and ^{75}Se both produced γ rays that contributed about 68% of a broad group that appeared at 66 keV. Since ^{118}Sn has a very low thermal-neutron capture cross section of about 10 mb for the production of ^{119}Sn^m, and the 65.7-keV transition from that isomer has a total ICC of about 5000, the emission of 65.7-keV γ rays is so much hindered that even very weak impurities with high activation cross sections can compete strongly if, unfortunately, they emit γ rays at nearly the same energy. Conveniently though the halflives of ^{182}Ta (120 d) and ^{75}Se (115 d) are significantly shorter than that of ^{119}Sn^m (293 d). We simply re-measured the source 19 months after it had first been activated, after which time the two contaminant activities had decreased by a factor of 7 or 8 compared to ^{119}Sn^m. In that spectrum the summed contribution of ^{75}Se and ^{182}Ta to the 66-keV group was only 7.6%, an amount easily corrected for. The already small contribution to the K x-rays from other tin isotopes was also reduced, to about 1%. Finally, since almost all other impurities were also shorter lived than ^{119}Sn^m, there were no intense γ rays left in the spectrum at energies above 65.7 keV, so the Compton background was reduced drastically at 66 keV, which consequently greatly improved the peak-to-background ratio for the peak whose intensity we needed to determine.

Some of the photons from a radioactive source scatter from nearby materials – including air – in the vicinity of the detector setup and, entering the detector, they form a continuum in the energy spectrum extending to lower energy from the peak created by the unscattered photons. For photons above ~50 keV this continuum is rather flat and extends to energies well below the corresponding peak so, by extrapolation, its contribution to the area of the peak can easily be determined and removed. However, for peaks with energies as low as 25.2 keV and 28.6 keV, the energies of the tin K_α and K_β x rays respectively, the continuum is more like a shelf that extends only 2-3 keV below the peak energy. At our energy resolution of ~1 keV in this region, an important part of the continuum gets "hidden" in, and potentially counted together with, the peak itself. The number of counts in the "hidden" continuum is very dependent not only on the source-detector geometry, but also on the details of its neighborhood. For this reason it is impossible to define a universal efficiency calibration with useful precision below ~50 keV. Rather, one must examine each geometry as a special case, which must be calibrated based on its specific properties.

We followed two different approaches to this part of the analysis. In the first, described fully in our paper on ^{134}Cs and ^{137}Ba [4], we employed Monte Carlo calculations with the CYLTRAN code – the same code used in our calibration procedures [2] – to simulate the scattering "shelf"; then we scaled up the result to match the small component of the shelf visible in the data; and finally used that scaled-up result to determine the component of the shelf contained within the peak.

Our second approach was to measure a calibration source, ^{109}Cd, which decays by electron capture to ^{109}Ag followed by the emission of a unique 88.0-keV M4 γ transition. The K x rays of silver, following both the electron capture decay and the electron conversion of the 88.0-keV transition, form prominent x-ray groups situated at 22.1 keV (K_α) and 25.0 keV (K_β). The K x-rays together with the 88.0-

keV γ ray can be used with a formula similar to eq. (1) to deduce ε_K at silver K x-rays energies if we use calculated α_K values for 88.0-keV transition in ^{109}Ag. By taking the mean value of calculated 'hole' and 'no hole' α_K values with an uncertainty encompassing both, we obtain an α_K value that is independent of the treatment of the atomic vacancy. Then by short interpolation from silver K x-ray energies to tin K x-ray energies, we can arrive at ε_K values for tin with a total uncertainty of about ±1%. This result and the CYLTRAN-based value are in good agreement (within 0.3%), so we can confidently use the combined result for ε_K in Eq. (1) to extract the α_K value for the 65.7-keV γ transition from ^{119}Sn^m.

Our still preliminary value, α_K = 1610(27), is in good agreement with the 'hole' calculation, which predict 1618 in the "frozen orbital" approximation, and in disagreement with the 'no hole' calculation, which predicts 1544. The current status of our series of measurements is given in Fig. 1, where it can be seen that our new result confirms and strengthens our conclusion that the atomic vacancy created by the internal conversion process must be taken into account when calculating ICCs.

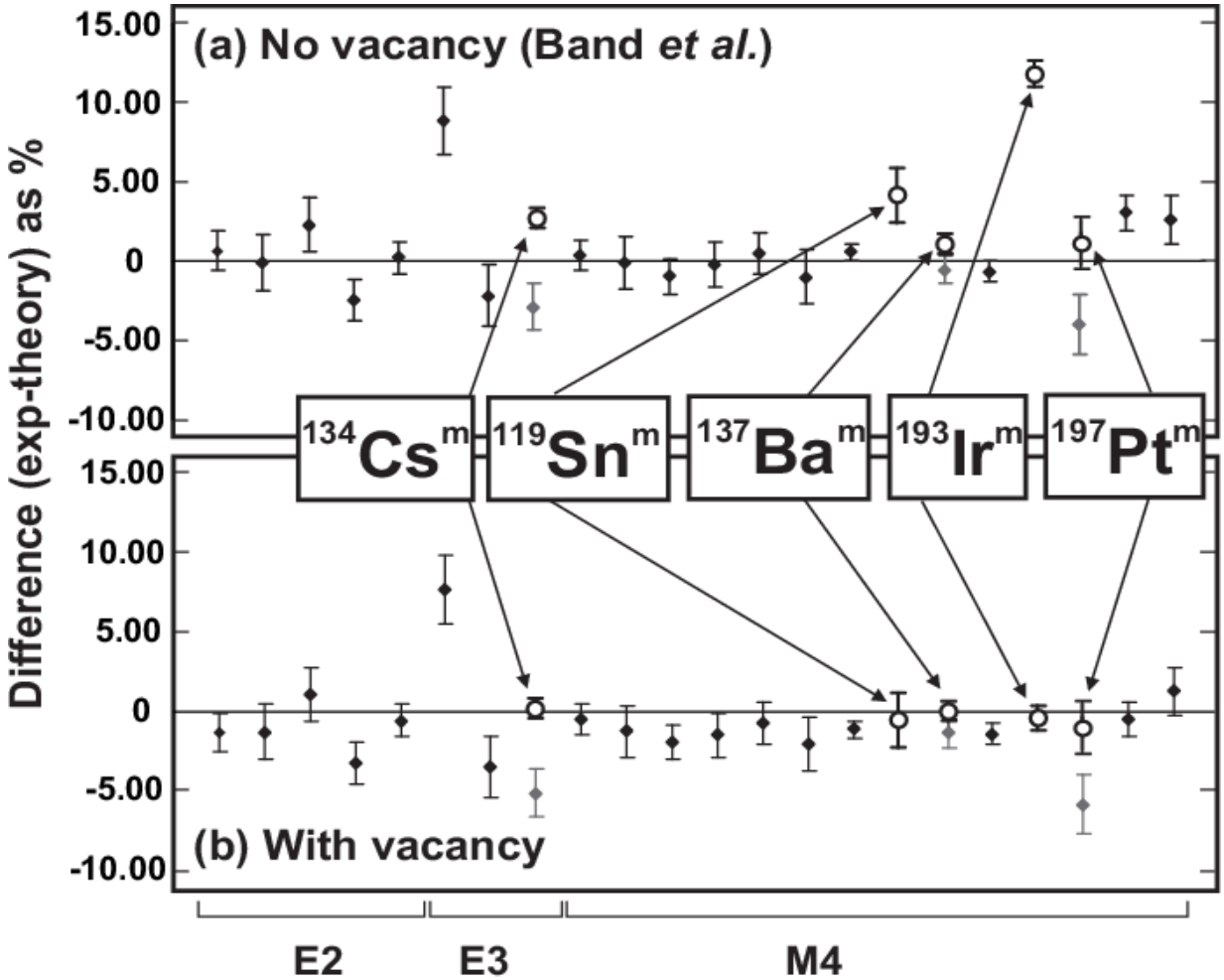

FIG. 1. Percentage differences between the measured and calculated ICCs for two Dirac-Fock calculations: one (a) is without the atomic vacancy and the other (b) is with it included in the ``frozen orbital'' approximation. The points shown as solid diamonds in both plots correspond to the twenty cases listed in Ref. [1] with better than 2% precision; as indicated at the bottom, five are for *E*2 transitions, three for *E*3, and the remainder are for *M*4 transitions. The points shown as open circles correspond to our five more-recently measured α_K values. For the cases of ^{134}Cs^m, ^{137}Ba and ^{197}Pt, the earlier Raman values are shown in grey; for ^{119}Sn^m and ^{193}Ir^m there were no earlier values with sub-2% precision.

[1] S. Raman *et al.*, Phys. Rev. C **66**, 044312 (2002).

[2] J.C. Hardy *et al.*, Appl. Radiat. Isot. **56**, 65 (2002) ; R. G. Helmer *et al.*, Nucl. Instrum. Methods Phys. Res. **A511**, 360 (2003); R. G. Helmer *et al.*, Appl. Radiat. Isot. **60**, 173 (2004).

[3] N. Nica *et al.*, Phys. Rev. C **70**, 054305 (2004); Phys. Rev. C **80**, 064314 (2009); Phys. Rev. C **71**, 054320 (2005); Phys. Rev. C **77**, 034306 (2008).

[4] N. Nica *et al.*, Phys. Rev. C **75**, 024308 (2007).

[5] E. Schönfeld and H. Janssen, Nucl. Instrum. Methods Phys. Res. **A369,** 527 (1996).

[6] N. Nica *et al.*, *Progress in Research,* Cyclotron Institute, Texas A&M University (2011-2012), p. I-10.

United States nuclear structure data program (USNDP) and evaluated nuclear structure data file (ENSDF) at Texas A&M University

N. Nica[1] and J. C. Hardy
[1]Under contract with Brookhaven National Laboratory

Since 2005 we have been an important partner in the nationwide *United States Nuclear Data Program* (USNDP), which is part of the *Nuclear Structure and Decay Data* (NSDD) international nuclear data evaluation network. USNDP is in fact the backbone of the NSDD network, making the greatest effort in completion of the goals of the nuclear-structure data-evaluation communities. Nuclear data evaluation is a national-interest activity financed by DOE, through which relevant nuclear-science results in virtually all world publications are retrieved and put together in a large *Evaluated Nuclear Structure Data File* (ENSDF) database according to *general policies,* a set of rules that make possible a standard approach through which the data are uniformly evaluated.

This activity is carried by a relatively small group of professionals located mostly in national institutes but also hosted by a few universities. The nuclear data network is the nodal point for the wide dissemination of nuclear knowledge to many users, from those in basic science to those engaged in commercial applications in American and international businesses. The output is published in the Nuclear Data Sheets, an Elsevier publication, and also is disseminated by different on-line databases, which can be retrieved at the NNDC site (http://www.nndc.bnl.gov), IAEA Vienna's site (http://www-nds.iaea.org) and several other locations.

For eight years now at Texas A&M we have covered mass chains from essentially all the regions of the periodic table. Up to the past year we have published in Nuclear Data Sheets the superheavy A=252 mass chain [1]; the very data-rich mid-mass chains, A=147 [2] and A=140 [3]; the relatively lighter chains, A=97 [4] and A=84 [5]; and, in collaboration with B. Singh and a group of authors from McMaster University, Canada, we also published the A=77 [6], A=37 [7], A=36 [8], and A=34 [9] chains. Another mass chain, A=148, which was completed then, is now in the process of final corrections after the review process. Since nuclear-data evaluation depends critically on the experience of the evaluator, with a veteran evaluator typically completing only a couple of mass chains per year, coverage of such a wide range of A chains in a short time at a contracted effort of 0.67 FTE per year is a considerable accomplishment.

During the past year we covered a relatively heavy mass chain, A=141, which has been submitted and is currently being reviewed. We have also started the evaluation of A=158, by considering all world publications since 2003, when the previous full evaluation of this mass chain was published. The chain includes Pr, Nd, Pm, Sm, Eu, Gd, Tb, Dy, Ho, Er, Tm, Yb, Lu, Hf, Ta, and W, a total of 16 nuclei. More than 250 papers have been published during this interval. The work is in progress.

[1] N.Nica, Nucl. Data Sheets **106**, 813 (2005).
[2] N.Nica, Nucl. Data Sheets **110**, 749 (2009).

[3] N.Nica, Nucl. Data Sheets **108**, 1287 (2007).
[4] N.Nica, Nucl. Data Sheets **111**, 525 (2010).
[5] D.Abriola *et al.*, Nucl. Data Sheets **110**, 2815 (2009).
[6] B. Singh, N.Nica, Nucl. Data Sheets **113**, 1115 (2012).
[7] J. Cameron, J. Chen, B. Singh, and N. Nica, Nucl. Data Sheets **113**, 365 (2012).
[8] N. Nica, J. Cameron, and B. Singh, Nucl. Data Sheets **113**, 1 (2012).
[9] N. Nica and B. Singh, Nucl. Data Sheets **113**, 1563 (2012).

Measurement of branching-ratios in the β decay of ^{38}Ca

H.I. Park, J.C. Hardy, V.E. Iacob, M. Bencomo, L. Chen, V. Horvat, N. Nica, B.T. Roeder, E. Simmons and R.E. Tribble

A major upgrade to our data-acquisition electronics was completed in 2012 based on the lessons we had learned [1, 2] from our two previous branching-ratio measurements of ^{38}Ca and our off-line tests with a ^{22}Na source. One key improvement was to reduce the number of events that triggered as β-γ coincidences but were recorded as incomplete, from 3.5% to 0.3%, by minimizing the chance of overlap between successive β-γ coincidence pulses. Another improvement we implemented was to independently measure electronic dead-times on a cycle-by-cycle basis by inserting pulser signals from a constant frequency pulse generator in coincidence with gating signals from β-singles events, γ-singles events, and β-γ coincidence events. These improvements allowed our third measurement of the ^{38}Ca branching ratios in the fall of 2012 to be fully successful.

Once again, the ^{1}H(^{39}K, 2n)^{38}Ca reaction in inverse kinematics was used to produce pure ^{38}Ca nuclei at a ^{39}K beam energy of 30*A* MeV, and our fast tape-transport system was used to repetitively move collected samples to a well-shielded counting location where they were stopped between a 1-mm-thick plastic scintillator for β particles and our well-calibrated 70% HPGe detector for the γ rays. Time-tagged β-γ coincidences were recorded event by event.

At the beginning of this experiment, we thoroughly examined the response of our system immediately after the counting began as the sample arrived at the counting location. In the analysis of our last experiment we could find no β-γ coincidence events recorded for the first 45 ms of the 1.6-s count time and we were concerned that our system might have been effectively blocked for that period as a result of a high counting rate, possibly linked to the primary beam that had only just been interrupted. Our investigation concluded instead that the blank period in our data stream was caused by a delay in the operation of our tape-brakes, which meant that the tape came to rest 45 ms after the electronic stop signal had been issued to them. To accommodate this fact, we delayed the beginning of the count period by 60 ms, thus ensuring that the implanted ^{38}Ca nuclei were precisely positioned between the detectors before the counting period began. We also set a 0.5-s interval between the end of one cycle and the beginning of the next in order to leave sufficient time for the data from that cycle to be transferred to the computer.

Our time base for the measurement thus became 1.6-s collect, 0.229-s move, 1.54-s count, and 0.5-s delay for each cycle. During 7 days of beam time, approximately 9 million β-γ coincidence events were collected from over 370 million β singles in 60,847 cycles separated into 61 separate runs. A measurement of β-γ coincidences with a ^{22}Na source followed at the end of the branching-ratio experiment for ^{38}Ca. Since the branching ratio for ^{22}Na β^+ decay is precisely known and is essentially 100%, this measurement served the purpose of independently checking the response of our system to positrons and high-energy γ rays comparable to those from ^{38}Ca.

The analysis of this experiment is nearly complete and will lead to our final result for the superallowed branching ratio of ^{38}Ca, with its associated uncertainty budget. We expect that we will be able to quote the branching ratio for the Gamow-Teller branches from ^{38}Ca to a relative precision of about

0.3%. Since these branches represent ~23% of the decays from ^{38}Ca, the relative precision on the superallowed Fermi branch, which is determined by subtraction from 100%, will be at or below 0.1%. It thus would be the first measurement of a T_Z = -1 emitter with significant non-superallowed branches to be measured with a precision of 0.1%, and will complete all the data required for a precise *ft*-value result for ^{38}Ca.

To our knowledge, this promises to be the most precise branching-ratio measurement ever made for short-lived beta emitter. It will also provide the first mirror pair of $0^+ \rightarrow 0^+$ superallowed emitters (^{38}Ca and ^{38}K^m) and will make possible a more demanding test of the isospin symmetry-breaking correction, δ_C, used to extract V_{ud} from the measured *ft* values. By improving our ability to discriminate among the different calculations of δ_C, measurements of T_Z = -1 emitters like ^{26}Si, ^{34}Ar and ^{38}Ca, can potentially lead to reduced uncertainties on δ_C and ultimately to reduced uncertainties on V_{ud} as well as the unitary sum for the Cabibbo-Kobayashi-Maskawa matrix.

[1] H.I. Park, J.C. Hardy, V.E. Iacob, M. Bencomo, L. Chen, J.R. Goodwin, V. Horvat, N. Nica, B.T. Roeder, L. Trache and R.E. Tribble, *Progress in Research*, Cyclotron Institute, Texas A&M University (2011-2012), p. I-7.

[2] V.E. Iacob, J.C. Hardy, and H.I. Park, *Progress in Research*, Cyclotron Institute, Texas A&M University (2011-2012), p. V-21.

Optical pumping model of the polarization for the TRINAT experiment

R. S. Behling, B. Fenker, M. Mehlman, D. Melconian and P. D. Shidling

The TRIUMF Neutral Atom Trap (TRINAT) has an active experimental program to measure angular correlations in the β^+ decay of spin-polarized ^{37}K. An overview of our recent progress including a successful run in December 2012 is described in our other report. This report will focus on our progress in developing a better model of the optical-pumping process that polarizes the trapped atoms.

Optical pumping uses circularly polarized laser light to drive the potassium atoms' single valence electron to an extreme Zeeman sublevel which, due to the hyperfine coupling of atomic and nuclear angular momenta, corresponds to complete atomic and nuclear polarization. An atom in a ground state absorbs a circularly polarized photon, which promotes it to an excited state and imparts an additional unit of angular momentum to the atom. Once in the excited state, the atom quickly decays; the emitted photon can have any polarization. Through a series of repeated absorptions and emissions, the atom undergoes a biased random walk to an extreme sublevel. Once in this sublevel, called the stretched state, the atom can no longer absorb a photon as there is no excited state with the appropriate quantum numbers to conserve angular momentum. A schematic diagram of this process is shown in the Fig.1. Once an atom reaches the stretched state, it is both trapped in that state and completely polarized, an ideal combination for our polarized decay studies.

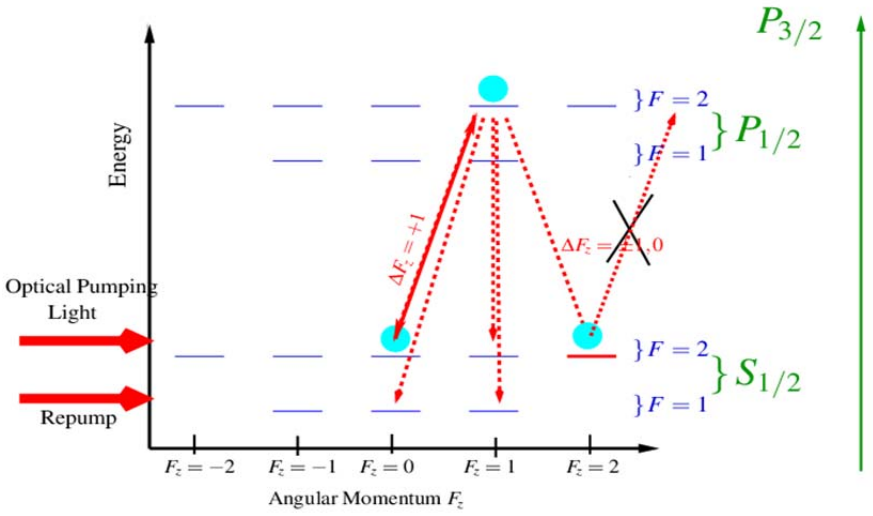

FIG. 1. Outline of the optical pumping process including the steps in the biased random walk. The quantum number F is the combined nuclear and atomic angular momentum. The stretched state is highlighted in red.

Using our current apparatus we are able to achieve polarization of 99%. To measure the polarization with the necessary precision (< 1%) requires a detailed atomic model of the process. The excited state population is monitored experimentally by photoionizing only atoms in these states and observing the resulting photoions. As atoms accumulate in the stretched state, they are no longer able to

be excited and possibly photoionized. Therefore, a decrease in photoionization implies an increase in nuclear polarization, and an accurate model is required to quantitatively relate the two.

In the last year, we have improved our model to correctly account for effects that could have a negative impact on the degree of nuclear polarization. Previous models have used the rate-equation approach that essentially treats the atoms classically [1, 2]. Our improved model uses the density matrix formalism to treat the atoms quantum mechanically [3]. One important effect that is now included is the existence of coherently trapped populations, or CPT states [4]. These states arise from a coherence between two ground states with the same F quantum number but different F_Z when the main optical-pumping laser and repump laser (see figure above) have an energy difference exactly equal to the energy difference of the two states. The result of this coherence is a state that does not absorb the optical-pumping light and is also not polarized. Since atoms in this state are not available to be photoionized, we cannot experimentally distinguish unpolarized atoms trapped in the CPT states from polarized atoms trapped in the stretched state and we must rely on our model to correctly relate the decreasing fluorescence to increasing polarization. Our improved density matrix model correctly considers CPT states whereas the previous rate-equation approach was unable to include them.

Another important advantage of this approach is that any magnetic field transverse to the optical pumping axis can be precisely modeled [5]. A transverse magnetic field causes atoms to precess out of the stretched state and become depolarized. Although this misalignment is estimated be less than 2°, it can have a significant impact on the degree of nuclear polarization and is now included in our theoretical model.

The improved optical-pumping model allows for a more precise determination of the nuclear polarization, an important systematic uncertainty in previous versions of the experiment [1]. For the December 2012 run, we have too few photoion events to use this technique to determine the polarization, but the improved model will still be useful in off-line studies of stable ^{41}K as well as in recommending ideal frequencies for the optical-pumping lasers. In the future, we plan to increase the power of the photoionization laser in order to create enough photoions to measure the nuclear polarization of radioactive ^{37}K as described above. In April 2013, Benjamin Fenker successfully presented this model for a non-thesis option M.S. Degree.

In order to measure the polarization for our recent run, we will rely on a measurement of the position asymmetry of recoiling Ar ions on a micro-channel plate using a delay line anode for the necessary position sensitivity. The recoil asymmetry along the polarization axis is only sensitive to tensor interactions which are well constrained by other experiments [6, 7]. Therefore, the standard model prediction is well known and an experimental measurement of the asymmetry can be used to extract information about the degree of polarization. We are currently performing this analysis and will complete it in the upcoming year.

[1] D. Melconian *et al.*, Phys. Lett. B **649**, 370 (2007).
[2] Y. Nafcha *et al.*, Phys. Rev. A **52**, 3216 (1995).
[3] P. Tremblay and C. Jacques, Phys. Rev. A **41**, 4989 (1990).
[4] S. Gu *et al.*, Opt. Comm. **220**, 365 (2003).
[5] F. Renzoni *et al.*, Phys. Rev. A **63**, 1 (2001).

[6] S.B. Treiman, Phys. Rev. 110, **448** (1958).
[7] N. Severijns and O. Naviliat-Cuncic, Phys. Scripta **T152**, 014018 (2013).

Update on the progress of the ^{37}K β asymmetry experiment

R. S. Behling, B. Fenker, M. Mehlman, D. Melconian and P. D. Shidling

The standard model of particle physics makes predictions for the spin polarized observables of a nucleus that undergoes beta decay. The TRINAT collaboration made up of members from the Texas A&M University Cyclotron Institute and the TRIUMF laboratory in Vancouver BC have a well-established program of measuring these spin polarized observables in the beta decay of alkali atoms confined in a magneto optical trap. For a number of years an experiment has been preparing to measure for the first time the beta asymmetry of ^{37}K.

The beam for this experiment was taken in December 2012 at the TRIUMF laboratory. This experiment was an upgrade to a previous experiment carried out by the TRINAT collaboration in 2002 that did not publish a result for the beta asymmetry because of an uncontrolled systematic in the background. The upgrade to the experiment was extensive and the goal of the December run was not only to show physics improvement by publishing a meaningful value for the beta asymmetry but to also to demonstrate engineering improvements and characterize the system that the collaboration will now use to produce more precise measurements in the future. The experiment was successful in that we were able to have the whole system operate and run in most ways according to the design specification and according to preliminary analysis will have a measurement that will be statistics limited to the 1.5% level of precision. The new parts of the experiment that were successfully demonstrated were a new larger vacuum chamber to house the experiment, detection of shake-off electron, a new method of trapping the atoms, a new scheme for optically pumping the atoms, new detectors to measure the radioactive decay of the trapped ^{37}K, new VME modules to record the data, and finally new software to control the data acquisition.

The large vacuum chamber was designed so that a more uniform electric field could be achieved in the region between the atom cloud and the MCP detectors. The original design specification for the apparatus was that a 1 kV/cm electric field would be applied to this region allowing for total separation of charge states +1 and +2 in the ion time of flight spectrum. This goal was achieved but on the eve of the commencement of the experiment a spark shorted two of our electrostatic hoops together and we decided to run at a more modest 350 V/cm field to avoid further damaging the apparatus. Even at this lower voltage we had 100% collection of the shake-off electrons coming from the beta decay. The addition of this shake-off electron detector was one of the largest improvements over the previous experiment. Its value has already been shown in the data analysis by greatly reducing background from decays not originating in the trap.

In this experiment we used a new scheme for trapping the atoms know as an AC-MOT. We originally decided to implement this scheme because it would allow eddy currents in the wall of the chamber to die away faster than the traditional DC-MOT. This decrease in eddy currents would translate into more counting time. The AC-MOT delivered on this point. As a trade-off, the increased dispersion of the eddy fields heated the experimental apparatus more than the previous trap setup. This increased heating lead to a spike in the partial pressure of hydrogen in the system. The hydrogen pumping efficiency of the system had already been compromised by the failure of a non-evaporable getter pump.

The increased hydrogen load together with the decreased pumping efficiency meant that the measured trap lifetime of 0.6 s, about half of the radioactive lifetime of ^{37}K, was limited by collisions with stray hydrogen. These losses were a major contributor to the low count rates that we observed. These problems have all been subsequently addressed and should not be a problem in future experiments.

From previous TRINAT experiments we tried to improve on our ability to polarize the atoms since the quantity that we observe is really the asymmetry multiplied by the polarization. To improve the polarization of the atoms we would need to improve the circular polarization of the laser light and would also need to be increase the power in the beams. We successfully accomplished both of these goals. With stable ^{41}K we are able to demonstrate >99% polarization. During the experiment the number of ^{37}K that were in the trap was much lower than in previous experiments and the reasons for this decrease were simply that the TiC target did not produce as much ^{37}K as it previously had as well as the aforementioned vacuum problems. This decrease in the number of atoms meant that the same technique that we previously used to measure the polarization by counting photoions was not available to us. In this case we will have to use the polarization that we determine from the recoil asymmetry in conjunction with the lower limits that we can place on the asymmetry from our test with stable potassium in our final physics result.

Lastly the data acquisition worked according to specification. Before the experiment we made the decision to digitize all of the waveforms from the silicon strip detectors. We have subsequently built up a lot of knowledge about how the detector behaves and have developed strategies for working with the ~6 billion waveforms. As a result of our experiences we are seeking to digitize the waveforms from the ion MCP which will greatly simplify the trigger logic for the experiment and to write a peak finding algorithm for the silicon detectors that will run on FPGAs of the data acquisition boards alleviating the need to store all of the waveforms on disk. The analysis of the data is ongoing and we expect to publish the results by the end of this year.

Current status of the TAMUTRAP measurement Penning trap

R. S. Behling, Y. Boran, B. Fenker, M. Mehlman, D. Melconian and P. D. Shidling

The Texas A&M University Penning Trap Facility (TAMUTRAP) is a new ion trap facility dedicated to the study of fundamental interactions and symmetries and providing a low-energy radioactive ion beam (RIB) for various other applications. Over the past year, the geometry for the large, open-access Penning trap has been finalized and shown to be theoretically competitive with traps employed in other prominent facilities.

The initial experimental program for TAMUTRAP will be centered on measuring the beta-neutrino correlation parameter, $a_{\beta\nu}$, in $T = 2, 0^+ \rightarrow 0^+$ superallowed beta-delayed proton decays. In these experiments, $a_{\beta\nu}$ will be determined by observation of the proton energy distribution, which imposes three primary constraints on the design geometry of the apparatus: (i) the trap must provide a cold, spatially localized source of ions; (ii) the geometry must allow for the full containment of the primary decay products of interest; (iii) provision should be made for position sensitive detectors held at arbitrary voltage to be placed at the ends of the trap in order to detect decay products. In addition, the trap geometry should generate an electric field that is harmonic in shape to allow for the possibility of performing precision mass measurements, and the electrodes must be able to be machined, assembled, and must fit within the 210 mm diameter bore of the existing 7T solenoidal magnet.

In work recently published in *Nuclear Instruments and Methods in Physics Research Section A* [1], the final geometry of the TAMUTRAP measurement Penning trap was determined, taking into account the aforementioned design constraints. The resulting structure is a novel, cylindrical Penning trap with a new length/radius ratio different from all existing Penning traps, and an unprecedented 90 mm inner electrode radius (see Fig. 1). The analytic solutions to the electric field were checked against simulation, and match to high precision. These values, which are comparable to those presented by

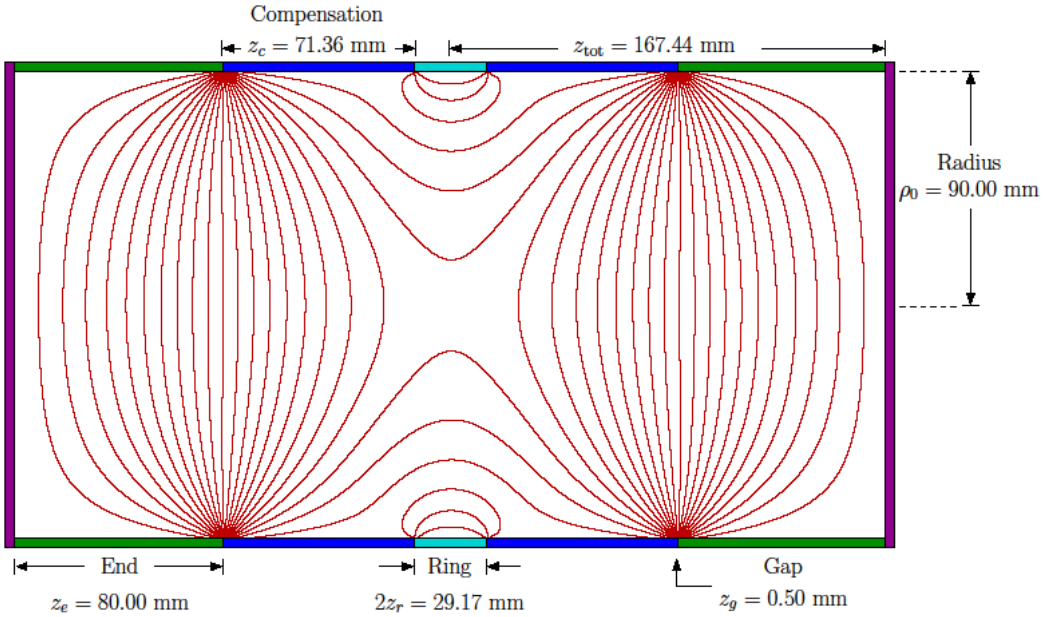

FIG. 1. The optimized trap geometry with calculated electric field lines overlaid.

existing mass measurement facilities, suggest that TAMUTRAP should be capable of performing mass measurements in addition to its primary program.

In the upcoming year, work on the TAMUTRAP Penning trap system will be centered on the development of the mechanical design of the trap structure itself and further work on the beam line leading up to it. Progress on the mechanical design will include investigation into the position-sensitive silicon detectors to be placed at the ends of the trap, development of mounting schemes for trap electrodes, and research of materials and machining processes to be involved in fabrication. It is expected that significant progress toward these milestones will be made in the upcoming year.

[1] M. Mehlman *et al.*, Nucl. Instrum. Methods Phys. Res. **A712**, 9 (2013).

Update on the study of the $^{14}C+n\leftrightarrow{}^{15}C$ system

M. McCleskey, A.M. Mukhamedzhanov, V. Goldberg, and R.E. Tribble

The $^{14}C+n\leftrightarrow{}^{15}C$ system has been used to evaluate a new method [1] to obtain spectroscopic factors (SFs). As part of this investigation, the ANC was determined which was then used to calculate the astrophysically important $^{14}C(n,\gamma)^{15}C$ rate. All of the experiments were conducted at Texas A&M Cyclotron Institute (TAMU-CI) and have been described in previous reports ([2],[3]). The analysis and results were presented in [4] and this report covers new calculations that have been performed, specifically the utilization of the Koning-Delaroche (KD03, [5]) global optical potential parameterization. This parameterization has the advantage of having been fit to scattering data over a larger energy range than CH89. In the case of the 60 MeV $^{14}C(d,p)^{15}C$ reaction, the neutron energy range of CH89 was exceeded, and thus KD03 should be much more reliable for that reaction. Also, an examination of ^{15}C via its mirror, ^{15}F is presented.

Inverse kinematic $d(^{14}C,p)^{15}C$ reaction

The $d(^{14}C,p)^{15}C$ reaction with a ^{14}C energy of 11.7 MeV/u was measured using the TECSA [6] silicon detector array and was described in previous reports. The angular distribution was calculated using the adiabatic distorted wave approximation (ADWA, [7]) and the normalization at forward angles used to extract the ANC. In the ADWA single nucleon potentials are used for the incoming proton and neutron evaluated at half the deuteron energy. This calculation with CH89 potentials was described previously [4] but has since been performed using potentials from the KD03 parameterization. The results for these new

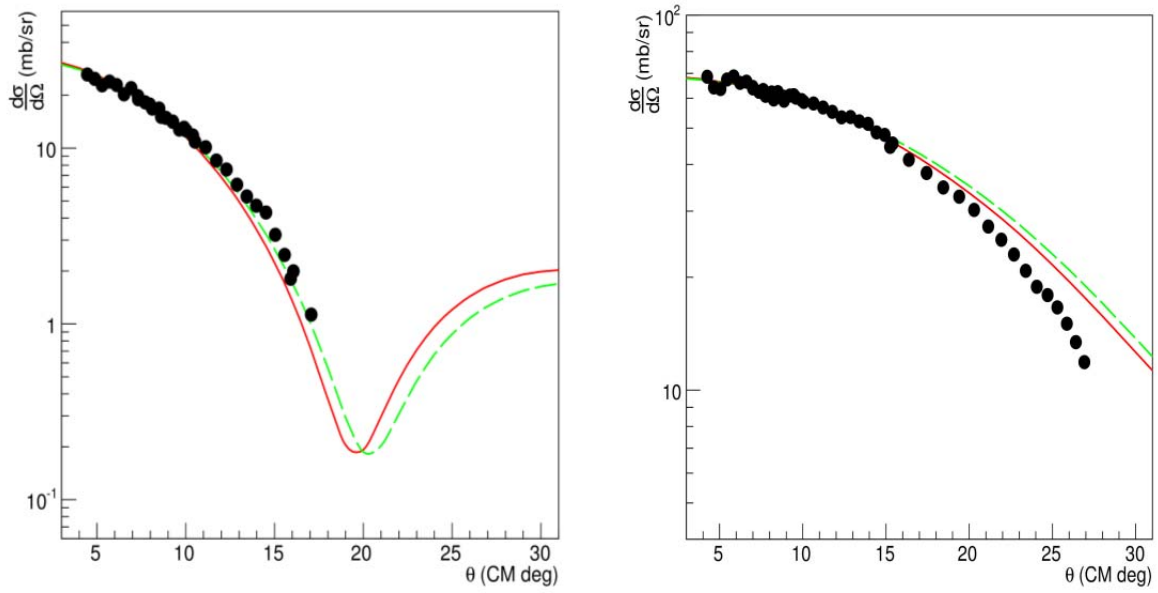

FIG. 1. On the left is the transfer to the $2s_{1/2}$ ground state. Black dots mark the experimental data points and the red and green lines are the ADWA calculation using CH89 and KD03 respectively. On the right is the same plotted for the 740 keV $1d_{5/2}$ first excited state.

calculations are shown in Fig. 1. The new ANC values are $C^2_{2s1/2} = 1.77 \pm .21$ fm^{-1} for the ground state and $C^S_{1d5/2} = (4.08 \pm .49) \cdot 10^{-3}$ fm^{-1} for the first excited state. The final results for the ANCs of the ground state and first excited state including these new calculations are presented in Table I.

Table I. Summary of ANCs found in the different measurements presented in this work.

experiment	$C^2_{2s1/2}$ (fm^{-1})	$C^2_{1d5/2}$ (fm^{-1})
HI transfer	2.09±0.29	$(4.48\pm0.58)\cdot10^{-3}$
$d(^{14}C,p)^{15}C$	1.77±0.21	$(4.08\pm0.49)\cdot10^{-3}$
average	**1.88±0.18**	$\mathbf{(4.25\pm0.38)\cdot10^{-3}}$

60 MeV ^{14}C(d,p)^{15}C reaction

The forward kinematic ^{14}C(d,p)^{15}C reaction was measured with a deuteron energy of 60 MeV. At this energy it was expected that this reaction cross section would have a strong dependence on the interior portion of the DWBA transfer matrix element. In [4] it was found to be almost completely peripheral for the ground state and only slightly non-peripheral for the $d_{5/2}$ first excited state. This analysis was based on calculations using CH89 potentials. These calculations have been repeated using KD03 potentials which should be more valid at this higher energy. The results show a stronger dependence on the interior, however, this reaction is still dominated by the exterior and surface contributions to the reaction rate, limiting the information that can be obtained about the ^{15}C SF. The results of the new calculations are shown in Fig. 2.

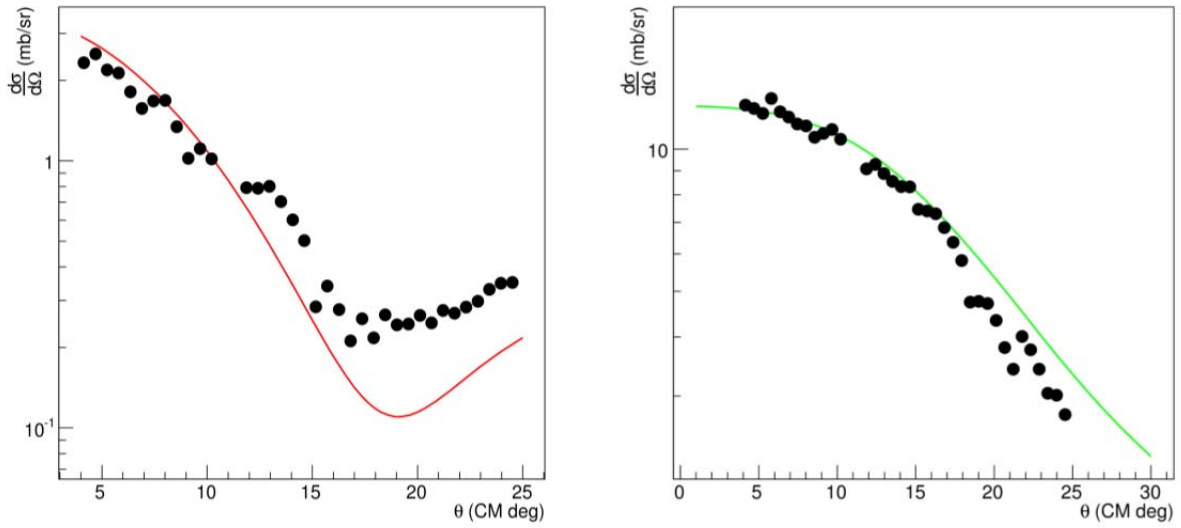

FIG. 2. On the left is the angular distribution for ^{14}C(d,p)^{15}C transfer to the ground state (black dots) and the ADWA calculation (red), the same is shown on the right for transfer to the $d_{5/2}$ excited state (black dots- experiment, green line ADWA).

As described in [1] and [4], a function

$$R^{DW}(b_{nlj}) = |\frac{\tilde{T}_{int}}{b_{nlj}} + \tilde{T}_{ext}|$$

was defined where *T* stands for the transfer matrix element, and *b* is the single particle ANC. The transfer matrix element has been split into two parts, one which is integrated over the interior region ($\tilde{T_{int}}$) and is dependent on the SPANC and another ($\tilde{T_{ext}}$) which is integrated over the exterior and is not dependent on the SPANC. For a peripheral reaction, $\tilde{T_{int}}$ is, by definition, negligibly small and *R* and thus the cross section is determined by $\tilde{T_{ext}}$. However, if a reaction has a non-negligible interior contribution, comparison of the above equation to its experimental counterpart

$$R^{\exp} = \frac{\frac{d\sigma}{d\Omega}^{\exp}}{C_{lj}^2}$$

will fix the single particle ANC. This can then be used to calculate the SF using the relation

$$SF_{nlj} = \frac{C_{nlj}^2}{b_{nlj}^2}.$$

The result of these calculations performed using the KD03 parameterization is shown in Fig. 3.

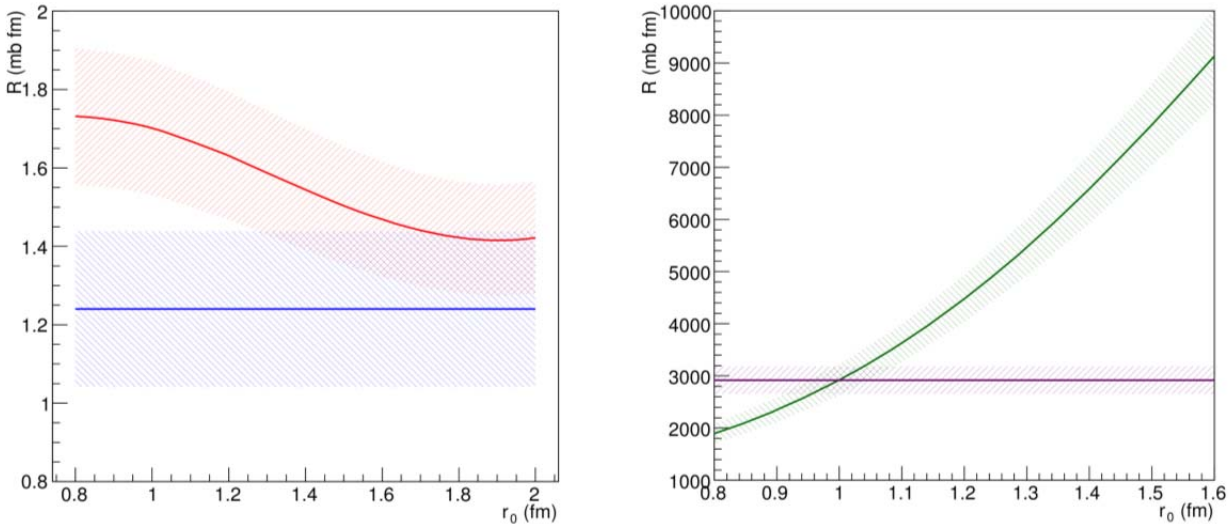

FIG. 3. R_{DW} (red) and R_{exp} (blue) for transfer to the ground state (left) and the $d_{5/2}$ first excited state (R_{DW} green, R_{exp} purple) (right). The uncertainties are shown by the hatched areas. In the calculation this is taken to be 10% and reflects the systematic uncertainty.

The ground state shows a relatively weak dependence on the choice of binding potential geometry and thus on the SPANC. This is a sign that the contribution to the transfer from the interior of the target nucleus is small and cannot be reliably determined. Based on the divergence around r_0=1.25 fm, this gives an upper limit for the SF for transfer to the ground state of ~0.93.

While Fig. 3 shows the ground state dependence of the calculated cross section on the binding potential geometry is weak, a stronger dependence on the binding potential geometry is observed for the transfer to the first excited state. As seen on the right in Fig. 3, R_{calc} overlaps with R_{exp} over the range r_0 from around 0.91 to 1.08 fm, which corresponds to SF values from 1.62 to 1.18. These values are considerably higher than expected, which indicates that the interior contribution to the transfer matrix element is not being correctly calculated and that a more sophisticated microscopic approach needs to be developed. The difficulty in correctly calculating this interior portion combined with the fact that most transfer reactions are dominated by peripheral and surface components highlights the difficulty in determining spectroscopic factors by means of transfer reactions.

Study of ^{15}C via its mirror, ^{15}F

In this section we will use the ^{15}C-^{15}F mirror symmetry to obtain a restriction on the SF of the two lowest states in these nuclei. To do this we examine experimental data on the levels in question with the aim to fix the potential parameters, which then can be used further to obtain SF and ANC. The *n* binding energies (BE) for the ground ($1/2^+$) and for the first excited ($5/2^+$) of ^{15}C are well known to be 1.218 and 0.478 MeV respectively. The compilation of the data for the two lowest states in ^{15}F can be found in [8]. We averaged these data to obtain the B.E. of the proton for the ground state in ^{15}F as – 1370 ± 70 keV with the width of 750 ± 100 keV, and for the first excited $5/2^+$ state: -2780 ± 40 keV with the width of 275 ± 40 keV [9, 10, 11, 12]. Assuming a Coulomb potential of a uniformly charged sphere of radius parameter R_{c0}=1.45 fm, r_0 and a were varied for the real binding potential which was taken to be of the Woods-Saxon shape. For each pair of r_0 and a the real depth was adjusted to reproduce the correct neutron binding energy for ^{15}C. Taking into account the proton's effect on the Coulomb potential in ^{15}F, these parameters were then used to calculate the binding energy of the corresponding proton in the mirror system. The results of these calculations are presented in Fig. 4.

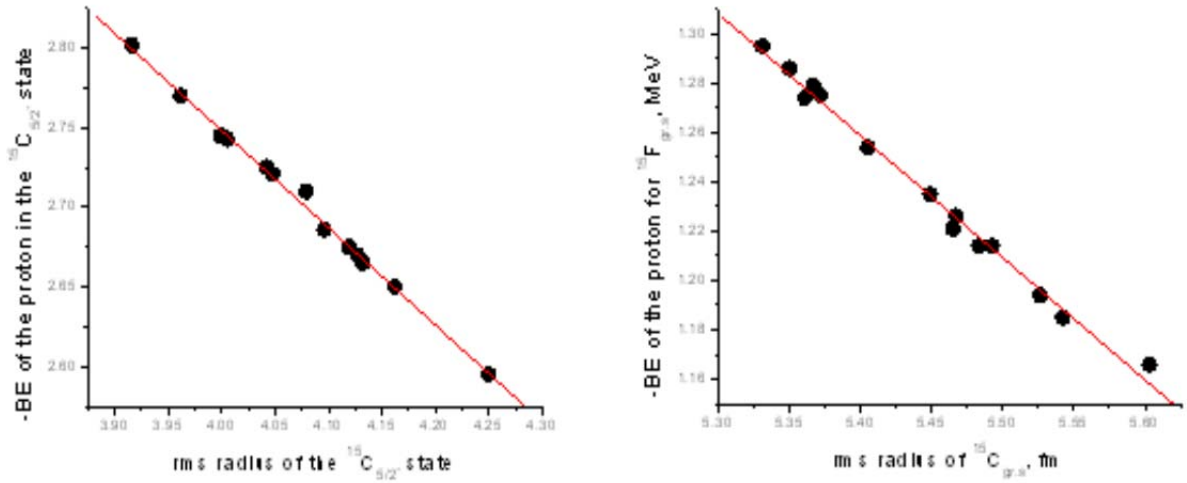

FIG. 4. Calculation of the binding energy of the proton in the ground state and first excited of ^{15}F as a function of binding potential geometry.

As seen on the left in Fig. 4, the experimental BE for the $d_{5/2}$ state corresponds to the rms radius of 3.97 fm in ^{15}C. From these considerations one can then obtain a restriction on the SF, which is defined as

$$SF = \frac{\Gamma}{\Gamma_{sp}}$$

the ratio of the width of the state to the calculated one using shell model wave functions. It is known that that the most sophisticated way to calculate widths of the broad states is to consider a pole in a complex plane [9]. Here we used the dependence of the maximum of the wave function upon the BE, as the method also gives close results [9]. Moreover, this approach was used to fit the data by the experimentalists in the works [10,11]. The calculated widths with parameters r_0=*1.18* and a=*0.6* are 0.590 MeV (for the ground state) and 230 keV (for the $5/2^+$ state in ^{15}F). After correction of the width calculated for the ground state for the experimental B.E, it becomes 720 keV. The calculated values are still smaller than the experimental ones. Taking into account the experimental uncertainties in the widths and the excitation energies, we obtain $SF_{gr.s.} \geq 0.90$ and for the first excited state, $SF_{\text{first ex.s.}} \geq 0.93$. We tested and neglected the weak dependence (~15 keV for the excited state) of the penetrability on the specific values of r_0 and a.

[1] A.M. Mukhamedzhanov and F.M. Nunes. Phys. Rev. C **72**, 017602 (2005).

[2] M. McCleskey *et al.*, *Progress in Research*, Cyclotron Institute, Texas A&M University (2010-2011) p. I-5.

[3] M. McCleskey *et al.*, *Progress in Research*, Cyclotron Institute, Texas A&M University (2009-2010) p. I-42.

[4] M. McCleskey *et al.*, *Progress in Research*, Cyclotron Institute, Texas A&M University (2011-2012) p. I-19.

[5] A.J. Koning and J.P. Delaroche, Nucl. Phys. **A713**, 231 (2003).

[6] B.T. Roeder *et al.,* Nucl. Instrum. Methods Phys. Res. **A634**, 71 (2011).

[7] R.C. Johnson and P.J.R. Soper, Phys. Rev. C **1**, 976 (1970).

[8] H.T. Fortune, Phys.Rev. C **74**, 054310 (2006).

[9] A. Mukhamedzhanov *et al*,, Phys.Rev. C **81**, 054314 (2010).

[10] V.Z. Goldberg *et al.*, Phys.Rev. C **69**, 031302 (2004).

[11] W.A. Peters *et al.*, Phys.Rev. C **68,** 034607 (2003).

[12] F.Q.Guo *et al.*, Phys. Rev. C **72**, 034312 (2005).

Status of AstroBox and analysis of ^{23}Al β-delayed proton decay data

L.Trache, E. Simmons, A. Spiridon, M. McCleskey, B. T. Roeder, A. Saastamoinen,
R. E. Tribble, E. Pollacco,[1] M. Kebbiri,[1] J. P. Mols,[1] M. Raillot,[1] G. Pascovici[2]
[1]*IRFU, CEA Saclay, Gif-sur-Yyvette, France*
[2]*National Institute of Physics and Nuclear Engineering, Bucharest-Magurele, RO-077125, Romania*

AstroBox is a new detector for measuring very low energy protons from beta-delayed proton decays. The development of this detector was motivated by results obtained in an ongoing study of such decays relevant for nuclear astrophysics. Previously, the study was done with a setup of Si detectors [1,2]. In an effort to lower the β-background in the 100-400 keV region and increase the energy resolution we designed the AstroBox, a detector based on a gas medium and Micromegas [3]. This new detector was commissioned at the Cyclotron Institute in measurements that were conducted in March 2011 and October 2011. Summaries of these measurements were given in previous annual reports in 2011 [4] and 2012 [5].

During 2012, the analysis of the ^{23}Al β-delayed proton decay data measured with the AstroBox detector in 2011 was continued. A spectrum of the protons from this analysis is shown in Figure 1. The spectrum agrees very well with earlier measurements of the ^{23}Al decay measured with silicon detectors here at TAMU [1], and elsewhere [6]. However, the advantage of the new measurement with AstroBox is that the spectrum in Figure 1 was obtained without the subtraction of β^+ background in the 100-400 keV that was needed in previous analyses.

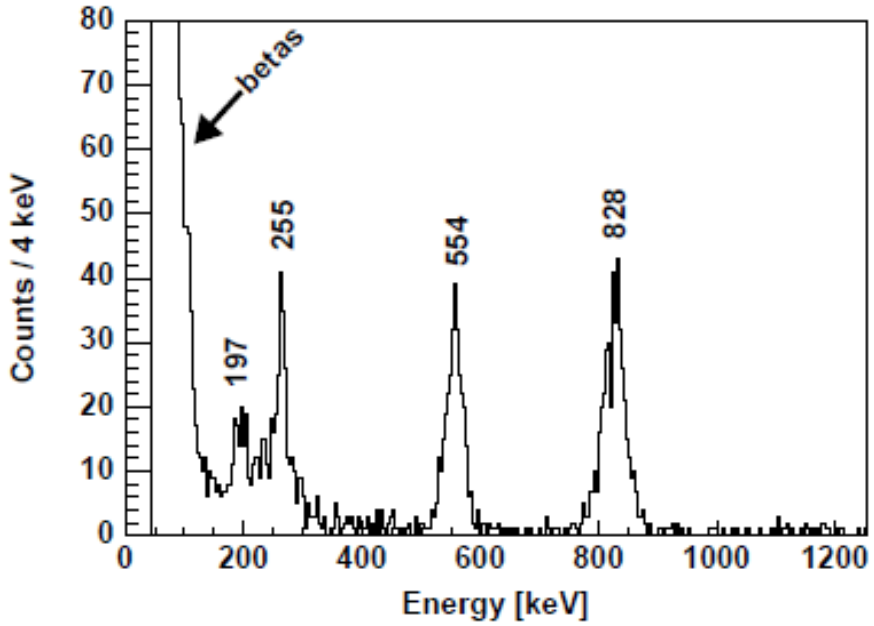

FIG. 1. ^{23}Al β-delayed proton decay spectrum. The energies of the protons are taken from Ref. [6].

The spectrum shown in Fig. 1 was compared with Monte-Carlo simulations of the ^{23}Al decay in AstroBox using the GEANT4 toolkit [7]. The simulation included details about the design of the detector, and data from the ^{23}Al β-delayed proton decay given in previous measurements. The results of these simulations are shown in Fig. 2. The blue line in the figure reproduces the low-energy part of the spectrum, which arises from the energy deposits of the β^+ particles from the ^{23}Al. The blue line also reproduces the proton decay spectrum if the energies of the protons from the previous publications [6] are assumed in the simulations.

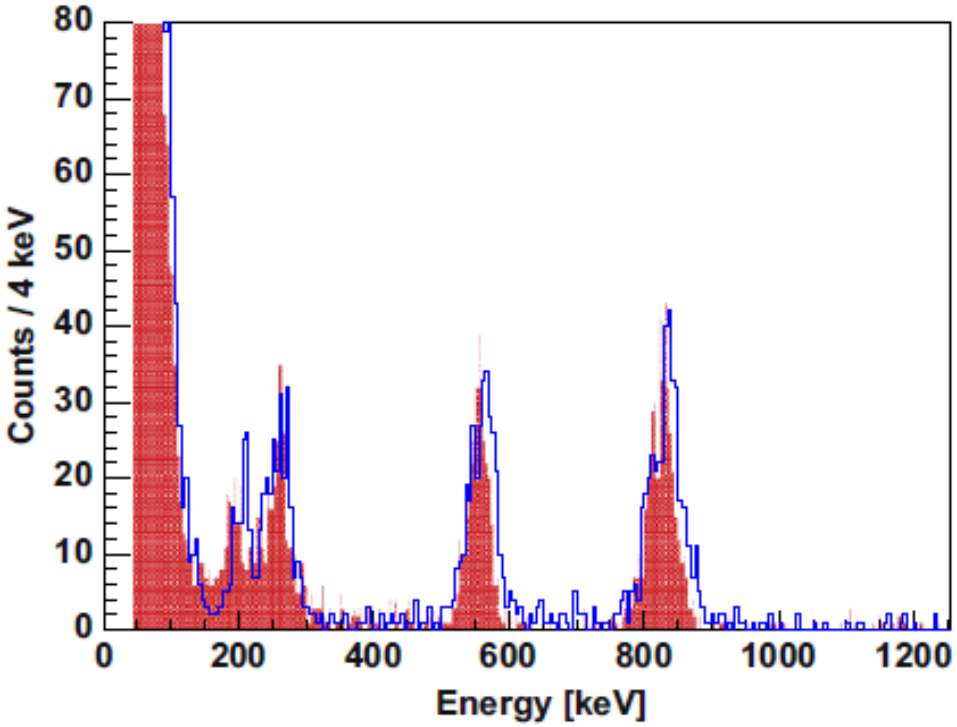

FIG. 2. GEANT4 simulation of the ^{23}Al β-delayed proton decay in AstroBox compared with the data given in Figure 1. The red shading represents the data and the blue line represents the simulation. See text for discussion.

In conclusion, AstroBox, a new detector using micromegas, has been commissioned and used in experiments. To date, three measurements have been conducted, two measurements of ^{23}Al decay and one measurement of ^{27}P decay, which is mentioned in a separate report [8]. The detector has been shown to reduce the background from β^+ particles in the region of 100-300 keV by a factor of about 100 versus previous measurements with implantation in silicon detectors [1]. Further measurements with this detector are planned in the coming year. Finally, an article detailing the design of the detector and the results of the test measurements has been recently submitted to Nuclear Instruments and Methods A [9].

[1] A. Saastamoinen *et al.*, Phys. Rev. C **83**, 045808 (2011).
[2] M. McCleskey *et al.*, Nuclear Instrum. Methods Phys. Res. **A700**, 124 (2013).

[3] Y. Giomataris, Ph. Rebourgeard, J.P. Robert, and G. Charpak, Nucl. Instrum. Methods Phys. Res. **A376**, 29 (1996).

[4] E. Simmons *et al.*, *Progress in Research*, Cyclotron Institute, Texas A&M University (2010-2011) p. V-32; http://cyclotron.tamu.edu/2011 Progress Report/index.html.

[5] L. Trache *et al.*, Progress in Research, Cyclotron Institute, Texas A&M University (2011-2012) p. V-52; http://cyclotron.tamu.edu/2012 Progress Report/index.html.

[6] O.S. Kirsebom, H.O.U.Fynbo, A.Jokinen, M.Mardurga, K.Riisager, A.Saastamoinen, O.Tengblad, J.Aysto, Eur. Phys. J. A **47**, 130 (2011) 130.

[7] GEANT4 version 4.9.4, S. Agonstinelli *et al.*, Nucl. Instrum. Methods Phys. Res. **A506**, 250 (2003).

[8] E. Simmons *et al.*, Progress in Research, Cyclotron Institute, Texas A&M University (2012-2013) p. I-28; http://cyclotron.tamu.edu/2013 Progress Report/index.html.

[9] E. Pollacco *et al.*, Nuclear Instrum. Methods Phys. Res. **A723**, 102 (2013).

Progress in the analysis of the delayed proton and gamma decay of ^{27}P for nuclear astrophysics

E. Simmons, L. Trache, A. Banu, A. Saastamoinen, M. McCleskey, B. Roeder, A. Spiridon, R. E. Tribble, T. Davinson,[1] P. J. Woods,[1] G. J. Lotay,[1] J. Wallace,[1] and D. Doherty[1]
[1]*School of Physics, University of Edinburgh, Edinburgh, United Kingdom*

One of the first and most well observed gamma-ray lines in the interstellar medium is that of 1.809 MeV, coming from the β-decay of the ground state of ^{26}Al. The observation of this line provided more proof of the existence of a dynamic universe. However, the creation site of ^{26}Al is still under debate, requiring a fuller understanding of the creation and destruction reactions involving both the isomeric and ground state of ^{26}Al. In order to study the destruction reaction of ^{26m}Al(p,γ)^{27}Si*, which is dominated by resonant capture, an indirect method was employed, that of the β-delayed proton and gamma decay of ^{27}P. Due to selection rules, the same levels of interest, those above the proton threshold in ^{27}Si, were populated from the β-decay of ^{27}P. Determination of the energy, spin and parity of these resonance states, along with their partial gamma and proton widths, allows for the determination of their resonance strengths and thus, their contribution to the astrophysical reaction rate.

This experiment was done in November 2010 [1] with the K500 superconducting cyclotron at TAMU with a beam of $^{28}Si^{+10}$ at 40 MeV/u impinging on a hydrogen gas target kept at LN_2 temperatures and a pressure of 2 atm in the MARS beam line. The nuclei of interest, ^{27}P, were created in a (p, 2n) fusion evaporation reaction. The productivity measured at the beginning of the experiment determined that there was about 26 pps of ^{27}P and approximately 18% total impurities with the coffin (momentum) slits at ± 1.0 cm. With the coffin slits closed to the ± 0.4 cm needed for implantation, the rate dropped to about 10.5 pps.

The ^{27}P nuclei were then implanted, with the use a rotating aluminum degrader, in the center of a thin BB2 (45 μm thick) double sided strip detector, referred to as the proton detector. Silicon detectors were placed on either side of this proton detector, referred to as β-detectors, in order to reduce the background through coincidence requirements implemented in the electronics acquisition trigger. The beam from the K500 cyclotron was pulsed in order to measure the β-p and β-γ coincidences simultaneously.

In order to obtain an internal energy calibration ^{28}P was implanted in the center of the proton detector. It was chosen due to the fact that it is also a β-delayed proton emitter with known protons in the energy region of interest. Once this was done, the thin 45 μm proton detector was replaced with a detector similar in every regard save that it was 104 μm thick. This thicker proton detector allowed for the momentum slits to be opened further and thus, allowed a higher beam rate to be obtained. At this point ^{24}Al was implanted in the proton detector in order to obtain data on its known gammas, giving an extended energy calibration up to 8 MeV. With the thicker BB2-104 still in place, ^{27}P was again implanted in order to study the resulting gammas with the increased beam rate.

In the previous year, better extended energy calibrations have been obtained by a more careful selection of calibration peaks as well as using multiple sub-ranges, each with their own energy calibration, and making the necessary adjustments for the recoil energy not recorded in the detectors. The

extended efficiency calibrations were also improved, taking into account the sum peak issue that arose for the ^{60}Co and ^{152}Eu sources used in the close geometry of this experimental setup. With these new and better calibrations, and a better understanding of the effect of the close geometry involved, several gamma peaks in the ^{27}P spectrum that had been previously un-assigned turned out to be sum peaks, however, there are still new gammas to be fit into the decay scheme. The background, ^{24}Al and ^{28}P gamma spectra have had all their peaks identified, including several peaks in the background spectrum that were found to be from material activation created during this experiment (aluminum activation of the degrader) and some created in previous experiments (lead activation of the shielding placed around HpGe 1). Fig. 1 shows the current known peak assignments in the ^{27}P gamma spectrum.

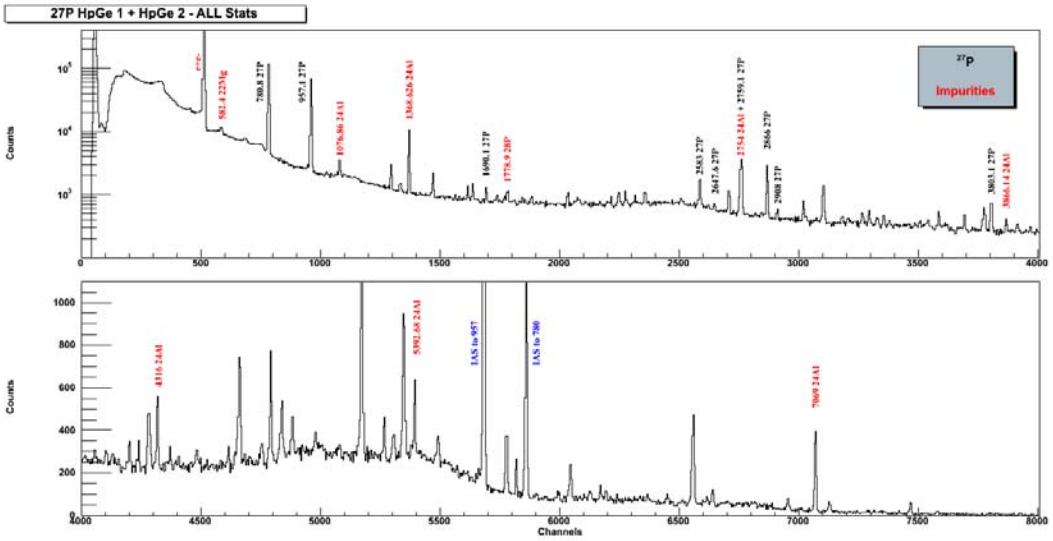

FIG. 1. The ^{27}P Gamma spectrum created from all good statistics.

The proton analysis has had several significant improvements. First, a ROOT macro was created to better fit the alpha source peaks and thus obtain a better gain matching of all strips on both sides of the proton detectors. Careful evaluation of the individual strips required the discarding of a few of them but once done, the results were significantly better than what had been previously obtained. With these improvements, all peaks have been identified in all spectra; those in ^{27}P (both proton detectors), ^{28}P and in ^{24}Al. An internal calibration will be created with the peaks found in the ^{28}P spectrum which will not be affected by the dead layer of the detectors, as the alpha source data had been, allowing for an accurate energy assignment of the proton peaks found in the ^{27}P spectrum. However, in the energy region of interest (around 200 keV) the β-background was still the dominant feature due to the low total proton branching ratio (previously estimated at 0.07 %). Background subtraction attempts are ongoing with ROOT and a new (lower) limit on the total proton branching ratio is expected.

[1] E. Simmons *et al.*, in *Progress in Research*, Cyclotron Institute, Texas A&M University (2011 – 2012), p. I-27

[2] A. Saastamoinen *et al.*, Phys. Rev. C **83** 045808 (2011).

Feasibility study of time-inverse measurement of the stellar reaction ^{22}Mg(α,p)^{25}Al

A. Banu,[1] D. Votaw,[1] B. T. Roeder, G. G. Rapisarda, M. McCleskey, A. Saastamoinen,
E. Simmons, A. Spiridon, L. Trache, R. E. Tribble and C. A. Gagliardi
[1]*James Madison University, Department of Physics and Astronomy, Harrisonburg, VA 22807*

The reaction rate for ^{22}Mg(α,p)^{25}Al, which is of interest for the (α,p) process that powers Type I X-ray bursts, is currently under investigation at the Cyclotron Institute.

Type I X-ray bursts (XRBs) are the most frequent thermonuclear explosions observed in the galaxy. It is thought that an XRB occurs in binary star systems where a neutron star accretes matter from its companion star [1]. As the accreted hydrogen- and helium-rich matter builds up on the surface of the neutron star the temperature and the pressure increase and a thermonuclear runaway occurs reaching peak temperatures of T ~ 1.5 GK, and is observed as X-ray burst. The fact that the bursts do not destroy the binary star system makes X-ray binaries useful as a way to study matter under extreme temperature and density conditions. The principal nuclear reaction sequences in XRBs have recently been presented in detail by Fisker et al. [2]. They are mainly characterized by helium burning via the (α,p)-process (a sequence of alternating (α,p) reactions and (p,γ) reactions) and hydrogen burning via the rp-process (a sequence of *rapid proton* capture reactions and β-decays). Reactions like ^{22}Mg(α,p)^{25}Al, ^{26}Si(α,p)^{29}P, ^{30}S(α,p)^{33}Cl, and ^{34}Ar(α,p)^{37}K are considered to play a significantly important role in determining the nucleosynthetic path for the (α,p) process in XRBs and for understanding XRB light-curve evolution [3]. Moreover, current sensitivity studies on XRB nucleosynthesis have identified the reaction ^{22}Mg(α,p)^{25}Al as being influential for the XRB total energy output [4].

We report here on a feasibility test performed in November 2012 to measure the experimentally unknown cross section of the ^{22}Mg(α,p)^{25}Al reaction at astrophysical relevant energies. The measurement was performed in inverse kinematics for the study of the time-inverse reaction ^{25}Al(p,α)^{22}Mg. A low-temperature oven coupled to the ECR2 ion source at the Texas A&M University Cyclotron Institute was operated at a temperature of ~540 °F to extract a ^{25}Mg^{10+} primary beam for the first time at the newly refurbished K150 cyclotron. The primary beam was accelerated at 11 MeV/nucleon, the highest energy available at the time due to the maximal operational K150 deflector voltage of 62.6 kV, and bombarded a cryogenic gas cell to produce the secondary beam ^{25}Al at ~7 MeV/nucleon via the ^{25}Mg(p,n) reaction. The entrance and exit windows of the gas cell were made of Havar foil of 4 μm thickness and the pressure in the gas cell was p = 1 atm. Out of a total current of 80 nA for the ^{25}Mg^{10+} primary beam, a current of 15 nA for a fully stripped ^{25}Mg^{12+} primary beam was transmitted on the primary target. As illustrated in Fig. 1, the resulting ^{25}Al beam separated by the Momentum Achromat Recoil Separator (MARS) had a purity of ~94.6% and was produced at a rate of about 1.4×10^4 pps.

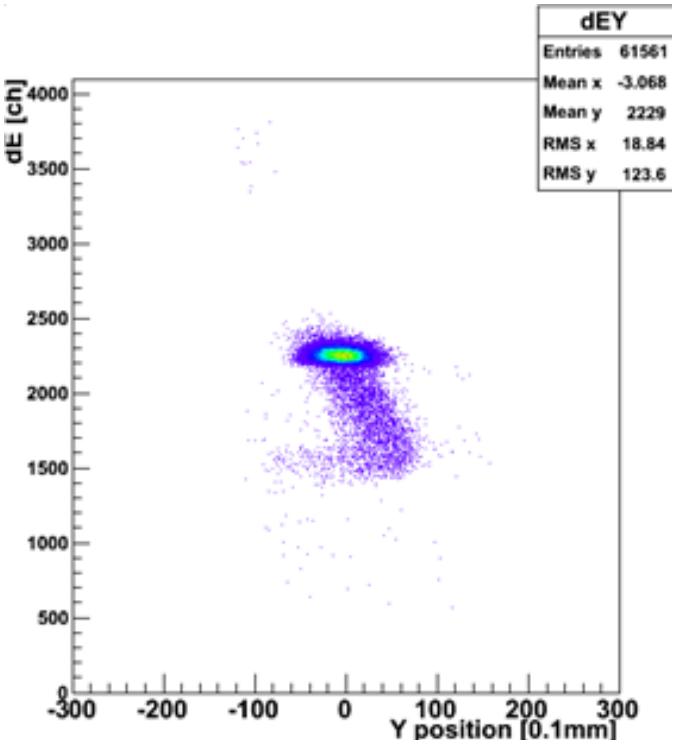

FIG. 1. Plot of energy versus y position in the MARS target detector.

The beam-spot size measured with the MARS silicon position sensitive target detector was about 4 mm × 4 mm (FWHM). A solid CH_2 target of ~1 mg/cm^2 thickness was used as reaction target and was located at the final focal plane of MARS. To disentangle the reaction induced-background due to the carbon present in the target, additional measurements using a pure carbon target, of ~2 mg/cm^2 thickness, were carried out.

We used an experimental setup that provided reaction channel selection and particle scattering angle determination. It consisted of four modular *ΔE-E* silicon telescopes (of 5 × 5 cm^2 active area) arranged in a symmetrical 'cross' configuration, as illustrated in Figure 2. The front *ΔE* detectors were 16-strip position-sensitive detectors, 140-μm thick (the vertical detectors) and 65-μm thick (the horizontal detectors). The back *E* residual detectors had the same area coverage of 5 × 5 cm^2 but the vertically positioned detectors were 1000-μm thick while the horizontal ones were 500-μm thick. A plastic scintillator detector was placed at 0° downstream of the reaction target and the Si-detector array and served for beam normalization of the reaction cross section evaluation.

For laboratory energies of ~7 MeV/nucleon at which the ^{25}Al secondary beam was produced here, the corresponding maximum laboratory angular range for the reaction products of interest – alpha particles and ^{22}Mg – was 18° and 3.3°, respectively. To accommodate these angular ranges for the detection of both alpha particles and ^{22}Mg heavy ions, the measurements were carried out at two distances from the CH_2 target to the cross-silicon detector array: 18 cm and 58 cm. At the shorter distance of 18 cm, the angular coverage in the *vertical detectors* was between ~4° and ~19° while in the horizontal detectors was between ~16° and ~30°. At the further distance of 58 cm, the angular coverage in the *vertical*

detectors was between ~1° and ~6° while in the horizontal detectors was between ~5° and ~30°. In regard to the possible energy ranges for the two main reaction products of interest here, the energies for the alpha particles span from 3 MeV/nucleon up to 11 MeV/nucleon while for the ^{22}Mg heavy ions from ~6 MeV/nucleon up to 7 MeV/nucleon. Taking into account the thicknesses of the Si detectors in the 'cross'-array and the two target-detector distances at which the measurements were performed, the heavy ions could only be detected in the vertical ΔE detectors when the 'cross'-array was positioned at the 58 cm distance from the reaction target. Because the energy loss range for heavy ions is more than one order of magnitude higher than energy loss range for the alpha particles, we chose to sacrifice the 'bottom'-ΔE detector by lowering its amplification settings to allow the detection of ^{22}Mg-alpha particle coincidences between the 'bottom'-ΔE detector and any of the other three ΔE detectors, our signature that the reaction channel of astrophysical interest here was identified.

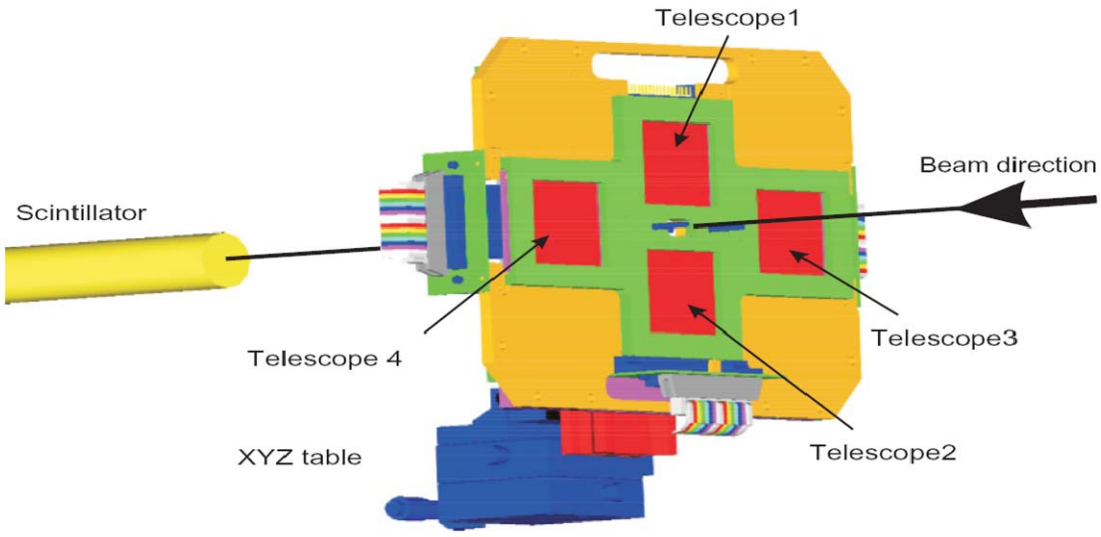

FIG. 2. A 3-dimensional view of the detector assembly employed: the 'cross'-silicon-detector array and a plastic scintillator detector. See text for details.

For a total of about 5-beam-on-target days, we were able to acquire coincidence data for ~36 hours. When comparing the coincidence data taken on the CH_2 target vs. the pure Carbon target, we did observe heavy ions of appropriate energy loss in the 'bottom'ΔE detector of the 'cross-array, as we would expect for the ^{22}Mg heavy ions, only for the CH_2-target data. While data analysis is currently in progress, it remains to be determined the nature and the origin of the heavy ions we did detect in coincidence with light particles.

In conclusion, we have successfully conducted a feasibility test for the time-inverse measurement of the stellar reaction ^{22}Mg(α,p)^{25}Al in which we achieved the production for the first time at the K150 cyclotron of both the primary and secondary beams of interest, ^{25}Mg and ^{25}Al, respectively. Preliminary results of the data analysis seem to validate our experimental approach. The ^{25}Al secondary beam was produced at laboratory energy of ~7 MeV/nucleon corresponding to a relative energy in the center of mass for the system ^{22}Mg-alpha of 3MeV, which is very close to the astrophysically relevant energy regime of 1.7 – 3.2 MeV for the X-ray burst peak temperature of 1.5 GK. Because of the very small cross

sections at the astrophysically relevant energy regime, we plan next to perform measurements of the time-inverse reaction ^{25}Al(p,α)^{22}Mg at higher laboratory energy for the ^{25}Al beam than 7 MeV/nucleon such that we can be sure that we indeed identified the ^{22}Mg-alpha reaction channel of astrophysical interest. An increase of at least one order of magnitude is also expected for the production rate of the ^{25}Al secondary beam using either of the K150 or K500 cyclotrons available at TAMU.

This research is presently partially funded through the J-1035 Jeffress Memorial Trust grant.

[1] H. Schatz, K. E. Rehm, Nucl. Phys. A **777**, 601 (2006).
[2] J.L. Fisker, H. Schatz and F.-K. Thielemann, The Astrophys. J. Suppl. S **174**, 261 (2008).
[3] J.L. Fisker, F.-K. Thielemann, and M. Wiescher, Astrophys. J. **608**, L61 (2004).
[4] A. Parikh, J. Jose, F. Moreno and C. Iliadis, The Astrophys. J. Suppl. S **178**, 110 (2008).

Level Structure of ^{10}C

V. Z. Goldberg and G. V. Rogachev[1]
[1]*Department of Physics, Florida State University, Tallahassee, Florida 32306*

In this work (more details can be found in [1]), we are attempting spin-parity assignments for the excited levels in ^{10}C below7 MeV using the data [2, 3] and new results for the $T = 1$ α-cluster states in ^{10}B [4]. Isotope invariance allows us to relate the data available for ^{10}Be and ^{10}B with the ^{10}C spectrum. We apply the Coulomb displacement energies and most importantly, widths and decay modes of the resonances to suggest the spin-parity assignments.

I. POTENTIAL MODEL

The conventional Woods-Saxon potential was used to evaluate the Coulomb displacement energies that are sensitive to the orbital angular momentum, binding energy, and structure of the states and also the single-particle widths of the states. The depth of the well was adjusted for each state to fit thebinding energy in ^{10}Be. A radius of $R = 1.25 \times 9^{1/3}$ fm and a diffuseness of $a = 0.65$ fm were used for the centralpart of the potential. For the spin-orbit potential we use Vso = 6.4 MeV, Rso = $1.3 \times 9^{1/3}$, and $a$so = 0.64 fm. The Coulomb potential was that of the homogeneously charged sphere of $Rc = 1.17 \times 9^{1/3}$. The parameters of the single particle potential fit the ground-state (g.s.) binding energies for mirror pairs ^{9}Be-^{9}B and ^{13}C-^{13}N. The $2s1/2$ and $1d5/2$ single-particle states were also included into the fit for the ^{13}C-^{13}N pair. We obtained agreement for the states included in the fit to within 100 keV. The Coulomb shifts of α-cluster states (analogs of 0^{+}_{2} and 2^{+}_{3} in the ^{10}Be spectrum) were calculated using the Woods-Saxon potential from Ref. [3] with $V = -119$ MeV, radius and charge radius of 2.58 fm and 2.27 fm respectively, and diffuseness of $a = 0.677$ fm. Such a potential generates the correct binding energy for the 0^{+}_{2} level in ^{10}Be and the correct excitation energy of 2^{+}_{3} , and also produces deeply bound "forbidden" states to account forthe Pauli principle. Note that the results of potential model calculations are not very sensitive to the specific choice of potential parameters as long as the excitation energies of the states are reproduced.

II. ANALYSIS

The analysis starts with fitting the well depth of the potential to reproduce the binding energy of the states in ^{10}Be. Then the excitation energy for the corresponding isobaric analog state in ^{10}B is calculated. For this, we use the average between the energy relative to the threshold for ^{10}B decay into n + ^{9}B (the same as the energy relative to the ^{10}Be decay into ^{9}Be + n) and the energy relative to the threshold for ^{10}B decay into ^{9}Be + p (calculated with the potential found for ^{10}Be and exchanging the neutron for the proton). The single-particle nucleon (or α for the 0^{+}_{2} and 2^{+}_{3} levels) widths Γsp are determined from the potential model. The width of the resonance is defined using the behavior of the wave function in the interior as in Ref. [5]. The known widths of the $T = 1$ resonances in ^{10}B (mainly ^{9}Be + p) [13] are proportional to the spectroscopic factors (SFs). We used the expression $C^2S = \Gamma\text{exp}/\Gamma\text{sp}$, where C is an isospin Clebsch-Gordan coefficient ($C^2 = 1/2$ for the ^{9}Be + p decay of ^{10}B). The ratios of the experimental

proton widths (when known) of the resonances to the calculated single particle widths were considered as the spectroscopic factors [^{9}Be(g.s) + n for ^{10}Be or ^{9}B(g.s) + p for ^{10}C]. Reduced widths for proton and neutron decay should be the same for the T = 1 states in ^{10}B if isospin is conserved. When the known partial proton widths in ^{10}B were used to obtain the SFs, the corresponding Γexp/Γsp ratio is multiplied by a factor of 2 to get a SF in ^{10}Be and ^{10}C. These values were considered as experimental values and summarized in the seventh column of Table I. The SFs from the ^{9}Be(d,p) reactions [6, 7] are given in the fourth column of Table I. We then calculated theoretical SFs in the framework of the shell model (SM) using the code COSMO [8] (column 3 of Table I). The *psd* valence space with WBP interaction [14] was used. 0–2 $\hbar\omega$ excitations were considered for the positive parity states and 1–3 $\hbar\omega$ for the negative parity state. As it is clear from Table I, generally there is reasonable agreement between the experimental and

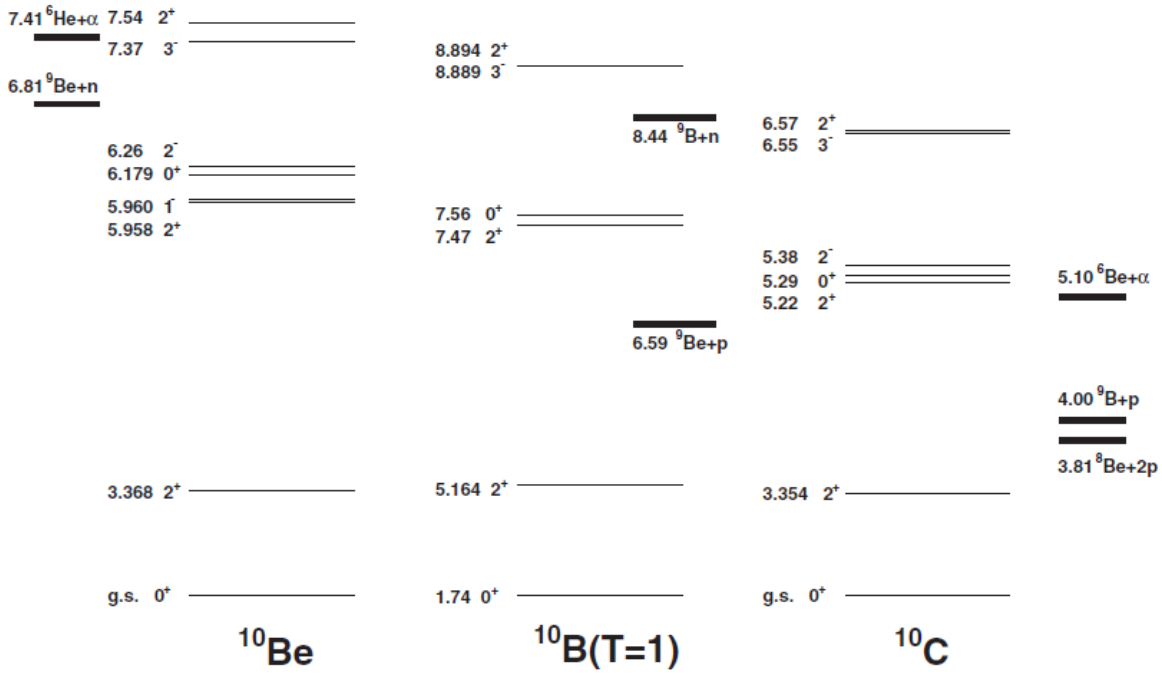

FIG. 1. Levels diagram for the $A = 10$, $T = 1$ isobaric multiplet.

calculated SFs. We used the SM predictions to calculate the Coulomb displacement energies of these negative parity states in ^{10}C, but we realize that the uncertainty of these calculations is much larger than for the other states. Fortunately, the width of the 2−1 state in ^{10}C is determined by the l= 0 SF and is not affected by this discrepancy. As for the width of the 1− state we present the lower limit. It is worthwhile to note the remarkable stability of the differences in excitation energies for the cluster 0+ and 2+ levels calculated in ^{10}Be and ^{10}C. This equidistance is quite different from what should be expected for single-particle nucleon resonances with l= 0 and l = 2. The well known Thomas-Ehrman effect [9, 10] shifts down the l= 0 unbound single-particle levels in mirror proton-rich nuclei. It is different for the α-particle resonances mainly due to larger reduced mass decreasing the role of the orbital momenta. This behavior can be considered as a specific characteristic of the cluster states.

TABLE I. $T = 1$ excited states above 5 MeV in $A = 10$ nuclei.

							^{10}Be	^{10}B($T = 1$)	^{10}C				
J^π	ℓ_N	S_{th}[a]	$C^2S_{exp}(^{10}Be)$[b]	$\Gamma_p(^{10}B)$ (keV)	$\Gamma_{sp}(^{10}B)$ (keV)	$2\times\frac{\Gamma_p}{\Gamma_{sp}}$[c]	E_{exp} (MeV)	E_{exp} (E_{calc}) (MeV)	E_{calc} (MeV)	Γ_{calc}[g] (keV)	E_{exp} (MeV)	Γ_{exp} [16] (keV)	Γ_{exp} [20] (keV)
2_2^+	1	0.73	0.54	65(10)	200	0.65(10)	5.958	7.47 (7.50)	5.16	210(30)/170	5.22	294(16)	225(45)
1_1^-	0	0.40		100(10)	1240	0.16(2)[d]	5.960	7.43 (7.49)	5.1[e]	>180			
	2	0.15											
0_2^+	1	0.07		2.65(18)	250	0.021(2)	6.179	7.56 (7.58)	5.39	10[h]	5.287	106(11)	
2_1^-	0	0.11	0.132	210(60)	2700	0.15(4)	6.263	7.74 (7.79)	5.4[e]	370(100)	5.38 [21]		300(60)
	2	0.53	0.065										
3_1^-	2	0.57	0.53	75(10)[f]	350	0.43(6)	7.371	8.89 (8.93)	6.70	140(20)/175	6.553	214(31)	
2_3^+	1	0.03	0.007	7(2)[f]	2200	0.006(2)	7.542	8.89 (8.87)	6.70	90[h]	6.568	172(31)	190(35)

[a]Theoretical spectroscopic factor S_{th} for the $N\otimes 3/2^-_{g.s.}$ configuration. The square of the isospin Clebsch-Gordan coefficient, which is unity for ^{10}Be and ^{10}C, and 1/2 for $T = 1$ states in ^{10}B, is omitted.
[b]SF from ^{9}Be(d, p) experiments [22,23].
[c]This column gives the SF for the corresponding state determined from the ratio of the known proton partial width of the $T = 1$ states in ^{10}B to a single-particle width calculated with the potential model. The ratio is then multiplied by a factor of 2 to account for the isospin Clebsch-Gordan coefficient.
[d]The 1^- at 7.43 MeV in ^{10}B has mixed isospin, and the experimental spectroscopic factor determined from the width of this state may be unreliable. See text for additional comments.
[e]Assuming an experimental $\ell = 0$ SF and a theoretical $\ell = 2$ SF, we estimate uncertainty of $\pm$200 keV for this value due to uncertainties in the SF.
[f]The proton partial width in ^{10}B that was used to determine the SF is from Ref. [18].
[g]The widths for all states except for the cluster 0_2^+ and 2_3^+ were calculated as a product of the spectroscopic factor given in column 7 and the single-particle width for the $p + ^9$B system. If the SF from the (d, p) reaction (column 4) is outside of the uncertainty given in column 7, then the second width that corresponds to the SF from (d, p) is also shown (after the slash).
[h]The width for this state was calculated as a sum of the α single-particle width from the $\alpha + ^6$Be potential model and the partial width for the proton decay to the ^{9}B(g.s.).

It is seen (Table I, column 11) that the α-cluster states may be relatively narrow resonances in ^{10}C. Thus, the 100 keV resonance at 5.29 MeV [2] can only be the 0^+_2 state, and the 170 keV resonance at 6.6 MeV is likely the 2^+_3 cluster state. The calculated widths of the cluster states, 0^+_2 and 2^+_3, are too small, however, if only the cluster decay (with $S\alpha = 1$) and the proton decay to the ground state in ^{9}B are taken into account. Several charged-particle decays are energetically possible for the ^{10}C excited states, while the mirror decays are not possible in ^{10}Be. The account of the decays to the excited states in ^{9}B for all states (except for the 0^+_2 and 2^+_3) results in a 10–15% increase of the widths shown in Table I. As for the cluster 0^+_2 and 2^+_3 states, the lowest $2p$ decay is a new and important channel. It is the only channel which can provide for the increase of the width of the 0^+_2 state. A simplified consideration of the $2p$ decay as a di-proton decay in the potential model shows that, if the spectroscopic factor for this decay is about 0.15, then it provides for 100 keV of the total width. In this case the $2p$ decay will be dominant, in agreement with the experimental observation in Ref. [2]. A similar consideration for the 2^+_3 cluster state would result in the increase of its width by ~100 keV, also improving the agreement with the experimental data. Now our interpretation of the results of Ref. [2] is the following.

A. States near 6.6 MeV in ^{10}C

The group at 6.6 MeV excitation energy in ^{10}C consists of two nearly degenerated levels: 3− at 6.55 MeV and 2+ at 6.57 MeV. (Here and below we are using experimental excitation energies given in column 12 of Table I, which are known with a precision of 50 keV [2].) The major mode of decay for the 2+ level is into α + ^{6}Be (this state was found to be an extreme α-cluster state in Ref. [4]). The analog 3−

state in ^{10}B has relatively large reduced α +^{6}Li(0+; T = 1) width as well ($SF\alpha$ = 0.42 [3]).We expect a much stronger population of the 3− state than the 2+ state in the inelastic scattering [2] because of the collective enhancement of L = 3 transitions in light nuclei in this energy region [11]. Therefore, we suppose that the authors of Ref. [2] observed the structure at 6.56MeV, which looked like a broad level decaying to α +^{6}Be with a width of <370 keV that is due to unresolved 3^-_1 and 2^+_3 . However, the dominant mode of the 3− level decay is to ^{9}B +p. This decay results in observation of the strong population of the level at 6.553 MeV with a width of 214(31) keV [2] (which is the real width of the 3− level because the 9B + p partial width of the 2+ level is negligible). We estimate that the admixture of the 2p+^{8}Be decay for the 2^+_3 level is ~1/2 of the total width. This results in observation of the narrow structure of 172 keV (the width of the 2+ level) in the 2p + ^{8}Be channel, reported in Ref. [2]. The energy of the cluster 0^+_2 and 2^+_3 levels depends on the presence of the 2p + ^{8}Be configuration. The admixture of this configuration at the level of 15% of the maximum diproton width, which was needed to explain the widths of the 0^+_2 and 2^+_3 resonances, results in a decrease of ~100 keV of the excitation energy of the 0^+_2 and 2^+_3 states, improving the agreement between the calculated and experimental Coulomb displacement energies. The maximum diproton width was calculated using the 2p + ^{8}Be potential model. As for the 3− state, the calculated excitation energy in ^{10}C should be corrected for the admixtures of the cluster and the collective configurations.

B. States near 5.3 MeV in ^{10}C

The narrowest resonance in the 5.2–5.3MeV group is 0+ at 5.29 MeV. The dominant decay mode for this state is 2p + ^{8}Be because of small penetrability for the α + ^{6}Be channel. (A similar decay is observed for the $2+_3$ level at 6.6 MeV). All other resonances close to 5.2 MeV should decay into the ^{9}B + p channel. The dominant population of this structure can be explained if 2^+_2 and 1^-_1 contribute to the peak at 5.2 MeV. While the measurements in Ref. [2] presented more detailed information on the ^{10}C states in question than the former experiments, there is an evident difference at 5.38MeV where a peak with width of 300(60) keV was reported in the ^{10}B(^{3}He,^{3}H) reaction [12]. The excitation energy and width of this peak are close to our calculations for the 2− state. The states with abnormal parity can be populated in inelastic scattering experiment of Ref. [2] only due to the second-order effects. Therefore, we suppose that the 2− state was not observed in Ref. [2].

III. SUMMARY

We considered states in the 5–7 MeV excitation energy region in ^{10}C and proposed spin-parity assignments for these states. In particular we showed that the states (0+ and 2+) with the cluster (α + ^{6}Be) structure have the narrowest widths in this excitation region. We apply a rather common procedure of using shell-model wave functions to calculate the Coulomb shifts and widths for the states with evident single-particle spectroscopic factors. A similar procedure with cluster potentials accounting for the configurations forbidden by the Pauli principle was used to explore the isospin invariance for the cluster states. While different cluster potentials are conventional instruments to consider cluster states, it is difficult to find examples of the applications for the mirror nuclei. This is because the experimental data on cluster states in mirror nuclei are very rare. We noticed a remarkable (in comparison with the behavior

of the nucleon single-particle states) equidistance of 0+–2+ cluster state energies in mirror nuclei. Our test calculations showed that more complete data on the unknown members of the cluster band (we expect a 4^+ state at 10.1 MeV with a width of ~600 keV) would provide for important information on the details of the cluster potential, first of all on the number of nodes of the cluster wave function. This number is determined by the specific orbitals occupied by the nucleons in the cluster and has an influence on the moment of inertia of the band. The spin-parity assignments suggested here became possible due to recent experimental data containing information on the different decay modes of the states. As seen in Fig. 1, more decay channels are open for the states in the proton-rich member of the $T = 1$ multiplet, the exotic $2p$ decay being the lowest one. We have shown that the observation of this channel in Ref. [2] appeared to be very useful for the identification of the cluster levels. The $2p$ partial width is much larger than the single-particle width for the cluster states. When we began this work we hoped that we would obtain an indication for the need to increase the Coulomb radius to an unusually large value for some (cluster) states. Indeed, the calculated excitation energies for the 0^+ and the 2^+ states are higher than the experimental ones by ~100 keV. A 50% increase of the Coulomb radius would be needed to match the experimental data. However, the results of calculations depend on the proper accounting for the presence of the $2p$ channel and also on the number of nodes of the cluster wave function. Based on our analysis we conclude that the partial widths for the $2p$ decay of the cluster 0^+ and 2^+ states are ~100 keV. It is interesting to see if these can be reproduced by the microscopic many-body calculations. We presented evidence that novel measurements of the properties of the proton rich nuclei could be very useful. Even if the quantum characteristics determination is not directly possible in these experiments, the comprehensive analysis of the properties of the states in the isobaric multiplet can be reliable, and a test of the theoretical approaches can be more complete.

The authors acknowledge support of Grant No. TE-FG02-93ER40773 of US Department of Energy and Grant No. PHY-0754674 of National Science Foundation .

[1] V.Z. Goldberg, G.V. Rogachev Phys. Rev. C **86**, 044314 (2012).
[2] R.J. Charity, T.D. Wiser, K. Mercurio *et al.*, Phys. Rev. C **80**,024306 (2009).
[3] R.J. Charity, J.M. Elson, J. Manfredi *et al.*, Phys. Rev. C **84**, 014320 (2011).
[4] A.N. Kuchera, G.V. Rogachev, V.Z. Goldberg *et al.*, Phys. Rev. C **84**, 054615 (2011).
[5] A.M. Mukhamedzhanov, B.F. Irgaziev, V.Z. Goldberg *et al.*, Phys. Rev. C **81**, 054314 (2010).
[6] J.P. Schiffer, G.C. Morrison, R.H. Siemssen, and B. Zeidman, Phys. Rev. **164**, 1274 (1967).
[7] S.E. Darden, G. Murillo, and S. Sen, Nucl. Phys. **A266**, 29 (1976).
[8] A.S. Volya, continuum shell model code COSMO, http://www.volya.net
[9] R.G. Thomas, Phys. Rev. **81**, 148 (1951).
[10] J.B. Ehrman, Phys. Rev. **81**, 412 (1951).
[11] S. Dixit *et al.*, Phys. Rev. C **43**, 1758 (1991).044314
[12] S.E. Darden, G. Murillo, and S. Sen, Nucl. Phys. **A266**, 29 (1976).
[13] D.R. Tilley, J.H. Kelley, J.L. Godwin, D.J. Millener *et al.*, Nucl. Phys. **A745**, 155 (2004).
[14] E.K. Warburton and B.A. Brown, Phys. Rev. C **46**, 923 (1992).

Investigation of ^{27}P with the AstroBox prototype detector

E. Simmons, L. Trache, M. McCleskey, A. Saastamoinen, R. G. Pizzone,[1]
G. G. Rapisarda,[1] B. Roeder, A. Spiridon, R.E. Tribble, E. Pollacco,[2]
G. Pascovici,[3] M. Riallot,[2] J. P. Mols,[2] and M. Kebbiri[2]
[1]*INFN Laboratori Nazionali del Sud & DMFCI Universita di Catania, 95123 Catania, Italy*
[2]*IRFU, CEA Saclay, Gif-sur-Yvette, France*
[3]*Institut fuer Kernphysik der Universitaet zu Koeln, D-50937 Koeln, Germany*

An experimental program to measure β-delayed proton decay has been done using the MARS beam line at TAMU and a configuration of silicon detectors, where the fragment of interest is implanted in a thin double sided strip detector and the subsequent decay is measured (for an example see [1]). In an attempt to reduce the β response while retaining high resolution at low energies for the protons of interest (10-15 keV FWHM at 200 keV), a new type of gas-filled detector utilizing a Micro Pattern Gas Amplifier Detector (MPGAD), called the AstroBox, has been developed [2-3]. Fig. 1 below shows the raw results from both the silicon configuration and the first AstroBox test run.

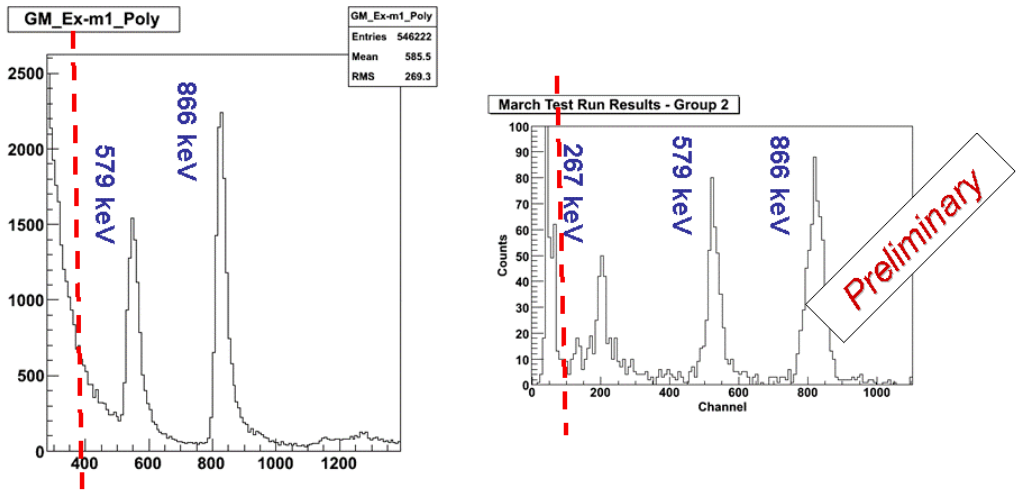

FIG. 1. The left-hand side shows the preliminary results with the silicon detector setup for the study of the β-delayed proton decay of ^{23}Al. The right-hand side shows the preliminary results achieved with the AstroBox prototype detector for the same nucleus.

As with the experiment performed with the silicon detectors in Nov. 2010 [3], a beam of $^{28}Si^{+10}$ at 40 MeV/u was obtained from the K500 superconducting cyclotron and impinged on a hydrogen gas target kept at LN_2 temperatures and a pressure of 2 atm in the MARS beam line. The ^{27}P nuclei were slowed down and implanted in the center of the P05 filled AstroBox detector with the use of a 10 mil aluminum degrader foil. It was decided to start with the known β-delayed proton emitter of ^{25}Si, which has a total

proton branching ratio of 35%, in order to optimize the detector. Ideally, ^{28}P was the desired nucleus for this task due to the fact it has several low energy protons, however, its total proton branching ratio (0.0013 %) was much lower than even ^{27}P (estimated at 0.07 %). With the beam time of this experiment reduced to 7 days due to some trouble with the K500 at higher beam energies for the nuclei of interest and other demands on the beam time, ^{25}Si was chosen over that of ^{28}P. Once the detector had been optimized ^{27}P was to be implanted in the center region.

Several improvements to the setup were applied coming directly from the experience of the previous two test runs. Namely, in order to include the heavy ion signals, a second ADC with a different acquisition trigger was needed, which was achieved by utilizing the interrupt request (IRQ) feature in the VM-USB VME controller to access different readout lists for different event types (heavy ion implant vs. decay). Additionally, a low cost in-house beam pulsing NIM module was created. This new unit has the advantage of having NIM logic outputs for beam on, "move", beam off, and gating grid on, as well as an optically isolated TTL output for the beam off signal that can be patched to the phase shifter on the K500 RF console. Additionally, this new unit is easily set up (in terms of beam on, beam off etc.) via a GUI. Scalar units were also included in the electronics to monitor all 3 active detector pads of the AstroBox, for both beam-on (heavy-ions) and beam-off (proton) signals.

The production rate for ^{25}Si was about 65 pps with the coffin (momentum) slits open at ± 1.0 cm. With the momentum slits closed to the ± 0.4 cm needed for implantation, the rate dropped to about 19 pps. Later, when switching to ^{27}P, there was only about 13 pps of the desired nucleus with the momentum slits at ± 0.4 cm. Due to a problem within the detector itself, one that began midway through the experiment and grew considerably worse, along with the limited primary beam intensity and beam time, we were unable to observe protons. However, in the beginning, we did successfully see the correct heavy ions associated with ^{25}Si during the beam-off part of the decay measurement. The problem with the AstroBox detector was found after the run and corrected. Analysis of the data is ongoing in the hopes of aiding future endeavors.

[1] A. Saastamoinen *et al*., Phys. Rev. C **83** 045808 (2011).

[2] L. Trache *et al*., in *Progress in Research*, Cyclotron Institute, Texas A&M University (20101– 2012), p. V-52

[3] E. Pollacco *et al.* Nucl. Instrum. Methods Phys. Res. A (submitted)

[4] E. Simmons *et al*., in *Progress in Research*, Cyclotron Institute, Texas A&M University (2011 – 2012), p. I-27

Spin physics with STAR at RHIC

Z. Chang, P. Djawotho, C. A. Gagliardi, M. M. Mondal, R. E. Tribble
and the STAR Collaboration

Our group continues to play major roles in STAR investigations of both longitudinal and transverse spin phenomena in polarized *pp* collisions at RHIC. During the past year, we finalized the analysis of STAR data that were recorded during 2009 to determine the longitudinal double-spin asymmetry, A_{LL}, for inclusive jet production at mid-rapidity in 200 GeV *pp* collisions. We also laid the groundwork for the determination of A_{LL} for inclusive jet production at mid-rapidity in 510 GeV *pp* collisions with data that STAR recorded during 2012, and made progress toward a determination of the transverse single-spin asymmetry, A_N, for jet-like events at forward rapidity using data that STAR recorded during 2011.

One of the primary goals of the RHIC spin program is to determine the gluon contribution to the proton spin. At RHIC energies, jet production at mid-rapidity is dominated by *gg* and *qg* scattering. This makes A_{LL} for inclusive jet production a sensitive probe of gluon polarization. Last year, we completed a preliminary analysis of data that STAR recorded in 2009 to determine A_{LL} for inclusive jet production in 200 GeV *pp* collisions [1].

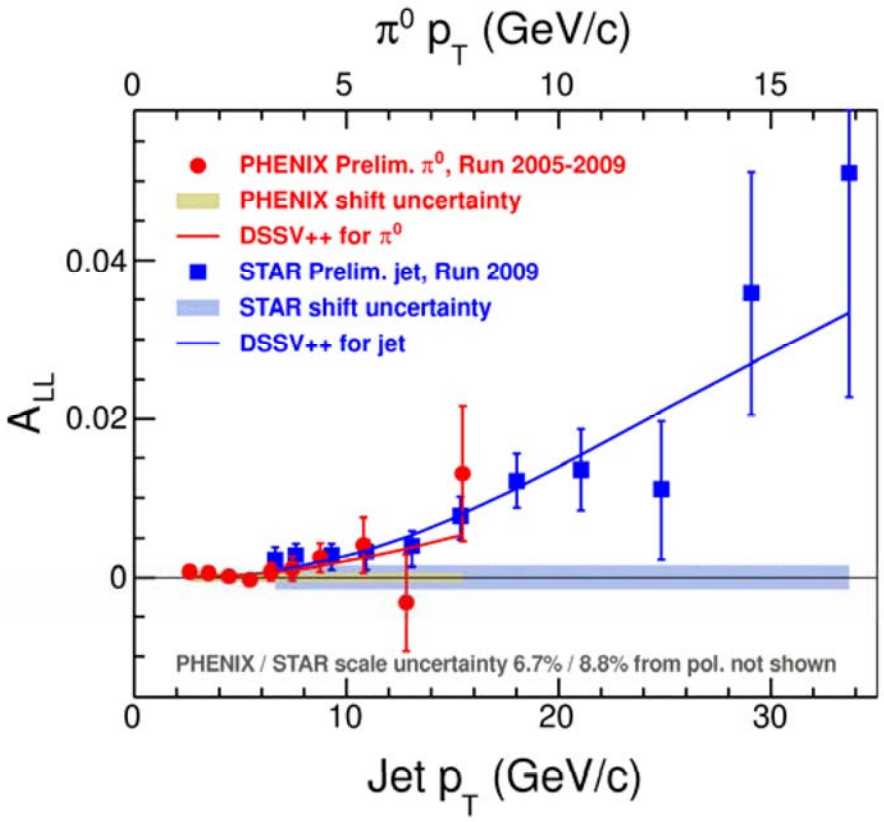

FIG. 1. A_{LL} for inclusive pion and jet production in 200 GeV *pp* collisions from PHENIX and STAR, respectively. The solid curves show the results for the DSSV++ global analysis

The preliminary 2009 STAR inclusive jet A_{LL} results [1] continue to generate a great deal of interest. Recently, the DSSV group [2] performed a preliminary revision of their polarized parton distribution global analysis, DSSV++, which includes the preliminary 2009 inclusive jet A_{LL} results from STAR and preliminary 2009 inclusive π^0 A_{LL} results from PHENIX. The new fit provides an excellent description of the STAR data, as shown in Fig. 1. They find that the integral of $\Delta g(x)$ over the range $0.05 < x < 0.2$, which is well measured with 200 GeV *pp* collisions at RHIC, is $0.10^{+0.06}_{-0.07}$, and conclude that the 2009 results provide the first indication of non-zero gluon polarization within the *x* range that is sampled at RHIC [3]. When they extrapolate the DSSV++ fit over all *x*, they find $\Delta G \sim 0.3$, albeit with very large uncertainties. This is about twice the quark contribution to the proton spin, and would be sufficient to satisfy the spin sum rule.

For the preliminary 2009 inclusive jet results, systematic uncertainties associated with trigger and reconstruction bias are 50-100% of the statistical uncertainties for several low to intermediate-p_T bins. These systematics arise primarily from the subprocess-dependence of our Jet Patch trigger, together with underlying event contributions that cause lower-p_T partons to be reconstructed as higher energy jets. During the past year, we completed a detailed study of the systematic uncertainties as a function of jet algorithm and resolution parameter. We obtained a significant reduction in these systematic effects by switching from the mid-point cone algorithm with a radius R=0.7 to the Anti-k_T algorithm with a resolution parameter R=0.6, at the expense of a 10-15% increase in the statistical uncertainties. We have now completed the final analysis of the 2009 data, and are preparing the paper for publication.

Mr. Z. Chang is using 2012 STAR data to determine A_{LL} for inclusive jet production in 510 GeV *pp* collisions for his dissertation research. A_{LL} values of only 0.001~0.002 are expected for the low-p_T jet bins that provide information regarding gluon polarization at the lowest *x* values. Thus, it's essential to minimize the systematic uncertainty associated with the determination of the relative luminosities of the various spin states at STAR. This past year, Mr. Chang performed a detailed analysis of the scaler data for three different STAR subsystems – the Beam-Beam Counter (BBC), the Vertex Position Detector (VPD), and the Zero-Degree Calorimeter (ZDC). He found that the VPD provides the best measure of the relative luminosities for the 2012 STAR data. The present estimate is that the relative luminosity determination will contribute a systematic uncertainty to A_{LL} of ±0.0004.

Another major goal of the RHIC spin program is to unravel the origin of the large transverse single-spin asymmetries for inclusive π^0 production that have been seen at forward rapidities at RHIC [4]. The asymmetries have been attributed to the Sivers effect, a correlation between the spin of the incident proton and the transverse momentum of the quark or gluon that experiences the hard scattering, the Collins effect, which arises from the spin-dependent fragmentation of polarized scattered quarks, or a combination of the two. The Sivers effect provides a window into parton orbital motion because it requires interference between amplitudes involving partons with different orbital angular momenta. The Collins effect provides a means to explore quark transversity, the third collinear, leading-twist parton distribution function. (The other two are the unpolarized distribution and the helicity distribution, which is explored in longitudinally polarized collisions as discussed above.)

Isolating the origin(s) of the large transverse single-spin asymmetries is going to require π^0 observations over a wider kinematic range, studies of additional hadron species, jets, and photons, as well as coincidence measurements. This past year, STAR published cross section and asymmetry measurements for inclusive π^0 and η meson production at pseudorapidity η=3.68 that span the range $0.4 < x_F < 0.75$ [5]. The cross sections are consistent with perturbative QCD expectations. At $x_F > 0.55$, the results indicate that A_N for the η is larger than that for the π^0; there is only a 3% probability that the two are equal. At present, it is not clear whether such a difference can arise from the Sivers or Collins effects.

Looking forward, we are developing the ability to reconstruct jet-like events with the STAR Forward Meson Spectrometer (FMS). The FMS provides electromagnetic calorimetry over the full azimuth for the range $2.5 < \eta < 4$. The Sivers effect should produce a spin asymmetry for jet-like events, whereas the Collins effect should produce an azimuthal asymmetry in the distribution of fragments about the jet thrust axis. In addition, the large acceptance of the STAR detector provides the opportunity to correlate the jet-like events in the FMS with additional final-state products emitted at other pseudorapidities in order to elucidate the underlying reaction mechanism.

During the past year, group members served as principal authors for two STAR papers [5,6], chair of the god-parent committee for two papers [6,7], and member of the god-parent committee for another paper [8].

[1] P. Djawotho, for the STAR Collaboration, arXiv:1106.5769.

[2] D. de Florian, R. Sassot, M. Stratmann, and W. Vogelsang, Phys. Rev. Lett. **101**, 072001 (2008); Phys. Rev. D **80**, 034030 (2009).

[3] E.C. Aschenauer *et al*. (RHIC Spin Collaboration), arXiv:1304.0079.

[4] B.I. Abelev *et al*. (STAR Collaboration), Phys. Rev. Lett. **101**, 222001 (2008).

[5] L. Adamczyk *et al*. (STAR Collaboration), Phys. Rev. D **86**, 051101(R) (2012).

[6] L. Adamczyk *et al*. (STAR Collaboration), Phys. Rev. D **86**, 032006 (2012).

[7] L. Adamczyk *et al*. (STAR Collaboration), arXiv:1302.6184.

[8] L. Adamczyk *et al*. (STAR Collaboration), Phys. Rev. D **85**, 092010 (2012).

SECTION II

HEAVY ION REACTIONS

Factors influencing residue cross section in ^{48}Ca-induced reactions

D. A. Mayorov, T. A. Werke, M. C. Alfonso, M. E. Bennett, and C. M. Folden III

In fusion reactions of ^{40}Ar with isotopes of lanthanide elements, Vermeulen et al. [1] observed surprisingly low production cross sections for weakly deformed elements near the N = 126 isotone line. In some cases, the measurement was up to a factor of 100 below predictions. The discrepancy was resolved by considering collective effects [2-4], which are most significant for production of weakly deformed nuclei. Rotational excitations enhance the nuclear level density at the fission saddle, while being absent for the near-spherical ground state of that nucleus. This in turn raises the fission probability for the excited nucleus formed in the fusion reaction in the ^{40}Ar experiments, while leaving the neutron emission channel unaffected. The same effects are of relevance to the field of transactinide elements ($Z \geq 103$), as present day efforts to produce ^{299}120 near the predicted shell closures Z = 120, N =184 are ongoing [5, 6]. However, there is a relatively small list of publications concerning this topic. Investigation on the production of weakly deformed nuclei in fusion reactions is, therefore, of particular interest. In the present report we show preliminary data for ^{48}Ca-induced reactions on targets of ^{154}Gd, ^{159}Tb, ^{162}Dy, and ^{165}Ho studied at the Cyclotron Institute. The products in these reactions are weakly deformed nuclides near the N = 126 shell. The measured difference in excitation functions can be understood in terms of a simple model for calculating survival probabilities dependent primarily on the fission barrier, B_f, and neutron separation energy, B_n. The ^{48}Ca data discussed here is part of a larger systematic study also including ^{50}Ti- and ^{54}Cr-induced reactions which is described in detail in [7].

Beams of $^{48}Ca^{6+}$ or $^{48}Ca^{7+}$ (≈ 5 MeV/u) were delivered by the K500 cyclotron for irradiation of ^{154}Gd (1.0 mg/cm^2 $^{154}Gd_2O_3$ on 2 μm Ti), ^{159}Tb (497 μg/cm^2), ^{162}Dy (403 μg/cm^2 on 75 μg/cm^2 ^{nat}C), and ^{165}Ho (498 μg/cm^2) targets, in three temporally separated experiments. The ^{154}Gd target was prepared by molecular plating the metal nitrate salt on a 2 μm thick Ti backing foil, and is described in a separate contribution to this report. Beam dose on target was continuously monitored by two collimated ion-implanted Si charged-particle detectors positioned at ±30^o to the beam axis. The beam energy was varied using 0 (no degrader), 1.20, 2.25, 3.45, 4.50, 5.10, and 6.29 μm Al degraders in order to measure the excitation functions for the studied reactions. A ^{nat}C foil was also used for reaction residue charge equilibration. Products of interest would transverse the Momentum Achromat Recoil Spectrometer (MARS) [8] and implant into the focal plane position sensitive silicon detector. Discrimination between α-decays and implantation events was achieved by pulsing the beam or using an upstream micro-channel plate detector. The measured alpha spectra are shown in Fig. 1. In reactions with ^{162}Dy and ^{165}Ho targets, the 4n and 5n products have nearly identical half-lives and α-decay energies. Therefore, the alpha peak represents the sum of these two reaction products.

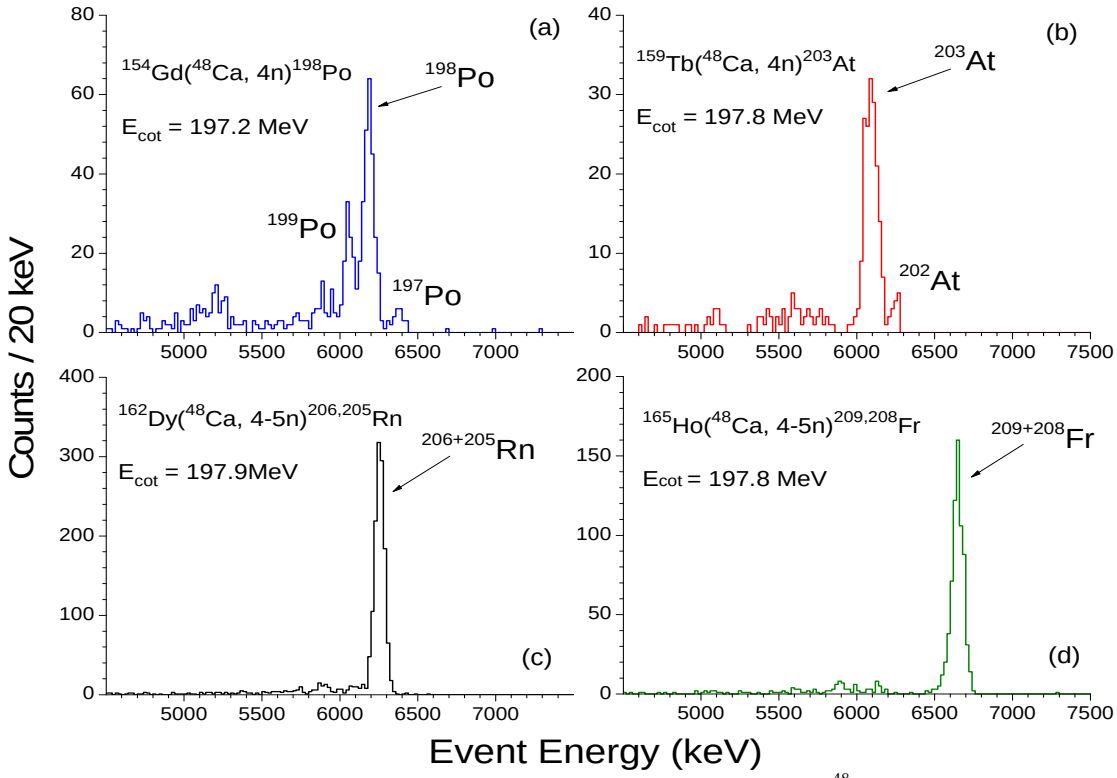

FIG. 1. Energy spectra for α-decaying evaporation residues produced in ^{48}Ca-induced reactions on lanthanides and implanted in a position-sensitive silicon detector placed at the focal plane of the MARS spectrometer.

Fig. 2a shows the measured excitation functions for the production of the 4*n* evaporation residues in reactions of ^{48}Ca with ^{154}Gd, ^{159}Tb, ^{162}Dy, and ^{165}Ho, plotted as a function of the laboratory-frame projectile energy at center-of-target, E_{cot}. Reactions with ^{159}Tb, ^{162}Dy, ^{165}Ho show a nearly invariable maximum cross section with the highest production cross section of 7.9±2.0 mb measured for the reaction ^{162}Dy(^{48}Ca, 4-5n)^{206,205}Rn. The maximum production cross section falls to 2.3±0.4 mb for the ^{154}Gd(^{48}Ca,4n)^{198}Po reaction.

The magnitude of B_f and B_n heavily influences the survival of the excited nucleus synthesized in the fusion reaction, and therefore the evaporation residue cross section. Fig. 2b shows the difference B_f - B_n plotted as a function of neutrons emitted in a series of neutron emission steps (up to 4*n*) from the excited compound system formed in each reaction. The fission barriers are calculated according to the refined rotating-liquid-drop-model [9] and neutron binding energies are taken from [10]. The use of highly neutron-rich ^{48}Ca results in relatively neutron-rich compound nucleus, thereby lowering the B_n of that nuclide relative to its lighter isotopes and aiding survival against fission. The clustering observed in Fig. 2b for all targets except ^{154}Gd suggests that the survival probability for these reactions should be equal in magnitude, which is consistent with the experimental data. In the case of the ^{154}Gd target, the smaller fission barriers and larger neutron separation energies reduce the production cross section.

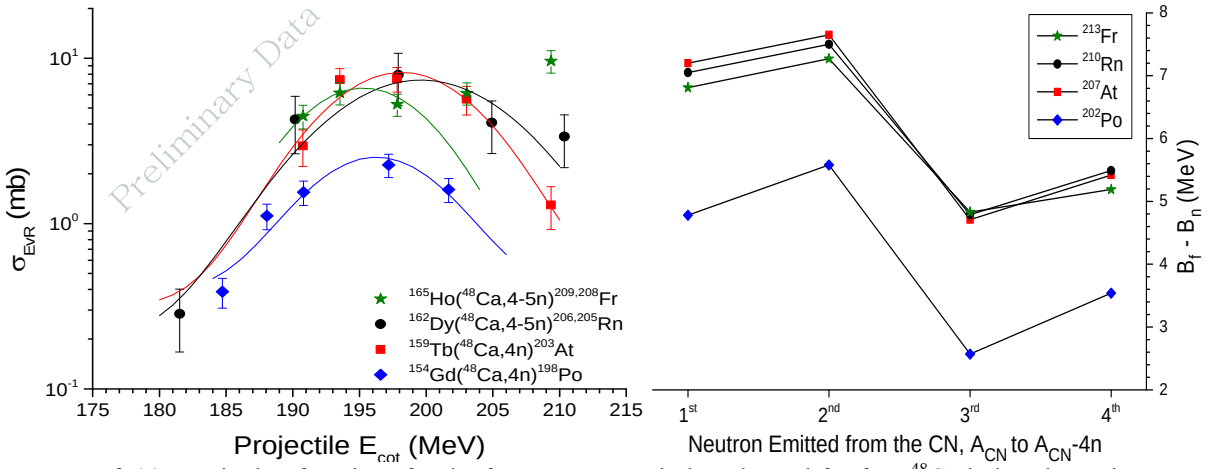

FIG. 2. *Left* (a): Excitation functions for the four-neutron emission channel for four ^{48}Ca-induced reactions. Note that the rise in the high-energy tail for the ^{48}Ca+^{165}Ho data is a transition from the 4n to the 5n product, both of which decay with nearly identical half-lives and alpha energies. Lines are drawn to guide the eye. *Right* (b): Plot of the difference in the fission barrier [9] and neutron separation energy [10] as a function of neutron emitted from the compound nucleus. The compound nucleus formed in each ^{48}Ca reaction is indicated in the legend.

The survival probability W_{sur} is expressed theoretically as [11]

$$W_{sur} = P\left(E^*_{CN}, x\right) \cdot \prod_{i=1}^{x} \left[\Gamma_n / \left(\Gamma_n + \Gamma_f\right)\right]_i \qquad (1)$$

where $P\left(E^*_{CN}, x\right)$ [12] determines the probability of emitting exactly x neutrons from an excited nucleus with excitation energy E^*_{CN}, Γ_n is the neutron decay width and Γ_f is the fission decay width. The decay width can be estimated from B_f and B_n using the method of Vandenbosch and Huizenga [13]:

$$\frac{\Gamma_n}{\Gamma_f} = \frac{4A^{2/3} a_f (E - B_n)}{K_o a_n [2a_f{}^{1/2}(E - B_f)^{1/2} - 1]} \exp[2a_n{}^{1/2}(E - B_n)^{1/2} - 2a_f{}^{1/2}(E - B_f)^{1/2}] \qquad (2)$$

with the level density having the form,

$$a_n = \tilde{a}_n [1 + (\delta S_n^{A-1} / E)(1 - \exp(-E/d))] \qquad (3)$$

$$a_f = \tilde{a}_f [1 + (\delta S_f^{A} / E)(1 - \exp(-E/d))] \qquad (4)$$

where E is the intrinsic excitation energy of the compound system, a is the energy-dependent level density parameter, $\tilde{a}$ is the energy-independent level density parameter, δS is the shell correction energy in the ground state for neutron emission or at the saddle point for fission, and $d \approx 16.4$ MeV [4]. Equation

2 models the "washing-out" of nuclear shell corrections [14]. The constant $K_o = \hbar^2 / g m_n r_o^2 \approx 9.8$ MeV, where g is the spin degeneracy and m_n the mass of the neutron, and r_o is the radius parameter.

Using Eq. 1-4 and including collective effects as prescribed in [4], W_{sur} for the 4n products of interest in each ^{48}Ca-induced reaction at E_{cot} corresponding to the maximum of each excitation function in Fig. 2a were calculated and are shown in column 7 of Table I. This simple model reproduces the ratios of the experimental cross sections to within a factor of ≈ 2. For instance, the ratio of experimental cross section $\sigma_{EvR}(^{206,205}Rn) / \sigma_{EvR}(^{198}Po) = 3.5 \pm 1.1$, while $W_{sur}(^{206,205}Rn) / W_{sur}(^{198}Po) \approx 1.8$. The ratio of the product of capture cross section and survival probability for these two reactions is ≈ 1.6.

The capture process describes the approach of the projectile to the target over an interaction barrier taken as the sum of Coulomb and nuclear forces. The diffused barrier formula [15] was used to calculate the capture cross section shown in Table I. In the above calculation, B_f at $l = 0$ were used with agreeable results. With increasing angular momentum, however, the liquid-drop fission barrier does diminish and entirely vanish at $l = l_{critical}$ [16]. This leads to a reduction in survival probability. Future analysis will incorporate the effect of average angular momentum on the production cross section. Furthermore, since experimental fission barrier data is not available for the neutron-deficient nuclides considered here, the impact of alternative models for fission barriers on W_{sur} should be examined. With W_{sur} having exponential dependence on B_f, a small change in the barrier height can produce a significant change in the survival probability.

Table I. Maximum measured 4n evaporation residue cross sections for ^{48}Ca+^{154}Gd, ^{159}Tb, ^{162}Dy, and ^{165}Ho reactions along with the corresponding projectile energies at center-of-target and excitation energy. Estimates of σ_{cap} and W_{sur} are given for the same energies.

E_{cot} (MeV)	E^*_{CN} (MeV)	Target	Residue	4n σ_{EvR} (mb)	σ_{cap} (mb)	W_{sur}
197.2	50.3	^{154}Gd	^{198}Po	2.3±0.4	180	0.30
197.8	51.4	^{159}Tb	^{203}At	7.5±1.3	185	0.63
197.9	49.9	^{162}Dy	^{206,205}Rn	7.9±2.0	163	0.54
197.8	47.7	^{165}Ho	^{209,208}Fr	5.3±0.8	138	0.42

The excitation functions for four ^{48}Ca-induced reactions on targets of ^{154}Gd, ^{159}Tb, ^{162}Dy, and ^{165}Ho have been measured. The measured production cross sections are highly correlated to $B_f - B_n$, which significantly affects the survival probability. Using a simple model for survival probability in preliminary analysis of the data, the differences observed in the maxima of the excitation functions can be explained, and it is the survival that plays a dominant role in the magnitude of the production cross section. Future work will continue excitation function measurements with ^{50}Ti and ^{54}Cr projectiles on the same targets to quantify the dependence of the cross section on the projectile.

[1] D. Vermeulen *et al.*, Z. Phys. A **318**, 157 (1984).
[2] P. Armbruster, Rep. Prog. Phys. **62**, 465 (1999).
[3] A.R. Junghans *et al.*, Nucl. Phys. **A629**, 635 (1998).

[4] V.I. Zagrebaev *et al.*, Phys. Rev. C **65**, 014607 (2001).
[5] M. Bender, and P.-H. Heenen, J. Phys.: Conf. Ser. **420**, 012002 (2013).
[6] Ch. E. Düllmann *et al.*, GSI Scientific Report (2011).
[7] C.M. Folden III *et al.*, J. Phys.: Conf. Ser. **420**, 012007 (2013).
[8] R.E. Tribble, R.H. Burch, and C.A. Gagliardi, Nucl. Instrum. Methods Phys. Res.**A285**, 441 (1989).
[9] A.J. Sierk, Phys. Rev. C **33**, 2039 (1986).
[10] *National Nuclear Data Center* (2013), available at http://www.nndc.bnl.gov.
[11] W. Loveland, J. Phys.: Conf. Ser. **420**, 012004 (2013).
[12] J.D. Jackson, Can. J. Phys. **34**, 767 (1956).
[13] R. Vandenbosch, and J.R. Huizenga, *Nuclear Fission* (Academic, New York, 1973), p.323.
[14] A.V. Ignatyuk, G.N. Smirenkin, and A.S. Tishin, Sov. J. Nucl. Phys, **21**, 255 (1975).
[15] W.J. Swiatecki, K. Siwek-Wilczynska, and J. Wilczynski, Phys. Rev. C **71**, 014602 (2005).
[16] S. Cohen, F. Plasil, and W. J. Swiatecki, Ann. Phys. **82**, 557 (1974).

Characterization of a gas stopper for heavy element chemistry studies

M. C. Alfonso, D. A. Mayorov, T. A. Werke, and C. M. Folden III

A new gas stopper optimized for online heavy element chemistry experiments has been designed, fabricated, and characterized at the Cyclotron Institute at Texas A&M University. The design of the gas stopper is described in detail in [1]. Offline tests using ^{216}Po ($t_{½}$ = 145 ms [2]) emanating from a ^{228}Th source suggest that the extraction efficiency is approximately 70%, and that the extraction time is comparable to or less than the ^{216}Po half-life. In November 2012, the device was characterized using the products of the ^{118}Sn(^{40}Ar, 6n)^{152}Er reaction, which were delivered from the MARS spectrometer. The gas stopper was mounted at the MARS focal plane, and two detectors just downstream of the window and just downstream of the extraction nozzle were used to measure the efficiency as a function of incident ion energy, gas flow rate, and electric field settings. The setup and preliminary results are shown in Fig. 1. The peak extraction efficiency of the gas stopper in online tests was approximately 40%. This is comparable to other gas stoppers in use at laboratories worldwide [3-6], and suggests that a planned online chemistry research program is feasible.

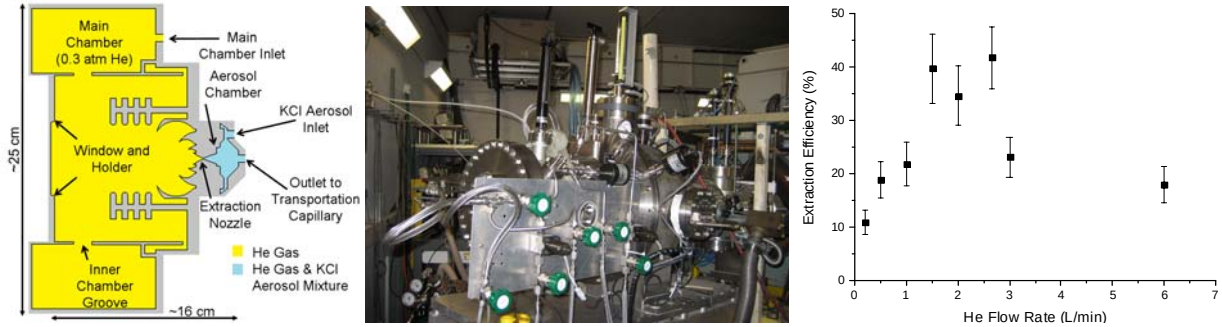

FIG. 1. Left: Schematic of the Texas A&M gas stopper. Ions pass through the window and enter the He-filled chamber (shown in yellow). A series of electrodes (shown in gray) creates an electric field that draws the ions through the extraction nozzle into the aerosol chamber (shown in blue) for transportation to a chemistry experiment. Center: The gas stopper mounted at the MARS focal plane position. Right: Preliminary results of the extraction efficiency of the gas stopper as a function of the He flow rate in the device.

[1] M.C. Alfonso and C.M. Folden III, *Progress in Research*, Cyclotron Institute, Texas A&M University (2011-2012), p.II-46; http://cyclotron.tamu.edu/2012%20Progress%20Report/2%20Heavy%20Ion%20Reactions/II_46-51_development%20of%20a%20gas%20stopper.pdf.

[2] *National Nuclear Data Center* (2013); available at http://www.nndc.bnl.gov.

[3] G. Savard *et al.*, Nucl. Instrum. Methods Phys. Res. **B204**, 582 (2003).

[4] M. Wada *et al.*, Nucl. Instrum. Methods Phys. Res. **B204**, 570 (2003).

[5] U.W. Kirbach *et al.*, Nucl. Instrum. Methods Phys. Res. **A484**, 587 (2002).

[6] L. Weissman *et al.*, Nucl. Phys. **A746**, 655c (2004).

Fabrication of lanthanide targets for nuclear reaction studies

D. A. Mayorov, T. A. Werke, M. E. Bennett, and C. M. Folden III

Thin targets are necessary in separator-based heavy-ion reaction studies to minimize the projectile energy uncertainty due to energy straggling, and to reduce the angular straggling of recoiling products, leading to higher particle transmission to the separator focal plane. Enriched Gd targets with thicknesses in the range 400 - 1000 μg/cm^2 have been prepared by molecular plating for use in a systematic study of fusion-evaporation reactions, focusing on factors affecting the de-excitation of the compound nucleus (see Ref. [1] for details). In molecular plating, a positively charged inorganic metal complex is plated onto a thin backing foil in electrical contact with a cathode by application of a high voltage (200 – 1200 V) to an anode. One distinguishing feature of molecular plating is the resulting chemical form of the target as metal oxide. Due to the high potential difference involved, the microliter volumes of the metal complex solution must be dissolved in excess organic solvent, commonly isopropanol or acetone, prior to plating.

Schematics of the plating cell used in the present work are shown in Fig. 1. The cell design is based on a design developed at Lawrence Berkeley National Laboratory, with minor modifications [2]. In

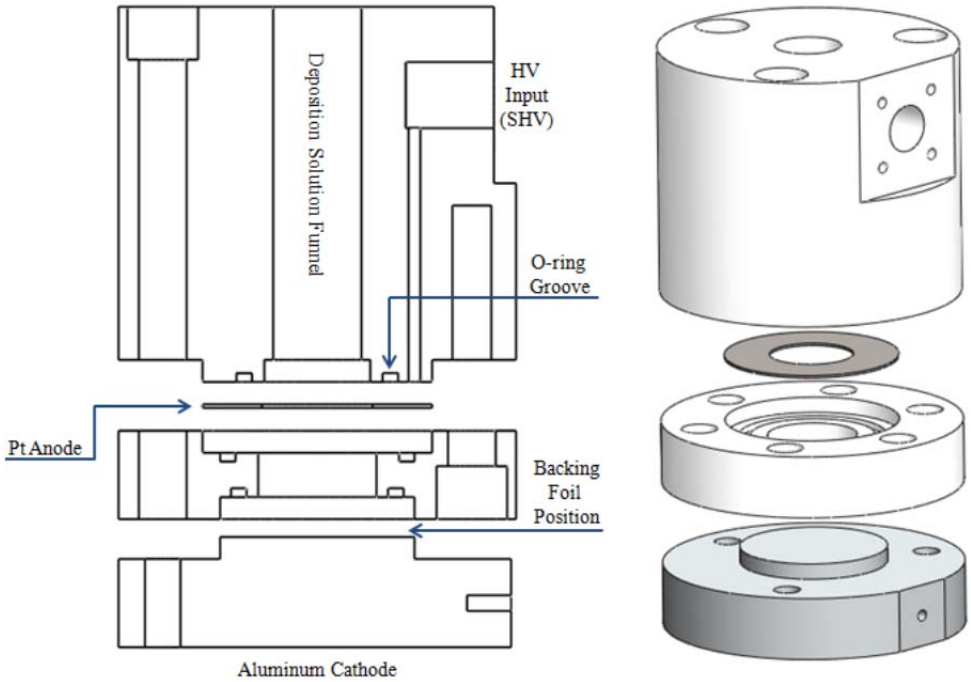

FIG. 1. Cross sectional and a 3-dimensional view of the molecular plating cell. The cell body and centerpiece need to have low electrical conductivity, low chemical absorption, and high chemical resistivity properties, criteria well accommodated by the polyether ether ketone (PEEK) plastic. The anode is a platinum washer. The cathode base is constructed of aluminum and contains a tap to attach wiring for circuit ground.

preparing the Gd targets, enriched oxide of the metal (starting material) was dissolved in dilute HNO_3 to prepare $Gd(NO_3)_3$, a water-soluble ionic salt. The resulting solution was dried under Ar gas to remove excess water. This eliminates a potential source of additional current, which may compromise the quality

of the target film due to bubbling (H_2 evolution) and/or heating of the cathode. The $Gd(NO_3)_3$ was dissolved in ≈10 mL of anhydrous isopropanol and 7 μL of 0.1 M HNO_3, yielding the deposition solution. This solution was injected into the cell funnel and plated at 800 V over 30 minutes onto a 2 μm Ti backing (3/4" outer diameter) with current densities in the range of 3.5 - 5 mA/cm^2, followed by 40 minutes of drying of the film at 250^o C. Target films on thin Al backings were also prepared. During the plating, the solution was continuously stirred. The final area of the target films was 2.27 cm^2.

Following the above procedure, a ≈1.0 mg/cm^2 $^{154}Gd_2O_3$ (≈87% by weight ^{154}Gd) target was prepared for separator-based work involving production studies of Po isotopes via fusion with ^{48}Ca. The target thickness was determined by α-particle energy loss measurements. The enrichment of the ^{154}Gd was >99.8%, measured by Secondary Ion Mass Spectrometry at the Material Characterization Facility at Texas A&M University. In addition, targets of ^{nat}Ho and ^{208}Pb were also prepared utilizing the plating cell [3]. The presently described method provides capabilities for future production of lanthanide and actinide targets, with procedures available in literature [4-6].

[1] C.M. Folden III *et al.*, J. Phys.: Conf. Ser. **420**, 012007 (2012).
[2] K.E. Gregorich, Private Communication (2011).
[3] M.E. Bennett *et al.*, J. Radioanal. Nucl. Chem. (2013). Accepted.
[4] K. Eberhardt *et al.*, Nucl. Instrum. Methods Phys. Res. A**521**, 208 (2004).
[5] G. Mullen *et al.*, Nucl. Instrum. Methods Phys. Res. **A115**, 75 (1974).
[6] W. Parker *et al.*, Nucl. Instrum. Methods Phys. Res. **A26**, 61 (1964).

Excitation functions of ^{45}Sc-induced reactions: towards future superheavy element synthesis

T. A. Werke, D. A. Mayorov, M. C. Alfonso, M. E. Bennett, and C. M. Folden III

The study of fusion-evaporation reactions at near-Coulomb barrier energies is critical to understanding the production of heavy and superheavy elements (SHEs). Using a ^{48}Ca (Z = 20) beam on actinide targets, elements with Z = 113 - 118 have been synthesized by the Dubna-Livermore Collaboration [1-4]. A lack of available target material means that beams with Z > 20 such as ^{45}Sc must be developed to produce the next SHEs. Very little experimental data exists on fusion evaporation cross sections using a ^{45}Sc beam. By experimentally measuring excitation functions of ^{45}Sc-induced reactions on lanthanide targets, we can study the effects of changing the projectile from ^{48}Ca to the much less neutron-rich ^{45}Sc. These studies will also provide insight towards the likelihood of producing superheavy elements with ^{45}Sc projectiles.

The heavy elements group at Texas A&M University has studied intermediate mass fusion-evaporation reactions using a metal beam with Z ≥ 20 bombarding lanthanide targets to produce actinides near the N = 126 shell. Heavy ion fusion-evaporation reactions have been studied using ^{45}Sc projectiles accelerated by the K500 cyclotron at the Cyclotron Institute. The reaction systems were selected with several desirable properties in mind, such as large alpha-decay branches and short half-lives [5,6]; see Table I for details. Beam energies were varied using a series of ^{nat}Al degraders with thicknesses of 0 (no degrader), 1.2, 2.25, 3.45, 4.5, 5.1, and 6.29 μm. The beam dose was monitored by Rutherford scattering on two circular silicon detectors at ±30° to the beam axis in the target chamber. The ^{45}Sc primary beam bombarded a self-supporting target of 498-μg/cm^2 ^{159}Tb, and a 403-μg/cm^2 ^{162}Dy target that is supported by 75-μg/cm^2 ^{nat}C. Unreacted primary beam and unwanted reaction products were separated using the Momentum Achromat Recoil Spectrometer (MARS) [7]. MARS filters products using a two stage scheme consisting of an achromatic magnetic rigidity selection section followed by a Wien Filter. The separation factor of primary beam and unwanted reaction products is approximately on the level of 10^{15} [8]. Evaporation residues were tuned through MARS and implanted in a single focal plane silicon strip detector. A microchannel plate detector serves as a veto detector to discriminate implants from the subsequent alpha decays. Preliminary results are reported here.

Table I. Selected properties for the reactions of ^{45}Sc +^{159}Tb, ^{162}Dy and ^{48}Ca +^{159}Tb. N_{CN} is the number of neutrons in the compound nucleus. Z_pZ_t is the charge product of the projectile and target nuclei. The half-life and alpha branching ratio (b_α) are given for the 4n evaporation residue (EvR). σ_{calc} is the predicted maximum cross section for the 4n EvR calculated by the method of Zagrebaev *et al.* in [9,10]. Half-lives are taken from [5]. Alpha branching ratios are taken from [6].

Projectile	Target	CN	N_{CN}	Z_pZ_t	$t_{1/2}$ (s)	b_α (%)	σ_{calc} (mb)
^{45}Sc	^{159}Tb	^{204}Rn	118	1365	$1.03^{+020}_{-0.11}$	86^{+14}_{-4}	0.46
^{45}Sc	^{162}Dy	^{207}Fr	120	1386	0.55 ±0.01	95 ± 5*	0.14
^{48}Ca	^{159}Tb	^{207}At	122	1300	444 ± 12	31 ± 3	14

* No uncertainty given. Value estimated from [6].

Experimental data have been collected for the reaction systems of ^{45}Sc + ^{159}Tb, ^{162}Dy and are shown in Figs. 1 and 2, where E_{cot} is the center-of-target beam energy in the laboratory frame**.** The figures also show excitation functions for other similar reactions on the same targets. The data show that reactions using ^{45}Sc projectiles have cross sections that are two orders of magnitude less than the theoretical calculations using the method of Zagrebaev [9,10], and that are three orders of magnitude less than ^{48}Ca-induced reactions on the same target.

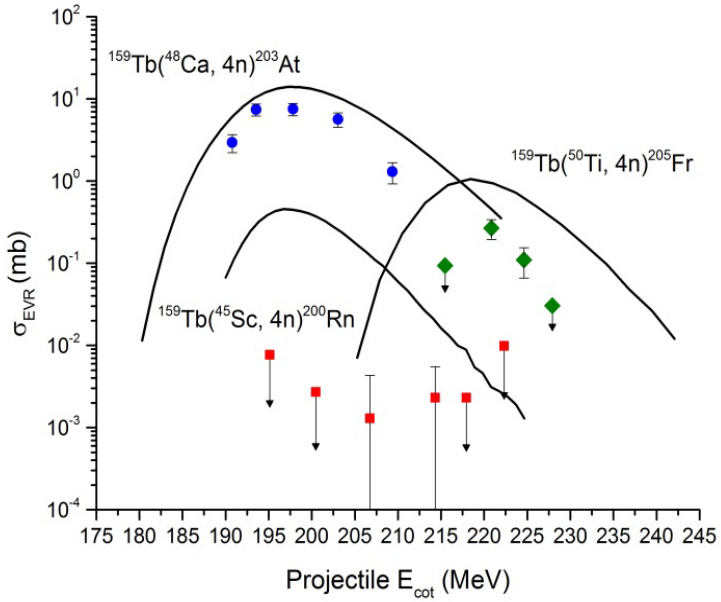

FIG. 1. Excitation functions for projectiles of ^{48}Ca, ^{45}Sc, and ^{50}Ti on a ^{159}Tb target. Solid lines are theoretical predictions from Zagrebaev *et al.*[9,10].

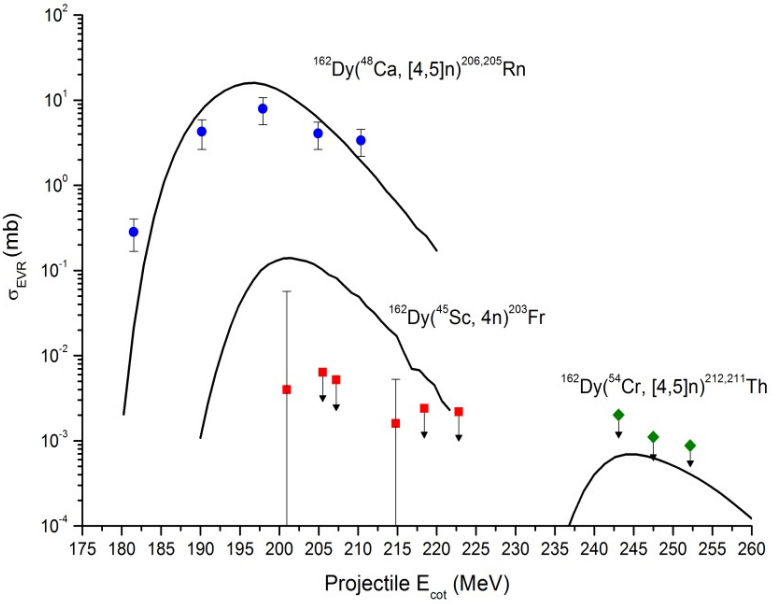

FIG. 2. Excitation functions for projectiles of ^{48}Ca, ^{45}Sc, and ^{54}Cr on a ^{162}Dy target. Solid lines are theoretical predictions from Zagrebaev *et al.* [9,10].

The theoretical description of the fusion-evaporation process is almost universally presented as a progression of three steps, shown in Fig. 3**.** The projectile-target system overcomes an interaction barrier and comes into contact, evolves into a single excited nucleus, and finally decays by several nucleon evaporations (the 4n channel is depicted in Fig. 3) and gamma emission into the ground state. The

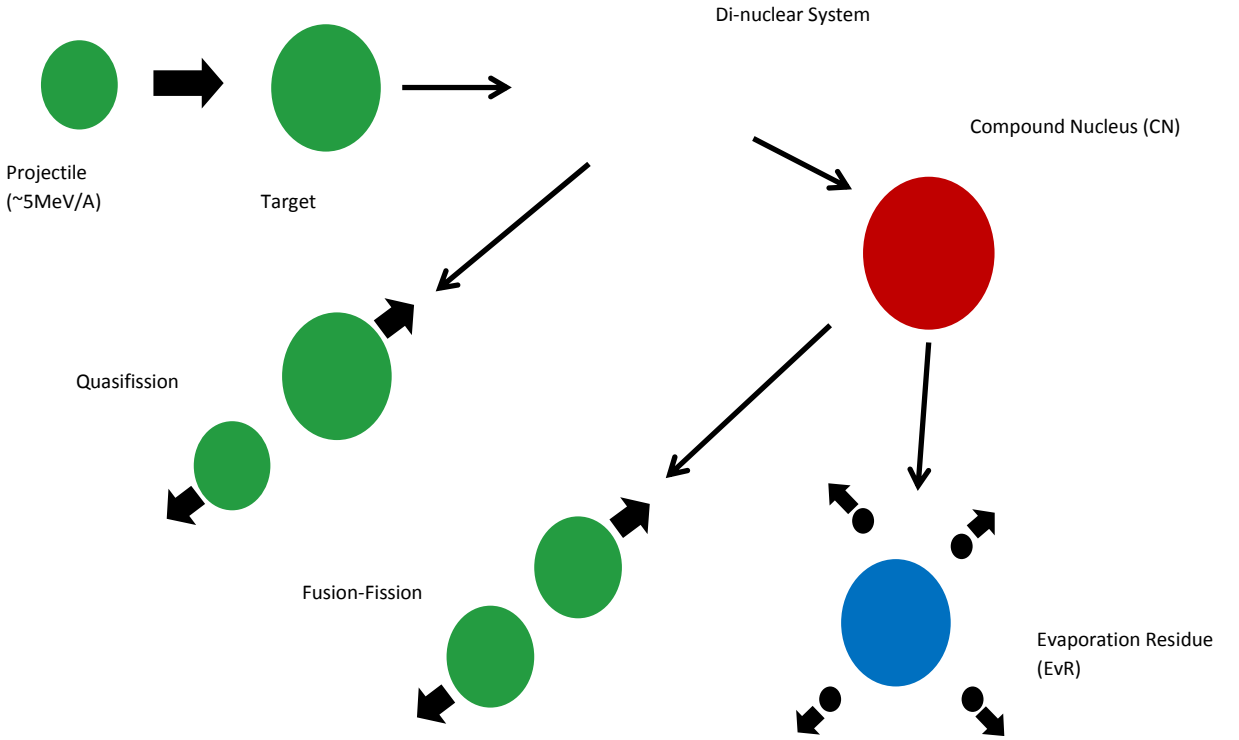

FIG. 3. Depiction of the fusion-evaporation process. The projectile and target capture and fuse to form the compound nucleus (CN). The CN de-excites via nucleon emissions to give the evaporation residue (EvR).

fusion-evaporation cross section is commonly represented as the product of three terms [11]:

$$\sigma_{EvR} = \sigma_{capt}(E) P_{CN}(E^*, l) P_{xn}(E^*, l) \qquad (1)$$

where E is the center of mass projectile energy, E* is the excitation energy of the compound nucleus, and l is the angular momentum of the compound system. $\sigma_{capt}(E)$ is the capture cross section for the projectile to overcome the interaction barrier and form a di-nuclear system. $P_{CN}(E^*, l)$ is the probability of forming the compound nucleus, and $P_{xn}(E^*, l)$ is the probability of the compound nucleus evaporating x neutrons and reaching the ground state of the evaporation residue. The large reduction in 4n EvR cross section for the ^{45}Sc-induced reactions must arise from one of the three terms in equation (1). $\sigma_{capt}(E)$ is relatively well understood and can be calculated within a factor of two [1,2]. Values of $\sigma_{capt}(E)$ for the reactions in Figs. 1 and 2 are calculated using the method of Zagrebaev *et al.* [9] and are shown in Table II. These data indicate that $\sigma_{capt}(E)$ changes by about a factor of 1.5, which is not enough to account for the three orders of magnitude difference in the EvR cross sections. $P_{CN}(E^*, l)$ depends on the charge

product of the target and projectile, Z_pZ_t. Table I shows that the values of Z_pZ_t change by less than 5% from ^{48}Ca beam to ^{45}Sc beam, and previous data suggests that $P_{CN}(E^*, l)$ should have a value between 0.25 to 1 for the reaction systems [13]. This is also insufficient to account for the three orders of magnitude difference in the EvR cross sections between the ^{48}Ca-induced reactions and the ^{45}Sc-induced reactions.

Table II. Calculated values of the capture cross section for the reactions in Figs. 2 and 3 using the method of Zagrebaev *et al.* [9].

Reaction	$\sigma_{capt}(E)$ (mb)
^{48}Ca+^{159}Tb	378
^{45}Sc+^{159}Tb	214
^{50}Ti+^{159}Tb	431
^{48}Ca+^{162}Dy	420
^{45}Sc+^{162}Dy	341
^{54}Cr+^{162}Dy	449

The final quantity in Eq. (1), $P_{xn}(E^*, l)$, depends on the decay widths for neutron emission, Γ_n, and fission, Γ_f, as shown in Eq. (2).

$$P_{xn}(E^*, l) = P(x, E^*) \prod_{i=1}^{x} \left(\frac{\Gamma_n}{\Gamma_n + \Gamma_f}\right)_{i,E^*,l} \quad (2)$$

$P(x, E^*)$ denotes the probability for emitting exactly x neutrons. Using transition state theory, the dependence of the quantity Γ_n/Γ_f on the neutron binding energy, B_n, and the fission barrier, B_f [14,15] can be shown:

$$\frac{\Gamma_n}{\Gamma_f} \propto \exp[2a_n^{\frac{1}{2}}(E^* - B_n)^{\frac{1}{2}} - 2a_f^{\frac{1}{2}}(E^* - B_f)^{\frac{1}{2}}] \quad (3)$$

where a_n and a_f are the level density parameters for neutron emission and fission, respectively. A small neutron binding energy and a large fission barrier increases the probability of the excited CN emitting neutrons to give the desired EvR. Due the exponential dependence in Eq. (3), small changes in $B_n - B_f$ result in a large change to Γ_n/Γ_f. The factor Γ_n/Γ_f is then taken to the power of x, further amplifying the effects of $B_n - B_f$ on $P_{xn}(E^*, l)$. The data show that the ^{48}Ca-induced reactions have values of $B_n - B_f$ that are 7 MeV more negative than the corresponding ^{45}Sc-induced reactions as shown in Fig. 4. This result is due to the relative neutron deficiency of ^{45}Sc projectiles compared to the neutron rich ^{48}Ca projectile. In the CN, neutron deficiency means a larger neutron binding energy and a smaller fission barrier; both of these effects work against the likelihood of neutron emission. This result likely explains the majority of the three orders of magnitude difference in the 4n EvR cross sections between the ^{48}Ca-induced reactions and the ^{45}Sc-induced reactions.

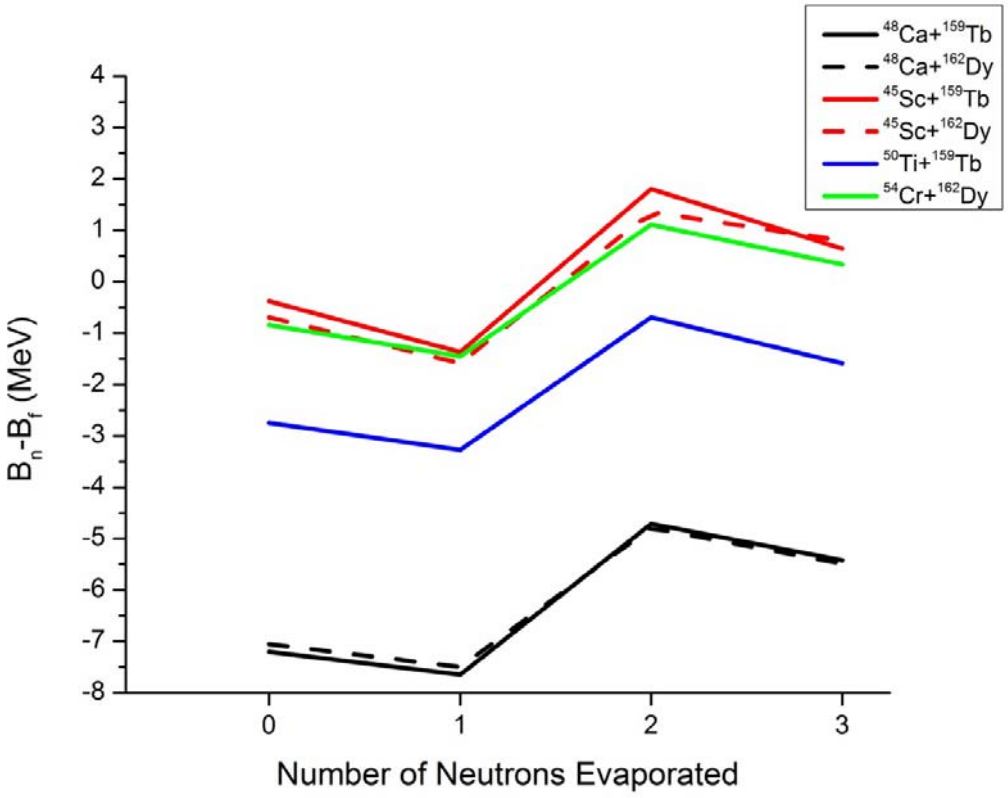

FIG. 4. Values of B_n-B_f for the reaction systems in Figs 2 and 3.

Complete fusion evaporation cross sections have been measured for reactions of ^{45}Sc + ^{159}Tb, ^{162}Dy at Texas A&M University. The cross sections are three orders of magnitude lower than cross sections for ^{48}Ca projectiles on the same target. The relative neutron deficiency of ^{45}Sc compared to ^{48}Ca results in a large reduction in the survival probability for the ^{45}Sc-induced reactions and likely accounts for the majority of the difference in EvR cross sections. This suggests that ^{45}Sc-induced reactions will likely have very small cross sections for the production of new SHEs. ^{50}Ti-induced reactions will create more neutron-rich compound nuclei and likely result in larger EvR cross sections. Future experiments will revisit the ^{45}Sc beam reactions, as well as use other metal beams with $Z \geq 20$ on lanthanide targets to help to better quantify these effects.

[1] Y. Oganessian, J. Phys. G. **34**, R165 (2007).
[2] Y.T. Oganessian *et al.*, Phys. Rev. C **74**, 044602 (2006).
[3] Y.T. Oganessian *et al.*, Phys. Rev. Lett. **104**, 142502 (2010).
[4] Y.T. Oganessian *et al.*, Phys. Rev. C **72**, 034611 (2005).
[5] National Nuclear Data Center, *Chart of the Nuclides*; available at http://www.nndc.bnl.gov/.

[6] R.B. Firestone and L.P. Ekstrom, *WWW Table of Radioactive Isotopes - Nuclide Search*; available at http://ie.lbl.gov/toi/nucSearch.asp.
[7] R.E. Tribble, R.H. Burch, and C.A. Gagliardi, Nucl. Instrum. Methods Phys. Res. **A285**, 441 (1989).
[8] C.M. Folden III *et. al.*, Nucl. Instrum. Methods Phys. Res. **A678**, 1 (2012).
[9] V. Zagrebaev *et. al.*, *Empirical model code of the NRV*; available at http://nrv.jinr.ru/nrv/.
[10] V. Zagrebaev *et. al.*, *Monte Carlo code of the NRV*; available at http://nrv.jinr.ru/nrv/.
[11] V. Zagrebaev and W. Greiner, Phys. Rev. C **78**, 034610 (2008).
[12] W. Loveland, arxiv:1207.2095v1 (2012).
[13] C.M. Folden III *et. al.* , J. Phys.: Conf. Ser. **420** 012007 (2012).
[14] A.J. Sierk, Phys. Rev. C **33** (1986).
[15] W.D. Myers and W. J. Swiatecki, *Table of Nuclear Masses according to the 1994 Thomas-Fermi Model*; available at http://ie.lbl.gov/txt/ms.txt.

Ionization chamber development for super heavy elements search

S. K. Wuenschel, E. J. Kim, M. Barbui, J. B. Natowitz, H. Zheng, N. Blando, and K. Hagel

We reported previously an experimental search for super heavy elements (SHE) [1]. During the experiment and in subsequent analysis, we found that it would be necessary to solve a number of problems encountered during that previous experiment. Neutrons were responsible for generating false signals in the silicon detectors. In order to counteract that effect, small area thin silicon detectors were then inserted both in order to conclusively identify alpha particles as well as to lower the probability of false signals from n-Si reactions in the silicon detector. With these modifications in the previous run, we observed a number of alpha particles emanating from the catcher foil. The geometry was, however, very low.

In order to increase the geometry we have designed and constructed a set of ionization chambers that have a much larger area than the silicon ΔE-E telescopes inserted in the previous experiment. Gas in the IC is also effectively very thin, indeed much thinner than a 50 μm silicon detector, so the possibility of a reaction with the neutrons is expected to be significantly reduced.

The ICs that we designed and built are of the traditional design in that they consist of a cathode at ground, a grid mounted on a frame separated from the anode by a few millimeters. A depiction of the detectors is shown in Fig. 1. In the figure, we show the chamber with the two plates and grid as well as a planned PPAC in the front and two silicon detectors in the back in order to achieve particle identification with the ΔE-E technique. The backmost silicon detector is a 300 μm Micron 7 strip detector. The silicon detector just in front of that is expected to be a 50μm Micron 16x16 strip detector.

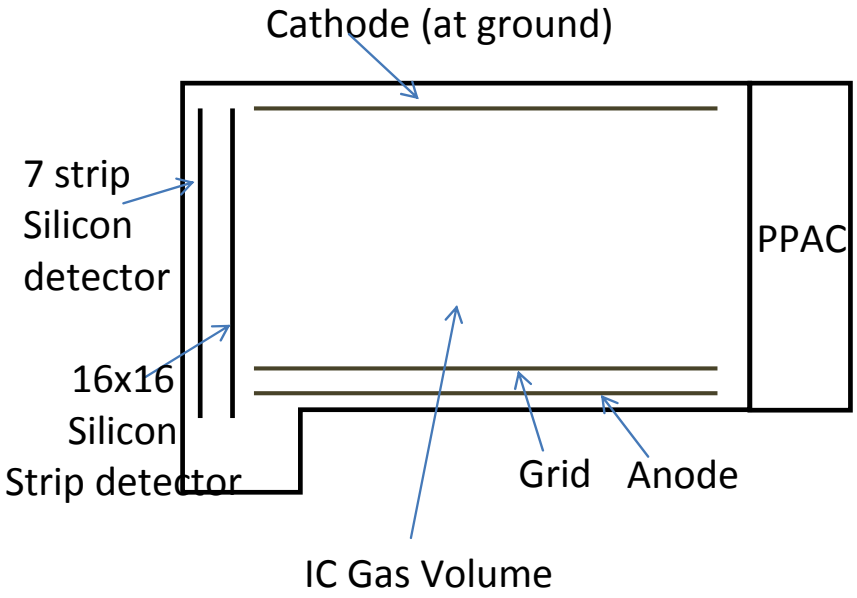

FIG. 1. A depiction of the Ionization chamber with a proposed PPAC at the entrance as well as the silicon detectors in back.

We performed tests on the ICs with a ^{228}Th source. Fig. 2 shows a ΔE-E plot of energy lost in the IC vs. residual energy in the silicon detector (one detector was used in these tests. We see that the different lines of the alphas from the ^{228}Th source follow the expected ΔE-E trend.

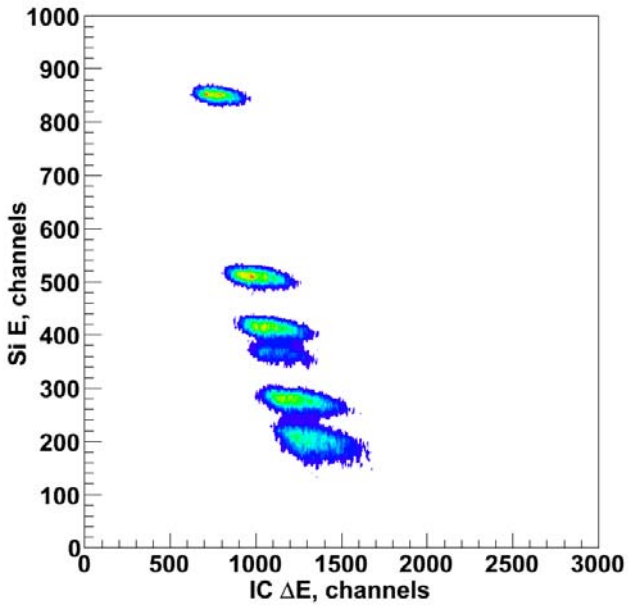

FIG. 2. ΔE-E plot of Ic vs silicon detector using a ^{228}Th source.

The line trends show that the IC can be used to identify alpha particles. The resolution in the IC, however, requires improvement in order to be able to have adequate resolution in the total energy in order to estimate the mass of the possible heavy elements should they be produced in the experiment. We are currently working to increase the high voltage that can be applied before sparking occurs. This should improve the resolution.

The PPAC that is depicted at the entrance to the IC in Fig. 1 is in the planning stages. Once this PPAC is built and implemented, we will have the ability, by inserting, in addition, the 16x16 strip detector, to track the origin of detected alpha particles to the active catcher that is currently being built by our collaborators in Krakow, Poland.

[1] M. Barbui *et al.*, *Progress in Research*, Cyclotron Institute, Texas A&M University (2011-2012), p. II-1.

Probing custerization in ^{40}Ca ^{40}Ca reaction at 35 MeV/A

K. Schmidt, K. Hagel, M. Barbui, S. Wuenschel, G. Giuliani, H. Zheng, E. Kim,
N. Blando, A. Bonasera and J. B. Natowitz

Bose-Einstein condensation is known to occur in weakly and strongly interacting systems such as dilute atomic gases and liquid ^{4}He [1]. During the last decade it was theoretically shown that dilute symmetric nuclear matter may also experience Bose particle condensation [2,3] More precisely, for low temperatures and densities smaller than one fifth of the nuclear saturation density, nuclear matter organizes itself in α-clusters, while for higher densities deuteron condensation is preferred. This possible new phase of nuclear matter may have its analog in low-density states of α-conjugate lighter nuclei, in the same way as superfluid nuclei are the finite-size counterpart of superfluid nuclear and neutron matter. This means that under some circumstances, the alpha condensation, i.e. bosonic properties, might dominate nucleon properties even in finite nuclei [4]. A natural way to pursue this is to apply experimental techniques developed for the investigation of low density nuclear gases to collisions of nuclei expected to have a significant alpha cluster character. Such nuclei might show a more natural predilection to evolve into a Bose Condensate. We have initiated a search for evidence of Bose Condensates using the NIMROD array. Our experiments employed 10, 25, 35 MeV/u beams of ^{40}Ca and ^{40}Si incident on ^{40}Ca, ^{28}Si , ^{12}C and ^{180}Ta targets. The first three targets allow an exploration of collisions of alpha conjugate nuclei. In the ^{180}Ta case the projectile excitation and decay is of primary interest. The data are currently being analyzed. Our expectation is that a Bose Condensate would manifest itself as an assemblage of alpha conjugate products with particular kinematic correlations. Therefore the first step of the analysis was to probe α clusterization in ^{40}Ca + ^{40}Ca at 35MeV/A reaction.

We initiated the analysis of the reaction from reconstructing the excitation energy of each event E* through calorimetry

$$E^* = \sum_{i=1}^{M} K_{cp}(i) + M_n\langle K_n\rangle - Q$$

The excitation energy E* was defined as the sum over accepted particles center of mass kinetic energy (K_{cp} and K_n) minus the reaction Q-value. The average kinetic energy of the neutrons was calculated as the proton average kinetic energy with a correction for Coulomb barrier energy. In Fig. 1 we plot the 3 heaviest fragment masses as a function of parallel velocity in different windows of E*.

Low excitation energies are associated with less violent collisions, therefore in both the experimental data and theoretical calculations we see heavy projectiles (mainly of A=28, 32 and 36 in the experiment) as well as light nuclei. With increasing excitation energy the violence of the collisions increases, we observe a very strong neck-like emission which consists mainly of α like fragments (A=12, 16, 20, 24). Their parallel velocity decreases with the decreasing mass. This has been described in [5] as the "hierarchy effect": the ranking in charge induces on average a ranking in average parallel velocity where the heaviest fragment is the fastest and is more focused in the forward direction.

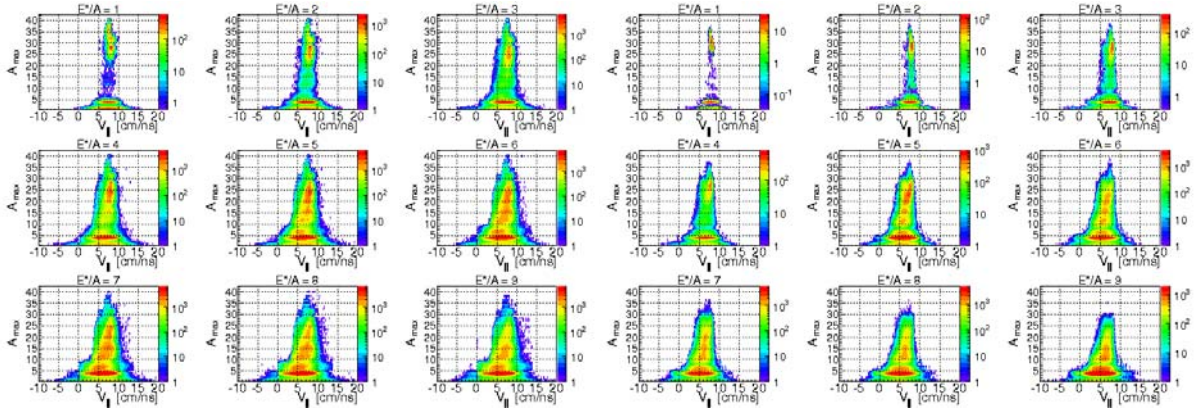

FIG. 1. Three heaviest fragment masses as a function of their parallel velocity in different windows of excitation energy E*/A, left: experimental results, right: theoretical predictions.

Since very strong α clusterization is observed, we attempt to quantify this behavior. In the following we focus on events with α-like mass = 40. 1.3% of experimental events are characterized by α-like mass = 40 whereas the AMD predicts around half that amount, 0.77%. Both experiment and theoretical calculations suggest that the most probable decay modes are those with one heavy α-like mass fragment and several α particles in the exit channel. The contribution of each branch however shows differences between experiment and calculations.

In the experiment the second most probable exit channel is the (^{28}Si, 3α.) Since we are interested in 3α events we focus on this channel. and compare it to (^{28}Si,^{12}C). We show in Fig. 2 the invariant velocity plots of these two decaying branches products. We observe that to a close approximation ^{28}Si moves with the beam velocity (8.21cm/ns) in both cases. The parallel velocity of ^{12}C is consistent with the velocity of the "neck" (see Figure 2) and oscillates around 4-7 cm/ns. Although we observe α particles emerging from the projectile, the majority of them come from a source of intermediate parallel velocity similar to that of ^{12}C. Therefore it will be our priority to focus on the effects related to "neck" emission in further analysis. We will treat it as a separate source of α particles and study its properties.

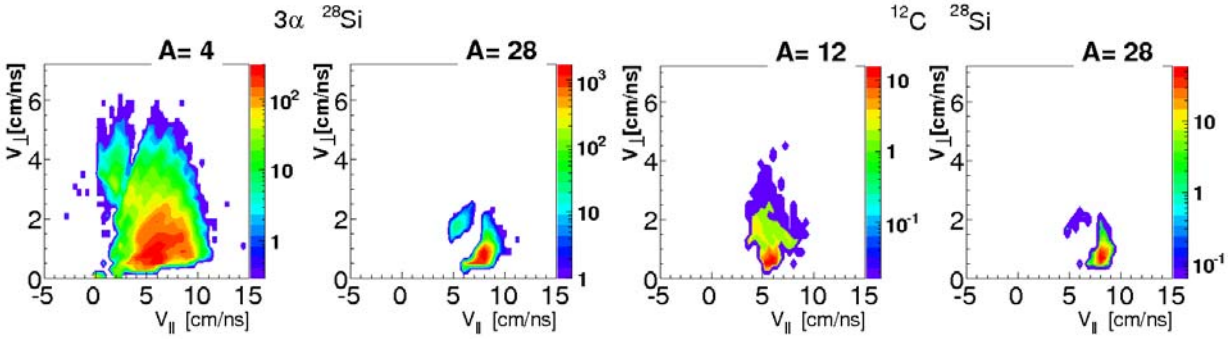

FIG. 2. Invariant velocity plots of 3□+^{28}Si (left) and ^{12}C+^{28}Si (right).

Correlation functions (CF) are defined as the ratio between the correlated (physical) yield Y_{corr} and the product of single particle yields, generically termed as uncorrelated spectrum Y_{uncorr}, measured under the same conditions,

$$1 + R(X) = \frac{Y_{corr}(X)}{Y_{uncorr}(X)}$$

Y_{uncorr} can also be built by mixing particles from different events. Information on the α-particle unstable excited states of ^{12}C populated by the $^{40}Ca+^{40}Ca$ at 35 MeV/nucleon reaction may be extracted from the 3α-CF and Nα-CF. Although 3α-CF is rather intuitive, the Nα-CF requires some explanation. In N-α events there are $\binom{N}{3}$ combinations of such triples of α particles, that could originate from the decay of ^{12}C. We have found all of them and built the E* distribution, which constitues the $Y_{corr}(X)$ in the definition of CF. In order to built the uncorrelated distribution of E* we used α-particles originating from different events. Moreover, we have distinguished between the triples emitted from "neck" and PLF, putting a cut on reconstructed source parallel velocity $V_z \in (4,7)$[cm/ns] for "neck" emission and $V_z \geq 7$[cm/ns] for PLF. In the following figures (Fig. 3 and Fig. 4). we present the CF distributions for alphas originating from neck or PLF, from 3α or Nα events, we compare the experimental data with AMD calculation.

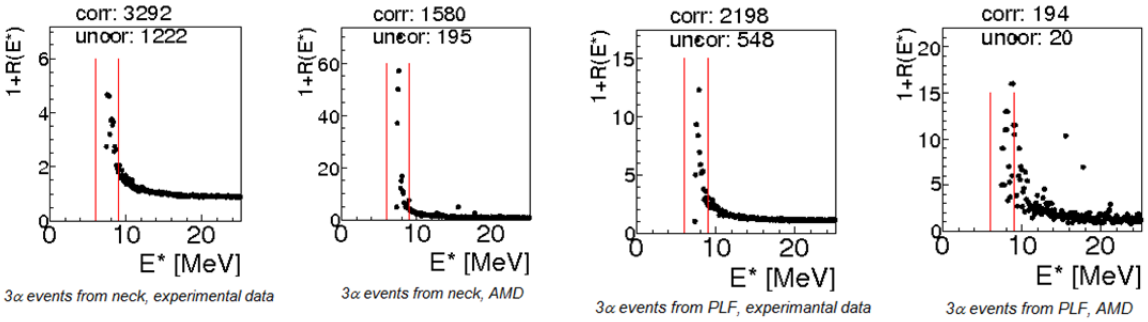

FIG. 3. CF distributions for 3α – events originating from "neck" and PLF, comparison of experimental data and AMD calculations.

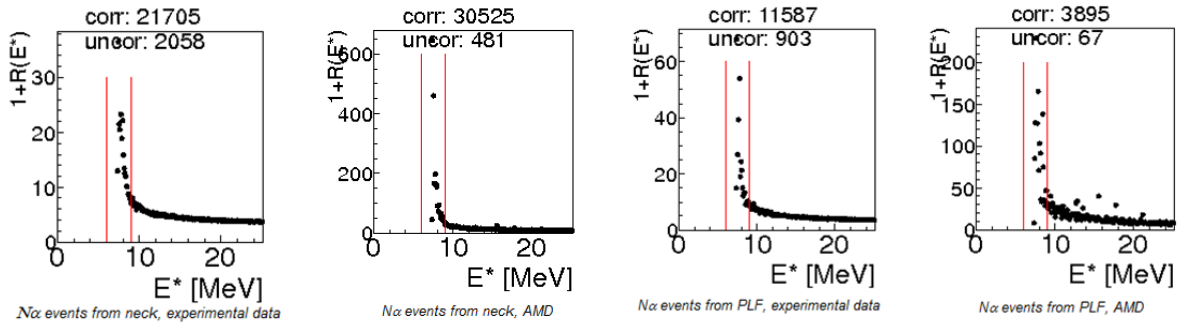

FIG. 4. CF distributions for Nα – events originating from "neck" and PLF, comparison of experimental data and AMD calculations.

All CFs manifest a peak broadening, centered at E*=7.61. It corresponds to the Hoyle state (E^* = 7.654 MeV). Unfortunately the granularity of Nimrod detecting system does not allow us to observe the complex region of excitations, characterized by the strong E* =9.64 MeV, 3^- state and by the broad E* =10.3 MeV, 0^+ state submerging a possible 2^+ state at 9.7 MeV [6,7].

We demonstrated so far that the ^{40}Ca+^{40}Ca nuclear reaction at 35MeV/nucleon populates excited states of ^{12}C nuclei which decay by 3-α emission. We will now examine only those triples, by putting a cut on excitation energy 7≤E*≤9 MeV. A popular way to visualize competing 3-α particle decay mechanisms is the Dalitz plot. In the following pictures we show E_{cm} Dalitz plots for 3α originating from Nα events and from ^{12}C decay, which in turn origins from neck or PLF. The first and the third plot corresponds to experimental data, while the second and the fourth one to AMD simulations. The Dalitz plots (Fig. 5) do not manifest any direct emission in three α-particles with equal energies (DDE) pattern as in [8]. However, the differences in decay mechanism can be noticed, when ^{12}C originates from neck or from PLF. The next step of the analysis will be to explain those differences, provide the theoretical Coulomb trajectories for different shapes of decaying nuclei, examine the shape of experimental decaying nuclei.

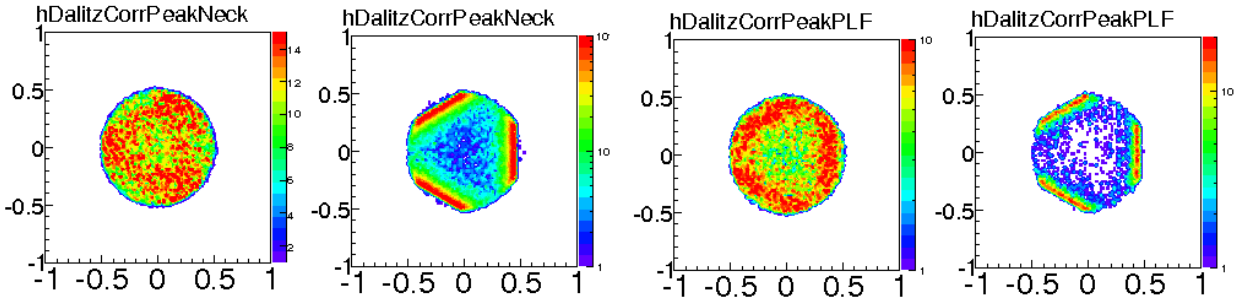

FIG. 5. Dalitz plots for 3-α originating from ^{12}C decay, which in turn originates from neck (the first two plots) and from PLF (the last two plots). Experimantal data are shown in the first and the third plot, AMD calculations in the second and the fourth one.

[1] L.P. Pitaevski and S. Stringari S, Bose-Einstein Condensation, (Clarendon Press, Oxford 2003).

[2] G. Roepke *et al.*, Phys. Rev. Lett. **80**, 3177 (1998).

[3] M. Beyer *et al.*, Phys. Lett. B **448**, 247 (2000).

[4] T. Sogo *et al.*, Phys. Rev. C **79**, 051301 (2009).

[5] J. Colin *et al.*, Phys. Rev. C **67**, 064603 (2003).

[6] M. Itoh *et al.*, Nucl. Phys. **A738**, 268 (2004).

[7] M. Freer *et al.*, Nucl. Phys. **A834**, 621c (2010).

[8] Ad. Raduta *et al.*, Phys. Lett. B **705**, 65 (2011).

Investigating the experimental capabilities of the quadrupole thermometer

S. Wuenschel, J. B. Natowitz, M. Barbui, N. Blando, A. Bonasera, G. Guilani,
K. Hagel, E. J. Kim, K. Schmidt, and H. Zheng

Fragmentation Reliably quantifying temperature is a significant challenge in experimental efforts to study the nuclear equation of state. Over the years, a variety of thermometers have been developed, the most recent being the momentum quadrupole thermometer [1]. This was first implemented using the Maxwell-Boltzmann distribution of a classical ideal gas and employed to quantify temperature differences resulting from neutron/proton asymmetry present in the fragmenting nuclear system [2,3]. Recently a Fermi-Dirac distribution has been employed. This approach may provide information on quantum effects in particle and cluster emission [4,5].

In an effort to better understand the information accessible in quadrupole thermometer based studies, data acquired at 47MeV/u using an early version of the NIMROD detector array have been reexamined. This data set spans systems from ^{4}He+^{112,124}Sn to ^{64}Zn+^{112,124}Sn [6]. We will constrain ourselves here to the most central events (bin 4) of the ^{40}Ar+^{112}Sn system.

Various thermometers have previously been shown to be sensitive to the identity of the fragment chosen as the probe [2,3,6]. This behavior has also been observed in this data set as shown in Fig. 1. The general trend in the quadrupole fluctuation thermometer has been shown to be T(^{1}H)<T(^{2}H)<T(^{3}H)~T(^{3}He) with T(^{4}He) varying in its relative magnitude [2,3]. This ranking of temperatures implies different sources or times of fragment emission. The issue of fragment emission time has been addressed in earlier studies employing slope and double isotope thermometers by cutting on the fragment surface velocity [6,7].

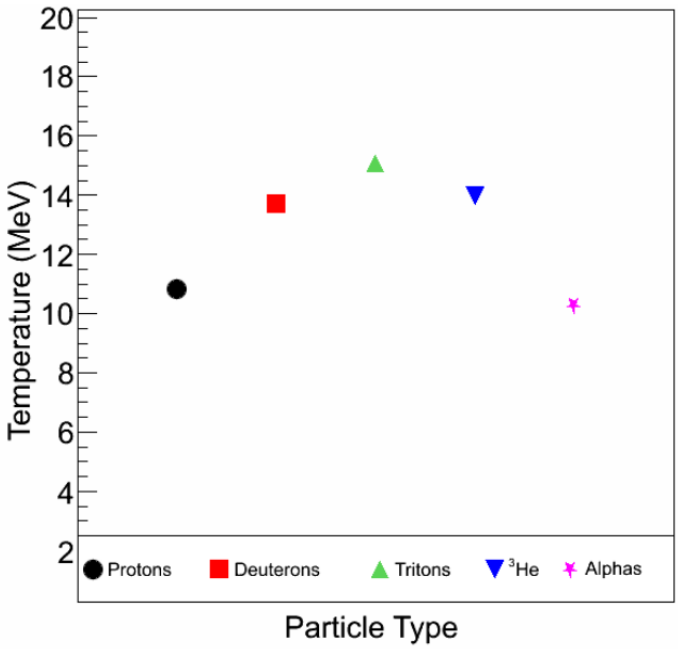

FIG. 1. Temperature as a function of particle type for ^{40}Ar+^{112}Sn.

To further probe features of the momentum quadrupole thermometer, a simple toy model of an isotropically emitting source was constructed. This model provides information on what effects, if any, could be expected from velocity cuts on the quadrupole thermometer. The initial calculations assume a Maxwell-Boltzmann distribution. The results of binning single source data along the transverse direction are shown in Fig. 2. Here the data are presented for two input temperatures as an integral of increasing transverse velocity. A third mixed source is also shown. It can be seen from this simulation that transverse cuts are unable to provide quality differentiation between sources well separated in

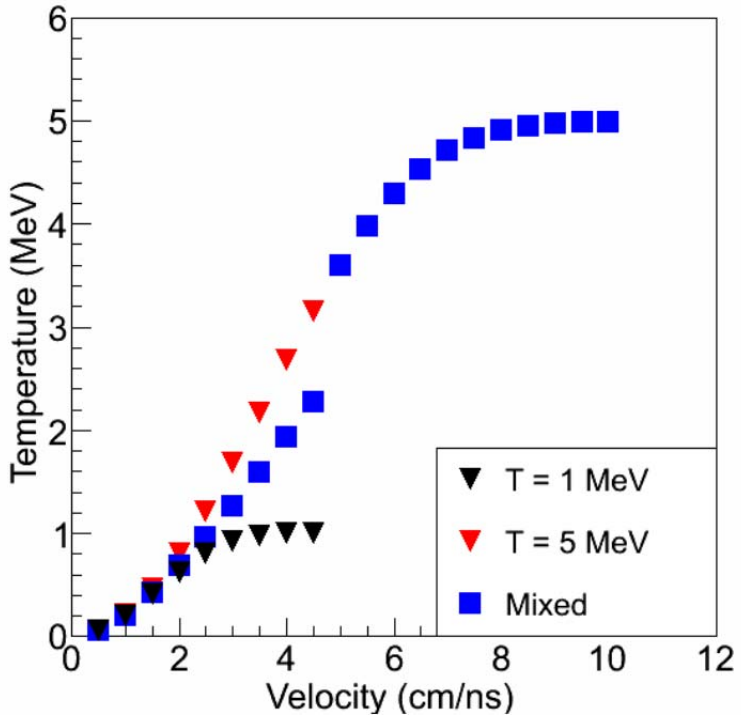

FIG. 2. Temperature derived from model as an integral of increasing transverse velocity. Sources are: black triangles T=1MeV, red triangles T=5 MeV, blue squares are an equal mixture of the previous sources

temperature. Thus, the continuum of sources that we observe in experimental data will not be differentiated by this method.

The top panel of Figure 3 shows the results of binning the quadrupole fluctuation data in equal increments of the velocity along the z –axis. For a single source, we observe a predominantly flat behavior of the derived temperature. Two additional sources, of equal intensity, were then added with offsets of +/- 4.5 cm/ns along the z-axis. The relative yield distribution of each source is seen in the center panel of Figure 3 and the derived temperatures in the bottom panel. From these figures, we see that the quadrupole based temperatures are sensitive to the source mixing. In each velocity window, this will depend upon the relative intensities and temperatures of the contributing sources.

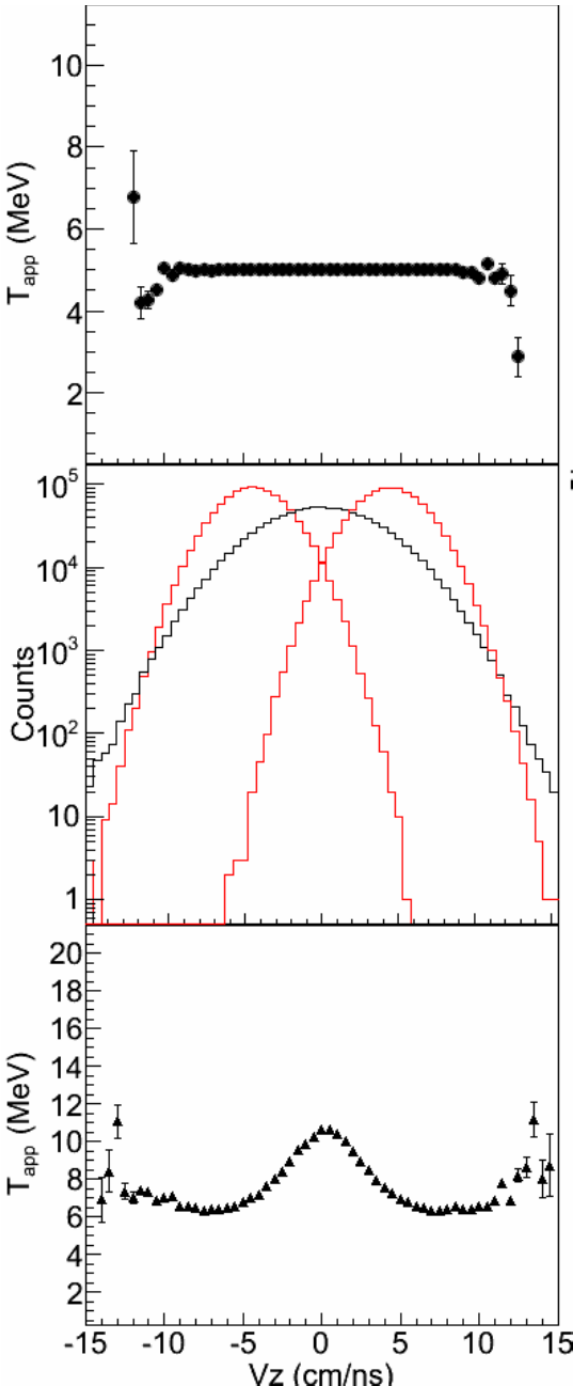

FIG. 3. (Top) Temperature derived from toy model as a function of z-axis velocity for a single source T= 5 MeV. (Middle) Yield of three sources as a function of z-axis velocity. Center source has T=12 MeV and outer sources have T=5 MeV. (Bottom) Temperature as a function of z-axis velocity for mixed sources

In Fig. 4, we have plotted experimental momentum quadrupole temperatures as a function of z-axis velocity obtained from bin 4 events from the reaction ^{40}Ar+^{112}Sn for Z=1,2 isotopes. In the previous studies [6] these data were fit assuming three contributing sources, a projectile like, target -like and intermediate velocity source. That assumption indicated different temperatures and multiplicities for the different sources. This is also evident in Figure 4, where we see that the experimental behavior of the momentum quadrupole thermometer for each particle type varies significantly as a function of the z-axis velocity.

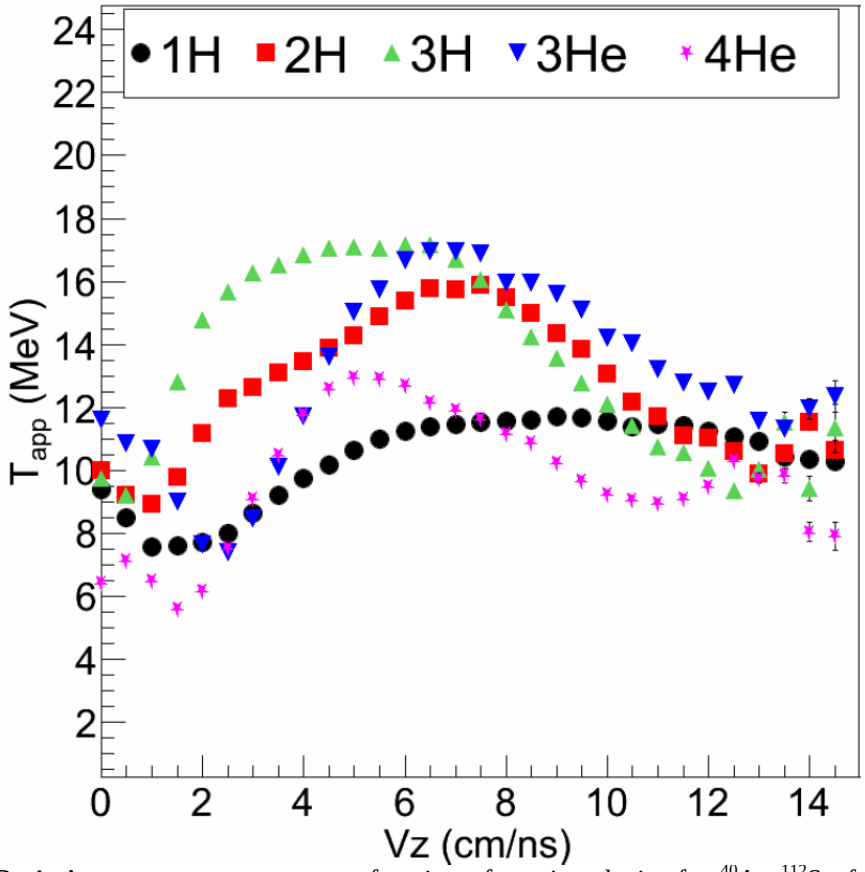

FIG. 4. Apparent temperature as a function of z-axis velocity for ^{40}Ar+^{112}Sn for particle types.

Unlike the fitting assumptions no a-priori definition of three well-defined sources has been made in constructing Figure 4. Given that the data reflect a continuous evolution of emission processes results of this type may lead to a better understanding of the reaction dynamics and provide a better method of source definition.

[1] S. Wuenschel *et al.*, Nucl. Phys. **A843**, 1 (2010).
[2] S. Wuenschel, Ph. D. Thesis Texas A&M University, 2010.
[3] A.B. McIntosh *et al.*, Phys. Lett. B **719**, 4 (2013).
[4] H. Zheng and A. Bonasera. Phys. Lett. B **696**, 178 (2011).

[5] J. Mabiala, A. Bonasera, *et al.*, arXiv:1208.3480v1 (2012)
[6] L. Qin *et al.*, Phys. Rev. Lett. **108**, 172701 (2012); L. Qin, Thesis Texas A&M University, 2008.
[7] K. Hagel *et al.*, Phys. Rev. C **62**, 034607 (2000).

Exploring the alpha cluster structure of nuclei using the thick target inverse kinematics technique for multiple alpha decays

M. Barbui, K. Hagel, V.Z. Goldberg, J.B. Natowitz, H. Zheng, G. Giuliani,
G.Rapisarda, S. Wuenschel and X.Q. Lin[1]
[1]*Institute of modern physics, Chinese Academy of Sciences, Lanzhou, China*

The alpha clustering properties of ^{24}Mg were investigated with the Thick Target Inverse Kinematics (TTIK) technique [1] using the reaction ^{20}Ne+α. This technique is particularly suited for this study because it allows the exploration of a large range of incident energies in the same experiment. Moreover, in the inverse kinematics, the reaction products are focused at forward angles and can be detected with detectors covering a relatively small portion of the solid angle in the forward direction.

^{20}Ne beams of energy 3.7 AMeV and 11 AMeV were delivered by the K150 cyclotron at Texas A&M University. The effective beam energies after the entrance window were 2.9 AMeV and 9.7 AMeV respectively. The reaction chamber was filled with ^{4}He gas at a pressure sufficient to stop the beam at 10 to 4 centimeters from the detectors (10.3 and 50 PSI respectively). In this way we could detect light particles emitted at zero degrees. The energy of the light reaction products was measured by three silicon detector telescopes placed at a radial distance of 48 cm from the entrance window. Each telescope consisted of two 5x5 cm^2 Micron Semiconductors DC quadrant detectors (Design G). The time of flight of the detected particles was also measured relative to the cyclotron radiofrequency. A monitor detector was used to measure the intensity of the incident beam. A schematic picture of the experimental setup is given in Fig.1.

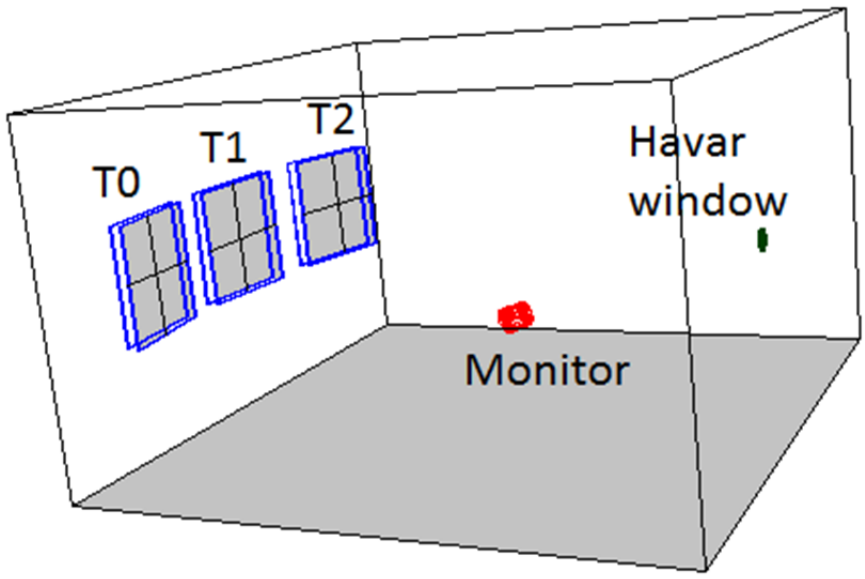

FIG. 1. Experimental setup. T0, T1 and T2 are the silicon detector telescopes.

After the energy and time calibration of the detectors, alpha particles were separated from protons and other light particles with proper gates on ΔE-E and E-Time plots. High Z reaction products are stopped in the gas before reaching the detectors.

According to the Ikeda picture [2] ^{24}Mg can be described as ^{20}Ne + α, ^{16}O + 2α, ^{12}C + 3α or a cluster of 6 α particles. Each configuration is expected to be observable at excitation energies around the corresponding threshold values. In this experiment the TTIK method was used to study multiple α-particle decays as well as elastic scattering. We observed alpha particle multiplicities up to 3, when the ^{20}Ne beam energy was 2.9 AMeV, while at 9.7 AMeV we observed alpha particle multiplicities up to 6. The events with alpha particle multiplicity 1 and 2 are analyzed here.

The results obtained on the elastic resonant α scattering (alpha multiplicity 1) are shown in Fig. 2. The resonant elastic scattering differential cross-sections, in the center of mass frame, are plotted as a function of the ^{24}Mg excitation energy. Our differential cross-sections are compared with those measured in Ref. [3] at similar angles. New results are obtained at 180^o up to ^{24}Mg excitation energies of about 35 MeV. We have an energy resolution of 30 keV at 180^o, worsening with decreasing angles. It is interesting to note that 28.5 MeV is the threshold energy for the decomposition of ^{24}Mg into 6 alpha particles.

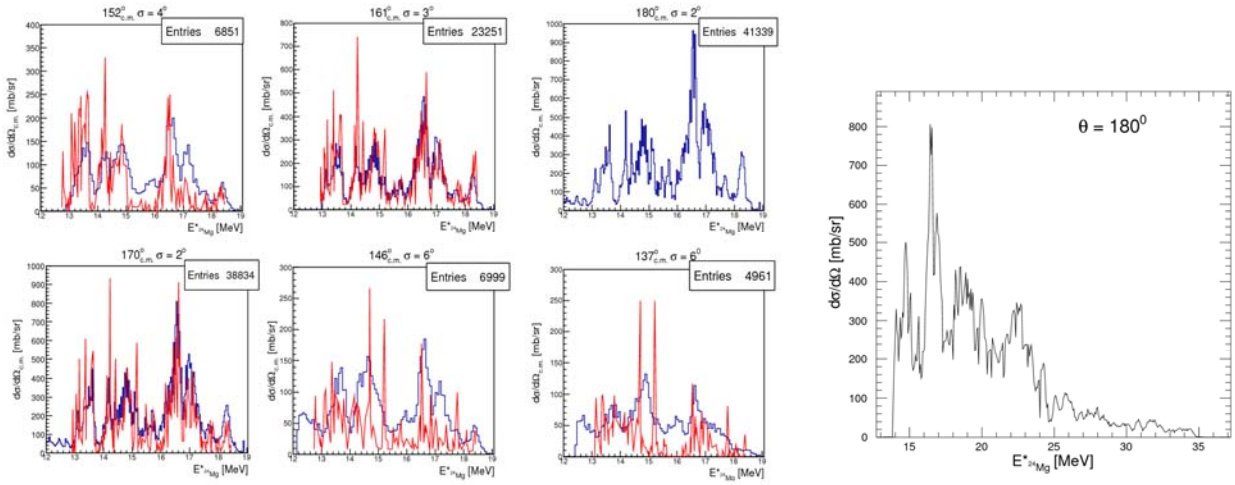

FIG. 2. Resonant elastic scattering cross-sections. Left panel: obtained at 2.9 AMeV ^{20}Ne; Right panel: obtained with the 9.7 AMeV ^{20}Ne. The red lines show the cross-sections measured in Ref. [3] at 156^o, 164^o, 168^o, 143^o and 139^o.

Fig. 3 shows the energies of the two alpha particles detected in events with alpha multiplicity 2. Uncorrelated events have been estimated by randomly mixing two alpha particles from the experimental distribution of multiplicity one events. The subtracted two dimensional plots are shown in Fig. 3.

A reconstruction code developed to analyze this experiment was used to derive the interaction point inside the gas volume. This code uses the kinematics, the alpha particle energies and a double check with the measured times of flight.

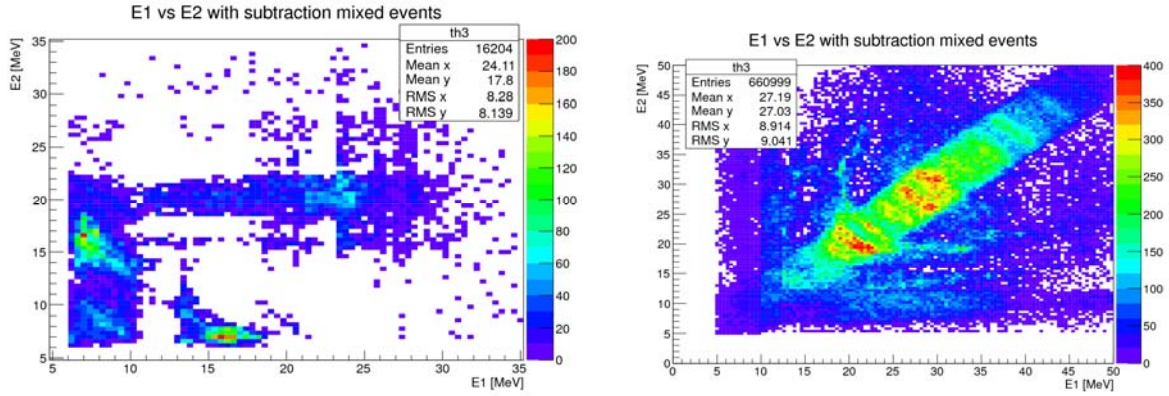

FIG. 3. Energy of the two detected alpha particles in case of 2.9 AMeV (left panel) and 9.7 AMeV beam (right panel).

At the incident energy of 2.9 AMeV we observed 2 alpha particles with quite different energies. We hipotize that a resonant alpha scattering populates a ^{24}Mg excited state that have enough energy to emitt one alpha particle and leave the ^{20}Ne in an excited state that alpha decays to the ground state of ^{16}O. Using this assumption in the reconstruction code we obtained the excitation energy of the ^{24}Mg (from the reconstructed interaction point and the beam energy loss) and the excitation energy of the ^{20}Ne (using the energy of the second alpha particle). The result is shown in Fig.4. It is interesting to note that the excitation energy of ^{24}Mg is in this case very close to the energy threshold to observe the decay in ^{16}O and two alphas.

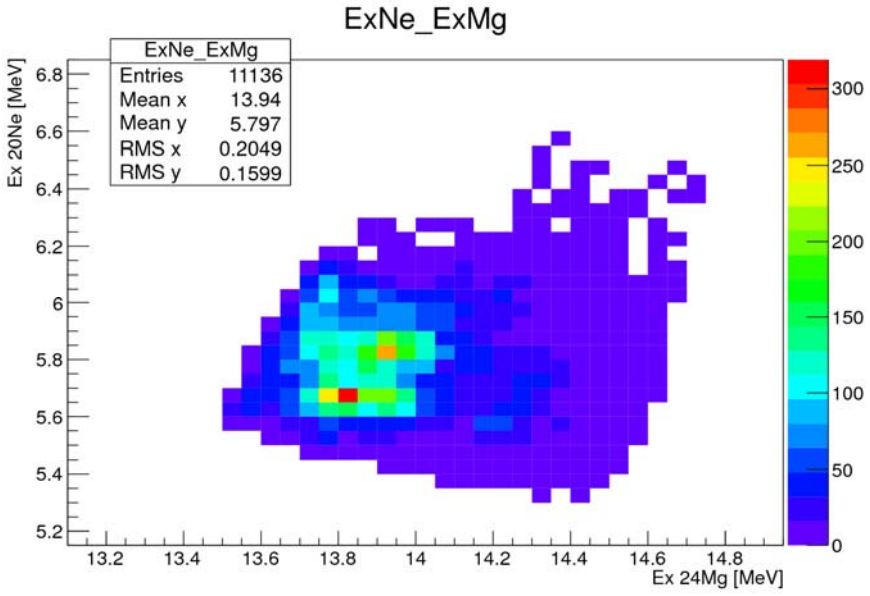

FIG. 4. Reconstructed excitation energies for ^{24}Mg (x-axis) and ^{20}Ne (y-axis).The initial energy of the ^{20}Ne energy was 2.9 AMeV.

At the incident energy of 9.7 AMeV we observed several groups of 2 alpha particles with similar energy emitted mostly at angles close to 0^o in the laboratory frame. We explain these, as alpha particles coming from the splitting of a ^{8}Be. Therefore, the hypothesis in the reconstruction of the events is that the resonant scattering populates a ^{24}Mg state with enough energy to decay in ^{8}Be + ^{16}O. The reconstructed excitation energies of the ^{24}Mg are presented in Fig. 5.

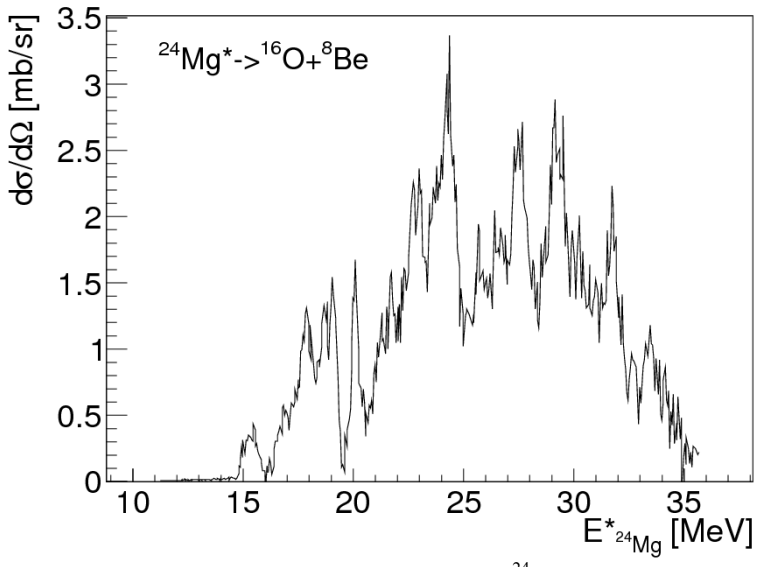

FIG. 5. Reconstructed excitation energy of the ^{24}Mg, measured with a ^{20}Ne 9.7 AMeV at 180^o in the center of mass. Very preliminary.

Fig.5 shows a surprisingly high number of resonance peaks in the ^{24}Mg excitation function. These structures might be related with the multiple alpha cluster structure in ^{24}Mg. The broad peaks at about 28 and 32 MeV are particularly interesting because they lie very close to the energy threshold for the splitting of ^{24}Mg into 6 alphas. Further analysis of the data is necessary to get a final answer.

Another experiment with an improved experimental setup is planned for the near future. A better time resolution is necessary in order to have a better reconstruction of the events. Moreover a larger angular coverage at forward angles is necessary to increase the detection efficiency if we want to be able to improve detection of the events in which the ^{24}Mg decays in 6 alphas.

[1] K. Artemov *et al.*, Sov. J. Nucl. Phys. **52**, 406 (1990);
[2] K. Ikeda, N. Takigawa, and H. Horiuchi, Prog. Theor, Phys. Suppl. Extra Number, 464 (1968);
[3] Abegg *et al.*, Phys. Rev C **43**, 2523 (1990).

Alternative reaction paths to heavy elements

K. Hagel, M. Barbui, S. Wuenschel, K. Schmidt, G. Giuliani , H. Zheng, N. Blando, Z. Majka, A.Wieloch, Z. Sosin, S. Kowalski and J. B. Natowitz

The search for alternative reaction paths for heavy and super-heavy element production requires a careful experimental investigation. Mechanisms other than fusion, e.g., multi-nucleon transfer or very asymmetric fission of even heavier transient systems, could have favorable cross sections for production of new isotopes. In earlier work on this problem we used the BigSol Superconducting Time of Flight Spectrometer at Texas A&M to perform several surveys of projectile target combination and bombarding energy for collisions of two very heavy nuclei (A=197 to 238) in an effort to identify good candidate reactions for heavy and superheavy element production. This experiment indicated the possibility to produce heavy elements of Z above 100 however the experiment was discontinued when the spectrometer developed a He leak which made it not possible to sustain the necessary magnetic field. Although the spectrometer is now repaired it has been relocated for use in the TAMU exotic beam accelerator upgrade and is no longer directly accessible for the required beams from the K500 cyclotron. Given this, we proposed a new direction of investigation of these alternative reactions. It is based upon the implantation of heavy reaction products in a catcher foil and the detection of alpha particle decays characteristic of these heavy nuclei. Many super heavy elements are expected to decay by alpha particle emission. Results of calculations of alpha particle Q values predicted for various heavy elements are shown in Fig.1 (M. Bender, NN2012).

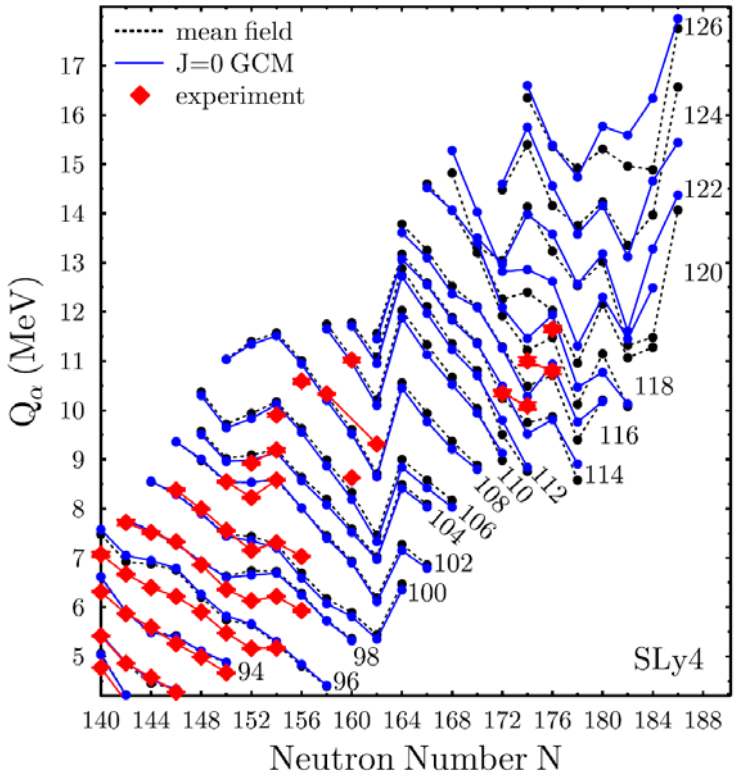

FIG. 1. Alpha Q-values for a range of heavy elements.

With increasing charge the alpha-particle Q-value increases (Momentum conservation in the decay leads to alpha particle kinetic energies which are ~2% less than the Q values.) and the expected half -lives decrease. The heaviest elements are characterized by unusually high alpha particle energies which distinguish them (in general) from the lighter elements. To aid in development of a new system to search for high energy alpha emission, we carried out test experiments in which heavy reaction products emitted in the angular range from 3° to 45° were implanted in a downstream catcher foil. Decays of the implanted nuclei were detected using ΔE and E silicon detectors placed in the backward position.The first test was in 2011. We have now constructed new detectors and done a more sophisticated test The latest test setup is depicted in Fig.2. The catcher was a polypropylene layer of thickness 7.5 μm placed at 4 cm from the target. Six newly constructed IC Si telescopes incorporating seven-strip silicon detectors surrounded the target and faced the downstream catcher foil. The 7.5 MeV/nucleon ^{197}Au beam was delivered by the K500 superconducting cyclotron and pulsed at different intervals in order to be able to identify species of different half-life (i.e. 100 ms beam-on, 100 ms beam-off; 10 ms beam-on, 10 ms beam-off etc.

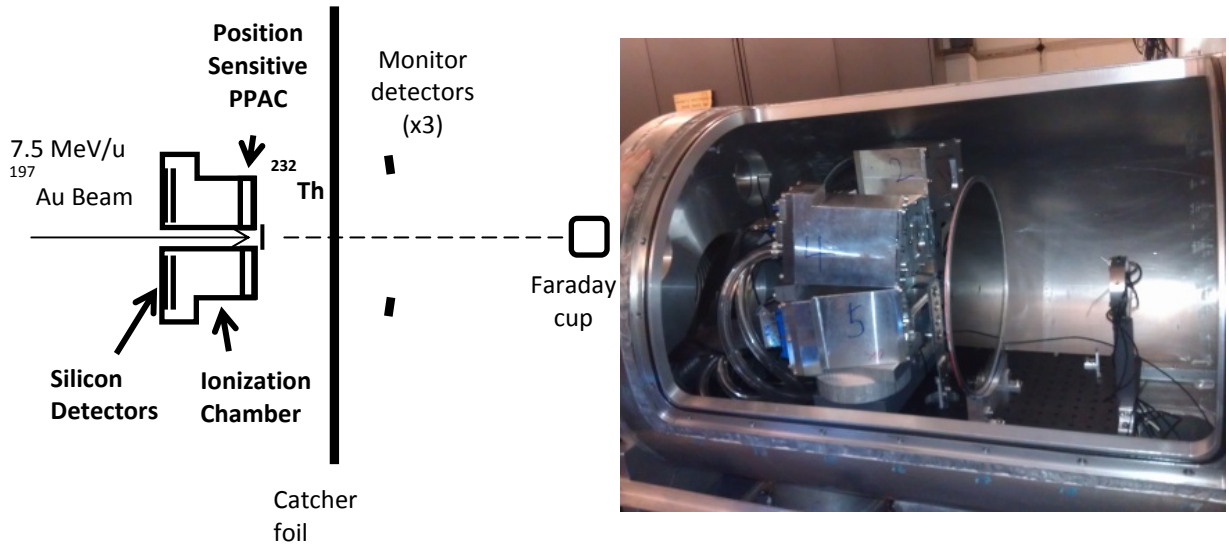

FIG. 2. Schematic (left) and photograph (right) of the test experiment (see text)

In Fig. 3 we present preliminary results for identified alpha particle detection during both beam-on (left side and beam-off (right side) times in reactions of 5-7.5AMeV ^{197}Au + ^{232}Th .. This figure includes alphas from all time sequences sampled. A large number of alpha activities, many with similar energies, were detected. The spectra indicate observation in-beam and out of beam of interesting high alpha-energy activities The analysis is underway. Concurrently, our colleagues in Poland (*Jagiellonian University, Krakow and Silesian University, Katowice)* are constructing a sophisticated active catcher system consisting of a high granularity array of scintillators read by photomultiplier tubes. This will allow us to identify the location of the implanted nucleus. We can then correlate a detected alpha decay with an implantation position and observe multiple decays from the same recoil implantation site.. They have

received a grant of $400,000 to construct and instrument this system. A first test of active catcher components was carried out in November 2012. A second test will take place in August 2013. We anticipate a run with an improved configuration in the winter of 2013.

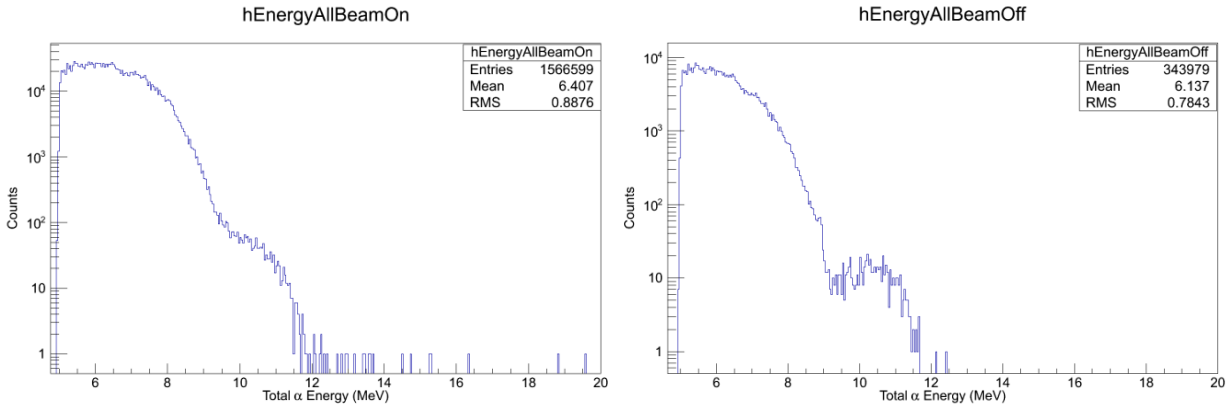

FIG. 3. Observed alpha particle decay energy distributions, beam-on(left) and beam-off (right).

Using break-up mechanisms in heavy ion collisions at low energies to constrain the asymmetry energy at Low Nuclear Density

Paul J. Cammarata, Lauren A. Heilborn, Justin Mabiala, Larry W. May, Alan B. McIntosh, Andrew Raphelt, Andrew Zarrella, and Sherry J. Yennello

Nuclear reactions just below the Fermi energy present a unique opportunity for probing the dynamics of nuclear matter below normal nuclear density using shape fluctuations, spin and relative multiplicities of the produced fragments. The results of these interactions are theorized to be dependent upon and sensitive to the asymmetry energy. Composite systems resulting from semi-peripheral collisions may exhibit prolate (elongated) shapes with a large associated angular momentum. More neutron-rich nuclear reactions are expected to have a greater sensitivity to the density dependence of the asymmetry energy through observing ternary or quaternary events from the breaking of the Projectile-Like-Fragment (PLF) and/or Target-Like-Fragement (TLF) [1]. Some of these effects have been recently observed in ^{124}Sn + ^{64}Ni and ^{112}Sn+^{58}Ni at 35 MeV/nucleon [2,3] and by Wilczyński *et al.* using ^{197}Au+^{197}Au at 15 MeV/nucleon [4-6] . However, using multiple systems at the same beam energy to correct for systematic effects and drawing comparisons to theoretical simulations is of high value in attempting to use the experimental results to determine additional constraints to the density dependence of the asymmetry energy at low nuclear density.

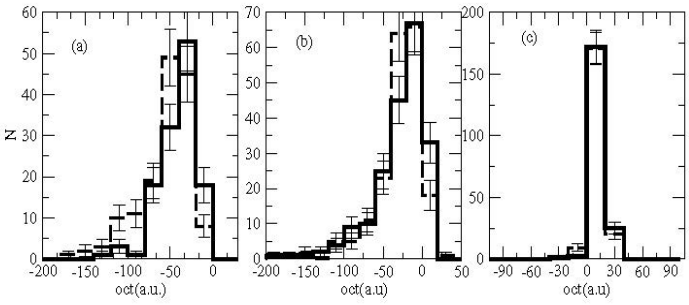

FIG. 1a. Octupole fluctuations of the primary fragments (in position space) for ^{132}Sn+^{64}Ni at 10A MeV. Figures (a) through (c) represent impact parameters 6 - 8 fm at freeze out, repsctively. Dashed lines represent asy-stiff and solid lines the asy-soft density dependance of the asymmetry energy respectively.

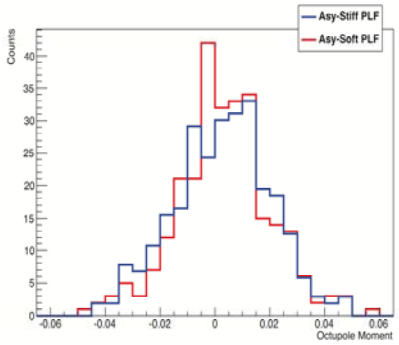

FIG. 1b. Octupole fluctuations of the Projectile-Like-Fragments (PLFs) from reactions of ^{124}Sn + ^{64}Ni at 15AMeV via TWINGO code for b= 6fm and t = 450fm/c (freeze out).

Results from DiToro *et al.* [1] (Fig.1a) and simulations using TWINGO code [7-12] (a Boltzmann-Nordheim-Vlasov stochastic mean field approach) have been used to calculate the fluctuations in quadrupole and octupole moments to facilitate the prediction of the relative expected ternary (quaternary) breaking of the PLF (and TLF) resulting from semi-peripheral interactions of heavy nuclei below the Fermi energy. In the case of ^{124}Sn+^{64}Ni at 15 MeV/nucleon, Fig. 1b shows the octupole fluctuations of the PLF extracted from the BNV mean field interaction. In this way we can see that there are noticeable differences in the quadrupole and octupole fluctuations with respect to the asymmetry energy. It is

expected that reactions using ^{124,136}Xe, in addition to ^{124}Sn, projectiles at 15 MeV/nucleon should exhibit the same signatures. Additionally, to gain insight into the observables pertinent to the experiment on long time scales, CoMD (Constrained Molecular Dynamics [13,14]) code has been used to show a noticeable difference in the multiplicity of the Z≥3 fragments as well as a number of additional observables.

The results from over 1 million events from ^{136}Xe+^{64}Ni, ^{124}Xe+^{58}Ni and ^{124}Sn+^{64}Ni reactions at 15 MeV/nucleon simulated through CoMD have been used to help design and build an experimental apparatus consisting of a combined recommissioning of the FAUST array [15] and the TAMU Quadrupole Triplet Spectrometer. The FAUST-Triplet Spectrometer (Fig. 2) will allow for Time-of-Flight (ToF) measurement of the PLFs produced from 0.5º to 45º off beam axis. Furthermore, the intermediate mass fragments (IMFs) produced in the ternary (quaternary) breaking of the PLF (and TLF) resultant from semi-peripheral reactions will be detected by both the ΔE-E technique for Z-identification

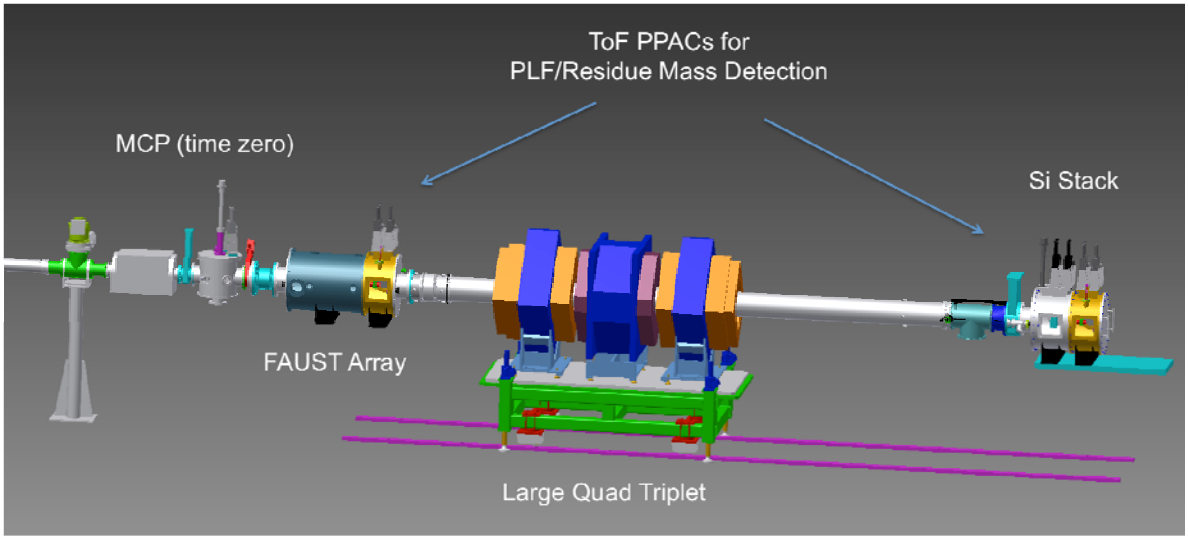

FIG. 2. Faust-Triplet Line in its current configuration.

and/or the ToF technique for mass identification. To achieve this, FAUST (68 Si-CsI telescopes arranged in 5 rings, covering 1.6 º to 45º in theta) has been upgraded with new charge sensitive preamplifiers that have an integrated fast-timing pickoff circuit with excellent timing resolution (100's of pico-seconds FWHM) resulting in a mass resolution of ~1-3 mass units for the PLFs and greater resolution for the IMFs. Furthermore, a micro-channel plate detector [16] has been installed upstream of the FAUST array to generate the start time to coincide with the timing from each of the Si detectors in FAUST allowing for 68 individual fast timing measurements per event.

The remainder of the coverage (from 0.5º to 1.6 º) will be in the Triplet (large triple quadrupole magnet) spectrometer using Parallel Plate Avalanche Counters (PPACs) [17] before and after the triplet (for ToF and position sensitivity) in conjunction with a 1000μm Si detector for total energy measurements to be able to mass-identify the particles transported through the spectrometer. The beam will be stopped before the PPACs in a small diameter beam block (covering 0-0.5º) allowing for maximum transmission of PLFs and/or IMFs that would have normally been lost down the throat of the FAUST array. Spectrometer settings have been determined via the TRANSPORT [18] code in conjunction with

historical calibrations of the spectrometer to optimize the transport of the most probable particles. The experiment is planned for the Fall of 2013.

Based on the expected experimental and current theoretical results, probing the fragmentation mechanism competition of the primary nuclei and neck fragmentation at low-intermediate energies in heavy, asymmetric systems should provide additional constraints on the asymmetry energy at low nuclear density. We have nearly completed the first round of initial simulations using CoMD and TWINGO to predict the prevalence of the reaction observables and for eventual comparison to collected experimental data. A large portion of these calculations were performed on several supercomputing facilities at Texas A&M University (Medusa/Orion at the Laboratory for Molecular Simulations, Chemistry Department and Hydra/Eos at theTexas A&M University Super-Computing Facility) as well as on the Lonestar cluster at the University of Texas at Austin.

[1] M.D. Toro, V. Baran, M. Colonna, G. Ferini, T. Gaitanos, V. Greco, J. Rizzo, and H. Wolter, Nucl. Phys. **A787**, 585 (2007), ISSN 0375-9474, proceedings of the Ninth International Conference on Nucleus-Nucleus Collisions(NN2006).

[2] E.D. Filippo, A. Pagano, E. Piasecki, F. Amorini, A. Anzalone, L. Auditore, V. Baran, I. Berceanu, J. Blicharska, J. Brzychczyk, *et al.* (REVERSE Collaboration), Phys. Rev. C **71**, 064604 (2005).

[3] P. Russotto, E. De Filippo, A. Pagano, E. Piasecki, F. Amorini, A. Anzalone, L. Auditore, V. Baran, I. Berceanu, J. Blicharska, *et al.*, Phys. Rev. C **81**, 064605 (2010).

[4] J. Wilczyn´ski, I. Skwira-Chalot, K. Siwek-Wilczyn´ska, A. Pagano, F. Amorini, A. Anzalone, L. Auditore, V. Baran, J. Brzychczyk, G. Cardella, *et al.*, Phys. Rev. C **81**, 024605 (2010).

[5] J. Wilczyn´ski, I. Skwira-Chalot, K. Siwek-Wilczyn´ska, A. Pagano, F. Amorini, A. Anzalone, L. Auditore, V. Baran, J. Brzychczyk, G. Cardella, *et al.*, Phys. Rev. C **81**, 067604 (2010).

[6] I. Skwira-Chalot, K. Siwek-Wilczyn´ska, J. Wilczyn´ski, F. Amorini, A. Anzalone, L. Auditore, V. Baran, J. Brzychczyk, G. Cardella, S. Cavallaro, et al., Phys. Rev. Lett. **101**, 262701 (2008).

[7] V. Greco, A. Guarnera, M. Colonna, and M. Di Toro, Phys. Rev. C **59**, 810 (1999). [8] A. Bonasera and F. Gulminelli, Physics Letters B **259**, 399 (1991).

[9] A. Bonasera, G. Burgio, and M. D. Toro, Physics Letters B **221**, 233 (1989).

[10] A. Bonasera, F. Gulminelli, and J. Molitoris, Physics Reports **243**, 1 (1994).

[11] R. J. Lenk and V. R. Pandharipande, Phys. Rev. C **39**, 2242 (1989). [12] A. Guarnera, Ph.D. thesis, University Caen, 1996.

[13] M. Papa, T. Maruyama, and A. Bonasera, Phys. Rev. C **64**, 024612 (2001).

[14] M. Papa, G. Giuliani, and A. Bonasera, Journal of Computational Physics **208**, 403 (2005).

[15] F. Gimeno-Nogues, D. Rowland, E. Ramakrishnan, S. Ferro, S. Vasal, R. Gutierrez, R. Olsen, Y.-W. Lui, R. Lafor- est, H. Johnston, et al., Nuclear Instruments and Methods in Physics Research Section A: Accelerators, Spectrometers, Detectors and Associated Equipment **399**, 94 (1997).

[16] W. Starzecki, A. Stefanini, S. Lunardi, and C. Signorini, Nuclear Instrum. Methods **193**, 499 (1982).

[17] H. Stelzer, Nucl. Instrum. Methods **133**, 409 (1976).

[18] K.L. Brown, F. Rothacker, D.C. Carey, and C. Iselin, Tech. Rep., Stanford Linear Accelerator Center, Calif.(USA); Fermi National Accelerator Lab., Batavia, Ill.(USA); European Organization for Nuclear Research, Geneva (Switzerland) (1977).

Experimental and simulation results for isoscailng of a reconstructed quasi-projectile

A. Raphelt, P. J. Cammarata, L. Heilborn, J. Mabiala, L. May,
A. B. McIntosh, A. Zarrella, and S. J. Yennello

To determine if experimental data follows the trends of an asy-stiff or asy-soft equation of state (EoS), and to probe the effects of the asymmetry energy, experimental data is often compared with theoretical predictions. This work compares observables from experimental reactions to results from several dynamical and statistical models. Isoscaling analysis [1] was carried out on the experimental and simulated data, both before and after a QP reconstruction. Quasi-projectile (QP) reconstruction is also performed for the experimental and theoretical data [2].

Charged particles and neutrons from the reactions of ^{70}Zn+^{70}Zn, ^{64}Zn+^{64}Zn, and ^{64}Ni+^{64}Ni at 35 MeV/A were detected in the NIMROD-ISiS array [3]. These reactions were also simulated using anti-symmetrized molecular dynamics (AMD) [4] and constrained molecular dynamics (CoMD) [5,6]. AMD simulations were run out to 300 fm/c, the results of which were then de-excited by the GEMINI statistical model [7]. The AMD and CoMD models were also run to a final time of 3000 fm/c to allow the fragments to de-excite dynamically. To compare the simulated results to experimental results, the simulation data was run through the same filter as the experimental data.

Isoscaling analysis is performed comparing each pair of neutron-rich to neutron-poor systems, for a total of three ratios. For each element in isoscaling, a linear fit is constructed through all of its isotopes. The slope of this fit is the isoscaling parameter, α , and is proportional to the asymmetry energy. Each element has a separate slope, so to provide a single α value for each isoscaling analysis, a global fit of the isoscaling data was performed that includes the two parameters of the isoscaling equation, the chemical potential of the neutrons and protons, α and β [1]. Using this fit, a single parameter, α, can be extracted to describe the isoscaling of two systems. Due to the difference in the N/Z of each of the systems, the resulting isoscaling parameter, α, depends on the two systems being used in the isoscaling ratio. To compare all of the systems together, a parameter of the asymmetry of the system is used to take into account the changing of α with the system. The value of Δ has been used to calculate the difference in the asymmetry of the fragments in the two sources used for the isoscaling ratio[8]. Relating the α from isoscaling to the Δ of the systems used in isoscaling gives us a way to compare not only each of the experimental points, but also the simulated data to the experimental data. This isoscaling analysis was first performed on system-to-system comparisons using the above reactions. A QP was then reconstructed from the simulation and experimental data and isoscaling was performed on the QP using the same technique as Wuenschel [2]. The QP reconstruction has been shown to improve the fit of the isoscaling [2]. This improvement is due to the improved definition of the systems used for the isoscaling ratio. The QP source is used as the source of the fragments in the isocaling ratio instead of the entire system. The results from the QP isoscaling are shown in Fig. 1.

Fig. 1 shows the plot of the global isoscaling parameter, α, vs. fragment asymmetry, Δ, for QP reconstruction results of theoretical simulations and experiment for one isoscaling comparison. The diagonal lines are fits to the results of the simulations, forced through the origin, where the slope of the

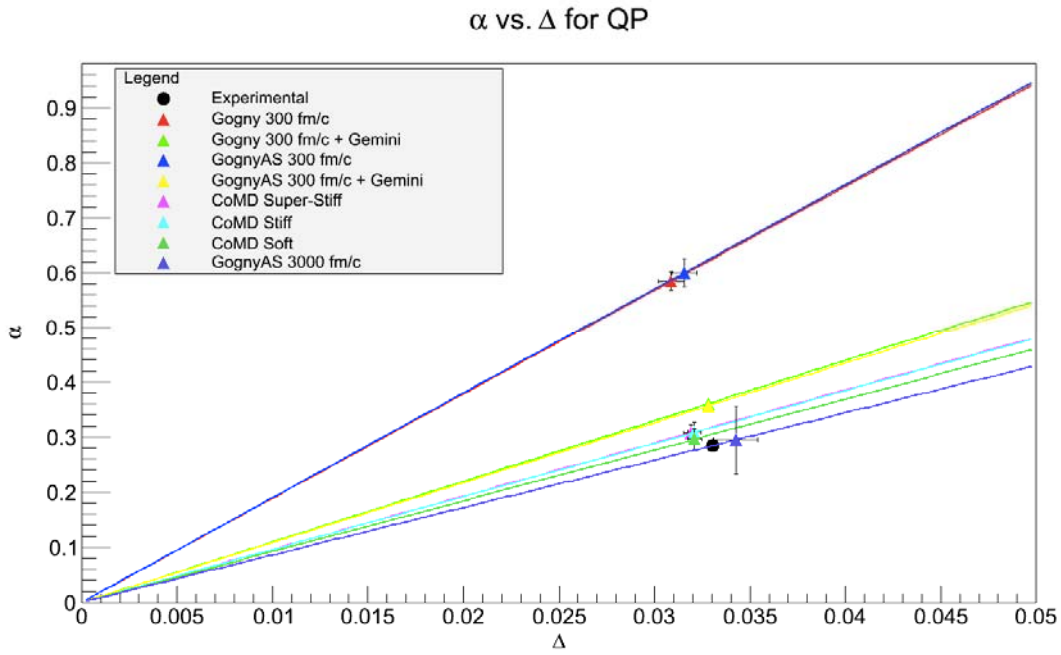

FIG. 2. Plot of global isoscaling parameter, α, vs. fragment asymmetry, Δ, for one isoscaling ratio from a reconstructed QP.

isoscaling is zero when a system is compared against itself. Lines are used to represent the relationship between α and Δ since they are linearly related, and changing the difference in asymmetry of the sources changes the isoscaling. For the QP reconstructed results, the experimental data matches reasonable to the AMD simulations at 300 fm/c with GEMINI, as well as the simulations at 3000 fm/c. The AMD at 300 fm/c has a larger α value than the simulations at longer time-steps, as well as the results from GEMINI. This suggests that the slope of isoscaling decreases over time.

Figure 2 shows how the α parameter from isoscaling changes with time

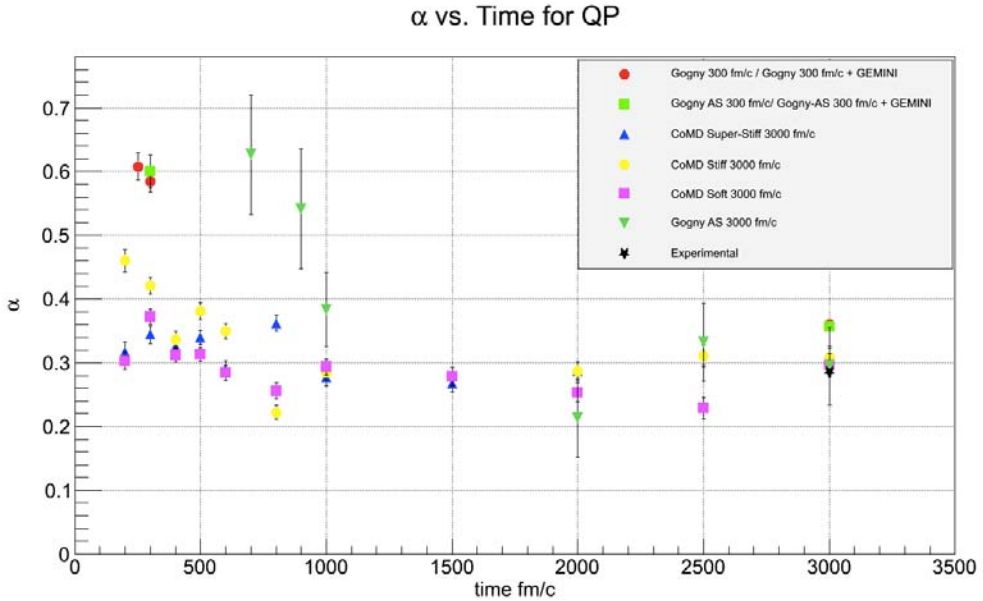

FIG. 1. Plot of global isoscaling parameter, α, vs. time for QP reconstruction of AMD and CoMD. The results of AMD at 300 fm/c with GEMINI are plotted at 3000 fm/c.

The AMD simulation at 300 fm/c has a larger α value than at 3000 fm/c or at 300 fm/c with GEMINI. In general, the α value from the simulations decrease over time. This result matches the results from the α vs. Δ plots where the α decreases with time.

The results from isoscaling show a large dependence on the time of the simulation when compared to the experimental results, but do not suggest an asymmetry energy dependence in the comparison. Also, the results from AMD at 3000 fm/c match well with the results from AMD at 300 fm/c with GEMINI in the isoscaling analysis, suggesting that the type of de-excitation in the simulation, statistical or dynamical, does not affect the results of the analysis.

[1] M. Tsang *et. al.*, Phys Rev Lett **86,** 5023 (2001).
[2] S. Wuenschel *et. al.*, Phys Rev C **79**, 061602 (2009).
[3] Z. Kohley *et. al.*, Phys Rev C **82** 064601 (2010).
[4] A. Ono *et. al.*, Prog Part Nucl Phys **53**, 501 (2004).
[5] M. Papa, T. Maruyama, and A. Bonasera, Phys Rev C **64**, 024612 (2001).
[6] M. Papa, G. Giuliani, and A. Bonasera, J. Comp. Phys. **208**, 403 (2005).
[7] R. Charity *et. al.*, Nucl Phys **A483**, 371 (1988).
[8] D.V. Shetty *et. al.*, Phys Rev C **70,** 011601 (2004).

Using light charged particles to probe the asymmetry dependence of the caloric curve

A. B. McIntosh, A. Bonasera, Z. Kohley, P. J. Cammarata, K. Hagel, L. Heilborn, J. Mabiala, L. W. May, P. Marini, A. Raphelt, G. A. Souliotis, S. Wuenschel, A. Zarrella, and S. J. Yennello

The nuclear equation of state (EoS) relates the thermodynamic parameters of the nuclear system: temperature, density, pressure, excitation energy, mass and asymmetry. The EoS directly impacts the physics of heavy ion reactions at all energies, nuclear structure (e.g., collective excitation), the processes at play in supernova explosions (including supernova nucleosynthesis), and many properties of neutron stars. Typically, the equation of state is investigated by examining the correlation between two thermodynamic parameters. Here, we study how the relation between temperature and excitation energy per nucleon depends on the neutron-proton asymmetry.

Excited quasi-projectile (QP) sources are isotopically reconstructed using charged particles and free neutrons measured with the TAMU NIMROD-ISiS array for collisions of ^{70}Zn+^{70}Zn, ^{64}Zn+^{64}Zn, and ^{64}Ni+^{64}Ni at E = 35MeV/nucleon. Equilibrated QP sources are selected by means of three successive cuts on particle and event characteristics (see [1, 2] and references therein). The largest uncertainty in the composition of the QP, and also in its excitation energy, arises from the free neutron measurement. Detailed simulations of the TAMU Neutron Ball have been performed [3]. The efficiencies are found not to depend on the model employed nor the neutron excess of the system under study. We have carefully analyzed the impact of the efficiency and the background signals in the Neutron Ball. Combined, these sources of uncertainty introduce an 11% uncertainty in neutron multiplicity. This corresponds to an uncertainty of 0.11MeV in excitation energy, and a maximum uncertainty of only up to 0.02 units in asymmetry (N-Z)/A. Our results below are robust with respect to these uncertainties.

The temperature of the QP is extracted using the momentum quadrupole fluctuation MQF thermometer [4], using five independent light charged particles (LCP) as probes (protons, deuterons, tritons, helions, and α-particles). The caloric curves are extracted for narrow selections in the neutron-proton asymmetry of the source, $m_s=(N_s-Z_s)/A_s$. These curves are shown in the top row of Fig. 1. With increasing asymmetry, the caloric curve shifts to lower temperatures. This is observed across all excitation energies for all MQF probes of the temperature. The magnitude of the shift is on the order of 1MeV between the two most extreme m_s bins. In the lower row of Fig. 1, the temperature difference is plotted between each curve and the central curve ($0.12<m_s<0.16$), used as a reference. This difference shows no dependence on excitation, with the exception of the small trend for alpha particles at low excitation. Also of note is the ordering of the caloric curves by particle type: protons and alphas have the lowest temperatures, followed by deuterons, tritons, and helions. Protons and alphas are relatively cheap to emit (Q~10MeV), deuterons more expensive (Q~15), and tritons and helions are the most expensive (Q~20). This temperature ordering observed is consistent with an emission-time-ordering of the particles due to their Q-value of emission.

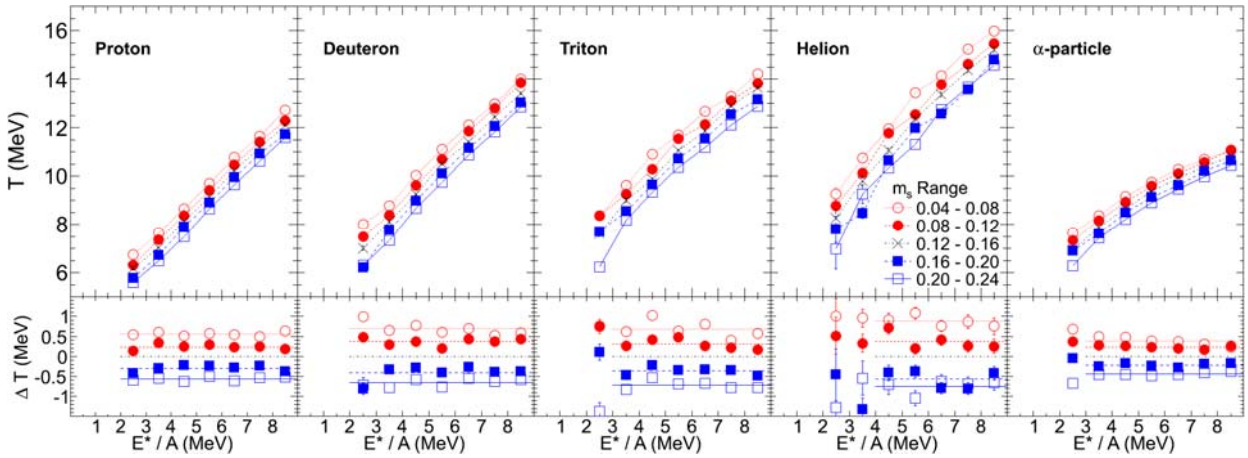

FIG. 1. (Top Row) Caloric curves for light charged particles, selected on source asymmetry (m_s=(N-Z)/A). (Bottom Row) Temperature difference between each caloric curve and the middle caloric curve ($0.12 \leq m_s \leq 0.16$), which is used as a reference. The horizontal lines correspond to the average difference over the indicated range in excitation. Error bars represent statistical uncertainties.

To be more quantitative about the asymmetry dependence of the caloric curve, we examine the decrease in temperature ΔT that occurs for a given increase in asymmetry Δm_s. To obtain this, we construct the difference between every pair of m_s-selected curves (10 total, for 5 curves). We have already seen that ΔT is essentially independent of excitation (Fig. 1, lower row). The excitation-averaged ΔT is linear as a function of Δm_s. This is true for all 7 probes of the temperature (5 MQF, and 2 Albergo).

The slopes of the $\Delta T/\Delta m_s$ correlations for the MQF thermometer follow an ordering. From smallest to largest they are ordered α, p, d, t, h. This ordering is reminiscent of the ordering of the temperatures seen in Fig. 1. This is consistent with an emission-time ordering scenario, where the composition of the QP must change with each particle emission. Thus the particles that are emitted early (high Q-value helions and tritons) are sensitive to the initial asymmetry of the QP, which we deduce. The particles emitted later on average (the low Q-value protons and alphas) are sensitive to the asymmetry at the time of their emission, which has changed somewhat from the deduced, initial value. If these two observations - the ordering of the temperatures and the ordering of the $\Delta T/\Delta m_s$ correlations - have a common origin as discussed, there should be a scaling. Therefore we examine in Fig. 2 the $\Delta T/\langle T \rangle$ vs Δm_s. The data for the MQF p, d, t, h collapse onto a single line. This suggests that we are sensitive to the emission-time ordering of the LCPs. The alphas do not quite follow this scaling, which may indicate differences in the production mechanism of alphas as compared to the other LCPs, such as production from regions of different density, or differences in coalescence. The correlations corresponding to the Albergo temperatures also do not scale to the other curves. This may be a manifestation of the differences in the methods (chemical vs kinetic) used to extract the temperature, and the fact that the Albergo temperature relies on multiple particle species which precludes conclusions about sensitivity to differences in the emission time for this thermometer.

In summary, we have reported a clear dependence of the nuclear caloric curve on the neutron-proton asymmetry. The dependence is observed for five probes of the temperature using the MQF thermometer. A sensitivity of the average emission order is observed in the temperatures and in the

magnitude of the asymmetry dependence. These two quantities exhibit a scaling. The observation is enabled by the excellent resolution and 4π character of the TAMU NIMROD-ISiS array which allows isotopic reconstruction of the excited quasi-projectiles.

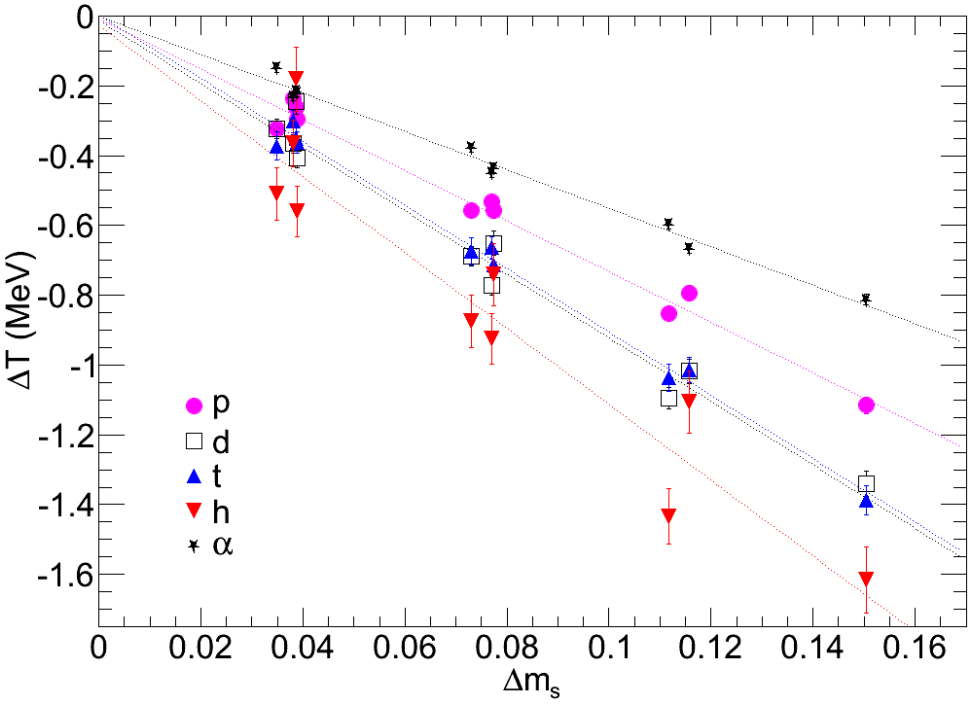

FIG. 2. Scaled change in temperature $\Delta T/\langle T\rangle$ with changing asymmetry Δm_s.

[1] A.B. McIntosh *et al.*, Phys. Lett. B **719**, 337 (2013).

[2] A.B. McIntosh *et al.*, Phys. Rev. C **87**, 034617 (2013).

[3] P. Marini *et al.*, Nucl. Instrum. Methods Phys. Res. **A707**, 80 (2013).

[4] H. Zheng and A. Bonasera. Phys. Lett. B **696**, 178 (2011).

Experimental correlation function using FAUST upgrade

L. Heilborn, P. J. Cammarata, J. Mabiala, A.B. McIntosh, L.W. May, A. Raphelt,
A. Zarrella, and S. J. Yennello

The proton-proton correlation function has been shown to be sensitive to the proton-neutron asymmetry of an excited quasi-projectile [1]. In the past, correlation functions have been examined in transport models such as the iBUU model[1]. In this work, Constrained Molecular Dynamics (CoMD) [2] is used to simulate nucleus-nucleus reactions, and construct pp correlation functions for 30 MeV/nucleon ^{48}Ca+^{64}Ni and ^{40}Ca+^{58}Ni reactions.

Proton-proton correlation functions from CoMD using two asymmetry energy implementations each for both systems (^{48}Ca+^{64}Ni and ^{40}Ca+^{58}Ni events), were examined. The basic shape of the correlation functions extracted is similar, because all impact parameters and total momenta of proton pairs were used. All have a ratio of correlated-to-uncorrelated around one at q_{Rel} above 60 MeV/c. The bump in the correlation function at a relative momentum of about 20 MeV/c is characteristic of attractive final-state pp interactions [3,4]. However, the softer equation of state for both the n-rich and n-poor systems exhibits a larger bump around 20 MeV/c, indicating more correlated proton pairs, overall. This effect will need to be disentangled from the density in the future, perhaps by more stringent source cuts on the violence of the collision. The correlation functions extracted from the super-stiff equation of state exhibit more anticorrelation at the lowest relative momenta.

Characteristic features of known correlation functions (the bump from pp interactions and the dip from Pauli blocking) can be reproduced by CoMD. Some difference exists in the shape of the correlation functions between those obtained from different formulations of the density-dependences of the asymmetry energy in CoMD

Further investigation into the correlation function extracted from the ^{40}Ca+^{58}Ni reaction with different density- dependences of the asymmetry energy in CoMD, at 45 MeV/A, is planned, along with an analysis on iBUU code. For comparison of experimental with simulated results, a software representation of the geometric and energy acceptance of the Forward Array Using Silicon Technology (FAUST) [5] will be used. The same data analysis performed upon the experimental results can then be compared to the molecular dynamics and transport model simulations.

Proton-proton correlation functions for ^{40}Ca+^{58}Ni will be measured experimentally at the Texas A&M Cyclotron Institute to be compared to CoMD and iBUU results. FAUST will be used to detect the free protons and other charged particles for this project. FAUST currently consists of sixty-eight 2x2cm 300 μm thick Si backed by CsI(Tl)/PD detectors, arranged to geometrically accept the particles originating from the QP [5] . The array has 89.7 % geometric coverage from 2.3º to 33.6º [5] .

In interferometry, a precise knowledge of the point of detection of the particles is essential, so improved angular resolution is of paramount importance when measuring a correlation function for a reaction [6]. In order to increase the angular resolution of charged-particle detection in the upcoming experiment, an upgrade of the array is planned using Dual-Axis Dual-Lateral (DADL) Si detectors. The

DADLs have uniform resistance across the front and back of the detectors and use charge-splitting to determine the position of a detected particle to within 200 μm [7].

Fig. 1 schematically shows the equipotential lines on the surface of a DADL detector. Both electrons and "holes" set in motion by incident radiation generate signal. The uniform potential and resistance over the face of the detector, along with the reverse bias on the p-n diode, allow the holes or electrons to be collected at the opposite edges of the face of the detector. The holes on the back of the detector split proportionally to the Back 1 and Back 2 signals, while the electrons go to the front, split proportional to the relative left-right position of the detected ion. These four signals allow the position of a fragment to be determined. Guard rings help to keep the potential uniform across the entire surface of the detector [7].

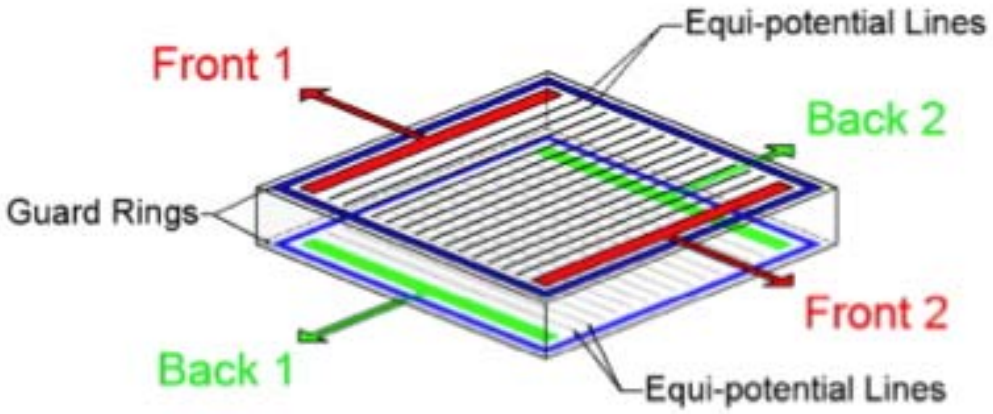

FIG. 1. Schematic of DADL, showing the equipotential lines on the uniformly resistive surface, which allows position to be determined by charge splitting.

The additional signals on each Si-CsI telescope will result in an 150% increase in the number of channels processed, so Application-Specific Integrated Circuit (ASIC) Heavy Ion Nuclear Physic (HINP) chip electronics will be used in order to deal with the increased number of signals. The addition of the two signals from the fronts or backs allows the energy of the incident particle to be determined. After experimentally gain-matching the signals generated by the uniform resistance of the detector, the ^{228}Th α spectrum in Fig. 2 was obtained. The energy resolution of the 8.785 MeV alpha peak is 1.4%. The FAUST array in its current configuration with the Quadrupole Triplet will be tested and run in-beam in spring and summer 2013, the upgrade to DADL detectors will follow this campaign.

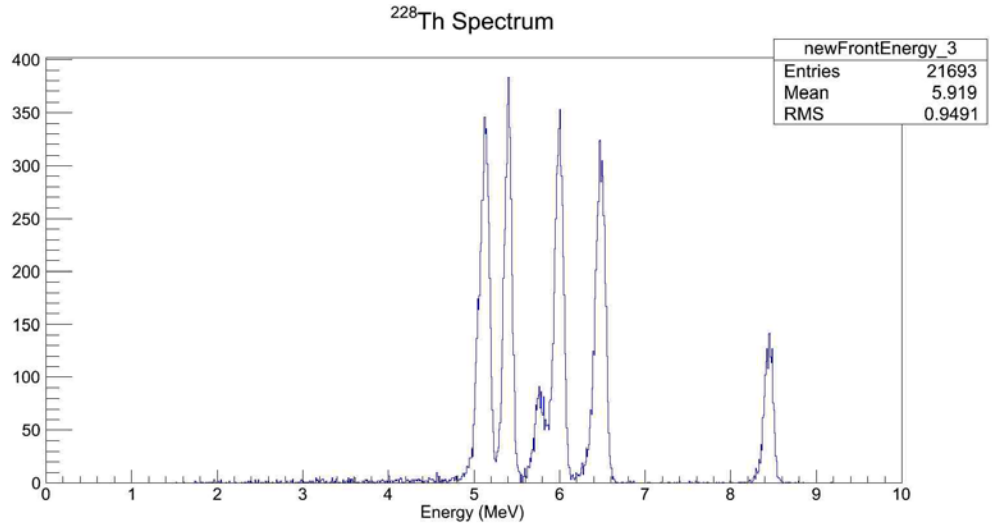

FIG. 2. Thorium-228 spectrum obtained from gain-matching process of a representative DADL detector.

[1] L.W. Chen, V. Greco, C.M. Ko, and B.A. Li, Phys. Rev. Lett. **90**, 162701 (2003).

[2] M. Papa, G. Giuliani, and A. Bonasera, J. Comp. Phys. **208**, 403 (2005), ISSN 0021-9991, http://www. sciencedirect.com/science/article/pii/S0021999105000847.

[3] R. Ghetti, C. Collaboration, et al., Nucl. Phys. **A674**, 277 (2000).

[4] V. Henzl *et al.*, Phys. Rev. C **85**, 014606 (2012).

[5] F. Gimeno-Nogues *et al.*, Nucl. Instrum. Methods Phys. Res. **A399**, 94 (1997), ISSN 0168-9002, http://www.sciencedirect.com/science/article/ pii/S0168900297009236.

[6] G. Verde *et al.*, Eur. Phys. J. A **30**, 81 (2006).

[7] S. Soisson *et al.*, Nucl. Instrum. Methods Phys. Res. **613**, 240 (XXX)

Determination of QP mass with measured neutrons

Andrew Zarrella, Paola Marini, Alan McIntosh, Paul Cammarata, Lauren Heilborn, Justin Mabiala, Larry W. May, Andrew Raphelt, Sherry Yennello

A detailed analysis of the free neutron detection efficiencies in the TAMU Neutron Ball was performed using the reaction simulation models HIPSE-SIMON [1] and CoMD [2]. Recently, our group has published a number of papers whose results rely heavily on a precise reconstruction of the quasi-projectile (QP) source created in peripheral nuclear collisions [3-6]. The results of our neutron detection analysis were applied to this QP reconstruction process in order to determine the precision with which we can reconstruct the emitting sources. Equation 1 was developed in order to determine the actual number of QP-emitted free neutrons (N_{QP}) given the total detected free neutron multiplicity (N_{det}) measured by the Neutron Ball on an event-by-event basis.

$$N_{QP} = \frac{N_{det} - N_{background}}{\left(\varepsilon_{QP} - \frac{N_T}{N_P}\varepsilon_{QT}\right)\varepsilon_{Cf}} \quad (1)$$

here, ε_{QP}, ε_{QT}, and ε_{Cf} correspond, respectively, to the effective detection efficiencies for neutrons originating from the QP, the QT (quasi-target) and an experimentally measured efficiency using a calibrated californium source. The N_T/N_P term is the ratio of the number of neutrons in the target and projectile. Symmetric reactions of ^{70}Zn, ^{64}Zn and ^{64}Ni were studied.

Fig. 1 and Table I relate the actual number of neutrons emitted from the QP and the number of neutrons calculated using Eq. (1) from events modeled by the two simulation codes. We see from Fig. 1 that the peaks of the distributions for the two simulation codes lies approximately on the black line corresponding to a 1-to-1 correspondence between the actual number of neutrons emitted from the QP and the number we calculate using Eq. (1). The HIPSE simulation code tracks the origin of fragments after the collision. Therefore, it is straight forward to compare the results of equation 1(N_{QP}) to the number of QP-tagged or actual free neutrons produced in the simulation (M^{raw}_{QPn}). For the CoMD simulation we calculated M^{raw}_{QPn} using a particle velocity cut which we describe in detail in Ref. [7]. This neutron velocity cut is similar to the experimental velocity cut for protons during QP reconstruction but corrected for the lack of Coulomb interaction.

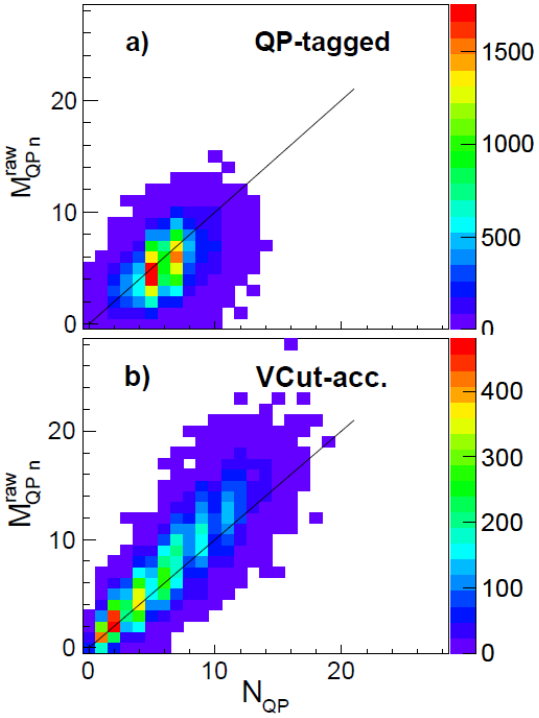

FIG. 1. The multiplicity of neutrons emitted from the QP ($M^{raw}_{QP\,n}$) versus the multiplicity of free neutrons assigned to the reconstructed QP (N_{QP}) for the reaction of ^{70}Zn + ^{70}Zn

Table 1 gives a numerical analysis of the information shown in figure 1. For a given number of

Table I. Average QP-emitted free neutron multiplicity and the width of that distribution for each value of reconstructed neutron multiplicity for CoMD and HIPSE-SIMON [7].

N_{QP}	$\langle M^{raw}_{QP_n} \rangle$	$\sigma(M^{raw}_{QP_n})$	$\langle M^{raw}_{QP_n} \rangle$	$\sigma(M^{raw}_{QP_n})$
	HIPSE		COMD	
0	1.46	1.10	0.51	0.74
1	2.13	1.21	1.47	1.08
2	3.02	1.64	2.69	1.34
3	3.67	1.68	3.76	1.58
4	4.06	1.75	4.66	1.78
5	4.72	1.88	5.88	2.03
6	5.28	1.97	6.81	2.16
7	5.94	2.04	8.44	2.52
8	6.59	2.14	9.61	2.49
9	–	–	10.63	2.73
10	–	–	11.58	2.65
11	–	–	12.49	2.77

calculated QP-emitted free neutrons (N_{QP}), the average number of actual QP-emitted neutrons is shown as well as the width of the distribution, σ. These results are shown for both simulations.

From these two figures we see that the calculated number of QP-emitted free neutrons corresponds very well with the actual number of neutrons emitted from the QP. The calculated multiplicities agree with the actual multiplicities to within 1.5 neutrons for about 92% of the analyzed events (N_{QP} = 1-8). The results of the study showed that our experimental procedure for determining the QP-emitted free neutron multiplicity was reasonably accurate and sufficiently precise as to allow for the study of well-defined QP sources [7]. Furthermore, the results suggest that our method of free neutron assignment during reconstruction is model independent.

[1] D. Lacroix *et. al*. Phys. Rev. C **69**, 2004.
[2] M. Papa *et. al*. J. Comp. Phys. **208**, 2005.
[3] A.B. McIntosh, *et. al*. Phys. Lett. B **719**, 2013.
[4] P. Marini, *et. al*. Phys. Rev. C **85,** 2012.
[5] A.B. McIntosh, *et. al*. Phys. Rev. C **87**, 2013.
[6] J. Mabiala, *et. al*. Phys.Rev. C **87**, 2013.
[7] P. Marini, A. Zarrella *et. al*. Nucl.Instrum. Methods Phys. Res. **A707**, 2013.

Critical scaling of excited nuclear systems from quantum fluctuations

J. Mabiala, A. Bonasera, H. Zheng, A. B. McIntosh, P. Cammarata, K. Hagel, L. Heilborn, Z. Kohley, L. W. May, A. Raphelt, G.A. Souliotis, A. Zarrella, and S.J. Yennello

The idea that nuclear systems may show some evidence for the occurrence of critical behavior related to a liquid-gas phase transition, stimulated by the van der Waals nature of the nucleon-nucleon interaction, has been a subject of many investigations [1-3]. Experimentally, heavy-ion reactions around the Fermi energy dominated by nuclear fragmentation are explored to investigate this possibility. To date, various experimental evidences have been observed which seem to be related to the nuclear phase transition. Some of these observations include the plateau of the nuclear caloric curve [2, 4] in a certain excitation energy range, the extraction of critical exponents in the charge or mass distribution of the multifragmentation system [5] and the negative branch of the heat capacity experimentally observed in nuclear fragmentation [6]. These signals and many others [7, 8] were only qualitative, giving information on the phase space region reached by the system but not on the detailed trajectory (pressure, volume, temperature) followed by the system to pass from one phase to the other. However, in previous works of Elliott *et al.* [9, 10] the systems studied were located in pressure-density-temperature space. In this current study we extend the work by Elliot *et al.,* adding the asymmetry degree of freedom of the fragmenting source to experimentally establish the dependence of the nuclear equation of state on this quantity.

We report the experimental temperatures and densities of the fragmenting system calculated by the quantum fluctuation method for protons presented in [11, 12]. In addition, pressures calculated through the grand partition function of Fisher's droplet model [13] are also presented. Since the protons represent the vapor part of the system, the derived densities and temperatures refer to the vapor branch of the 'liquid-gas'-like instability region. It is shown that the present data contain a signature of a liquid-gas phase transition. Scaling of physical observables to their critical values displays universality, i.e. independence from the proton-neutron asymmetry of the source.

The experiment was performed at the Texas A&M University Cyclotron Institute. Beams of ^{64}Zn, ^{64}Ni and ^{70}Zn at 35 MeV/nucleon were incident on ^{64}Zn, ^{64}Ni and ^{70}Zn targets, respectively [14]. Charged particles and neutrons were measured using the NIMROD-ISiS 4π detector array [15]. The granularity and excellent isotopic resolution provided by the array enabled the reconstruction of the quasi-projectile (*QP*), the hot projectile-like source produced in the early stage of the collision, in both *Z* and *A*. The NIMROD-ISiS charged particle array is housed inside the TAMU Neutron Ball. The Neutron Ball provides event-by-event multiplicity of free neutrons emitted during a reaction. The *QP* source was selected by means of event-by-event cuts on the experimental data as in Ref. [16] with its mass restricted to be in the range $54 \leq A \leq 64$. Its excitation energy was deduced using the measured free neutron multiplicity, the charged particle kinetic energies, and the Q-value of the breakup. Data were sorted into four different source asymmetry $(m_s = (N - Z)/A)$ bins ranging from 0.04 to 0.24 with bin width of 0.05. In addition, effects of *QP* excitation energies on the thermodynamic quantities were investigated by gating the data into nine bins of 1 MeV in the range of 1-10 MeV/nucleon.

Figure 1 (left panel) shows the temperatures and densities of the selected *QP* of mass in the range $54 \leq A \leq 64$ plotted in the scaled values. The critical values ρ_c and T_c for each m_s bin were determined using Guggenheim's equation [17] to fit ρ versus T curves. It is shown that all the experimental data falls on the same curve. The extracted critical exponent $\beta = 0.35 \pm 0.01$ that defines the universality class of the system is in the range of extracted experimental values from a variety of systems [18]. Calculated

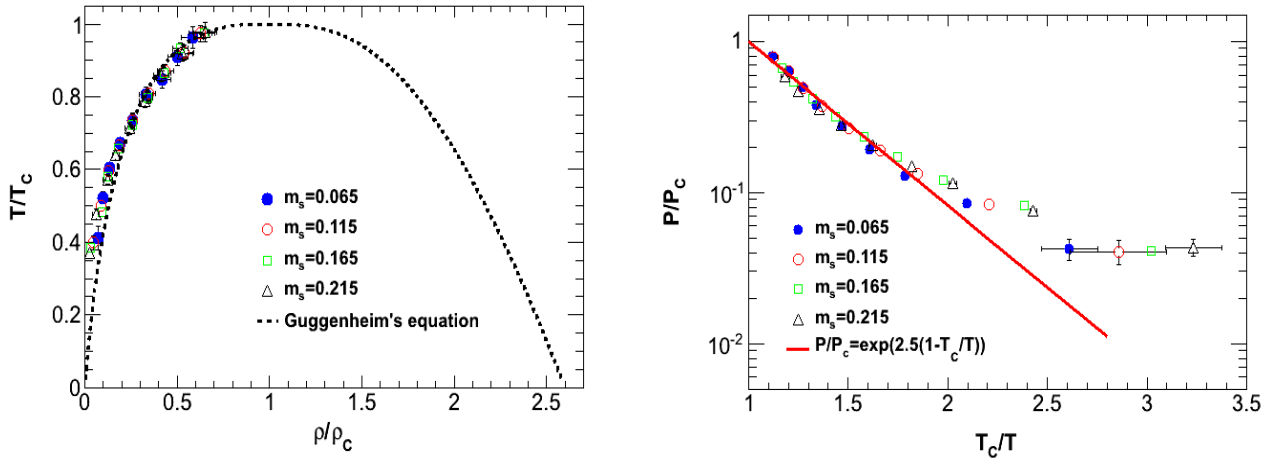

FIG. 1. (Left panel) Reduced temperature-reduced density coexistence curve. The dashed line shows a fit to Guggenheim's equation. (Right panel)The reduced pressure as a function of the inverse of the reduced temperature. The solid line shows a fit to the Clausius-Clapeyron equation where the value of 2.5 is the average of the $\Delta H/T_c$ values extracted from different m_s bins.

pressures (P) normalized to the critical values (P_c) are plotted versus the inverse of the reduced temperature (T_c /T) in Fig.1 (right panel). The values of P_c for different m_s bins are extracted using the Clausius-Clapeyron equation (P/P_c=exp[$\Delta H/T_c$(1-T_c/T)]) which describes several fluids up to T_c [19]. The quantity ΔH is the enthalpy of emission of a fragment from the liquid. The slope of the coexistence lines $\Delta H/T_c$= 2.5 is in agreement with the one obtained in Refs. [9, 10], but a factor of 2 lower than the values of macroscopic systems reported by Guggenheim in Ref. [19]. The experimental critical parameters (T_c , ρ_c and P_c) and the critical compressibility factor for each m_s bin are listed in Table I. The critical temperatures T_c and pressures P_c are observed to increase when increasing m_s while ρ_c decreases with increasing m_s. The critical compressibility factor values (P_c/ $\rho_c T_c$) are very close to those of real gases reported in [20] and are observed to increase with m_s. Strong evidence for a signature of a liquid-gas

Table I. Critical values and thermodynamic quantities for the four m_s bins.

m_s	T_c (MeV)	ρ_c (fm^{-3})	P_c (MeV/fm^3)	$P_c/\rho_c T_c$	$\Delta H/T_c$
0.065	12.12 ± 0.39	0.070 ± 0.006	0.211 ± 0.002	0.25 ± 0.02	31.50 ± 1.01
0.115	12.51 ± 0.35	0.066 ± 0.005	0.209 ± 0.001	0.25 ± 0.02	32.51 ± 0.90
0.165	13.11 ± 0.30	0.064 ± 0.004	0.232 ± 0.001	0.27 ± 0.02	31.46 ± 0.71
0.215	13.39 ± 0.21	0.061 ± 0.002	0.258 ± 0.002	0.31 ± 0.01	32.13 ± 0.50

phase transition in two-component systems has been found. These results provide a means to establish the

proton-fraction dependence of the nuclear equation of state in systems with large neutron excess such as neutron stars.

[1] H. Jaqaman *et al.*, Phys. Rev. C **27**, 2782 (1983).
[2] J. Pochodzalla *et al.*, Phys. Rev. Lett. **75**, 1040 (1995).
[3] L. Satpathy *et al.*, Phys. Rev. C **39**, 162 (1989).
[4] J.B. Natowitz *et al.*, Phys. Rev. C **65**, 034618 (2002).
[5] J.E. Finn *et al.*, Phys. Rev. Lett. **49**, 1321 (1982).
[6] M.D'Agostino *et al.*, Phys.Lett. B **473**, 219 (2000).
[7] B. Borderie *et al.*, Phys. Rev. Lett. **86**, 3252 (2001).
[8] M. Pichon *et al.*, Nucl. Phys. **A779**, 267 (2006).
[9] J. B. Elliott *et al.*, Phys. Rev. Lett. **88**, 042701 (2002).
[10] J. B. Elliott *et al.*, Phys. Rev. C **67**, 024609 (2003).
[11] H. Zheng and A. Bonasera, Phys. Lett. B **696**, 178 (2011).
[12] H. Zheng, A. Bonasera, Phys. Rev. C **86**, 027602 (2012).
[13] P. Finocchiaro *et al.*, Nucl. Phys. **A600**, 236 (1996).
[14] Z. Kohley, PhD Thesis, Texas A&M University, 2010.
[15] S. Wuenschel *et al.*, Nucl. Instrum. Methods Phys. Res. **A604**, 578 (2009).
[16] S. Wuenschel *et al.*, Nucl. Phys. **A843**, 1 (2010).
[17] E.A. Guggenheim, J. Chem. Phys. **13**, 253 (1945).
[18] K. Huang, Statistical Mechanics, Wiley & Sons, New York, 1987.
[19] E.A. Guggenheim, Thermodynamics, North-Holland, Amsterdam, 1993.
[20] C.S. Kiang, Phys. Rev. Lett. **24**, 47 (1970).

Toward understanding relativistic heavy-ion collisions with the STAR detector at RHIC

M. Cervantes, S. Mioduszewski, and the STAR Collaboration

We have advanced the spin-alignment measurement of bottomonium (Upsilon) production. In addition to the measurement in Run-9 p+p collisions at √s=200 GeV, we have performed the measurement for Run-11 p+p collisions at √s=500 GeV.

Upsilon Production Mechanism:

The Run-9 (√s=200 GeV) results were presented in Dr. Cervantes' Ph.D. thesis (2012). Due to the recent discovery of a code error in the acceptance correction to the distribution of Y as a function of cosθ, the final results have changed. However, the Run-11 data (with much more statistics) is fully consistent with the Run-9 result. Figure 1 shows the reconstructed mass from e^+e^- pairs (black) and like-sign pairs (red) from the Run-9 analysis (left panel) and the Run-11 analysis (right panel). The combinatorial background in the √s=500 GeV data is larger than in the 200 GeV data. The blue lines indicate the mass cuts used for the spin-alignment measurement.

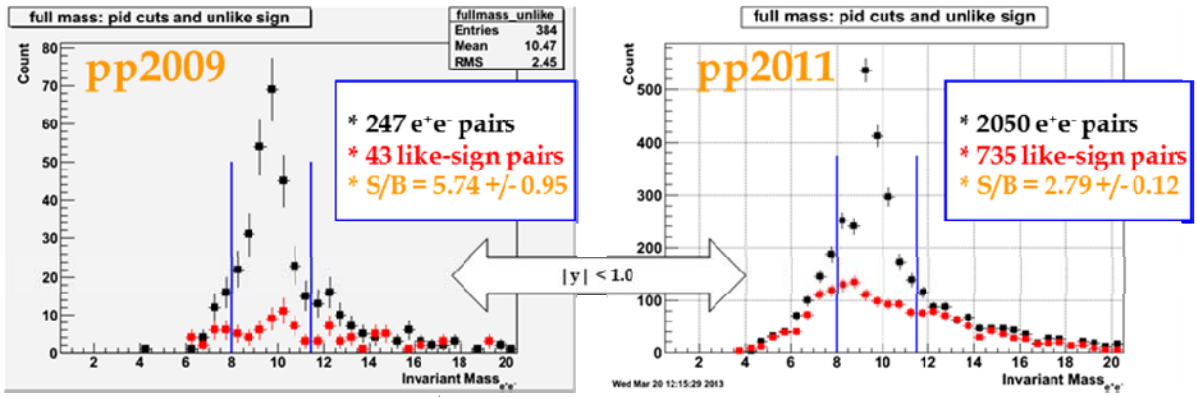

FIG. 1. Invariant mass distribution of e^+e^- pairs (black) and like-sign pairs (red) calculated in p+p events. The blue lines indicate the mass cuts used for the spin-alignment measurement.

The spin alignment measurement is parameterized as $dN/d(\cos\theta)=1+\alpha(\cos^2\theta)$, where θ is the angle between the direction of the decay e^+ momentum, measured in the Upsilon's rest frame with respect to the Upsilon's direction of motion, i.e. the polarization axis. This measurement contributes to the understanding of the production mechanism of heavy quarkonia because different production models (Color Singlet model vs. Color Octet model) predict different values of the polarization α, as a function of Y p_T. The Run-9 result is shown in Fig. 2.

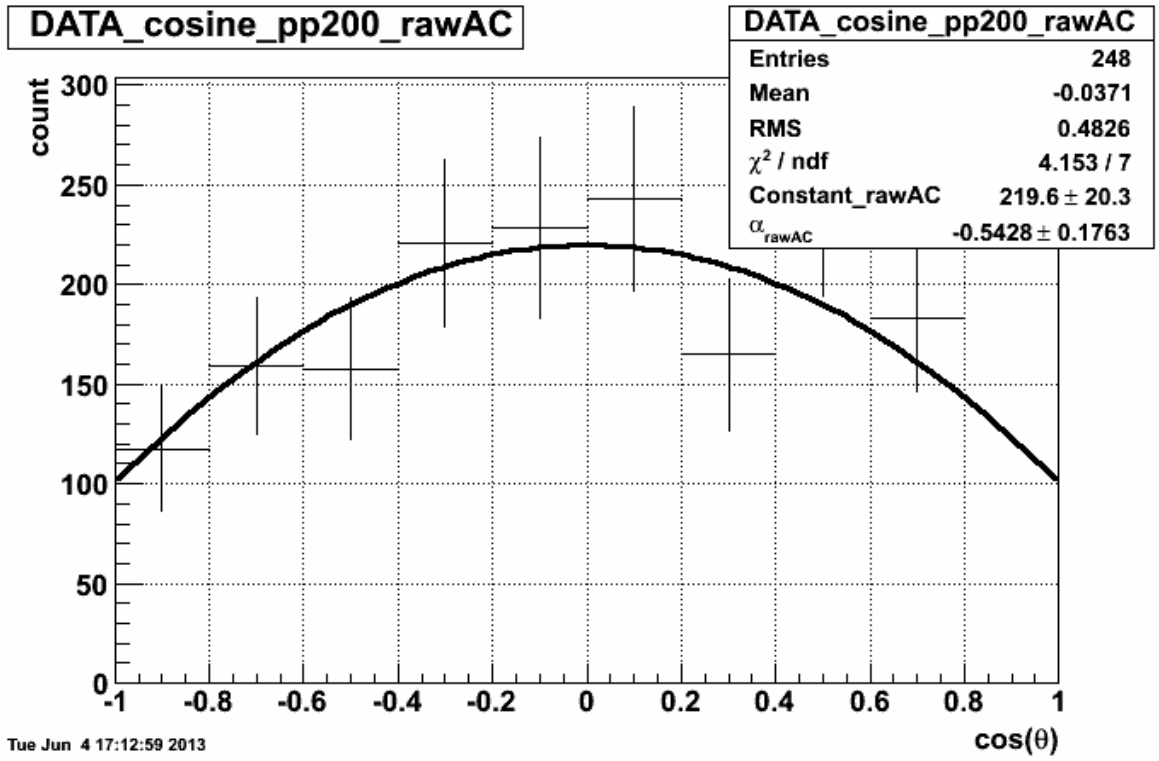

FIG. 2. Acceptance-corrected (Run-9) spin-alignment measurement dN/d(cosθ), in √s=200 GeV p+p collisions, fit with function $C[1+\alpha(\cos^2\theta)]$.

The polarization was found to be longitudinal, with a value of -0.54±0.18. The combinatorial background is small, as seen in Fig.1 (left), and flat in cosθ, and has not been subtracted. The Drell-Yan background, also still included in the measurement is estimated to contribute ~20% from a line-shape analysis.

In the Run-11 data set, the statistics are larger, and we are able to subtract the background by analyzing the invariant mass distribution (for like-sign and unlike-sign pairs) in each bin of cos(θ). A preliminary result of the dN/d(cosθ) distribution is shown in Fig. 3.

The polarization was again found to be longitudinal with a fit value of -0.53±0.18. The acceptance correction, the background subtraction, and the systematics of the result are currently being studied and finalized.

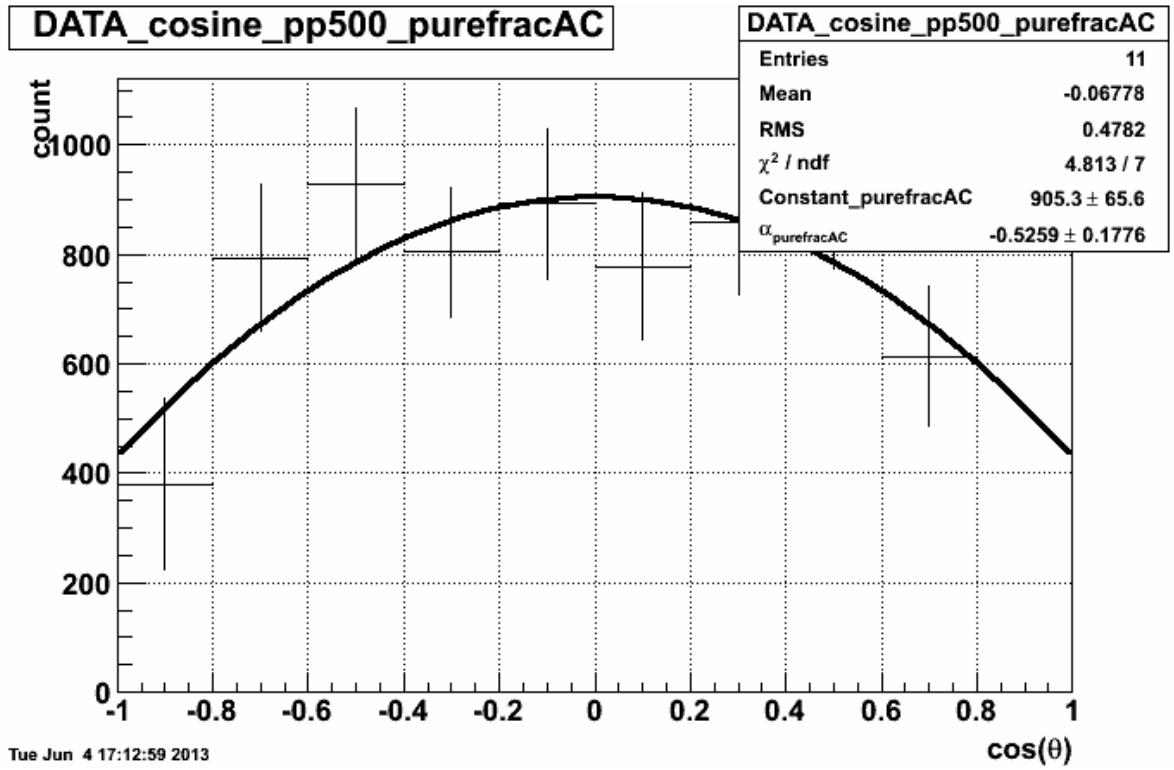

FIG. 3. Acceptance-corrected (Run-11) spin-alignment measurement dN/d(cosθ), in √s=500 GeV p+p collisions, fit with function $C[1+\alpha(\cos^2\theta)]$. The background (combinatorial and Drell-Yan) has been subtracted for this data set.

SECTION III

NUCLEAR THEORY

Coulomb renormalization and ratio of proton and neutron asymptotic normalization coefficients for mirror nuclei

A. M. Mukhamedzhanov

Asymptotic normalization coefficients (ANCs) are fundamental nuclear constants playing an important role in nuclear reactions, nuclear structure, and nuclear astrophysics. In this work the physical reasons for the Coulomb renormalization of the ANC are addressed. Using the Pinkston-Satchler equation the ratio for the proton and neutron ANCs of mirror nuclei is obtained in terms of the Wronskians from the radial overlap functions and regular solutions of the two-body Schr¨odinger equation with the short-range interaction excluded. This ratio allows one to use microscopic overlap functions for mirror nuclei in the internal region, where they are the most accurate, to correctly predict the ratio of the ANCs for mirror nuclei, which determine the amplitudes of the tails of the overlap functions. Calculations presented for different nuclei demonstrate the Coulomb renormalization effects and independence of the ratio of the nucleon ANCs for mirror nuclei on the channel radius. This ratio is valid both for bound states and resonances. One of the goals of this paper is to draw attention to the possibility of using the Coulomb renormalized ANCs rather than the standard ones, especially when the standard ANCs are too large.

The paper was published in Phys. Rev. C **86**, 044615 (2012). The work was supported by NSF, DOE and DOE-NNSA grants.

Electron- and photon-impact atomic ionisation

I. Bray,[1] D. V. Fursa,[1] A. S. Kadyrov, [1] A. T. Stelbovics,[1] A. S. Kheifets, [2] A. M. Mukhamedzhanov

[1]*ARC Centre for Antimatter–Matter Studies, Curtin University, GPO Box U1987, Perth, WA 6845, Australia*

[2]*Research School of Physical Sciences, The Australian National University, Canberra ACT 0200, Australia*

The past decade has seen extraordinary theoretical progress in the field of fully kinematically resolved atomic electron-impact ionisation, and its closely related field of double photoionisation. These processes were challenging to calculate due to formal and computational difficulties associated with break-up problems involving the longrange Coulomb potential. Presently, however, these processes can be calculated accurately for simple targets such as atomic hydrogen and helium, irrespective of the kinematics considered or the geometry of detectors. Collisions in the realm of atomic physics not only have many practical applications, but also form the testing ground for the underlying quantum collision theory, made possible by the wealth of available experimental data. Due to the long range nature of the Coulomb potential, charged particles continue to interact with each other even at infinite separation. For this reason the much-studied problem of electron-impact ionisation, and its very close relative of non-sequential double photoionisation, have lacked a proper formal foundation despite many successful computational implementations. In fact it was the success of the computational approaches to the problems that drove us to revisit the underlying formal theory. The purpose of this work is to review the recent progress in formal ionisation theory, and show how it relates to the successful computational techniques, which aim to fully solve the ionisation problems without resorting to approximations that limit the applicability of the methods. Such issues are best addressed using relatively simple targets such as atomic hydrogen and helium, where we can be very confident in the accuracy of the calculated target structure. Additionally, we restrict the detailed discussion to the lower energies, where high-energy approximations are inaccurate. We report on the computational progress, and how it has resulted in a deeper understanding of the formalism of Coulomb few-body problems.

The review paper was published in Physics Reports 520 (2012) 135–174. A.M. acknowledged the support by NSF and DOE grants.

Generalized Faddeev equations in the Alt-Grassberger-Sandhas form for deuteron stripping with explicit inclusion of target excitations and Coulomb interaction

A. M. Mukhamedzhanov, V. Eremenko, and A. I. Sattarov[1]
[1]*Department of Physics, Texas A&M University, College Station, Texas 77843, USA*

Theoretical description of reactions in general, and the theory for (*d*,*p*) reactions, in particular, needs to advance into the future. Here deuteron-stripping processes off a target nucleus consisting of *A* nucleons are treated within the framework of the few-body integral equations theory. The generalized Faddeev equations in the Alt-Grassberger-Sandhas (AGS) form, which take into account the target excitations, with realistic optical potentials provide the most advanced and complete description of the deuteron stripping. The main problem in practical application of such equations is the screening of the Coulomb potential, which works only for light nuclei. For the first time we present a formulation of the Faddeev equations in the AGS form taking into account the target excitations with explicit inclusion of the Coulomb interaction. By projecting the (A + 2)-body operators onto target states, matrix three-body integral equations are derived, which allow for the incorporation of the excited states of the target nucleons. Using the explicit equations for the partial Coulomb scattering wave functions in the momentum space we present the AGS equations in the Coulomb distorted wave representation without screening procedure. We also use the explicit expression for the off-shell two-body Coulomb scattering T matrix, which is needed to calculate the effective potentials in the AGS equations. The integrals containing the off-shell Coulomb T matrix are regularized to make the obtained equations suitable for calculations. For *NN* and nucleon-target nuclear interactions we assume the separable potentials what significantly simplifies solution of the AGS equations.

The work has been published in Phys. Rev. C **86**, 034001 (2012). The work was supported by NSF, DOE and DOE-NNSA grants.

Measurement of the -3 keV resonance in the reaction $^{13}C(\alpha,n)^{16}O$ of importance in the s-process

M. La Cognata,[1] C. Spitaleri,[1,2] O. Trippella,[1,3] G. G. Kiss,[1,4] G.V. Rogachev,[5] A. M. Mukhamedzhanov, M. Avila [5] G. L. Guardo,[1,2] E. Koshchiy,[5] A. Kuchera,[5] L. Lamia,[2] S. M. R. Puglia,[1,2] S. Romano,[1,2] D. Santiago,[5] and R. Sparta[1,2]

[1]*Istituto Nazionale di Fisica Nucleare, Laboratori Nazionali del Sud, 95123 Catania, Italy*

[2]*Dipartimento di Fisica e Astronomia, Universita` di Catania, 95123 Catania, Italy*

[3]*Istituto Nazionale di Fisica Nucleare, Sezione di Perugia, Perugia, Italy and Dipartimento di Fisica, Universita` di Perugia, 06123 Perugia, Italy*

[4]*Institute of Nuclear Research (ATOMKI), 4026 Debrecen, Hungary*

[5]*Department of Physics, Florida State University, Tallahassee, Florida 32306, USA*

The $^{13}C\alpha,n)^{16}O$ reaction is the neutron source for the main component of the s-process, responsible for the production of most nuclei in the mass range $90 \leq A \leq 204$. It is active inside the helium-burning shell in asymptotic giant branch stars, at temperatures $\leq$ 108 K, corresponding to an energy interval where the $^{13}C\alpha,n)^{16}O$ is effective from 140 to 230 keV. In this region, the astrophysical S(E)-factor is dominated by the -3 keV subthreshold resonance due to the 6.356 MeV level in ^{17}O, giving rise to a steep increase of the S(E)-factor. Notwithstanding that it plays a crucial role in astrophysics, no direct measurements exist inside the s-process energy window. The magnitude of its contribution is still controversial as extrapolations, e.g., through the R matrix and indirect techniques, such as the asymptotic normalization coefficient (ANC), yield inconsistent results. The discrepancy amounts to a factor of 3 or more right at astrophysical energies. Therefore, we have applied the Trojan horse method to the $^{13}C(^{6}Li,n\ ^{16}O)d$ quasi-free reaction to achieve an experimental estimate of such contribution. For the first time, the ANC for the 6.356 MeV level has been deduced through the Trojan horse method as well as the n-partial width, allowing to attain an unprecedented accuracy in the $^{13}C\alpha,n)^{16}O$ study. Though a larger ANC for the 6.356 MeV level is measured, our experimental S(E)-factor agrees with the most recent extrapolation in the literature in the 140–230 keV energy interval, the accuracy being greatly enhanced thanks to this innovative approach. In the analysis a new theory of the resonant Trojan Horse reactions based in the surface integral formalism was used [1]. The paper was published in Phys. Rev. Lett. **109**, 232701 (2012). A.M. acknowledged the support by NSF, DOE and DOE-NNSA grants.

[1] A.M. Mukhamedzhanov, Phys. Rev. C **84**, 044616 (2011).

Density and temperature of fermions and bosons from quantum fluctuations

Hua Zheng,[1, 2] Gianluca Giuliani,[1] Matteo Barbarino,[1] and Aldo Bonasera[1, 3]
[1]*Cyclotron Institute, Texas A&M University, College Station, TX 77843, USA*
[2]*Physics Department, Texas A&M University, College Station, TX 77843, USA*
[3]*Laboratori Nazionali del Sud, INFN, via Santa Sofia, 62, 95123 Catania, Italy*

Fragmentation experiments could provide informations about the nuclear matter properties to constrain the equation of state (EoS) [1-4]. To date a method does not exist to determine the densities and temperatures reached during collisions that takes into account the genuine quantum nature, which has been well known in some other fields [5-7], of the system. Long ago, Bauer stressed the crucial influence of Pauli blocking in the momentum distributions of nucleons emitted in heavy ion collisions near the Fermi energy [8]. We have recently proposed a method based on fluctuations estimated from an event-by-event determination of fragments arising after the energetic collision [9-11]. A similar approach has also been applied to observe experimentally the quenching of multiplicity fluctuations in a trapped Fermi gas [12-14] and the enhancement of multiplicity fluctuations in a trapped Boson gas [15]. We go beyond the method in [12-15] by including momentum quadrupole fluctuations as well to have a direct measurement of densities and temperatures for subatomic systems which it is difficult to obtain such informations in a direct way. We apply the proposed method to microscopic CoMD approach [16-22] which includes fermionic statistics. The resulting energy densities and temperatures calculated using protons and neutrons display a rapid increase around 3 MeV temperature which is an indication of a first-order phase transition. This result is confirmed by the rapid increase of the entropy per unit volume in the same temperature region.

Recent experimental data on low density clustering in nuclear collisions and a comparison to microscopic quantum statistical models suggested the possibility that in order to reproduce the data, a Bose condensate is needed [23-24]. We know that light nuclei display an α-cluster structure which could be exemplified by the so-called 'Hoyle' state in ^{12}C i.e. the first excited state of such a nucleus which decays into 3 α's [25]. The fact that the ground state of nuclei could be made of α clusters could justify their copious production in heavy ion collisions near the Fermi energy. Preliminary experimental results on ^{40}Ca+^{40}Ca performed at the Cyclotron Institute at Texas A&M University show that events with large multiplicity of α-like (i.e. ^{12}C, ^{16}O etc.) or d-like (i.e. ^{6}Li, ^{10}B etc.) fragments are found [26]. At the same time these effects raise the natural question whether α clustering and production could be a signature of a BEC [27-29]. In fragmentation reactions, CoMD predicts large yields of α clusters, but the experimental yield is largely underestimated [16-22]. We think the role of bosons in the model has been missed. Therefore, we add the boson correlations in the collision term and the boson yields are largely increased and closer to data. These features should be kept in mind when we discussing a possible BEC in the model.

A method for measuring the temperature based on momentum quadruple fluctuations of detected particles was proposed in [30]. A quadruple moment $Q_{xy} = p_x^2 - p_y^2$ is defined in a direction transverse to the beam axis (z-axis) to minimize non-equilibrium effects [9-11]. The average $\langle Q_{xy} \rangle$ is zero for a

given particle type in the center of mass of the equilibrated emitting source. Its variance is given by the simple formula:

$$\sigma_{xy}^2 = \int d^3p (p_x^2 - p_y^2)^2 f(p), \tag{1}$$

where *f(p)* is the momentum distribution of particles. In [30] a classical Maxwell-Boltzmann distribution of particles with temperature T_{cl} was assumed, which gives: $\sigma_{xy}^2 = \bar{N}(2mT_{cl})^2$, m is the mass of the fragment, $\bar{N}$ is the average number of particles. In heavy ion collisions, the produced particles do not follow classical statistics because of the quantum nature, the correct distribution function must be used in Eq. (1). Protons (p), neutrons (n), tritium (t), etc., follow the Fermi-Dirac statistics [9-10] while deuterons (d), alphas (α) etc., should follow the Bose-Einstein statistics[11].

For fermions, using a Fermi-Dirac distribution *f(p)* in Eq. (1), we obtain

$$\sigma_{xy}^2 = \bar{N}(2mT_{cl})^2 F_{QC}, \tag{2}$$

where F_{QC} is the quantum correction factor. When $T/\varepsilon_f < 1$ where $\varepsilon_f = \varepsilon_{f0}(\rho/\rho_0)^{2/3} = 36(\rho/\rho_0)^{2/3}$ MeV is the Fermi energy of the nuclear matter and $\rho_0 = 0.16 fm^{-3}$, one can do the low temperature approximation and expand F_{QC} to $O(T/\varepsilon_f)^4$. A detailed derivation can be found in [9]. At the beginning, we expected that this was sufficient when $T/\varepsilon_f < 1$ is fulfilled. It turns out that higher order terms are needed when $T/\varepsilon_f > 0.5$. Therefore, we parameterized the numerical result of F_{QC} as function of T/ε_f, which is indistinguishable from the numerical result. Details can be found in [10]. We outline the results as

$$F_{QC} = \begin{cases} \frac{4}{35}(\frac{T}{\varepsilon_f})^{-2}[1+\frac{7}{6}\pi^2(\frac{T}{\varepsilon_f})^2 + O(\frac{T}{\varepsilon_f})^4], (low\,T), \\ 0.2(\frac{T}{\varepsilon_f})^{-1.71}+1, \qquad (high\ order), \end{cases} \tag{3}$$

At the extreme case $T/\varepsilon_f << 1$, the quantum correction factor F_{QC} has the similar behavior at low temperature approximation and at the case including the higher order corrections. At high temperature T, F_{QC} for higher order corrections in Eq. (3) converges to unity, which the classical limit is recovered as expected. The momentum quadruple fluctuations in Eq. (2) depend on temperature and density through ε_f, thus we need more information in order to be able to determine both quantities.

Within the same framework we can calculate the multiplicity fluctuations of fermions [7, 31-32]. Similar to the momentum quadruple fluctuations, the low temperature approximation and including higher order corrections results are derived in [7, 31-32], respectively. Since Eq. (3) is the function of T/ε_f and in experiments or models one recovers the normalized multiplicity fluctuation $\left\langle (\Delta N)^2 \right\rangle / \bar{N}$, we express

T/ε_f as function of $\left\langle (\Delta N)^2 \right\rangle / \bar{N}$ for convenient to use. In the following paper, we will use x to replace $\left\langle (\Delta N)^2 \right\rangle / \bar{N}$ to simplify equations. Thus we have

$$\frac{T}{\varepsilon_f} = \begin{cases} \frac{2}{3}x, & (low\ T), \\ -0.422 + \frac{0.422}{(1-x)^{0.656}} + 0.345x - 0.12x^2, & (higher \quad order), \end{cases} \tag{4}$$

when $x<<1$, T/ε_f for higher order corrections becomes $0.635x$ which recovers to the low temperature approximation result as expected. Once the normalized multiplicity fluctuation of fermions is measured from experimental data or model, one can easily derive the value of T/ε_f from Eq. (4). Then one can substitute T/ε_f into Eq. (3) to obtain F_{QC} and solve Eq. (2) for T where momentum quadruple fluctuation can also be measured in experimental data or model. Knowing the T we obtain the Fermi energy from Eq. (4). Then one can derive the density of fermions from $\varepsilon_f = 36(\rho/\rho_0)^{2/3}$ MeV. Until now, the scenario for fermions is completed. The multiplicity fluctuation is the first quantity we should investigate when we study the properties of fermions.

For bosons, we need to use Bose-Einstein distribution in Eq. (1). There is difference from fermions. We need to consider the temperature below or above the critical temperature

$$T_c = \frac{3.31}{(2s+1)^{2/3}} \frac{\hbar^2}{m} \rho^{2/3}, \tag{5}$$

for a particle of spin S at a given density ρ. We obtain

$$\sigma_{xy}^2 = \bar{N}(2mT_{cl})^2 B_{QC}(1), \qquad (T < T_c), \tag{6}$$

$$\sigma_{xy}^2 = \bar{N}(2mT_{cl})^2 B_{QC}(z), \qquad (T > T_c), \tag{7}$$

Where $B_{QC}(z)=g_{7/2}(z)/g_{3/2}(z)$ is the quantum correction factor for bosons, the $g_n(z)$ functions are well studied in the literature and $z=e^{\mu/T}$ is the fugacity which depends on the temperature T and the chemical potential μ connecting with T_c. Below the critical temperature $B_{QC}(1)=0.4313$ and $B_{QC}(z)$ is always less than 1 above the critical temperature, thus the same quadrupole fluctuation implies a higher temperature in a Bose gas than in a classical gas. These features are in contrast to the behavior of fermion systems, for which the temperature is always smaller than the classical limit. The momentum quadrupole fluctuations depend on temperature and density through T_c, Eq. (5), thus we need more informations in order to be able to determine both quantities when $T>T_c$. We stress that Eqs. (6, 7) are derived under the assumption of a non-interacting Bose gas. Interactions will change somehow the results. However, from superfluid ^4He we know that the experimental critical temperature is not much different from the ideal gas result.

Within the same framework we can calculate the multiplicity fluctuations of boson numerically when $T>T_c$. When $T<T_c$ the multiplicity fluctuations are always infinite since the isothermal compressibility diverges for ideal bosons[7,31-32]. This phenomenon is of course not observed in experiments. Therefore, we need to include interactions between bosons (and fermions if present) near the critical point. We use Landau's phase transition theory near the critical point. More details of Landau's phase transition theory can be found in [11]. We obtain the normalized multiplicity fluctuations for bosons are

$$x = 0.155 \mid \tilde{t} \mid^{-1} -0.155, \qquad (T < T_c), \tag{8}$$

$$x = 0.62 \mid \tilde{t} \mid^{-1} +1, \qquad (T > T_c), \tag{9}$$

where $\tilde{t}=(T-T_c)/T_c$ is the reduced temperature. For practical purposes, we parameterized $B_{QC}(z)$ functions in Eq. (7) in terms of normalized multiplicity fluctuations x through ν [11]

$$B_{QC}(z) = -0.5764e^{-1.5963|\nu|^{0.6452}} + 1.0077, \tag{10}$$

where

$$\nu = \frac{\mu}{T} = -3.018e^{-2.8018(x-1)^{0.45}}(x-1)^{0.1142}, \tag{11}$$

Therefore, similar to fermions case, the multiplicity fluctuation of bosons is the first quantity to investigate. When $T>T_c$, one can use Eqs. (7, 10, 11) to calculate the temperature T and then use Eq. (9) to calculate the critical temperature T_c. It is straight forward to calculate the density of bosons using Eq. (5). When $T<T_c$, one can use Eqs. (5, 6, 8) to calculate the temperature and density of bosons.

To illustrate the strength of our approach we simulated $^{40}Ca+^{40}Ca$ heavy ion collisions at fixed impact parameter b=1 fm and beam energies E_{lab}/A ranging from 4 MeV/A up to 100 MeV/A. Collisions were followed up to a maximum time 1000 fm/c in order to accumulate enough statistics. The choice of central collisions was dictated by the desire to obtain full equilibration. This however, did not occur especially at the highest beam energies due to a partial transparency for some events. For this reason the quadrupole in the transverse direction, Eq. (1), was chosen. Furthermore, in order to correct for collective effects as much as possible, we defined a 'thermal' energy, eg. for proton, as:

$$\left\langle \frac{E_{th}}{A} \right\rangle = \frac{E_{cm}}{A} - [\left\langle \frac{E_p}{\bar{N}_p} \right\rangle - \frac{3}{2}\left\langle \frac{E_{pxy}}{\bar{N}_p} \right\rangle] - Q_{value}, \tag{12}$$

where $\langle E_p/\bar{N}_p \rangle$ and $\langle E_{pxy}/\bar{N}_p \rangle$ are the average total and transverse kinetic energies (per particle) of protons. Q_{value}=$8\bar{N}_p/Z$, 8 MeV is the average binding energy of a nucleon and Z the total charge of the system and $\bar{N}_p$ the average number of protons emitted at each beam energy. For the other particles, we use the same definition to calculate the thermal energies. For a completely equilibrated system, the

transverse kinetic energy (times 3/2) is equal to the total kinetic energy and the terms in the square brackets cancel. All the center of mass energy, E_{cm}/A, is converted into thermal energy (plus the Q_{value}). In the opposite case, say an almost complete transparency of the collision, the transverse energy would be negligible and the resulting thermal energy would be small. Our approximation will account for some corrections, and this will become more and more exact when many fragment types are included in Eq. (12). However, this approximation might be important in experiments where only some fragment types are detected or if, because of the time evolution of the system, different particles are sensitive to different excitation energies, for instance if some particles are produced early or late in the collision.

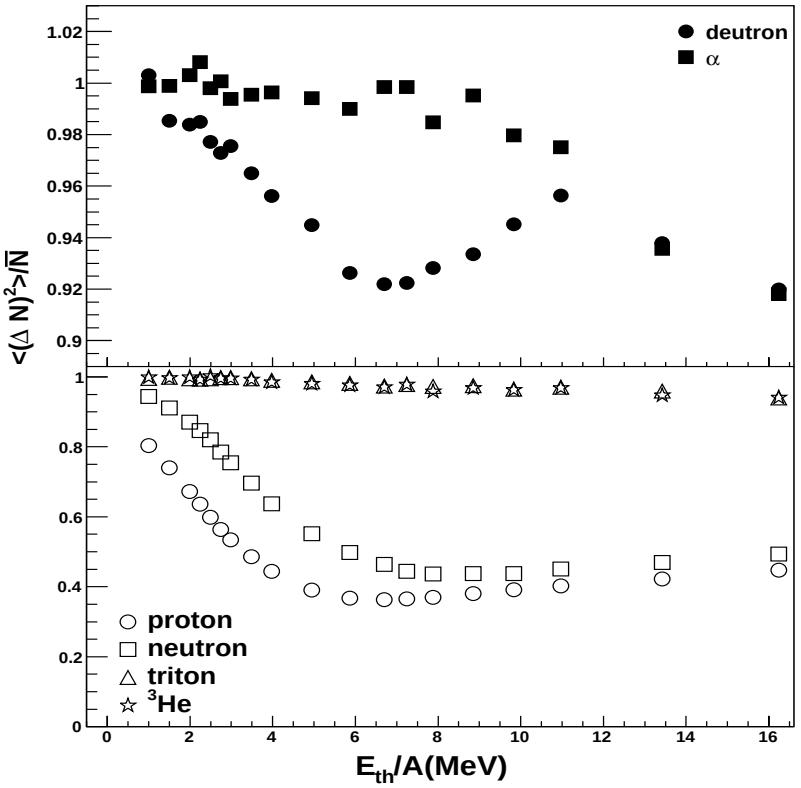

FIG. 1. Normalized multiplicity fluctuation versus excitation energy per particle. (Top panel) CoMD results for d and α particles. (Bottom panel) CoMD results for p, n, t and ^3He. Notice the change of scales in the two panels.

In Fig. 1, we show the normalized multiplicity fluctuations of particles from CoMD. The multiplicity fluctuations quenching for fermions are observed, analogous to [12-14]. Recently, Stein et al. looked at his experimental data, the similar multiplicity fluctuations quenching for fermions are found. More details can be found in [33]. These results are also confirmed in Mabiala's experimental data [34]. Since the multiplicity fluctuations are obtained, we can use Eqs. (2, 3, 4) to extract the temperature and density of the system. Meanwhile, in the same frame, it is straightforward to derive other thermodynamical quantities. One such quantity is the entropy S. Details can be found in [11].

To better summarize the results, we plot in Fig. 2 the excitation energy per particle $\langle E_{th}/A\rangle$, energy density $\varepsilon=\langle E_{th}/A\rangle\rho$ and the entropy density $\Sigma=\langle S/A\rangle\rho$ versus temperature. The so called caloric curve is well studied in the literature and it shows a well-defined mass dependence. In Fig. 2 we report the experimental data (open symbols) from [35], obtained in the mass region A=60-100, which is the closest to our system. Recall that the experimental values of the temperature were obtained using classical approximations, thus it is no surprise that they agree well with our classical results (full star). The classical calculation clearly shows a region of constant temperature (less than 6 MeV) which would indicate a phase transition. However, notice that the density is changing with changing temperature. For

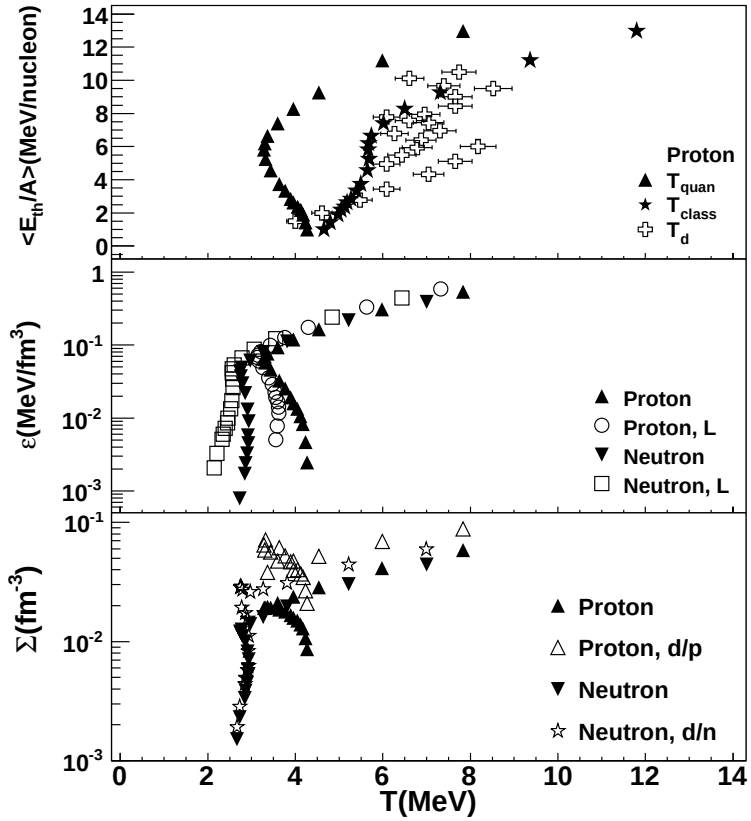

FIG. 2. (Top panel) Excitation energy versus temperature. The full triangles refer to quantum temperatures; the full stars refer to classical temperatures from fluctuations; the open crosses refer to experimental data using double ratio thermometer from [35] obtained for mass number A=60-100. (Middle panel) Energy density versus temperature. Full symbols refer to the higher order correction results and the open symbols refer to the low temperature approximation results. (Bottom panel) Entropy density versus temperature. The full symbols refer to the results from [10] and the open symbols refer to the results from particle ratio of the number of d to p (n) [4, 36].

this reason one might wonder on the physical meaning of the caloric curve and it could be better to investigate the energy density (middle panel). A rapid variation of the energy density is observed around 2 MeV for neutrons and 3 MeV for protons which indicates a first-order phase transition. As we can see from the figure, the higher order correction results give small corrections while keeping intact the relevant features obtained in the lowest approximation. This again suggests that in the simulations the system is

fully quantal. We also notice that Coulomb effects become negligible at $T>>3$ MeV where the phase transition occurs. The smaller role of the Coulomb field in the phase transition has recently been discussed experimentally in the framework of Landau's description of phase transitions[37-39]. The rapid increase of the entropy per unit volume (bottom panel) is due to the sudden increase of the number of degrees of freedom (fragments) with increasing T.

Comparing the charge particle distribution with the experimental data shows that we cannot reproduce the experimental data completely. This is not surprising since we only have one fixed impact parameter in the model while the experimental data includes all the possible impact parameters. The experimental filter should be taken into account as well, but these features are not relevant to our goals. The important point is that the α yield is underestimated, a feature which cannot be corrected by including other impact parameters or the experimental filter. The important ingredient which is missing in the model is the possibility of boson-boson collisions ($\alpha-\alpha$, d-d, etc.) and correlations. Therefore, we propose a modification of the collision term in CoMD to include the possibility of $\alpha-\alpha$ collisions. We refer to the modified version as $CoMD_\alpha$. We use Minimum Spanning Tree method (MST) to identify α particle at each time step, same as the cluster identification in CoMD. First one particle is chosen, then the three closest particles with the correct values of spin and isospin (i.e. two protons and two neutrons with opposite spin respectively) are selected within the radius of $2.4\sigma_r$ (the value used in the cluster identification) in coordinate space. If all the conditions are fulfilled, we identify the four particles as α. We run over all the particles and determine all the possible α particles. Each particle can belong only to one α. At each time step, we search for $\alpha-\alpha$ pair whose distance is smaller than 2.5 fm. We follow the mean free path method[1, 40-41] and define a collision probability for the $\alpha-\alpha$ pair:

$$\Xi_{ij} = 1 - e^{-\sqrt{1-\frac{V_c}{E_k}}\sigma\Pi\rho(r_i)v_{ij}dt}, \qquad (13)$$

where σ is the cross section, $\Pi=(1+\bar{f}_1)(1+\bar{f}_2)$ is the Bose-Einstein factor and $\bar{f}_i$ is the average occupation probability for α, i=1, 2, $\rho(r_i)$ is the local density, v_{ij} is the relative velocity of the two α particles, dt is the time step and $\sqrt{1-V_c/E_k}$ is the Coulomb barrier correction factor where V_c is the Coulomb energy between the two αs and E_k is their relative kinetic energy. For simplicity, we take σ as the $\alpha-\alpha$ geometric cross section in this study. Notice that in such an approximation, the strong resonances which lead to the formation of ^8Be are not included. We expect that such resonances will increase the α yields from ^8Be decay. However we have not be able to implement this effect in the present model. If an $\alpha-\alpha$ collision occurs, we calculate the Bose-Einstein factor Π before the collision and Π' after the collision. If $\Pi'>\Pi$, the collision will be accepted, otherwise, rejected. Thus, the Bose factors $(1+\bar{f}_i)$ increase the probability of collision in contrast to the Pauli blocking factors[1-2]. This will produce fluctuations larger than Poissonian, which is a signature of a BEC. Meanwhile, if the α particle does not suffer any collision in that time step, one of its nucleons can collide with another nucleon subject to Pauli blocking. This might break the α into nucleons. We repeat the same simulations as before using $CoMD_\alpha$.

Similar to Fig. 1, we plot the normalized multiplicity fluctuations of particles versus excitation energy per particle in Fig. 3. As we can see in the figure, d- and $\alpha-$ normalized fluctuations are generally larger than 1 (top panel). The multiplicity fluctuations of fermions (bottom panel) are less than 1 for most

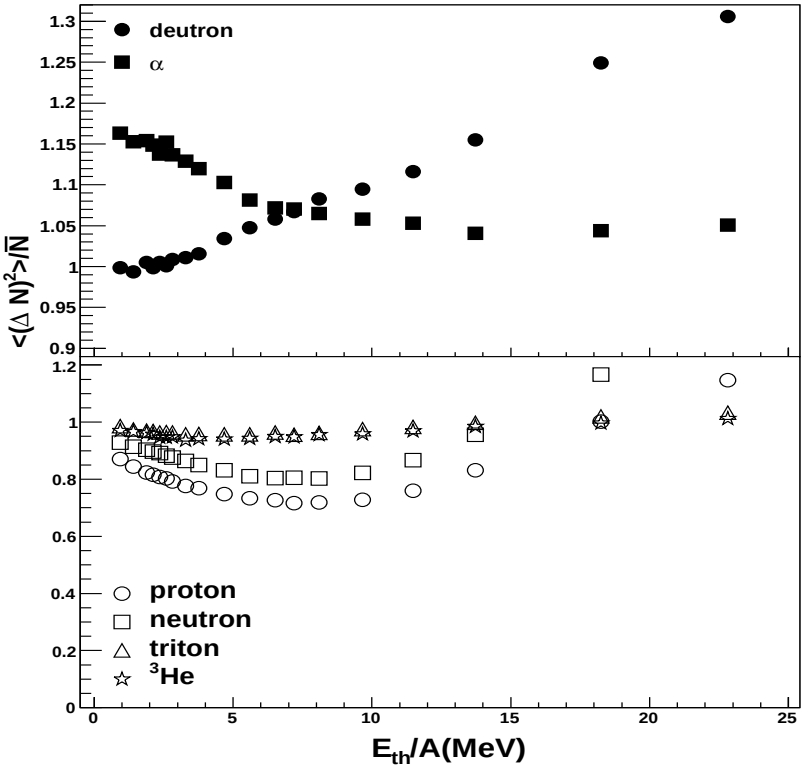

FIG. 3. Normalized multiplicity fluctuation versus excitation energy per particle. (Top panel) $CoMD_\alpha$ results for d and α particles. (Bottom panel) $CoMD_\alpha$ results for p, n, t and ^3He. Notice the change of scales in the two panels. The d fluctuations keep increasing at high energies because they are produced from the decay of α excited clusters. Similarly for the large fluctuations observed for p and n.

of the thermal energies. These results are what we expect. Since we consider the Pauli blocking for fermions and Bose-Einstein factor for bosons, the quantum effects for fermions and bosons should show up through the multiplicity fluctuations even if the system is a mixture of fermions and bosons. When the thermal energy is very high, the normalized fluctuations of fermions are larger than 1 as well, this suggests that the α particles are so excited to emit nucleons or d which carry the original large fluctuations of the parent. We also notice that the thermal energy of $CoMD_\alpha$ in Fig. 3 is larger than that of CoMD in Fig. 1 with the same beam energy. This simply tells us that we have more thermalization in $CoMD_\alpha$ than CoMD because of the large number of collisions in $CoMD_\alpha$, including the $\alpha-\alpha$ collisions.

In Fig. 4 , we plot the reduced densities for d and α versus reduced temperatures assuming the temperature is below the critical temperature (top panel) and the temperature is above the critical temperature (bottom panel). From Fig. 4, one can see that below the critical temperature, the $\alpha's$ densities

are too high and unphysical. But the densities of bosons are reasonable assuming the temperature is above critical temperature.

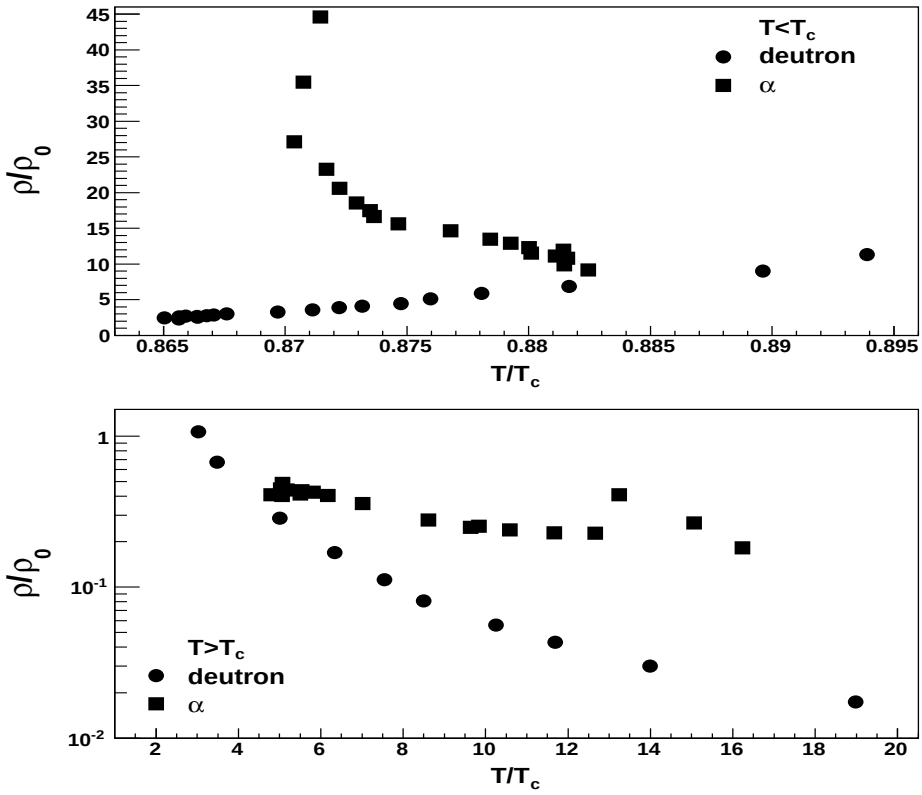

FIG. 4. (Top panel) Reduced density versus reduced temperature for bosons assuming $T < T_c$; (Bottom panel) reduced density versus reduced temperature for bosons assuming $T > T_c$.

In conclusion, we have addressed a general approach for deriving densities and temperatures of fermions or bosons from quantum fluctuations (momentum quadrupole fluctuations and multiplicity fluctuations). For fermions, the higher order corrections results are consistent with the low temperature approximation results at very low temperature. We have shown that for high temperatures and low densities the classical result is recovered as expected. For bosons system, quadrupole and multiplicity fluctuations using Landau's theory of fluctuations near the critical point for a Bose-Einstein condensate (BEC) at a given density ρ are derived. We apply our approach to the simulation data of CoMD which includes the fermionic statistics. The multiplicity fluctuations quenching for fermion particles, due to the quantum nature, are found. These results also are confirmed by recently experimental data investigations. We derived the energy densities and entropy densities at different excitation energies for p and n. Both quantities show a rapid variation in the same temperature region indicates a possible first-order phase transition. Considering the possibility of boson-boson collisions and correlations is missing in CoMD, the alpha production is underestimated compared to the experimental data. We proposed a modified version of the model, $CoMD_\alpha$, to include the possibility of $\alpha-\alpha$ collisions. The relevent Bose-Einstein factor in the collision term is properly taken into account. This approach increases the yields of bosons relative to

fermions closer to data. In the framework of $CoMD_\alpha$, we discussed the multiplicity fluctuations for particles and obtained the temperatures and densities for d and α. We suggest that multiplicity fluctuations larger than 1 for bosons, in contrast to fermions multiplicity fluctuations which are smaller than 1, is a signature of a BEC in nuclei.

[1] A. Bonasera, *et al.,* Phys.Rep. **243**, 1 (1994).
[2] G.F. Bertsch, *et al.,* Phys. Rep. **160, No 4**, 189 (1988).
[3] A. Bonasera, *et al.,* Revista del Nuovo Cimento, **23**, 1 (2000).
[4] L.P. Csernai, Introduction to relativistic heavy ion collisions. New York: Wiley, 1994.
[5] W.S. Corak, M.P. Garfunkel, C.B. Satterthwaite, A. Wexler, Phys. Rev. **98**, 1699 (1955).
[6] http://asd.gsfc.nasa.gov/arcade/cmb_spectrum.html.
[7] R.K. Pathria. Statistical mechanics. Singapore: Elsevier Pte Ltd, 2003, 2nd ed.
[8] W. Bauer, Phys. Rev. C, **51**, 803 (1995).
[9] H. Zheng, A. Bonasera, Phys. Lett. B, **696**, 178 (2011).
[10] H. Zheng, A. Bonasera, Phys. Rev. C, **86**, 027602 (2012).
[11] H. Zheng, G. Giuliani, A. Bonasera, Nucl. Phys. A**892**, 43 (2012).
[12] T. Müller, *et al.,* Phys. Rev. Lett. **105**, 040401 (2010).
[13] C. Sanner, *et al.,* Phys Rev Lett, **105**, 040402 (2010).
[14] C.I. Westbrook, Physics, **3**, 59 (2010).
[15] J. Esteve, *et al.,* Phys. Rev. Lett. **96**, 130403 (2006).
[16] A. Bonasera, Phys. Rev. C, **62**, 052202(R) (2000).
[17] M. Papa, T. Maruyama, A. Bonasera, Phys. Rev. C **64**, 024612 (2001).
[18] A. Bonasera, Nucl. Phys. **A681**, 64c (2001).
[19] S. Terranova, A. Bonasera, Phys. Rev. C **70**, 024906 (2004).
[20] S. Terranova, D.M. Zhou, A. Bonasera, Eur. Phys. J. A **26**, 333 (2005).
[21] M. Papa, G. Giuliani, A. Bonasera, J. Comp. Phys. **208**, 403 (2005).
[22] M. Papa, G. Giuliani, Eur. Phys. J. A **39**, 117 (2009).
[23] L. Qin, *et al.*, Phys. Rev. Lett. **108**, 172701 (2012).
[24] G. Röpke, *et al.,* Phys. Rev. Lett. **80**, 3177 (1998).
[25] D. Arnett, Supernovae and nucleosynthesis. Princeton Univeristy Press: 1996.
[26] K. Schmidt, *et al., Progress in Research*, Cyclotron Institute, Texas A&M University (2010-2011), p. II-81; Abstract proceedings APS-meeting, E. Lansing, MI, 2011, and K. Schmidt *et al.*, J. Phys. Conf. series **420**, 012088 (2013).
[27] A. Tohsaki, *et al.,* Phys. Rev. Lett. **87**, 192501(2001).
[28] Y. Funaki, H. Horiuchi, A. Tohsaki, P. Schuck, G. Röpke, Prog. Theor. Phys. **108**, 297 (2002).
[29] A.R. Raduta, *et al.,* Phys. Lett. B **705**, 65 (2011).
[30] S. Wuenschel, *et al.,* Nucl. Phys. **A843**, 1 (2010).
[31] L. Landau, F. Lifshits, Statistical physics. NewYork: Pergamon, 1980.
[32] K. Huang, Statistical mechanics. New York: Wiley, 1987, 2nd ed.
[33] B.C. Stein, *et al.,* arxiv: 1111.2965VI; J. Phys. G (submitted).

[34] J. Mabiala, *et al.,* Phys. Lett. B (submitted); arxiv: 1208.3480VI; J. Mabiala *et al.*, J. Phys.: Conf. series **420**, 012110 (2013).
[35] J.B. Natowitz, *et al.,* Phys. Rev. C **65**, 034618 (2002).
[36] P.J. Siemens, *et al.,* Phys. Rev. Lett. **43**, 1486 (1979).
[37] A. Bonasera, *et al.,* Phys. Rev. Lett. **101**, 122702 (2008).
[38] M.R. Huang, *et al*., Phys. Rev. C **81**, 044618 (2010).
[39] M.R. Huang, *et al*., Nucl. Phys. **A847**, 233 (2010).
[40] A. Bonasera, T. Maruyama, Progr. Theor. Phys, **90**, 1155 (1993).
[41] Z.G. Tan, A. Bonasera, C.B. Yang, D.M. Zhou, S. Terranova, Int. J. Mod, Phys. E, **16**, 2269 (2007).

Effects of initial fluctuations on bottomonium suppression in relativistic heavy ion collsions

T. Song, K. C. Han and C. M. Ko

Using the screened Cornell potential [1] and the next-to-leading order perturbative QCD [2,3] to determine, respectively, the properties of bottomonia and their dissociation cross sections in a quark-gluon plasma, we have studied in a 2+1 ideal hydrodynamics the effect of initial fluctuations on bottomonia production in relativistic heavy-ion collisions [4]. We find that while initial fluctuations hardly affect the yield of the 1S ground state bottomonium, their effect on other bottomonium states gradually increases with their excitation energies, as shown in the left window of Fig.1. Compared to the case with smooth initial conditions, the survival probabilities of excited bottomonium states are reduced at low transverse momentum in the case of large initial fluctuations, and this effect is more prominent if the bottomonia are produced earlier in heavy-ion collisions. Since the initial fluctuations are smoothed out quickly with time, bottomonia that take long time to form are little affected by the fluctuations. Presently, the formation times of bottomonia are not well determined. We have used the value of 1.8 fm/c for the 1S state and of 2.3 fm/c for the excited states of bottonomia from fitting the experimental data on their nuclear modification factors. In this case, the effect of initial fluctuations on the nuclear modification factor of bottomonia 1S and 2S states is, however, small as shown in the right window of Fig. 1.

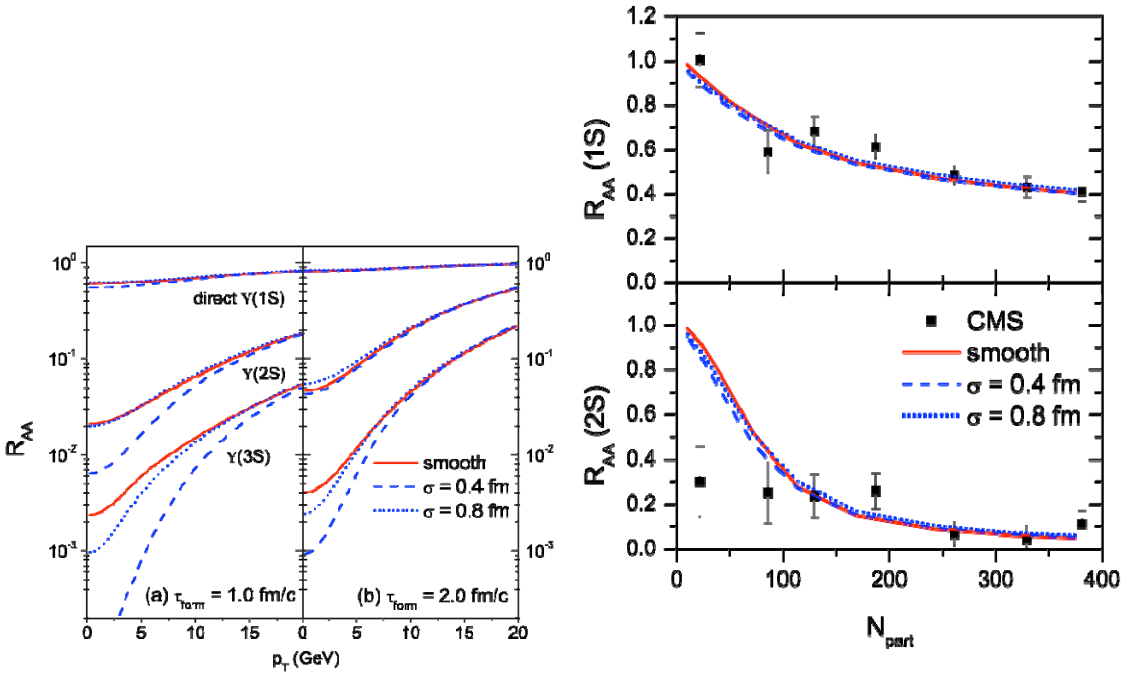

FIG. 1. Left wiondow: Nuclear modification factor R_{AA} of 1S (upper lines), 2S (middle lines), and 3S (lower lines) bottomonium states as functions of transverse momentum for smooth initial conditions (solid lines) and fluctuating initial conditions with smearing parameter σ = 0.4 fm (dashed lines) and 0.8 fm (dotted lines) in minimum-bias Pb+Pb collisions= 2.76 TeV. Panels (a) and (b) correspond to formation times of bottomonia 1.0 and 2.0 fm/c, respectively. Right window: Same as functions of participant number but with the formation times of 1S state and excited states taken to be 1.8 and 2.3 fm/c, respectively. Experimental data are taken from Ref.[5].

[1] F. Karsch, M.T. Mehr, and H. Satz, Z. Phys. C **37**, 617 (1988).
[2] T. Song and S.H. Lee, Phys. Rev. D **72**, 034002 (2005).
[3] Y. Park, K.I. Kim, T. Song, S.H. Lee, and C.Y. Wong, Phys. Rev. C **76**, 044907 (2007).
[4] T. Song, K.C. Han, and C.M. Ko, Nucl. Phys. A **897**, 141 (2013).
[5] S. Chatrchyan et al. [CMS Collaboration], arXiv:1208.2826 [nucl-ex].

Subthreshold cascade production in heavy ion collisions

L. Feng, L.W. Chen,[1] C.M. Ko, and S.H. Lee[2]

[1]*INPAC, Department of Physics and Shanghai Key Laboratory for Particle Physics and Cosmology, Shanghai Jiao Tong University, Shanghai 200240, China*

[2]*Institute of Physics and Applied Physics, Yonsei University, Seoul 120-749, Korea*

We have calculated the cross sections for the reaction YY→NΞ (Y = Λ, Σ) based on a gauged SU(3)-invariant hadronic Lagrangian in the Born approximation [1] and found that these cross sections are almost four times the cross sections for the reaction KY→πΞ that was considered in a previous study [2]. We then used these cross sections to study Ξ production in ^{40}Ar+KCl collisions at the subthreshold energy of 1.76 AGeV within the framework of a relativistic transport model that includes explicitly the nucleon, delta, pion, and perturbatively the kaon, antikaon, hyperons, and Ξ [3]. We found that the reaction YY→NΞ would enhance the abundance by a factor of about 16 compared to that from the reaction KY→ πΞ, resulting in an abundance ratio $\Xi^-/(\Lambda+\Sigma^0) = 3.38 \times 10^{-3}$ that is essentially consistent with that measured by the HADES Collaboration at GSI [4]. Our study has thus helped in resolving one of the puzzles in particle production from heavy ion collisions at subthreshold energies.

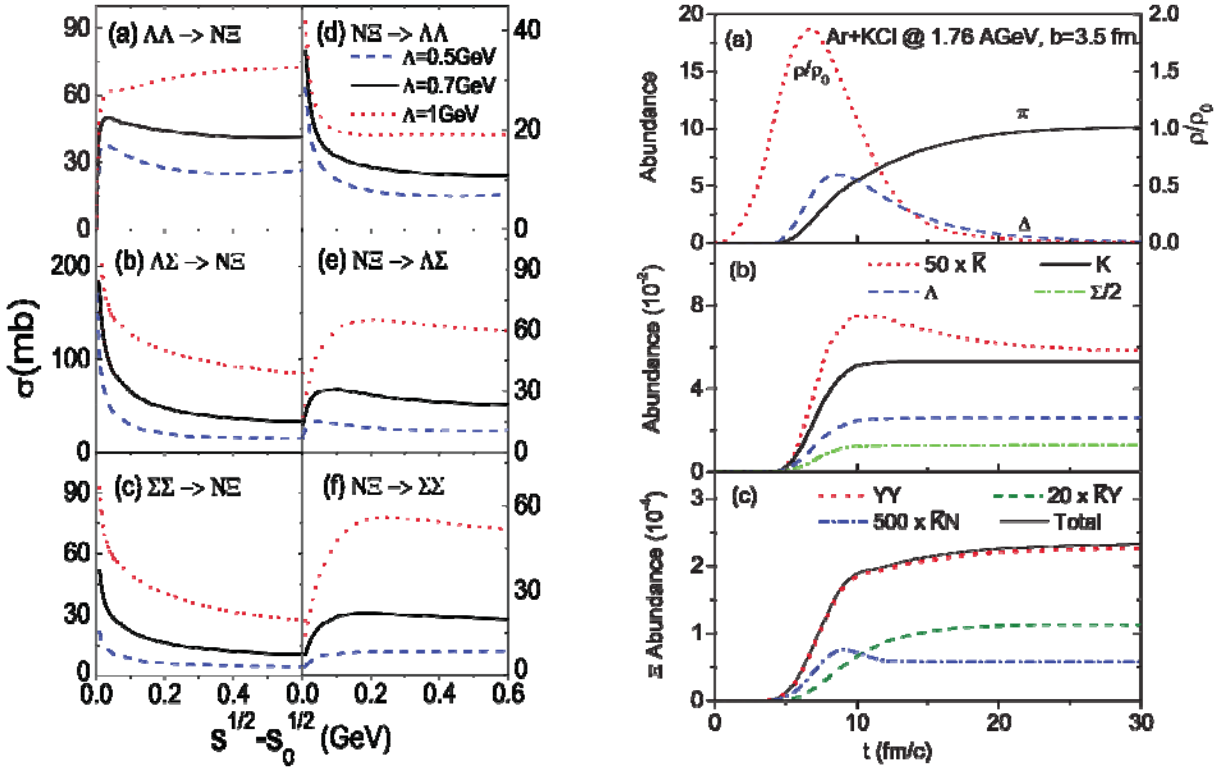

FIG. 1. Left window: Cross sections for (a) ΛΛ→NΞ, (b)ΛΣ→NΞ, (c)ΣΣ→NΞ, (d) NΞ→ΛΛ, (e) NΞ→ΛΣ, and (f) NΞ→ΣΣ as functions of the center-of-mass energy from the Born approximation with cutoff parameters Λ = 0.5 GeV (dashed lines), Λ = 0.7 GeV (solid lines), and Λ = 1 GeV (dotted lines). Right window: Time evolutions of (a) central baryon density (right scale) and the abundances (left scales) of π and Δ, (b) K, Λ, Σ, and antikaon, and (c) Ξ produced from different reactions.

[1] F. Li, L.W. Chen, C.M. Ko, and S. H. Lee, Phys. Rev. C **85**, 064902 (2012).
[2] C.H. Li and C.M. Ko Nucl. Phys. **A712**, 110 (2002).
[3] C.M. Ko and G.Q. Li, J. Phys. G **22**, 1673 (1996).
[4] N. Kaiser and W. Weise, Phys. Lett. B **512**, 283 (2001).

Charmonium production from nonequilibrium charm and anticharm quarks in Quark –gluon plasma

T. Song, K. C. Han and C. M. Ko

Using the transition amplitudes for J/ψ production from charm and anticharm quarks calculated up to NLO in pQCD [1,2] and including the medium effect on the J/ψ wave function and binding energy from a screened Cornell potential between charm and anticharm quarks in QGP [3], we have studied J/ψ production in QGP from nonequilibrium charm and anticharm quarks [4] that are described by the Tallis distribution [5]. We have found that nonequilibrium charm and anticharm quarks suppress the production rate of J/ψ in QGP, compared to the rate from completely thermalized charm and anticharm quarks as shown in the left window of Fig. 1. We have further used the calculated J/ψ production rate in QGP to study J/ψ production in heavy-ion collisions at the RHIC and LHC by using the PHYTIA simulation to obtain the initial charm and anticharm quark distributions and then follow their elastic scattering with light quarks and antiquarks as well as gluons in QGP via the cascade simulation. With the resulting charm and anticharm quark distributions parameterized by the Tsallis distribution, we have found that the suppression in the J/ψ production rate is stronger in higher energy collisions and at higher temperatures, although their time dependence is similar in all cases as shown in the right window of Fig.1. We have also compared our results to those in the literature obtained with the relaxation factor correction using the charm quark relaxation time and found that the latter is similar to our results as shown by the solid line in the right window of Fig.1.

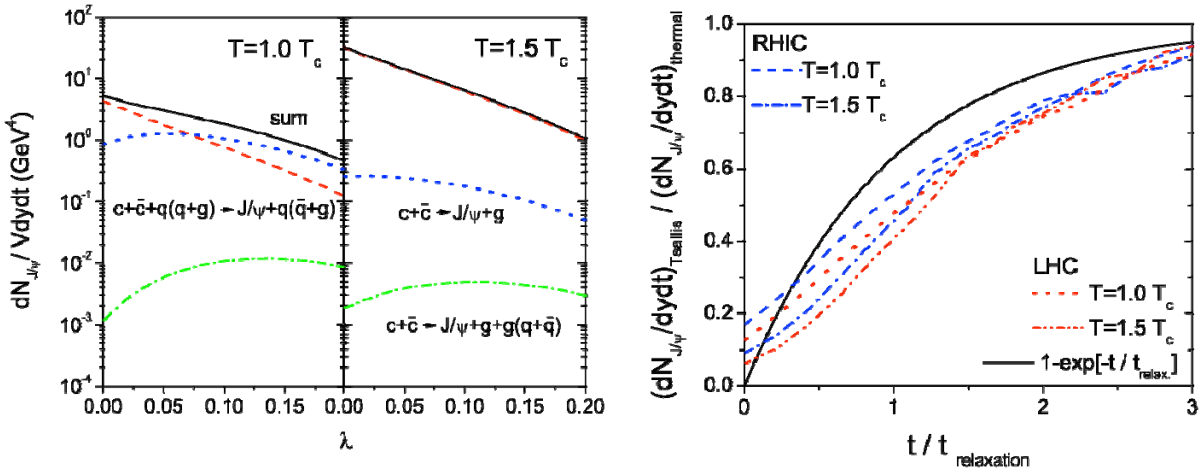

FIG. 1. Left window: Production rate of J/ψ per unit rapidity in QGP at temperatures T = 1.0 (left panel) and 1.5 T_c (right panel) as a function of λ (λ=0 corresponds to a thermally equilibrated distribution) from charm and anticharm quarks that have a Tsallis distribution. Right window: Time dependence of the ratio of the J/ψ production rate from nonequilibrium charm and anticharm quarks to that from completely thermalized charm and anticharm quarks in QGP at T= 1.0 and 1.5 T_c. The solid line is the result based on the relaxation factor correction.

[1] T. Song and S.H. Lee, Phys. Rev. D **72**, 034002 (2005).
[2] Y. Park, K.I. Kim, T. song, S.H. Lee, and C.Y. Wong, Phys. Rev. C **76**, 044907 (2007).
[3] F. Karsch, M.T. Mehr, and H. Satz, Z. Phys. C **37**, 617 (1988).
[4] T. Song, K.C. Han, and C.M. Ko, Phys. Rev. C **85**, 054905 (2012).
[5] C. Tsallis, J. Stat. Phys. **52**, 479 (1988).

Heavy quark potential at finite temperature

S.H. Lee,[1] K. Morita,[2] T. Song, and C. M. Ko

[1]*Institute of Physics and Applied Physics, Yonsei University, Seoul 120-749, Korea*

[2]*Yukawa Institute for Theoretical Physics, Kyoto University, Kyoto 606-8502, Japan*

Using the QCD sum rule with its operator product expansion reliably estimated from lattice calculations for the pressure and energy density of hot QCD matter [1], we have calculated the strength of the J/ψ wave function at origin [2] and find that it decreases with temperature when the temperature is above the transition temperature as shown in Fig.1. This result is seen to follow exactly that obtained from the solution of the Schroedingier equation for a charm and anticharm quark pair using the free energy from lattice calculations as the potential and is in sharp contrast to that using the deeper potential associated with the internal energy, which shows an enhanced strength of the J/ψ wave function at origin. Our result thus has resolved the long-standing question of whether the free energy potential or the internal energy potential should be used in analyzing the spectrum of heavy quark systems at finite temperature.

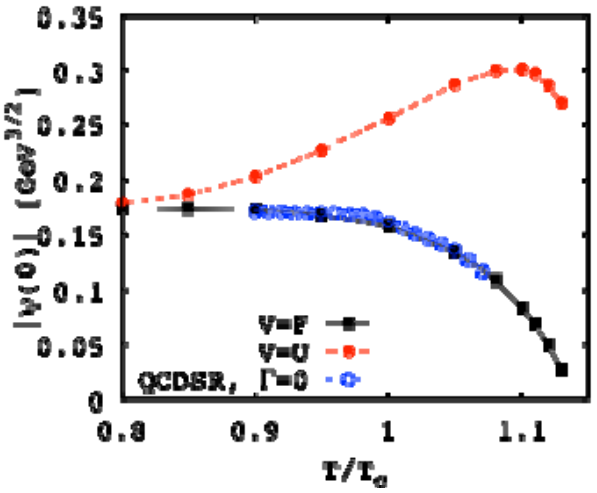

FIG. 1. Temperature dependence of |ψ(0)| obtained from the free energy (filled squares) and internal energy (filled circles) potentials together with that from the QCD sum rule (open circles).

[1] K. Morita and S. H. Lee, Phys. Rev. D **82**, 054008 (2010); Phys. Rev. C **85**, 044914 (2012).

[2] S.H. Lee, K. Morta, T. Song, and C.M. Ko, Phys. Rev. Lett. (submitted).

Dilepton production in heavy ion collisions at LHC

O. Linnyk,[1] W. Cassing,[1] J. Manninen,[2,3] E.L. Bratkovskaya,[2,3] P.B. Gossiaux,[4]
J. Aichelin,[4] T. Song, and C.M. Ko

[1]*Institut fur Theoretische Physik, Universitat Giessen, DE-35392 Giessen, Germany*

[2]*Institut fur Theoretische Physik, Johann Wolfgang Goethe University, Frankfurt am Main, Germany*

[3]*Frankfurt Institute for Advanced Studies, DE-60438 Frankfurt am Main, Germany*

[4]*Laboratoire de Physique Subatomique et des Technologies Associees, University of Nantes, 44072 Nantes Cedex 03, France*

We have studied dielectron pair production in proton-proton and central Pb+Pb collisions at $s_N^{1/2}$ = 2.76 TeV within two models [1]: an extended statistical hadronization model [2] and the Parton-Hadron-String Dynamics (PHSD) transport approach [3]. We find that the PHSD calculations roughly agree with the dilepton spectrum from hadronic sources with the cocktail estimates from the statistical hadronization model matched to available data at LHC energies. The dynamical simulations within the PHSD show a moderate increase of the low mass dilepton yield essentially due to the in-medium modification of the rho-meson. Furthermore, pronounced traces of the partonic degrees of freedom are found in the PHSD results in the intermediate mass regime. The dilepton production from the strongly interacting quark-gluon plasma (sQGP) exceeds that from the semi-leptonic decays of open charm and bottom mesons. Additionally, we have observed that a transverse momentum cut of 1 GeV/c further suppresses the relative contribution of the heavy meson decays to the dilepton yield, such that the sQGP radiation strongly dominates the spectrum for masses from 1 to 3 GeV, allowing a closer look at the electromagnetic emissivity of the partonic plasma in the early phase of Pb+Pb collisions.

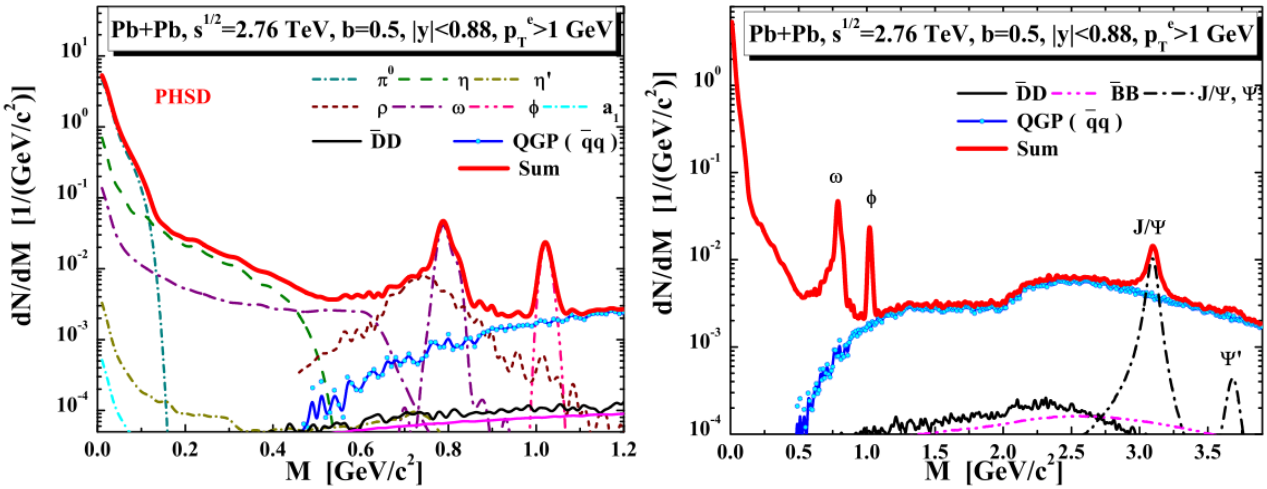

FIG. 1. Left window: Dielectron low invariant mass spectrum from different sources evaluated for the central Pb+Pb collisions at $s_{NN}^{1/2}$ = 2.76 TeV within the PHSD approach including vacuum spectral functions for the vector mesons with the transverse momentum cut p_T > 1 GeV on the single electron. Right window: Same for dielectron masses up to 4 GeV.

[1] O. Lynnk, W. Cassing, J. Manninen, E.L. Bratkovskaya, P.B. Gossiaux, J. Aichelin, T. Song, and C.M. Ko, Phys. Rev. C **87**, 014905 (2013).
[2] J. Manninen, E.L. Bratkovskaya, W. Cassing, and O. Linnyk, Eur. Phys. J. C **71**, 1615 (2011).
[3] W. Cassing and E. L. Bratkovskaya, Nucl. Phys. **A831**, 215 (2009).

Quarkonium formation time in quark-gluon plasma

T. Song, C. M. Ko, and S. H. Lee[1]

[1]*Institute of Physics and Applied Physics, Yonsei University, Seoul 120-749, Korea*

We have studied [1] the quarkonium formation time in QGP by using the approach based on the space-time correlator of heavy quark vector currents [2] . The imaginary part of the resulting heavy quark pair polarization function, which is the spectral function of heavy quark pair in $e^+ + e^-$ annihilation, is constructed by solving the Schroedinger equation with the heavy quark potential extracted from lattice calculations. The real part of the polarization function, which is related to its imaginary part by the dispersion relation, then provides the information on how different states of the heavy quark pair evolve with time. Using bottomonia as examples, we have found that the average formation time of a quarkonium from a heavy quark-antiquark pair increases with temperature and diverges near the dissociation temperature of the quarkonium as shown in the left window of Fig.1. Furthermore, the quarkonium formation time is longer if the heavy quark potential is taken to be their free energy instead of their internal energy from the lattice calculations. We have also found that the average relative velocity between the heavy quark pair before they form the quarkonium, calculated via the ratio of the mean distance between the heavy quark and antiquark in a quarkonium to its formation time, decreases with increasing temperature as shown in the right window of Fig.2. Surprisingly, the one obtained from the free energy potential is found to agree with the temperature dependence of the QCD coupling constant (scaled by 1.1) at the screening distance between heavy quark and antiquark pair extracted from the lattice free energy [3].

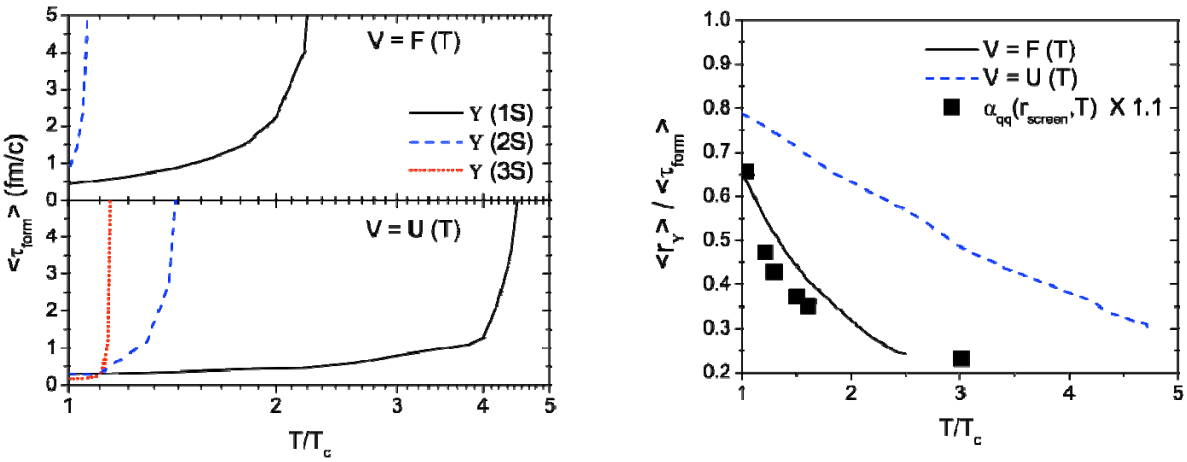

FIG. 1. Left window: Average formation times of Υ(1S), Υ(2S), and Υ(3S) as functions of temperature for the cases of free energy (upper) and internal energy (lower) potentials. Right window: Ratio of the mean distance between bottom quark and antibottom quark in Υ(1S) to its formation time as a function of temperature for the cases of free energy (solid line) and internal energy (dashed line) potentials. Solid squares are the temperature dependence of the QCD coupling constant (scaled by 1.1) at the screening distance between heavy quark and antiquark pair extracted from the lattice free energy [3].

[1] T. Song, C.M. Ko, and S.H. Lee, Phys. Rev. C **87**, 034910 (2013).
[2] D. Kharzeev and R.L. Thews, Phys. Rev. C **60**, 041901 (1999).
[3] O.Kaczmarek, F. Karsch, F. Zantow, and P. Petreczky, Phys. Rev. D **70**, 074505 (2004).

Jet fragmentaton via recombination of parton showers

K. C. Han, R. J. Fries, and C. M. Ko

We have studied [1] hadron production in jets by applying quark recombination [2,3,4] to jet shower partons. With the jet showers obtained from PYTHIA [5] and augmented by additional non-perturbative effects, we have computed hadron spectra in $e^+ + e^-$ collisions at $s^{1/2}$ = 200 GeV. Including contributions from resonance decays, we find that the resulting transverse momentum spectra for pions, kaons, and protons reproduce reasonably those from the string fragmentation as implemented in PYTHIA as shown in Fig.1. Our study thus indicates that hadron production from jets can be described by the recombination of shower partons inside the jets. In the presence of a quark-gluon plasma (QGP), our approach then provides a promising framework to study the medium modification of fragmentation functions by allowing shower partons to recombine with the thermal partons in the QGP.

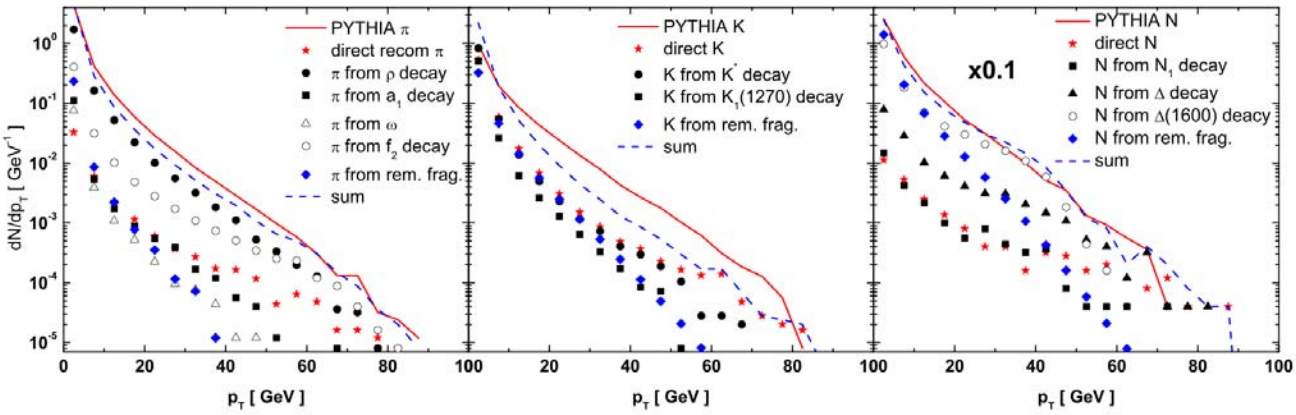

FIG. 1. Transverse momentum spectra of pions (left panel), kaons (middle panel), and nucleons (right panel) from the recombination of jet shower partons (dashed lines) and from the string fragmentation as implemented in PYTHIA (solid lines).

[1] K.C. Han, R. Fries, and C.M. Ko, Jour. Phys. Conf. Series **420**, 012044 (1213).

[2] R.J. Fries, B. Muller, C. Nonaka, and S. Bass, Phys. Rev. Lett. **90**, 202303 (2003).

[3] V. Greco, C.M. Ko, and P. Levai, Phys. Rev. Lett. **90**, 202302 (2003).

[4] R.C. Hwa and C.B. Yang, Phys. Rev. C **70**, 024904 (2004).

[5] T. Sjostrand, S. Mrenna, and P.Z. Skands, J. High Energy Phys. **0605**, 026 (2006).

Partonic mean-field effects on matter and antimatter elliptic flow

T. Song, S. Plumari,[1] V Greco,[1] C. M. Ko, and F. Li
[1]*Dipartimento di Fisica e Astronomia, Universit?di Catania, Via S. Sofia 64, 95125 Catania, Italy*

We have studied [1] the effect of partonic mean fields on the elliptic flows of quarks and antiquarks in a brayon-rich quark matter by using a transport model based on the NJL model [2]. For the scalar mean field, which is attractive for both quarks and antiquarks, it leads to a similar reduction of the quark and antiquark elliptic flow as first found in Ref.[3]. The vector mean field, on the other hand, has very different effects on quarks and antiquarks in the baryon-rich quark matter as it is repulsive for quarks and attractive for antiquarks. Using the quark coalescence model, we have further studied the elliptic flows of p, Λ, and K^+ and their antiparticles produced from the baryon-rich quark matter and found that the differences between particle and antiparticle elliptic flows are appreciable as a result of the different quark and antiquark elliptic flows. The magnitude of the relative integrated elliptic flow difference between particles and their antiparticles depends on the strength of the vector coupling, and this is shown in Fig.1. For the small vector coupling of g_v/G=1/6, the elliptic flow differences between p and anti-p, Λ and anti-Λ, and K^+ and K^- are about 49, 48, and 9%, respectively, which are about a factor of 1.5, 2.5, and 1/3 of corresponding values due to the effect of hadronic potentials given in Ref.[4]. If the effects of partonic and hadronic mean-field potentials were additive, then the final relative elliptic flow differences between p and anti-p, Λ and anti-Λ, and K^+ and K^- would be close to those measured in the BES experiments at RHIC [5,6]. Although a more quantitative study is needed before a definitive

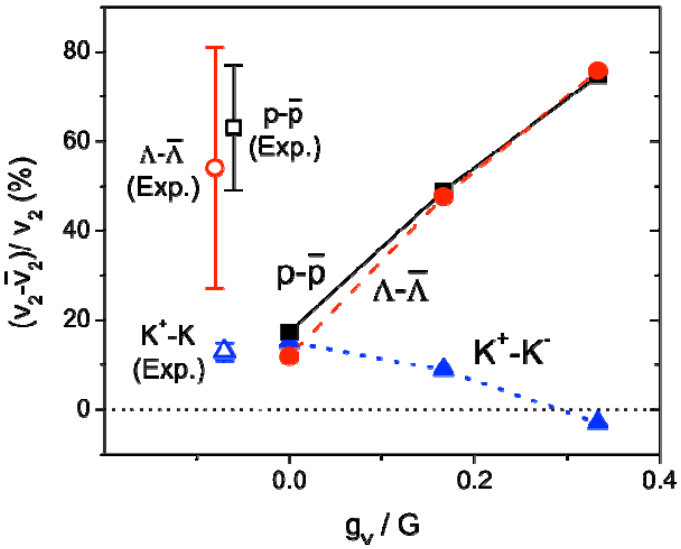

FIG. 1. Relative differences between integrated elliptic flows of mid-rapidity (|y|<1) p and anti-p (solid squares), Λ and anti-Λ (solid circles), and K^+ and K^- (solid triangles) at hadronization for several values of the isoscalar vector coupling.

determination of the strength of vector interactions in the baryon-rich QGP can be achieved, the upper bound inferred from the present study for the value of the vector coupling already has an important implication on the equation of state of baryon-rich quark-gluon plasma.

[1] T. Song, S. Plumari, V. Greco, C.M. Ko, and F. Li, Phys. Lett. B (submitted).
[2] Y. Nambu and G. Jona-Lasinio, Phys. Rev. **122**, 345 (1961); **124**, 246 (1961).
[3] S. Plumari, V. Baran, M. Di Toro, G. Feini, and V. Greco, Phys. Lett. B **689**, 18 (2010).
[4] J. Xu, L.W. Chen, C.M. Ko, and Z.W. Lin, Phys. Rev. C **85**, 041901 (2012).
[5] L. Kumar [STAR Collaboration], J. Phys. G **38**, 124145 (2011).
[6] B. Mohanty [STAR Collaboration], J. Phys. G **38**, 124023 (2011).

Energy dependence of pion in-medium effects on π^+/π^- ratio in heavy-ion collisions

J. Xu,[1] L. W. Chen,[2] C. M. Ko, B. A. Li,[3] and Y. G. Ma[1]

[1]*Shanghai Institute of Applied Physics, Chinese Academy of Sciences, Shanghai 201800, China*
[2]*NPAC, Department of Physics and Shanghai Key Laboratory for Particle Physics and Cosmology, Shanghai Jiao Tong University, Shanghai 200240, China*
[3]*Department of Physics and Astronomy, Texas A&M University-Commerce, Commerce, TX 75429-3011,*

Within the framework of a thermal model [1] with its parameters fitted to the results from an isospin-dependent Boltzmann-Uehling-Uhlenbeck (IBUU) transport model [2], we have studied the pion in-medium effect on the charged-pion ratio in heavy-ion collisions at various energies [3]. We find that due to the cancellation between the effects from pion-nucleon s-wave [4] and p-wave [5] interactions in nuclear medium, the π^+/π^- ratio generally decreases after including the pion in-medium effect as shown in Fig.1. The effect is larger at lower collision energies as a result of narrower pion spectral functions at lower temperatures.

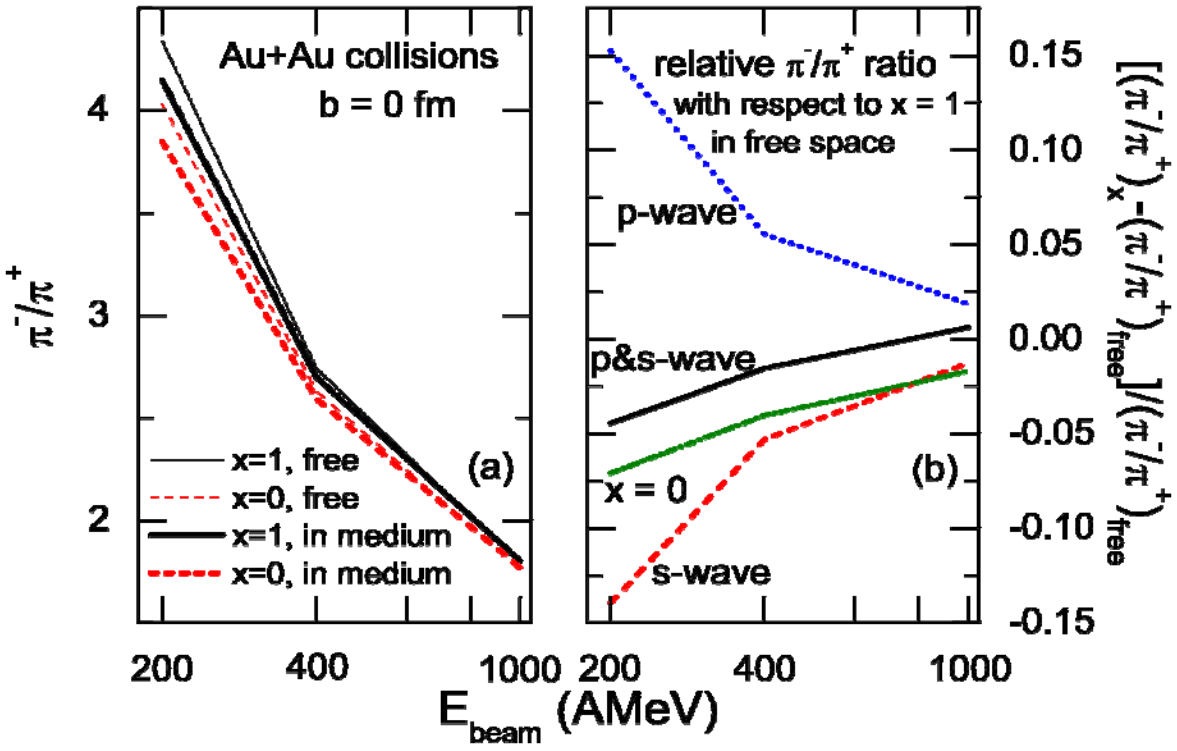

FIG. 1. Left panel: π^+/π^- ratios with and without pion in-medium effects from the thermal model calculation corresponding to central Au+Au collisions at different beam energies; Right panel: Relative π^+/π^- ratios from pion-nucleon s-wave interaction, p-wave interaction, both p-wave and s-wave interactions, and x=0 (stiffer symmetry energy) with respect to that from x=1 (softer symmetry energy) in free space at different collision energies.

[1] J. Xu, C.M. Ko, and Y. Oh, Phys. Rev. C **81**, 024910 (2010).

[2] C.B. Das, S. Das Gupta, C. Gale, and B.A. Li, Phys. Rev. C **67**, 034611 (2003).

[3] J. Xu, L.W. Chen, C.M. Ko, B.A. Li, and Y. G. Ma, Phys. Rev. C (submitted).

[4] N. Kaiser and W. Weise, Phys. Lett. B **512**, 283 (2001).
[5] G. E. Brown and W. Weise, Phys. Rep. **22**, 279 (1975); E. Oset, H. Toki, and W. Weise, Phys. Rep. **83**, 281 (1982); C. L. Korpa, M. F. M. Lutz, and F. Riek, Phys. Rev. C **80**, 024901 (2009).

Effects of initial fluctuations on jet-energy loss

H. Zhang,[1] T. Song, and C. M. Ko

[1]*Institute of Particle Physics and Key Laboratory of quark & Lepton Physics, Central China Normal University, Wuhan, 430079, China*

Based on the 2+1 dimension ideal hydrodynamics, we have studied the effect of initial fluctuations on jet energy loss in relativistic heavy-ion collisions within the description of the NLO perturbative QCD [1]. Our results show that fluctuating initial conditions lead to slightly more energy loss than smooth initial conditions as shown in Fig.1. A detailed analysis indicates that this is mainly due to the positive correlation between the fluctuation in the production probability of parton jets from initial nucleon-nucleon hard collisions and the fluctuation in the medium density along the path traversed by the jet. This effect is larger in non-central than in central relativistic heavy ion collisions and also for jet energy loss that has a linear ($\alpha = 1$) than a quadratic ($\alpha = 2$) dependence on its path length in the medium. Our results are opposite to those found in Ref.[2] for a static medium and also those in Ref.[3] using a 2+1 ideal hydrodynamics and with the jet energy loss depending on the local energy density, which show a reduced jet energy loss in the QGP for the fluctuating initial conditions.

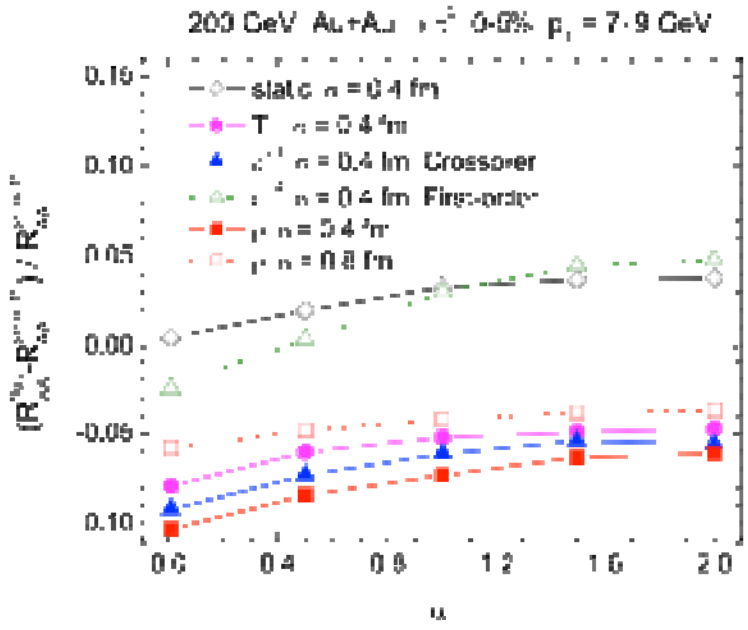

FIG. 1. Relative difference between the nuclear modification factors of p_T = 7-9 GeV hadrons as a function of the path-length dependence parameter α for different medium dependence in central Au+Au collisions.

[1] H. Zhang, T. Song, and C.M. Ko, Phys. Rev. C (in press).
[2] R. Rodriguez, R.J. Fries, and E. Ramirez, Phys. Lett. B **693**, 108 (2010).
[3] T. Renk, H. Jolopainen, J. Auvinen, and K.J. Eskola, Phys. Rev. C **85**, 044915 (2012).

Isoscalar and isovector giant resonances in ^{208}Pb

M. R. Anders and S. Shlomo

The study of collective modes in nuclei has been the subject of extensive theoretical and experimental studies during several decades, since it contributes significantly to our understanding of bulk properties of nuclei, their non-equilibrium properties and properties of the nuclear force. Very recently, a thorough study of isoscalar and isovector giant resonances of the doubly magic nuclei, ^{40}Ca and ^{48}Ca, for multipolarities: L=0-3 was conducted [1]. This work determined the sensitivities of E_{CEN} and of the isotopic differences $E_{CEN}(^{48}Ca) - E_{CEN}(^{40}Ca)$ to physical quantities, such as nuclear matter incompressibility coefficient, symmetry energy density, and effective mass, associated with the Skyrme interactions and compared the results with the available experimental data.

In this work we extend this theoretical investigation by considering the isoscalar and isovector giant resonances of multipolarities $L = 0 - 3$ of the doubly magic nucleus ^{208}Pb. For this purpose, we have carried out [2] fully self-consistent Hartree-Fock (HF) based RPA calculations of these giant resonances, for ^{208}Pb, using a wide range of 34 commonly employed Skyrme type interactions. These interactions, which were fitted to ground state properties of nuclei are associated with a wide range of nuclear matter properties such as incompressibility coefficient K_{NM} = 200 - 258 MeV, symmetry energy J = 27 - 37 MeV and effective mass m* = 0.56 - 1.00. We investigate the sensitivities of E_{CEN} to physical quantities, such K_{NM}, J and the symmetry energy density and effective mass, associated with the effective nucleon-nucleon interactions and compare the results with available experimental data. As examples we present below results of our calculations [2] for the isoscalar giant monopole resonance (ISGMR) and the

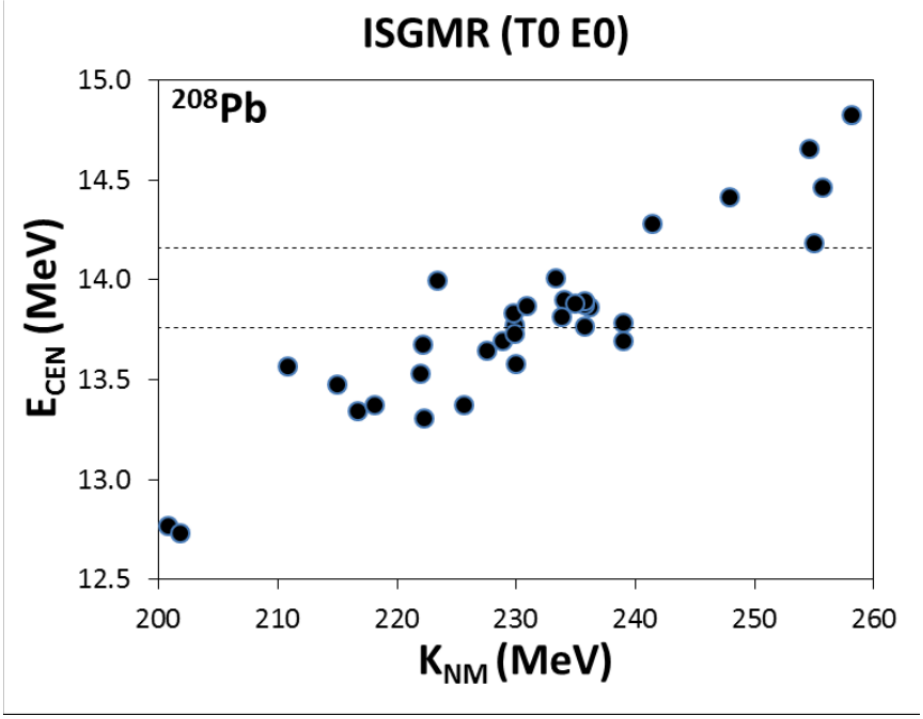

FIG. 1. ISGMR centroid energies vs K_{NM}.

isovector giant dipole resonance (IVGDR).

In Fig. 1. we compare the experimental data of the ISGMR centroid energies E_{CEN} of ^{208}Pb, shown as the regions between the dashed lines, with the results of fully self consistent HF based RPA calculations (full circles), using the Skyrme type interactions having nuclear matter incompressibility coefficients K_{NM} = 200-258. The energies shown were calculated over the experimental excitation energy range of 5 - 30 MeV. A clear correlation between E_{CEN} of ^{208}Pb can be seen with K_{NM}.

In Fig. 2, we show our results for the centroid energies of the IVGDR in ^{208}Pb as a function of J, the symmetry energy at saturation density ρ_0. An agreement with experimental data is obtained for several interactions. However, only weak correlation is obtained between the centroid energy J and E_{CEN}.

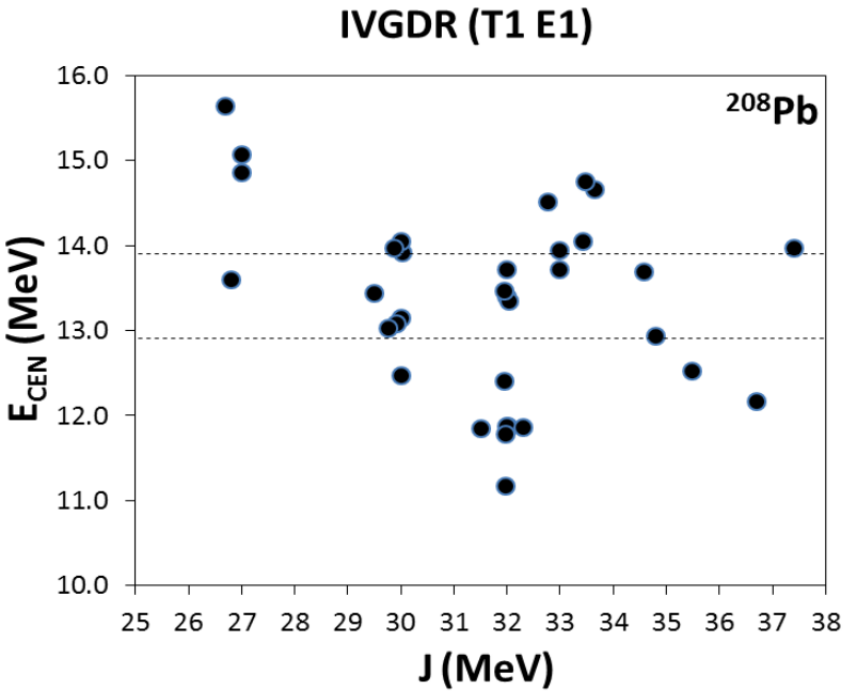

FIG. 2. Centroid energies of the IVGDR as a function J.

[1] M.R. Anders, S. Shlomo, Tapas Sil, D.H. Youngblood, Y.-W. Lui, and Krishichayan, Phys. Rev. C. **87**, 024303 (2013).

[2] M.R. Anders *et al.*, in preparation.

Correlations among nuclear matter properties of Skyrme interactions

M. R. Anders and S. Shlomo

Density Functional Theory is a powerful tool for the study of many body systems. The main challenge is to find the form of the energy density functional (EDF). The development of a modern and more realistic nuclear energy density functional (EDF) for accurate predictions of properties of nuclei is the subject of enhanced activity, since it is very important for the study of properties of rare nuclei with unusual neutron-to-proton ratios that are difficult to produce experimentally and likely to exhibit interesting new phenomena associated with isospin, clusterization and the continuum. In our work we consider the EDF associated with the Skyrme type effective nucleon-nucleon interaction. Adopting the standard parametrization of the Skyrme type interactions, it is common to determine the parameters of the EDF within the Hartree-Fock (HF) mean-field approximation by carrying out a fit to an extensive set of data on; (i) binding energies, (ii) single-particle energies, and (iii) charge root-mean-square (rms) radii. This approach has resulted with over 200 EDFs associated with the Skyrme type effective nucleon-nucleon interaction.

To better determine the values of the Skyrme parameters we include constraints on the values of nuclear matter (NM) properties, such as the incompressibility coefficient, symmetry energy density and nucleon effective mass. To determine the values of the NM properties, we have investigated the sensitivities of the centroid energies E_{CEN} of the isoscalar and isovector giant resonances of multipolarities $L = 0 - 3$ in ^{208}Pb to values of the NM properties. To obtain better insight into the effects of the constraint associated with properties of NM on the resulting EDF, we investigate [1] the correlations among the properties of NM, using a wide range of 34 commonly employed Skyrme type interactions. These interactions, which were fitted to ground state properties of nuclei are associated with a wide range of nuclear matter properties such as incompressibility coefficient K_{NM} = 200 - 258 MeV, symmetry energy J = 27 - 37 MeV and effective mass m* = 0.56 - 1.00. We consider the NM quantities: the effective mass m*; the incompressibility coefficient $K = 9\rho_0^2 \frac{d^2(E/A)}{d\rho^2}\Big|_{\rho_0}$; the skewness coefficient which is proportional to the third derivative $Q = 27\rho_0^3 \frac{d^3(E/A)}{d\rho^3}\Big|_{\rho_0}$; the symmetry energy coefficient $J = E_{sym}(\rho_0)$; the symmetry energy at 0.1 fm^{-3}, $J(0.1) = E_{sym}(0.1)$ the coefficient proportional to the slope, $L = 3\rho_0 \frac{d(E_{sym})}{d\rho}\Big|_{\rho_0}$, and the curvature $K_{sym} = 9\rho_0^2 \frac{d^2(E_{sym})}{d\rho^2}\Big|_{\rho_0}$ of the density dependence of the symmetry energy, respectively, κ, the enhancement factor of the energy weighted sum rule for the IVGDR, and the strength of the spin-orbit interaction W_0.

In Table I we present the Pearson Correlation Coefficients between the values of NM properties. Note the strong correlation between K and Q and between Q and m*/m, but the weak correlation between K and m*/m. J and L also have a fairly strong correlation while L and K_{sym} have a very strong correlation, and J and K_{sym} have a medium correlation. There are also medium correlations between J(0.1) and K_{sym}, m*/m and κ, and K and K_{sym}.

Table I. Pearson's correlation coefficient between NM properties.

	K	K' = -Q	J	L	K_{sym}	m*/m	J(0.1)	κ	W_0
K	1.00	-0.78	0.10	0.36	0.53	-0.39	-0.17	-0.10	0.12
K' = -Q	-0.78	1.00	0.01	-0.36	-0.63	0.83	0.36	-0.35	-0.13
J	0.10	0.01	1.00	0.72	0.45	0.03	0.36	-0.20	-0.10
L	0.36	-0.36	0.72	1.00	0.90	-0.19	-0.35	-0.11	0.22
K_{sym}	0.53	-0.63	0.45	0.90	1.00	-0.46	-0.52	-0.07	0.33
m*/m	-0.39	0.83	0.03	-0.19	-0.46	1.00	0.19	-0.59	-0.10
J(0.1)	-0.17	0.36	0.36	-0.35	-0.52	0.19	1.00	-0.18	-0.36
κ	-0.10	-0.35	-0.20	-0.11	-0.07	-0.59	-0.18	1.00	-0.18
W_0	0.12	-0.13	-0.10	0.22	0.33	-0.10	-0.36	-0.18	1.00

[1] M.R. Anders *et al.*, in preparation.

Giant resonances in ^{208}Pb and the nuclear matter equation of state

M. R. Anders and S. Shlomo

The equation of state (EOS) of nuclear Matter (NM) is an important ingredient in the study of properties of nuclei at and away from stability, the study of structure and evolution of compact astrophysical objects, such as neutron stars and core-collapse supernovae, and the study of heavy-ion collisions (HIC). In the vicinity of the saturation density ρ_0 of symmetric NM, the EOS can be approximated by

$$E_0[\rho] = E[\rho_0] + \frac{1}{18} K_{NM} \left(\frac{\rho-\rho_0}{\rho_0}\right)^2, \quad (1)$$

where $E_0[\rho]$ is the binding energy per nucleon and K_{NM} is the incompressibility coefficient which is directly related to the curvature of the EOS, $K_{NM} = 9\rho_0^2 \left.\frac{\partial^2 E_0}{\partial \rho^2}\right|_{\rho_0}$. Similarly, the EOS of asymmetric NM, with proton density ρ_p and neutron density ρ_n, can be approximated by

$$E[\rho_p, \rho_n] = E_0[\rho] + E_{sym}[\rho] \left(\frac{\rho_n-\rho_p}{\rho}\right)^2, \quad (2)$$

where $E_{sym}[\rho]$ is the symmetry energy at matter density ρ, approximated as

$$E_{sym}[\rho] = J + \frac{1}{3} L \left(\frac{\rho-\rho_0}{\rho_0}\right) + \frac{1}{18} K_{sym} \left(\frac{\rho-\rho_0}{\rho_0}\right)^2, \quad (3)$$

where $J = E_{sym}[\rho_0]$ is the symmetry energy at saturation density ρ_0, , and $L = 3\rho_0 \left.\frac{\partial E_{sym}}{\partial \rho}\right|_{\rho_0}$, and $K_{sym} = 9\rho_0 \left.\frac{\partial^2 E_{sym}}{\partial \rho^2}\right|_{\rho_0}$.

The saturation point of the equation of state (EOS) for symmetric (*N*=*Z*) nuclear matter (NM) is well determined from the measured binding energies and central matter densities of nuclei, by extrapolation to infinite NM. To extend our knowledge of the EOS beyond the saturation point of symmetric NM, an accurate value of the NM incompressibility coefficient K_{NM}, which is directly related to the curvature of the EOS of symmetric NM, is needed. An accurate knowledge of the dependence of the symmetry energy, $E_{sym}(\rho)$, on the matter density ρ is needed for the EOS of asymmetric NM.

There have been many attempts over the years to determine K_{NM} and $E_{sym}(\rho)$ by considering physical quantities which are sensitive to the values of K_{NM} and $E_{sym}(\rho)$. In this work we investigate the sensitivity of the strength function distributions of the isoscalar (T=0) and isovector (T=1) giant resonances with multipolarities L = 0-3 of ^{208}Pb to bulk properties of NM, such as K_{NM}, E_{sym} and the effective mass m*. For this purpose, we have carried out fully self-consistent Hartree-Fock (HF) based RPA calculations of the strength functions of these resonances, for ^{208}Pb, using a wide range of 34

commonly employed Skyrme type interactions. These interactions, which were fitted to ground state properties of nuclei are associated with a wide range of nuclear matter properties such as incompressibility coefficient K_{NM} = 200 - 258 MeV, symmetry energy J = 27 - 37 MeV and effective mass m* = 0.56 - 1.00. We investigate the sensitivity of E_{CEN} to physical quantities of nuclear matter (NM), such as the effective mass m*; the incompressibility coefficient $K_{NM} = 9\rho_0^2 \frac{d^2(E/A)}{d\rho^2}\Big|_{\rho_0}$; the skewness coefficient which is proportional to the third derivative $Q = 27\rho_0^3 \frac{d^3(E/A)}{d\rho^3}\Big|_{\rho_0}$; the symmetry energy coefficient $J = E_{sym}(\rho_0)$; the symmetry energy at 0.1 fm^{-3}, J(0.1) = E_{sym}(0.1) the coefficient proportional to the slope, $L = 3\rho_0 \frac{d(E_{sym})}{d\rho}\Big|_{\rho_0}$, and the curvature $K_{sym} = 9\rho_0^2 \frac{d^2(E_{sym})}{d\rho^2}\Big|_{\rho_0}$ of the density dependence of the symmetry energy, respectively, κ, the enhancement factor of the energy weighted sum rule for the IVGDR, and the strength of the spin-orbit interaction W_0.

In Table I we present the Pearson Correlation Coefficients between the values of E_{CEN} of the isoscalar and isovector giant resonances, respectively, and the properties of NM. It is seen from the Table that strong correlations were found between the energies of compression mode: ISGMR and K_{NM}, and between the energies of the ISGDR, ISGQR, and ISGOR and m*. Strong correlations are found between Q and all the isoscalar modes However, weak correlations were found between the IVGDR in ^{208}Pb and the values of J, L, or K_{sym}.

Table I. Pearson's correlation coefficient between the energies of Isoscalar (*T*=0) and Isovector (*T*=1) giant multipole (*L*=0-3) resonances in ^{208}Pb and NM properties.

	m*/m	K_{NM}	K' = -Q	J	J(0.1)	L	K_{sym}	κ	W_0 (x_w=1)
L0 T0	-0.52	0.90	-0.84	-0.06	-0.29	0.28	0.53	-0.01	0.29
L1 T0	-0.91	0.53	-0.85	-0.11	-0.11	0.06	0.36	0.47	0.20
L2 T0	-0.95	0.39	-0.84	-0.12	-0.25	0.13	0.43	0.55	0.31
L3 T0	-0.95	0.29	-0.77	-0.02	-0.14	0.13	0.39	0.59	0.12
L0 T1	-0.64	0.05	-0.43	-0.24	0.03	-0.26	-0.17	0.89	-0.04
L1 T1	-0.53	-0.11	-0.26	-0.29	0.19	-0.44	-0.38	0.85	-0.05
L2 T1	-0.71	0.02	-0.45	-0.30	0.06	-0.34	-0.20	0.87	0.03
L3 T1	-0.82	0.19	-0.63	-0.32	-0.11	-0.21	0.01	0.81	0.08

[1] M.R. Anders *et al.*, in preparation.

Density determinations in heavy ion collisions

G. Roepke,[1] S. Shlomo, A. Bonasera,[2] J. B. Natowitz, S. J. Yennello, A. B. McIntosh, J. Mabiala, L. Qin, S. Kowalski, K. Hagel, M. Barbui, K. Schmidt, G. Giulani, H. Zheng, and S. Wuenschel

[1]*Institut fur Physik, Universitat Rostock, Universitatsplatz 3, D-18055 Rostock, Germany*

[2]*Laboratorio Nazionale del Sud-INFN, v. S. Sofia 64, 95123 Catania, Italy*

Heavy ion collisions (HIC) are often used as a tool to investigate the properties of excited nuclear matter. Measured yields of different ejectiles as well as their energy spectra and their correlations in momentum space can be used to infer the properties of the emitting source. Despite the fact that a great deal of experimental data has been accumulated from HIC during the last few decades, reconstruction of the properties of the hot expanding nuclear system remains a difficult task. Two major problems are the complications inherent in incorporating nonequilibrium effects and in the treatment of strong correlations that are already present in equilibrated nuclear matter.

An often employed simple approach to handling these effects is the freeze-out approximation. Starting from hot dense matter produced in HIC, this approach assumes the attainment of local thermodynamic equilibrium after a short relaxation time. Chemical equilibrium may also be established in the expanding fireball as long as the reaction rates in the expanding hot and dense nuclear system are above a critical value. While more microscopic approaches employing transport models that describe the dynamical evolution of the many particle system are being pursued, a freeze-out approach provides a very efficient means to get a general overview of the reaction. Such approaches have been applied in heavy-ion reactions, to analyze the equation of state of nuclear matter but also in high-energy experiments (RHIC, LHC) to describe the abundances of emitted elementary particles. Much information on the symmetry energy, on phase instability, etc., has been obtained using this concept.

The main objective of our work is to determine the values of the temperature, T, matter density, n_B and asymmetry coefficient $\delta=(N-Z)/A$ characterizing the freeze-out state, from the five experimental yields, Yp, Yd, Yt, Yh and Yα of the light charged Z = 1, 2 species. This problem is easily solved within the nuclear statistical equilibrium (NSE), applicable in the region of low density and moderate temperature where medium effects can be neglected. Within the quantum statistical approach (QS) to nuclear matter, correlations and bound state formation are treated using Green's functions to derive in-medium few-body wave equations. In Figure 1 we compare the results obtained for T and n_B, deduced from experimental data on yield of particles with Z=1 and 2, using the NSE (Albergo's) approach, the QS approach, the Mekjian coalescence model and the quantum fluctuation analysis method (see Ref. [1] for details).

It is seen from the figure that the density values derived by both the coalescence and fluctuation methods are in rather good agreement with QS results that include medium effects, but in disagreement with the values derived from NSE. The NSE is applicable only at very low densities. The discrepancies with NSE are substantially reduced if medium effects, such as Pauli blocking, are taken into account.

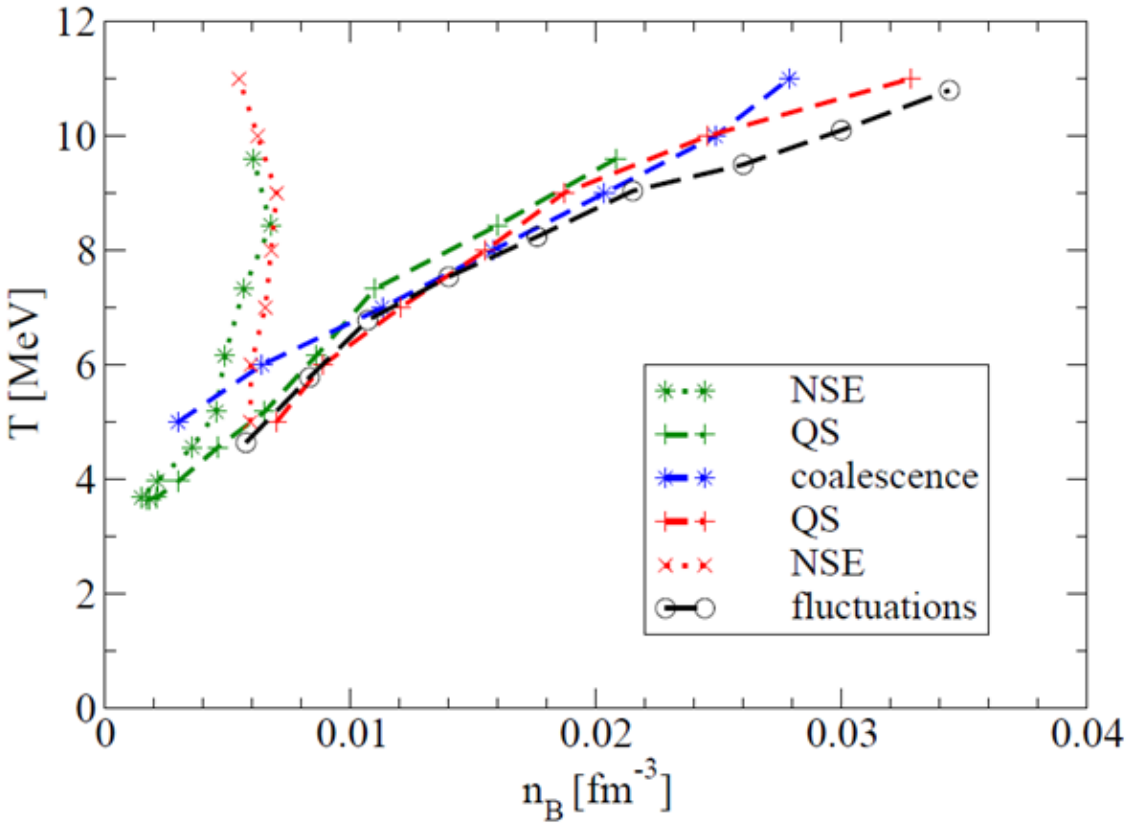

FIG. 1. (Color online) Baryon density derived from experimental data for yields of light elements.

[1] G. Roepke *et al.*, Phys. Rev. Lett. (submitted).

A T-matrix calculation for heavy-quark gluon scattering

K. Huggins and R. Rapp

Heavy quarks are invaluable probes of the Quark-Gluon Plasma (QGP) as created in ultrarelativistic heavy-ion collisions at RHIC and LHC. Their large mass, $m_Q >> T$ (T: temperature), renders a diffusion approach applicable so that their transport coefficients can be evaluated in controlled approximations; in particular, the predominantly space-like momentum exchange for on-shell scattering enables the use of potential approaches. In this way heavy-flavor observables can be connected to the properties of the fundamental QCD force in the medium [1]. In Ref. [2] we have constructed a potential-based thermodynamic ***T***-matrix approach to describe heavy-quark (HQ) diffusion and quarkonia in the QGP in a common framework. For the transport properties of charm and bottom quarks, we have focused on interactions with light quarks and anti-quarks of the medium, leading to a factor of 3-5 stronger interaction than obtained in perturbation theory.

In the present work [3], we extend the nonperturbative treatment to the gluon sector by evaluating ***T***-matrices for HQ interactions with thermal gluons. The input potential is again motivated by lattice-QCD computations of the HQ free energy, implemented via a field-theoretic ansatz for color-Coulomb and (remnants of) confining interactions [4]. This enables to evaluate corrections to the potential approach, specifically hard-thermal-loop corrections to the vertices, relativistic corrections deduced from pertinent Feynman diagrams, and a suitable projection on transverse thermal gluons. The resulting potentials are applied to compute scattering amplitudes in the three color channels of the HQ-gluon system. In the attractive triplet and sextet channel the resummations in the ***T***-matrix generate an appreciable enhancement of its imaginary part in the S-wave, especially close to the 2-particle threshold; in the repulsive 15-plet channel and for higher partial waves the nonperturbative enhancement is less pronounced. The pertinent ***T***-matrices are subsequently utilized to compute the HQ drag and friction coefficients in the QGP, see Fig. 1 for charm (left panel) and bottom quarks (right panel). When

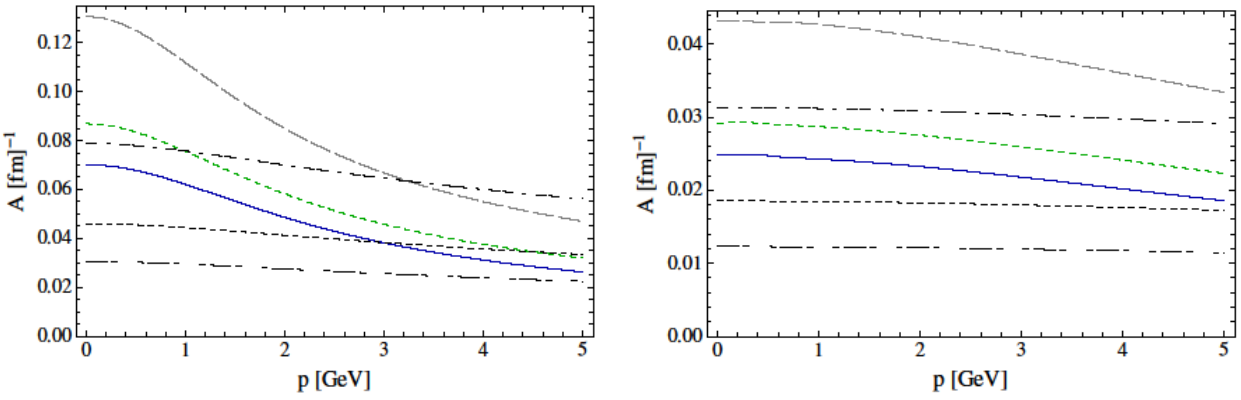

FIG. 1. Thermal relaxation rates of charm (left) and bottom quarks (right) in a hot gluon plasma evaluated from nonperturbative ***T***-matrix interactions at temperatures 1.2 T_c (solid), 1.5 T_c (green-dotted) and 2 T_c (dashed lines), compared to perturbative results at the same temperature (dash-double-dotted, dotted and dash-dotted lines).

approximating the input potential with the internal energy, the low-momentum friction coefficient (relaxation rate) is augmented by a factor of ~2.5(2) for charm (bottom) quarks at temperatures close to T_c. The enhancement is smaller at higher T, larger momentum, and when using the free energy as potential. The increased relaxation rate is expected to aid in the understanding of heavy-flavor data at RHIC and LHC.

[1] R. Rapp and H. van Hees, in *Quark-Gluon Plasma-4* (R.C. Hwa and X.N. Wang, eds.), World Scientific (Singapore, 2010) 111; arXiv:0903.1096 [hep-ph].

[2] F. Riek and R. Rapp, Phys. Rev. C **82**, 035201 (2010); New J. Phys. **13**, 045007 (2011).

[3] K. Huggins and R. Rapp, Nucl. Phys. **A896**, 24 (2012).

[4] E. Megias, A. Ruiz-Arriola and L.L. Salcedo, Phys. Rev. D **75**, 105019 (2007).

Sum rule analysis of vector and axial-vector spectral functions with excited states in vacuum

P. M. Hohler and R. Rapp

At low temperatures and chemical potentials, the QCD vacuum breaks chiral symmetry with the formation of the quark (or chiral) condensate. This symmetry is believed to be restored at high temperatures, but a definitive experimental signature of this restoration has not been observed. A promising way to identify chiral symmetry restoration is through the medium modifications of the spectral functions of chiral partners, such as ρ and a_1 mesons Much has been learned about the in-medium properties of the vector channel from dilepton data [1,2], but no experimental measurement of the in-medium axial-vector spectral function has been performed to date. To assist the experimental effort, theoretical tools can be used to relate the properties of the two channels so that chiral symmetry restoration can be inferred from existing data. One such tool are sum rules. Weinberg-type sum rules [3-5] relate the differences between the vector and axial-vector channels and to chiral order parameters, while QCD sum rules [6] are specific for each channel. Using the combination of these two sets of sum rules, one can hope to constrain and connect the in-medium spectral functions in the two channels. In order to identify the pertinent medium modifications, a firm understanding of the vacuum spectral functions is needed first.

In the present work [7], we simultaneously analyze vector and axial-vector spectral functions in vacuum using an extended model which combines a microscopic ρ spectral function [8] with Breit-Wigner ansaetze for the a_1 and the first excited states. Our model is quantitatively constrained by both experimental τ-decay data [9] and Weinberg sum rules. By using this combination of criteria, the model may be considered a non-trivial fit of the data, as displayed in Fig. 1. Novel features of our analysis include the study of excited states and the postulate that the high-energy continuum contribution is identical in vector and axial-vector channels, as should be the case in the perturbative regime. In particular, the use of the Weinberg sum rules leads us to infer the presence of an excited axial-vector state, a_1', about which rather little is known to date. Quantitatively, the inclusion of the a_1' improves the

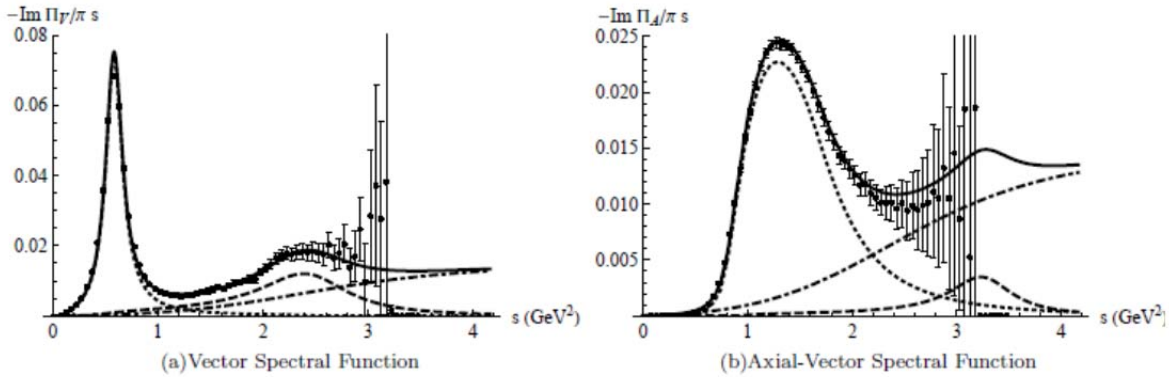

FIG. 1. Spectral functions in the vector (left) and axial-vector channel (right) compared to experimental data for hadronic τ-decays by the ALEPH collaboration [9]. The different curves highlight the contributions to the total spectral function (solid curve) from the ground-state resonance (dotted curve), the excited resonance (dashed curve), and the high-energy continuum (dot-dashed curve).

agreement of the four Weinberg-type sum rules from deviations of (3.6%, 43%, 7000%, -1400%) down to (-1.28%, ~0%, ~0%, -96%), where the positive (negative) sign indicates an excess in the vector (axial-vector) channel. As an additional check, we utilize the constructed spectral functions within their respective QCD sum rules to check the lesser established gluon and four-quark condensates. Requiring an agreement of the QCD sum rules within 1% or less, we find the gluon condensate to be (0.022±0.002) GeV^4, while the four-quark condensate factorization parameter turns out to be (2.1+0.3-0.2). We believe that these spectral functions provide a useful basis for future studies of medium modifications in order to shed light on the long-standing problem of testing chiral symmetry restoration with dilepton data.

[1] R. Rapp, J. Wambach, H. van Hees, in: R. Stock (ed.), Relativistic Heavy Ion Physics, Landolt-Boernstein New Series, vol. **I/23A** (4-1), Springer-Verlag, New York, 2010.

[2] I. Tserruya, in: R. Stock (Ed.), Relativistic Heavy Ion Physics, Landolt-Boernstein New Series, vol. **I/23A** (4-2), Springer-Verlag, New York, 2010.

[3] S. Weinberg, Phys. Rev. Lett. **18**, 507 (1967).

[4] T. Das, V.S. Mathur, and S. Okubo, Phys. Rev. Lett. **19**, 859 (1967).

[5] J.I. Kapusta, E.V. Shuryak, Phys. Rev. D **49**, 4694 (1994).

[6] M.A. Shifman, A.I. Vainshtein, V.I. Zakharov, Nucl. Phys. **B147**, 385 (1979); Ibid 448.

[7] P.M. Hohler and R. Rapp, Nucl. Phys. **A892**, 58 (2012).

[8] R. Rapp and J. Wambach, Eur. Phys. J. A **6**, 415 (1999).

[9] R. Barate *et al.*, ALEPH collaboration, Eur. Phys. J. C **4**, 409 (1998).

Quantitative sum rule analysis of low-temperature spectral functions

Nathan P. M. Holt, Paul M. Hohler, and Ralf Rapp

In vacuum and at low temperatures, the chiral symmetry of the QCD Lagrangian is spontaneously broken by a non-vanishing quark condensate. For isovector hadronic excitations, this manifests itself through a large splitting of the masses of the chiral partner mesons $\rho(770)$ and $a_1(1260)$. Chiral symmetry is believed to be gradually restored with rising temperatures and baryon densities, as the quark condensate "melts" away. The melting is expected to be accompanied by a disappearance of the mass splitting of chiral-partner hadrons, i.e., the ρ and a_1 spectral functions should degenerate when chiral symmetry is restored. A model-independent prediction for the low-temperature behavior of the spectral functions is chiral mixing [1], where the medium constitutes a lukewarm pion gas: To leading order in temperature, a mutual linear mixing of the vector and axial-vector spectral functions occurs. Further consequences of this mechanism can be explored using spectral representations in finite-temperature sum rules.

In the present work [2] we have employed chiral mixing to quantitatively analyze finite-temperature QCD and Weinberg-type sum rules. In particular, we have utilized: (i) updated vacuum spectral functions which quantitatively agree with sum rules and include both excited resonances and degenerate continua [2], (ii) finite pion-mass corrections, and (iii) a strict implementation of leading-order temperature effects. Chiral mixing induces a mutual flattening of the oscillatory pattern of "peaks" and "valleys" in the vacuum spectral functions, with the peaks in one channel filling in the valleys in the opposite channel. The in-medium spectral distributions thus tend to approach one another, as expected with increasing temperature. It further has been found that, while the Weinberg-type sum rules are trivially satisfied by leading-order chiral mixing, the QCD sum rules begin to break down at temperatures near 140 MeV and above, cf. Table I and Fig. 1 (some sensitivity to the definition of the Borel window at finite temperature is observed). Interestingly, the breakdown sets in at much higher temperatures when finite pion mass corrections are neglected. The latter are thus identified as a key factor in signaling the onset of new physics. It is encouraging to find this onset at temperatures where one typically expects corrections from higher resonances to become important.

Table I. Average deviation, $d_{V,A}$, of the QCD sum rule over the Borel window for axial-/vector channels at select temperatures (the second line quotes the chiral-mixing parameter, with ε=1/2 corresponding to chiral restoration). Values in parentheses are based on a frozen Borel window equal to the vacuum one.

T (MeV)	0	100	110	120	130	140	150	160	170	180
ϵ	0	0.06	0.08	0.10	0.13	0.16	0.20	0.23	0.28	0.32
$d_V(\%)$	0.24	0.32(0.29)	0.38(0.33)	0.48(0.39)	0.64(0.51)	0.85(0.64)	1.11(0.74)	1.43(0.97)	1.82(1.17)	2.29(1.39)
$d_A(\%)$	0.56	0.65(0.57)	0.70(0.58)	0.78(0.61)	0.90(0.67)	1.08(0.76)	1.30(0.88)	1.60(1.01)	1.98(1.17)	2.53(1.34)

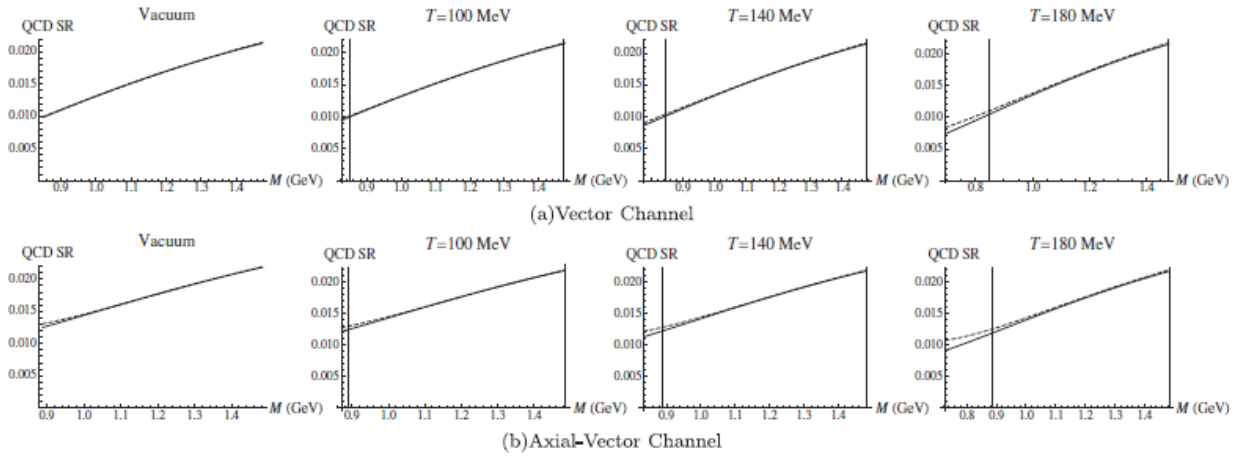

FIG. 1. Comparison of LHS (solid curve) and RHS (dashed curve) of the QCD sum rule for vector (upper panels) and axial-vector (lower panels) at select temperatures. The x-range of each plot indicates the Borel window at that temperature, while the vertical lines designate the Borel window in vacuum.

[1] M. Dey, V.L. Eletsky, and B.L. Ioffe, Phys. Lett. B **252**, 620 (1990).

[2] N.P.M. Holt, P.M. Hohler, and R. Rapp, Phys. Rev. D **87**, 076010 (2013).

[3] P.M. Hohler and R. Rapp, Nucl. Phys. **A892**, 58 (2012).

Predictions for direct photons for the p+Pb run at LHC

R. J. Fries and S. De

Proton-lead collisions are an important part of the program at the Large Hadron Collider. They provide a necessary baseline for Pb+Pb collisions. They also give us information about the partons in the lead nucleus wave function and how they are modified compared to a simple superposition of nucleons. A p+Pb run at 5.0 TeV was conducted at the LHC in early 2013. Members of the LHC experiments have asked the JET collaboration (of which RJF is a member) and other theorists to make predictions in time before the run. Ramona Vogt has compiled our calculations and other predictions in a long article published in [1].

With my collaborator Somnath De we have computed the yield of direct photons from p+Pb collisions at next-to-leading order (NLO) in the strong coupling using EPS09 nuclear parton distributions [2]. The main goal of these calculations is to provide a test for the EPS09 parameterization of nuclear parton distribution functions (nPDFs) and to provide a safe perturbative QCD baseline before any other cold nuclear matter effects (Cronin effect, energy loss, etc.) are taken into account. It will be very difficult to measure the Drell-Yan process (dilepton production) in p+Pb with the detectors available at LHC and thus direct photons are the next best tool to determine nPDFs in terms of purity of the process and theoretical control of the calculation. The figures below show spectra obtained from JETPHOX as a function of photon transverse momentum.

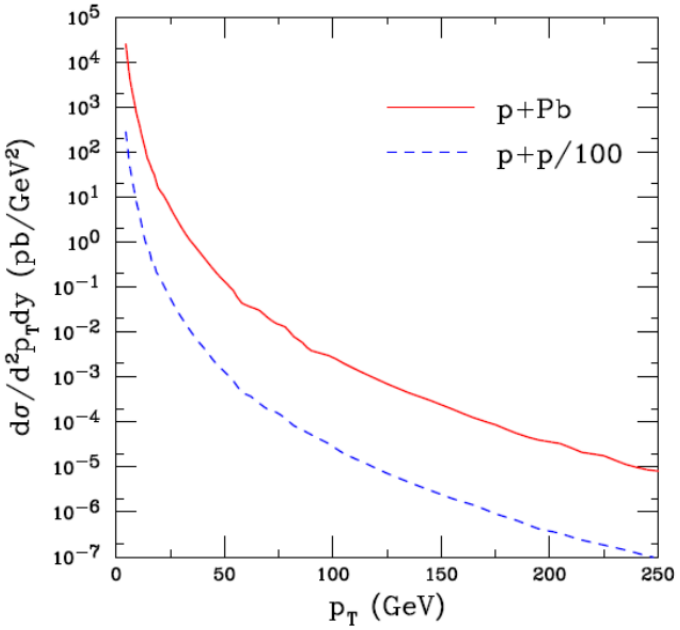

FIG. 1. The spectrum $dN/d^2P_T dy$ at y=0 for direct photons in p+Pb and p+p collisions at LHC at 5.0 TeV calculated at NLO with EPS09 nPDFs.

[1] Rainer J. Fries *et al.*, Int. J. Mod. Phys. E **22**, 1330007 (2013).

[2] K.J. Eskola, H. Paukkunen, C.A. Salgado, J. High Energy Phys. **0904**, 065 (2009).

The D_s Meson as a quantitative probe of diffusion and hadronization in heavy ion collisions

M. He, R. J. Fries and R. Rapp

Heavy charm and bottom quarks are powerful probes of the hot matter created in collisions of nuclei at high energies. Due to their large mass and the short lifetime of the system they are not expected to reach full kinetic equilibrium. However, the approach to thermalization encodes valuable information about the strength of the heavy-quark coupling to the medium.

Previously we have reported the development of a comprehensive formalism to calculate heavy-quark (HQ) diffusion in quark-gluon plasma (QGP), HQ hadronization with recombination and fragmentation, and subsequent diffusion of heavy mesons in hot hadronic matter [1]. Heavy-flavor relaxation rates are obtained from non-perturbative T-matrix calculations [2] in the QGP and phenomenological cross sections of D-mesons in the hadronic phase [3]. The background medium is modeled through ideal hydrodynamics carefully fitted to bulk-hadron observables from RHIC and LHC.

In the current reporting period we have suggested using the D_s meson (a charm-strange quark bound state) as a tool to disentangle the HQ hadronization mechanism and the importance of the hadronic phase for heavy-flavor diffusion [4]. We have checked the viability of our idea using our formalism [1]. We find that the nuclear modification factor R_{AA} of the D_s, when compared to the R_{AA} of the D meson, exhibits the influence of charm-quark recombination with thermal partons through the enhanced production of strange quarks in the fireball. On the contrary, charm fragmentation mechanisms would be undisturbed by the presence of thermal partons. Since the evolution of charm quarks figuring into the D_s and the D is identical up to hadronization, and since the hadronic phase does not significantly affect the R_{AA} of both D and D_s, a difference in their R_{AA} is associated with the amount of charm-quark recombination.

A similar idea applies when comparing the elliptic flow (v_2) of D_s and D mesons. Since the v_2 is very similar for both mesons after hadronization, and since the cross section for the D_s meson in hadronic matter is expected to be suppressed similar to that of multi-strange hadrons (which are known to exhibit an early freeze-out in heavy ion collisions), an observed splitting carries information about heavy-meson diffusion in the hadronic phase.

Fig.1 summarizes the predictions from our formalism for RHIC energies. Preliminary data from the ALICE experiment at LHC report a D_s R_{AA} which is consistently larger than the R_{AA} for the D meson, confirming the viability of our idea and hinting at an important role of quark recombination in open-charm meson observables.

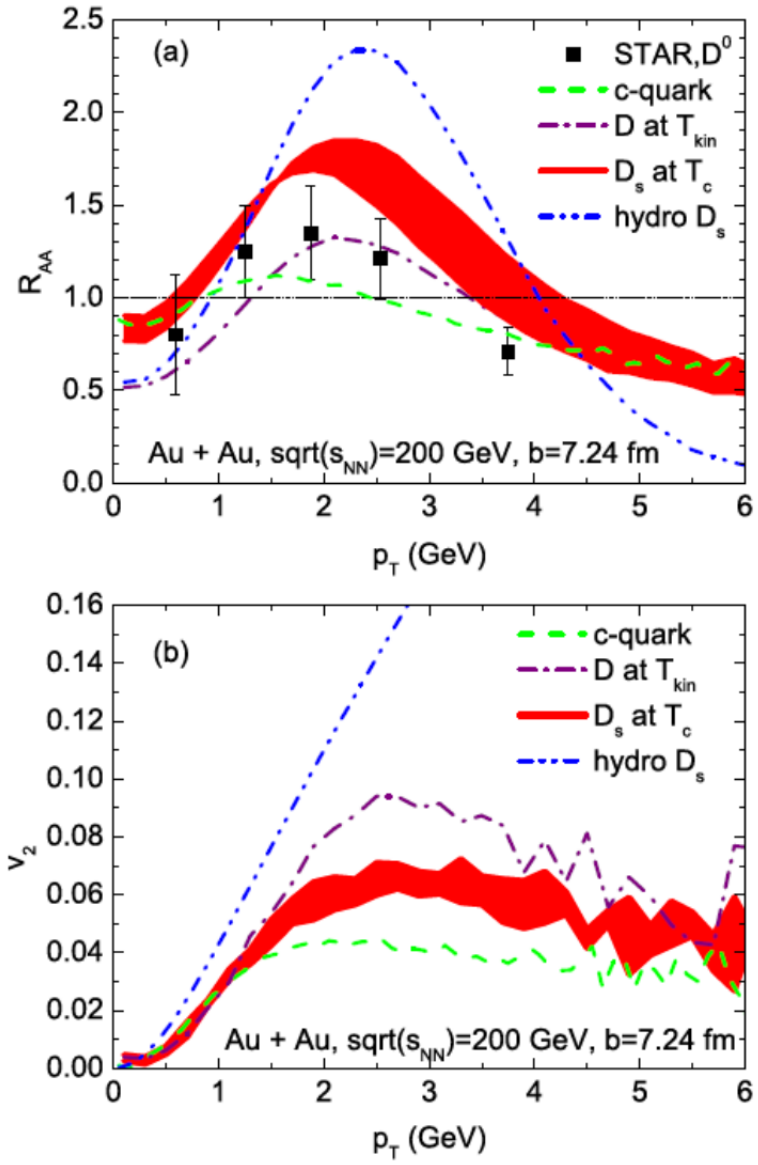

FIG. 1. Upper Panel: Nuclear modification factor R_{AA} for charm quarks before hadronization, D mesons at kinetic freeze-out and D_s mesons assumed to freeze-out just after hadronization, compared to fully thermalized D_s mesons calculated from hydrodynamics. The band for D_s mesons (due to uncertainties in the Cronin effect for the initial charm-quark spectra) is consistently above the D meson R_{AA}. STAR data are for minimum-bias D^0mesons [5]. Lower Panel: The same set of curves for the elliptic flow v_2. The D meson picks up a significant amount of additional flow in the hadronic phase. All curves are for semi-central Au+Au collisions at a center-of-mass energy of 200 GeV per nucleon pair.

[1] M. He, R. J. Fries and R. Rapp, Phys. Rev. C **86**, 014903 (2012).

[2] F. Riek and R. Rapp, Phys. Rev. C **82**, 035201 (2010).

[3] M. He, R.J. Fries and R. Rapp, Phys. Lett. B **701**, 445 (2011).

[4] M. He, R. J. Fries and R. Rapp, Phys. Rev. Lett. **110**, 112301 (2013).

[5] Y.F. Zhang, J. Phys. G **38**, 124142 (2011).

Directed flow from color glass condensate

R. J. Fries and G. Chen

The initial state of nuclear collisions at very high energies is thought to be a phase of Quantum Chromodynamics (QCD) called the Color Glass Condensate (CGC) in which the dynamics is governed by semi-classical gluon fields. We have used a generalization of the McLerran-Venugopalan (MV) model and an expansion of the classical gluon field around the time of collision (t=0) to calculate the evolution of the energy momentum tensor in Color Glass Condensate.

In the past reporting period we have finished our calculation of energy flow of the gluon field in the early collision. We have confirmed that there is a flow component α that is driven by gradients of the energy density (a "hydrodynamic flow" behavior) while there is a second, "anomalous" component β which amplifies hydrodynamic flow in certain directions while quenching it in others. We have found an intuitive abelian analogue in which the hydrodynamic flow of gluon fields is a result of Ampere's and Faraday's Law while the anomalous flow component β results from Gauss' Law.

We find very interesting phenomenological consequences for this flow. While the hydrodynamic component α is even in rapidity the anomalous component β is odd in space-time rapidity η. This phenomenon leads to a significant tilt of the fireball around a vector perpendicular to the event plane. After a further hydrodynamic expansion a non-trivial directed flow (v_1) of particles survives. The sign and rapidity-dependence of this flow is consistent with directed flow reported by the STAR collaboration at RHIC. To our knowledge it is the first time that the fireball tilt and directed flow have been calculated from an effective theory derived from first principles (color glass condensate). There are other very intriguing consequences of β for asymmetric collision systems like Cu+Au. A careful phenomenological analysis could deliver further confirmation for the existence of color glass condensate at RHIC and LHC energies.

Figs. 1 and 2 show some typical flow patterns. The results of this work have been published in

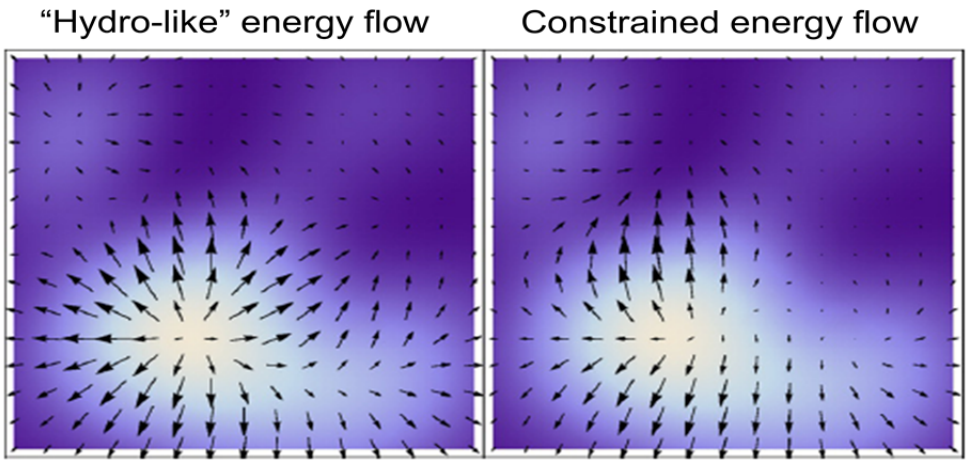

FIG. 1. The energy flow field (black arrows) in the transverse plane of the collision in a U(1) analogue, assuming random longitudinal (perpendicular to the plane) electric and magnetic fields which emerge from "seed fields" A_1 and A_2 as given by color glass. Background shading indicates energy density.Left: At η=0 there is only hydro-like flow. Right: The result at η=1 has contributions of β mixed in and shows a characteristic enhancement and quenching pattern of the flow field.

Ref.[1]. We are in the process of applying our results to the computation of initial conditions for hydrodynamics and important jet and heavy flavor observables.

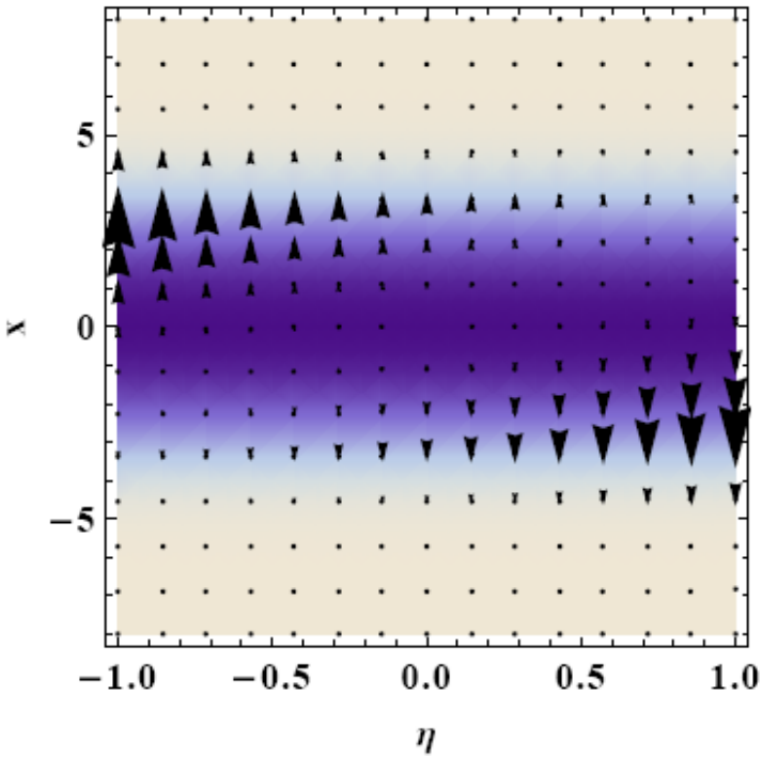

FIG. 2. The energy flow field of the classical gluon field (black arrows) in the x-η-plane at y=0 for a Au+Au collision at impact parameter b=6 fm. Energy density is indicated by shading [darker=larger energy density]. The directed flow that will lead to a tilting of the fireball is clearly visible.

[1] G. Chen and Rainer J. Fries, Phys. Lett. B **723**, 417 (2013).

Skyrme-Hartree-Fock calculations of the isospin-symmetry breaking correction in superallowed beta decay

I. S. Towner and J. C. Hardy

Over the past few years we have performed Hartree-Fock calculations of the isospin-symmetry breaking correction in superallowed beta decay, δ_{c2} , using many different parameter sets for the input Skyrme nucleon-nucleon interaction. For each set, we have applied a test [1] to the results: they should satisfy the requirements of the Conserved Vector Current (CVC) hypothesis. A figure of merit for this test is the chi-square per degree of freedom, χ^2/n_d . When Saxon-Woods eigenfunctions are used to calculate δ_{c2} , the test is passed with flying colours – the figure of merit is $\chi^2/n_d = 1.2$. With Hartree-Fock eigenfunctions, the figure of merit ranges from 5 to 16 depending on the Skyrme interaction used. To date, we have tried 20 different Skyrme interactions and none give an acceptable result for the test. The general flaw is too small a δ_{c2} correction in the high-Z cases, ^{62}Ga and ^{74}Rb, and too large a correction in ^{26}Al. There is another curious result from the Hartree-Fock calculations. If one considers a pair of mirror superallowed transitions, such as the decay of the $T_z = -1$ nucleus ^{26}Si→^{26}Al compared to the decay of a $T_z = 0$ nucleus ^{26}Al→^{26}Mg, one would intuitively expect the difference

$$\Delta\delta_{C2} = \delta_{C2}(T_z = -1) - \delta_{C2}(T_z = 0) \quad (1)$$

to be positive. This is simply a statement that there are more protons in the $T_z = -1$ nucleus and the Coulomb interaction between the protons is primarily responsible for the isospin-symmetry breaking. Certainly the Saxon-Woods calculations yield positive values for $\Delta\delta_{c2}$, while Hartree-Fock calculations typically give negative values.

These imperfections in the Hartree-Fock calculations seem to be suggesting there is a flaw in the way the Hartree-Fock procedure is being implemented. Certainly it is well known that the Hartree-Fock iteration scheme when applied to a nucleus with $N \neq Z$, will *not* conserve isospin even though the input Skyrme nucleon-nucleon interaction is isoscalar and the Coulomb potential has been turned off. Since we perform the Hartree-Fock calculation on the odd-mass nucleus with (A-1) nucleons, (see the discussion in the appendix of Ref. [2],) our results will suffer from some measure of spuriosity.

In the Saxon-Woods calculation, the central and spin-orbit potentials used for protons and neutrons are initially identical. Then the well-depth of the central potential is readjusted separately for protons and neutrons so that the experimental proton and neutron separation energies are reproduced as eigenvalues of the potential. A Coulomb potential is also included in the proton potential. If the Coulomb potential is turned off and the separation energies for protons and neutrons are made equal, then the isospin-symmetry correction δ_{c2} calculated with the Saxon-Woods code goes to zero, as it should. Thus, there is no spuriosity in the Saxon-Woods computation.

By contrast, if the same analysis is performed on the mean-field potentials produced by the Hartree-Fock procedure, namely turning the Coulomb force off and setting the proton and neutron separation energies equal, the calculated δ_{c2} correction does not go to zero. The reason is that the central

and spin-orbit potentials coming out of the Hartree-Fock code are not initially identical. To illustrate this consider just the first term in the Skyrme nucleon-nucleon interaction

$$V(\boldsymbol{r_1}, \boldsymbol{r_2}) = t_0(1 + x_0 P_\sigma)\delta(r_1 - r_2) + \ldots \tag{2}$$

and the mean-field potentials for protons and neutrons that this term produces:

$$U_p = \frac{1}{2} t_0 \left[(2 + x_0)(\rho_p + \rho_n) - (1 + 2x_0)\rho_p \right] + \ \ldots$$
$$U_n = \frac{1}{2} t_0 \left[(2 + x_0)(\rho_p + \rho_n) - (1 + 2x_0)\rho_n \right] + \ \ldots \tag{3}$$

Here ρ_p and ρ_n are proton and neutron densities constructed from the sum of the squares of the single-particle wave functions of the occupied states. Notice the structure of Eq. (3). The first term is isoscalar, while the second is an isovector/isoscalar equal mix. All the other pieces of the Skyrme interaction lead to terms in U_p and U_n with the same isospin structure. It is now obvious that if $N \neq Z$, then $U_p \neq U_n$ because the densities ρ_p and ρ_n are not the same, being separately normalized to the number of protons and neutrons respectively. Only when $N = Z$ can one produce mean-field potentials that are equal for protons and neutrons (in the absence of the Coulomb potential, of course).

To proceed, we will alter our protocol established in [2] and now insist the central and spin-orbit potentials for protons will equal that for neutrons at the end of the Hartree-Fock iterations. There are a number of ways to implement this, but it turns out the final values for δ_{c2} are rather insensitive to how this is accomplished. So we will average the proton and neutron densities and in Eq. (3) put $\rho_p \rightarrow (\rho_p + \rho_n)/2$ and $\rho_n \rightarrow (\rho_p + \rho_n)/2$ to obtain

$$U_p = U_n = \tfrac{3}{4} t_0 (\rho_p \ + \ \rho_n) + \ \ldots \tag{4}$$

With the new protocol, we have computed isospin-symmetry-breaking corrections for 20 nuclei for 12 Skyrme interactions. The unweighted average for each nucleus is recorded in the last column of Table I. The assigned error is compounded from two sources: half the spread between the highest and lowest result obtained with the different Skyrme interactions, and the spread among the different shell-model effective interactions used to compute the spectroscopic factors needed in the δ_{c2} computation. This latter error is also included in the error budget for the Saxon-Woods computations. Also in Table I are the previous Hartree-Fock results with the old protocol, as published in [2], and the Saxon-Woods values from [3]. Immediately one can see the new protocol has effected some improvements:

- The values of δ_{c2} in the high-Z cases of ^{62}Ga and ^{74}Rb are much larger and, within the stated errors, agreeing with the Saxon-Woods result.
- The mirror-transitions comparisons, $\Delta\delta_{c2}$ of Eq. (1), are firmly positive, as expected intuitively.

But there is a downside: the results for low-Z cases are also increased. To assess the impact of this we have subjected the sets of δ_{C2} values for each Skyrme interaction to the CVC test mentioned above. The figure of merit, χ^2/n_d , ranged from 2.7 to 5.7, much better than the range reported under the old protocol of 5 to 16, but still worse than1.4 obtained with Saxon-Woods radial functions. So the nucleus-to-nucleus variations in the δ_{c2} values required by the CVC hypothesis are still not being achieved in the Hartree-Fock computations.

TABLE I. δ_{C2} values (in percent units) calculated with Saxon-Woods eigenfunctions (as published in TH08 [3]), with Hartree-Fock eigenfunctions with the old protocol (as published in HT09 [2]), and with Hartree-Fock eigenfunctions with the new protocol. Also listed are the δ_{C2} differences for mirror transitions, $\Delta\delta_{C2}$ of Eq. (1), and the figure of merit, χ^2/n_d, from the CVC test (see [1]).

	TH08 SW	HT09 HF	new HF
^{10}C	0.165(15)	0.215(35)	0.32(3)
^{14}O	0.275(15)	0.255(30)	0.39(3)
^{18}Ne	0.411(25)	0.205(55)	0.36(4)
^{22}Mg	0.370(20)	0.250(55)	0.38(3)
^{26}Si	0.405(25)	0.335(55)	0.47(5)
^{30}S	0.700(20)	0.540(55)	0.76(7)
^{34}Ar	0.635(55)	0.510(60)	0.75(7)
^{38}Ca	0.745(70)	0.600(60)	0.87(9)
^{42}Ti	0.835(75)	0.535(60)	0.78(10)
^{26}Al	0.280(15)	0.410(50)	0.36(7)
^{34}Cl	0.550(45)	0.595(55)	0.61(10)
^{38}K	0.550(55)	0.640(60)	0.71(11)
^{42}Sc	0.645(55)	0.620(55)	0.64(10)
^{46}V	0.545(55)	0.525(55)	0.57(9)
^{50}Mn	0.610(50)	0.575(55)	0.65(10)
^{54}Co	0.720(60)	0.635(55)	0.72(11)
^{62}Ga	1.20(20)	0.93(16)	1.23(25)
^{66}As	1.35(40)	1.11(35)	1.41(40)
^{70}Br	1.25(25)	1.14(25)	1.49(25)
^{74}Rb	1.50(30)	1.29(16)	1.75(25)
$\Delta\delta_{C2}(A=26)$	0.126	−0.075	0.11
$\Delta\delta_{C2}(A=34)$	0.086	−0.085	0.14
$\Delta\delta_{C2}(A=38)$	0.194	−0.040	0.16
$\Delta\delta_{C2}(A=42)$	0.192	−0.085	0.15
χ^2/n_d	1.2	8.3	3.3

[1] I.S. Towner and J.C. Hardy, Phys. Rev. C**82**, 065501 (2010).
[2] J.C. Hardy and I.S. Towner, Phys. Rev. C**79**, 055502 (2009).
[3] I.S. Towner and J.C. Hardy, Phys. Rev. C**77**, 025501 (2008).

Beta-neutrino angular-correlation coefficient in ^{21}Na

I. S. Towner and J. C. Hardy

Recently [1], an 'exact' calculation of the beta-neutrino angular-correlation coefficient for ^{21}Na was published. The coefficient is defined as

$$a_{ev}(W) = a_{ev}^0 + \Delta a_{ev}(W) \tag{1}$$

with $a_{ev}^0 = (a_1^2 - \frac{1}{3}c_1^2)/(a_1^2 + c_1^2)$ being the major contribution, where $a_1 = g_V M_F$ and $c_1 = g_A M_{GT}$ with M_F and M_{GT} being the Fermi and Gamow-Teller matrix elements and g_V and g_A their respective coupling constants. Here W is the electron total energy expressed in electron rest-mass units. We computed the correction Δa_{ev} using the exact formalism of Behrens and Bühring (BB) [2] and found Δa_{ev}, when averaged over the electron energy spectrum, gave a correction of order 1%. Alternatively computing the correction with the formalism of Holstein [3] we found the correction to be much smaller, of order 0.05%. To try and resolve this discrepancy we have been working with the BB formalism, identifying the leading order terms and comparing them with those of Holstein.

The beta-decay differential decay rate is written as

$$d^5\Gamma = \frac{G^2}{(2\pi)^5} F(Z,W)(W_0 - W)^2 pW dW d\Omega_e d\Omega_\nu \left(f_1(W) + f_2(W)\frac{p}{w}\hat{\boldsymbol{p}}.\hat{\boldsymbol{k}} + \cdots\right) \tag{2}$$

where $\hat{\boldsymbol{p}}$ and $\hat{\boldsymbol{k}}$ are unit vectors in the directions of the electron and neutrino respectively. Here W_0 is the maximum value of W, p the electron momentum $p^2 = W^2 - 1$ in electron rest-mass units and $F(Z,W)$ the Fermi function. The beta-neutrino angular-correlation coefficient is defined as

$$a_{ev} = \frac{f_2(W)}{f_1(W)} \tag{3}$$

Holstein [3] gives expressions for the spectral functions with electromagnetic corrections to order (αZ). It is convenient to write out separately the Fermi and Gamow-Teller pieces, $f_1(W) = f_1^F(W) + f_1^{GT}(W)$ and $f_2(W) = f_2^{GT}(W) + f_2^{GT}(W)$, and show their electron energy dependence explicitly by writing them as

$$f_\alpha^F(W) = a_1^2 k_\alpha^F \left(1 + A_\alpha^F W + \frac{B_\alpha^F}{W} + C_\alpha^F W^2\right)$$
$$f_\alpha^{GT}(W) = c_1^2 k_\alpha^{GT} \left(1 + A_\alpha^{GT} W + \frac{B_\alpha^{GT}}{W} + C_\alpha^{GT} W^2\right), \qquad \alpha = 1,2 \tag{4}$$

For a mixed Fermi plus Gamow-Teller transition, these expressions are combined by defining

$$f_\alpha(W) = (a_1^2 + c_1^2)k_\alpha \left(1 + A_\alpha W + \frac{B_\alpha}{W} + C_\alpha W^2\right), \quad \alpha = 1, 2 \tag{5}$$

where, for example, $A_\alpha = (a_1^2 A_\alpha^F + c_1^2 A_\alpha^{GT})/(a_1^2 + c_1^2)$ and likewise for k_α, B_α and C_α.

In comparing our results from BB with the expressions of Holstein, we note two main differences:

- There is no electromagnetic (αZ) correction to Holstein's weak-magnetism form factor;
- Behrens-Bühring argue that (W_0R) and (αZ) are comparable small quantities and expressions evaluated to second order should contain terms in $(W_0R)^2$, $(W_0R)(\alpha Z)$ and $(\alpha Z)^2$. Holstein does not provide any corrections in order $(\alpha Z)^2$.

These differences do not represent errors, but reflect different approximations made in the derivations. There is little numerical consequence from the second item in this list. It is the electromagnetic correction to the weak-magnetism form factor that explains the differing beta-neutrino angular correlation values in ^{21}Na.

To illustrate this, we perform a shell-model calculation with the USD effective interaction [4] of the nuclear matrix elements involved in ^{21}Na beta decay. Note that the Gamow-Teller form factor, c_1, can alternatively be determined from the experimental *ft* value using $ft = \frac{6140}{B(GT)}$ and $|c_1| = \sqrt{B(GT)}$. Thus we have adjusted the g_A value so that when combined with the shell-model matrix element M_{GT} the experimental c_1 value is obtained. With these shell-model values we compute the beta-neutrino correlation coefficient, a_{ev}, (averaged over the electron energy spectrum) with the formulae from Eq. (4) and 'exactly' using a computer code [5] based on the Behrens-Büring formalism. In the exact computation, the spectral functions $f_1(W)$ and $f_2(W)$ are obtained in numerical form. We therefore use a least-squares fitting program to fit these tabular values to the expressions given in Eq. (4). In the fitting only two parameters could be usefully determined; so for $f_1(W)$ we fixed B_1 and C_1 to the values given by the formulae and determined k_1 and A_1. Likewise for $f_2(W)$, we fixed B_2 and C_2 and determined k_2 and A_2. The results are given in Table I. One sees the Behrens-Bühring formulae agree well with the 'exact'

Table I. Values of the coefficients in the spectral functions $\boldsymbol{f_1(W)}$ and $\boldsymbol{f_2(W)}$, Eq.(5), for the beta decay of ^{21}Na obtained from the formulae of Holstein and Behrens-Bühring and the 'exact' computation.

	k_1	k_1A_1(%)	k_1B_1(%)	k_1C_1(%)		
Holstein	1.00417	-0.027	0.115	-0.003		
BB formula	1.01133	-0.027	0.115	-0.003		
BB'exact'	1.01066	-0.020				
	k_2	k_2A_2(%)	k_2B_2(%)	k_2C_2(%)	a_{ev}	Δa_{ev}
Holstein	0.55489	0.188	0.000	0.002	0.55867	-0.00028
BB formula	0.55296	0.187	0.020	0.002	0.55286	-0.00592
BB'exact'	0.55243	0.195			0.55330	-0.00548

computed values, while the Holstein formulae appear deficient in the energy-independent coefficients k_1 and k_2. This we trace to the absence of the electromagnetic weak-magnetism term in the Holstein formulae.

[1] V.E. Iacob, J.C. Hardy, C.A. Gagliardi. J. Goodwin, N.Nica, H.I. Park, G. Tabacaru, L. Trache, R.E. Tribble, Y. Zhai, and I.S. Towner, Phys. Rev. C **74**, 015501 (2006).

[2] H. Behrens and W. Bühring, *Electron Radial Wave Functions and Nuclear Beta-decay* (Clarendon Press, Oxford, 1982); H. Behrens, H. Genz, M. Conze, H. Feldmeir, W. Stock, and A. Richter, Ann. Phys. **115**, 276 (1978).

[3] B.R. Holstein, Rev. Mod. Phys. **46**, 789 (1974).

[4] B.H. Wildenthal, in *Progress in Particle and Nuclear Physics*, ed. D.H. Wilkinson (Pergamon Press, Oxford, 1984) Vol. **11**, p. 5.

[5] J.C. Hardy and I.S. Towner, Phys. Rev. C **71**, 055501 (2005).

SECTION IV

SUPERCONDUCTING CYCLOTRON, INSTRUMENTATION AND RIB UPGRADE

K500 operations and development

D. P. May, G. J. Kim, H. L. Clark, and F. P. Abegglen

Introduction

During the 2012-2013 reporting period a total of 14 different beams, including 3 newly developed beams, were used for experiments, and there were a total of 16 beam tunings for these experiments. In addition, 3 new beams were developed using charge-bred ions from the charge-breeding ECR ion source ECR3. The SEE program and the charge-breeding effort are treated separately in this progress report.

Ion Sources

During the shutdown ECR1 was opened for examination, and it was found that there had been no further deterioration in the damaged spot that had developed over a plasma flute on the aluminum wall.

Cyclotron Beams

New beams of ^{14}N at 25 AMeV, ^{16}O at 12 AMeV, and ^{45}Sc at 5.1 AMeV were developed for experiments. Following the success of charge-breeding with the ECR3 ion source located in the new ion-guide cave, charge-bred beams of $^{85}Rb^{15+}$, $^{85}Rb^{17+}$ and $^{133}Cs^{24+}$ were injected into the K500 through the recently completed RIB injection line and accelerated to 10 AMeV, 15 AMeV and 10 AMeV, respectively.

Operations

For the period April 1, 2012 through March 31, 2013, the operational time is summarized in Table I, while Table II lists how the scheduled time was divided. There was an even larger amount of unscheduled maintenance than last year, again involving water leaks into the K500 vacuum. The greatest time was lost in June and July while somewhat less time was lost during October and November.

TABLE I. 2012-2013 Operational Time

Time	Hrs.	%Time
Beam on target	5030.50	**67.3**
Tuning, optics, set-up	10.00	**0.1**
Beam development	742.25	**9.9**
Scheduled maint.	65.25	**0.9**
Unscheduled maint.	1628.00	**21.8**
Idle time	0.00	**0.0**
Total	**7476.00**	**100.0**

TABLE II. 2012-2013 Scheduled Beam Time.

Time	Hrs.	%Time
Nuclear physics	1276.75	**21.0**
Nuclear chemistry	916.25	**15.1**
Atomic physics	0.00	**0.0**
Outside collaboration	0.00	**0.0**
Outside users	3135.50	**51.7**
Beam development	742.25	**12.2**
Total	**6070.25**	**100.0**

ECR2 development

D. P. May, B. T. Roeder, F. P. Abegglen, and H. Peeler

Introduction

During the last reporting period the ECR2 ion source was used extensively for the production of heavy-ion beams for the K150 cyclotron. Although the ECR2 location in a limited-access area directly above the K150 make it difficult to work on, a major repair and the implementation of two-frequency operation were accomplished.

Repairs

In August a leak developed in a water line leading to the plasma chamber. The repair made it necessary to move the source from its location above the K150 and extract the plasma chamber from the axial coils in order to gain access to the plastic tubing used for water-cooling of the chamber. Subsequently, all this plastic tubing was replaced. The source was then reassembled, reinstalled and realigned.

Beams from Solids

A low-temperature oven (Fig. 1), using the same type of Hot-Shot heating element and controller as the low-temp oven on ECR1, was constructed to fit the narrower radial aperture of ECR2. In November the oven was used to run a magnesium beam for an experiment on the K150 ($^{25}Mg^{10+}$ at 11

FIG. 1. Low-temperature oven.

AMeV). Because a high-temperature oven has not yet been acquired for ECR2 the sputter fixture was used to produce scandium. Sputtering required as high as 3.5 kV, leading to a somewhat unstable beam, but the beam was sufficient for an experiment.

Two-frequency Operation

In February a new injection plate with two wave guides for microwave injection was mounted onto the source (Fig. 2). Along with the standard 14.5 GHz microwave injection from a 2.25 kW transmitter using a narrow-band-width klystron, 11 GHz microwave injection was added using a wide band, 400 watt, travelling-wave-tube (TWT) transmitter excited by a frequency generator. Also, the 14.5 GHz klystron had been weakening to the point where the transmitter was limited to below 900 watts. A new one was purchased and installed in February so that now 1.5 kW can be reached. Running both transmitters definitely improves source performance, but more experimentation with magnetic-field configurations and microwave power levels is needed for optimization.

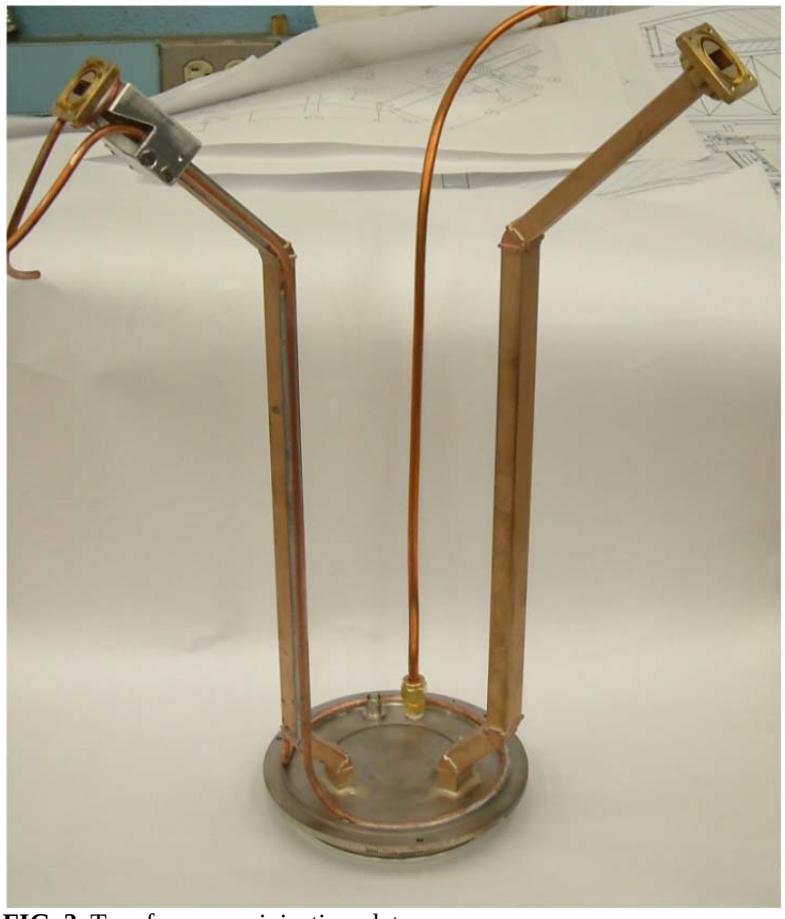

FIG. 2. Two frequency injection plate.

Texas A&M cyclotron radiation effects facility
April 1, 2012 – March 31, 2013

H. L. Clark, J. Brinkley, L. Chen, G. Chubarian, V. Horvat, B. Hyman, B. Roeder and G. Tabacaru

The activity of the Radiation Effects Facility (REF) decreased slightly over the previous reporting year. In this reporting period, the facility was used for 2,626 hours, which is a ~2% decrease over the 2,673 hours used in the 2011-2012 reporting period, however this year was the third highest usage year ever. Nearly 1,500 hours were lost in year 2012 to unscheduled maintenance. Users of the facility (and hours used) over the past year were: SEAKR (217.5), Intersil (213), Sandia National Lab (200), NAVSEA (147), Honeywell (144), NASA GSFC (131.5), Boeing Satellite Systems (111), HIREX-France (111), Aeroflex (102), BAE Systems (92), NASA JPL (90.5), Defense Threat Reduction Agency (87.5), International Rectifier (70.5), Thales Alenia Space Agency-France (59), NASA JSC (56), Northrop Grumman (55.5), General Dynamics (48), TRAD-France (48), VPT Inc (44.5), Xilinx Corp (44.5), EADS/IDA-France/Germany (44), Microsemi Corp (43), Maxwell Technologies (41.5), Texas Instruments (40), ATMEL-France (30), Sun Tronics (29.5), University of Michigan (29), Air Force (28), Bionetics (24), JD Instruments (24), Radiation Assured Devices (24), Woosong University-Korea (24), SEMICOA (18), Ball Aerospace (16), JAXA-Japan (16), Johns Hopkins (16), L-3 Communications (16), MSEI (16), DRS Sensors (14), Microsat-Canada (12), University of Maryland (12), Data Device Corp (11.5), Fuji Electric-Japan (8), Lockheed Martin (8) and Peregrine Semiconductor (8). New users

Table I. Radiation Effects Facility usage by commercial and government customers for this and previous reporting years.

Reporting Year	Total Hours	Commercial Hours (%)	Government Hours (%)
2012-2013	2,626	1,856 (71%)	770 (29%)
2011-2012	2,673	1,630 (61%)	1,043 (39%)
2010-2011	3,042	1,922 (63%)	1,121 (37%)
2009-2010	2,551	1,692 (66%)	859 (34%)
2008-2009	2,600	1,828 (70%)	772 (30%)
2007-2008	2,373	1,482 (62%)	891 (38%)
2006-2007	2,498	1,608 (64%)	890 (36%)
2005-2006	2,314	1,314 (57%)	1,000 (43%)
2004-2005	2,012	1,421 (71%)	591 (29%)
2003-2004	1,474	785 (53%)	689 (47%)
2002-2003	1,851	1,242 (67%)	609 (33%)
2001-2002	1,327	757 (57%)	570 (43%)
2000-2001	1,500	941 (63%)	559 (37%)
1999-2000	548	418 (76%)	131 (24%)
1998-1999	389	171 (44%)	218 (56%)
1997-1998	434	210 (48%)	224 (52%)
1996-1997	560	276 (49%)	284 (51%)
1995-1996	141	58 (41%)	83 (59%)

included ATMEL, Bionetics, EADS/IDA, Woosong University, JAXA, MSEI, DRS Sensors, Microsat, University of Maryland and Fuji Electric.

Table I compares the facility usage by commercial and government customers. The ratio from this reporting year (71% to 29%) is similar to the trend seen in previous reporting periods and commercial hours still dominate (see Fig 1). Commercial hours increased by 14% and government hours decreased by 26% over hours from 2011-2012. 15 and 25 MeV/u Kr and Xe were most utilized as well as 15 MeV/u Au. No new beams were added to SEELine users list. Much of the testing conducted at the facility continues to be for defense systems by both government and commercial agencies. It is expected that the facility will continue to be as active in future years. Almost 20% (352 hours) of the commercial hours were from foreign agencies from Canada, France, Germany, Japan and Korea. This is nearly a 300% increase from last year.

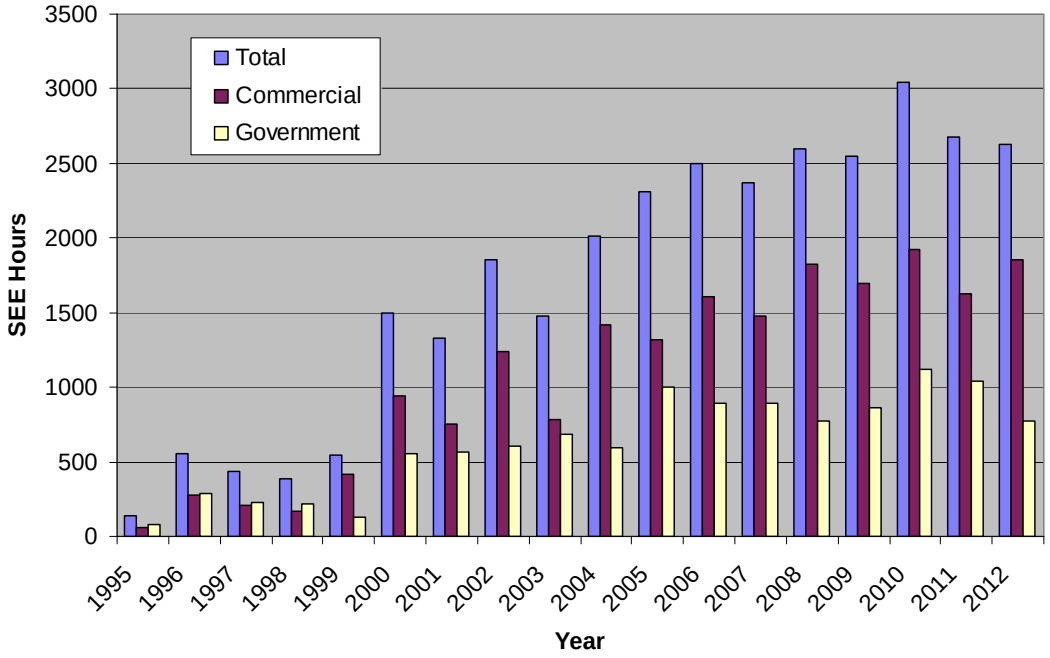

FIG. 1. Radiation Effects Facility usage by commercial and government customers for this and previous reporting years. The ratio from this reporting year (71% to 29%) is similar to the trends seen in previous reporting periods where commercial hours still dominate. Almost 20% (352 hours) of the commercial hours were from foreign agencies from Canada, France, Germany, Japan and Korea. This is nearly a 300% increase from last year.

Cyclotron computing

R. Burch and K. Hagel

This past year we, as per our mission to provide the Cyclotron Institute personnel the computational and network infrastructure necessary to execute their research programs in a timely and secure manner, added computational capacity, network infrastructure, and reallocated some of our commodity services to employ low power computers. We also upgraded the operating systems and compilers on the computational servers to enhance usability and maintainability. We are pursuing the migration of commodity and administrative services to inexpensive low power computers to better utilize rack space, power, and cooling in the server room.

The old condor submit server and the old condor management server were retired because of their large power/cooling footprint vs effective core ratio as well as because their hardware was not 64 bit capable. We therefore added two new lab computational servers, one replacing the lab's condor submit/compute server and a second for additional computational power. We also reallocated an old computational server to upgrade the condor management server. Both new servers were dual processor, threaded 8 core (32 effective cores) with 64 GByte RAM yielding an effective lab core count of 228. Together with servers owned by individual groups having an effective core count of approximately 500 for jobs

Since Scientific Linux (SL) updates are no longer being pushed out by the upstream vendor, we upgraded the operating systems on all lab and group computational servers from SL 4.x 32bit to SL 6.x 64bit. We also updated our Portland Group Fortran and Intel Fortran compilers to better take advantage of the hardware and software 64bit capability.

In an effort to further reduce replacement cost and server power/cooling footprint, we are in the process of migrating our web services from a ~400 Watt server to a ~35 Watt small form-factor fan-less PC. The 35 Watt server has been serving several of our web bases resourced with no sign of strain. Additionally, we are testing Raspberry-PI's (~6 Watt credit card sized fan-less PC's, ~$50 each) as possible replacement computers for our Dell PowerEdge authentication server and some web services to further reduce cost and power/cooling requirements.

The Cyclotron Institute building expansion was completed this year and we gained access to the Institute's new third floor. We provisioned the new floor with networking hardware, moving the student area network rack into the new third floor's IDF room and added a new rack and two 48port gigabit switches. The new IDF room provides for networking drops for both the second and third floor offices. In addition to the added wired capacity, we added wireless capacity; installing 5 wireless access ports, one in the data acquisition area, two on the second floor and two on the third floor. These access point are administered centrally allowing us to authenticate, monitor and, if need be, block wireless clients easily. All switches and access points are protected by several UPS's to guard against power issues and maintain network integrity.

The continued maintenance, search for faster, cooler, smaller, and cheaper hardware as well as upgrading software allows us to continue to supply the Institute with the stable, fast, and secure resources it needs to execute its mission.

Cyclotron Institute upgrade project

H. L. Clark, F. Abegglen, G. Chubarian, G. Derrig, G. Kim, D. May, B. Roeder and G. Tabacaru

On January 3, 2005 the Cyclotron Institute Upgrade Project (CIUP) began with the approval of the CIUP management plan by the Department of Energy Nuclear Physics Office. The project will extend at least to the second quarter of calendar year 2014. When completed, the upgraded facility will provide high-quality re-accelerated secondary beams in a unique energy range in the world. Funding for the upgrade comes from several sources: the Department of Energy, matching support from TAMU, the Robert A. Welch Foundation and beam time sales for testing electronics components at the Cyclotron Institute.

The CIUP is divided into three major tasks: (1) Re-commission of the existing K150 (88") cyclotron and refurbish beam lines; (2) Construct light-ion and heavy-ion guides and produce 1+ radioactive ions; (3) Transport and charge boost radioactive ions and accelerate in the K500 cyclotron.

As detailed in the Management Plan, effort made during this year on Task 1 included,

- Development of the 13.7 MeV/u ^{40}Ar heavy-ion beam and
- Construction of the internal cryopanel for the K150 high vacuum system.

Progress was also made on Tasks 2 and 3. This included,

- Placement of the ion guide equipment on the ion guide roof planks,
- Rebuild of Big Sol, commissioning of the CB-ECR ion source,
- Final design, construction and testing of the Light Ion Guide gas cell,
- Completion of the Heavy Ion Guide gas catcher and transport system equipment, and
- Assembly and commissioning of the n+ transport system. Below we report on a few of the accomplishments listed above.

K150 Cyclotron Development

With another year of cyclotron operation, we have worked to develop new beams and improve old ones, and we also managed to deliver K150 beams to more experiments than the year before. We have used the H^- source and strip-extraction technique to obtain proton and deuteron beams, and used the ECR2 ion source for all other positive ion beams. Currently the energy range for proton beams is 15 – 40 MeV, and for deuteron beams is 6.8 – 22.5 AMeV. For ECR2 beams, we have accelerated and extracted up to 12 AMeV for $^{13}C^{5+}$, 15 AMeV for $^{20}Ne9^{+}$, and 13.7 AMeV for $^{40}Ar^{14+}$. To extract the argon beam it required 88 kV on the deflector; this is the highest voltage used so far. The extracted intensity of the argon beam was only 11pnA, and so, much more work will be needed on the source, on the cyclotron vacuum, and other areas to get to the goal of 900 pnA. All the extracted beams from the K150 cyclotron are shown in Fig. 1. Thus far the H^- beams have achieved the best throughput, the ratio of the beam currents on the FC02 faraday cup (extracted beam) to the ILC02 cup (injected beam) to measure the injection and acceleration efficiency, at around 20 to 35%. Typical 1st harmonic ECR2 beams gave 10 to 15% throughput. The throughput for the 3rd harmonic beams averaged 1% or less, they will require more attention in the coming year. Because of the operational limits of the RF system, which is 5.6 – 16 MHz,

above 6.3 AMeV the cyclotron runs in the first harmonic mode, and below 5.6AMeV it operates in the 3rd harmonic mode; there exists an energy gap between 5.6 and 6.3 AMeV for the cyclotron.

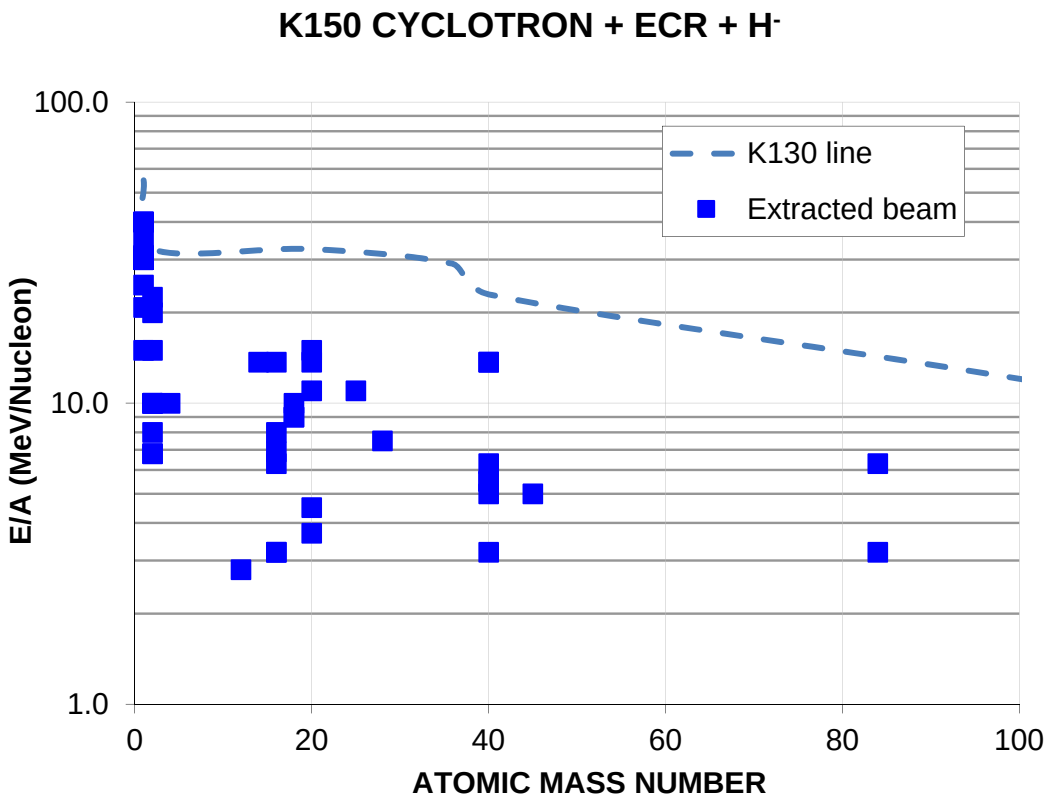

FIG. 1. Extracted beams from the K150 cyclotron with H^- and ECR2 sources since December 2009.

New K150 Beam Line for STAR/LIBERACE

We described in our last progress report the re-configuring of the old ion interaction beam line into cave 4 for the STAR/LIBERACE experiments. They ran seven times in 2012, using five proton (24 to 39 MeV) and deuteron (13 MeV) beams with the H^- source in the spring and summer, and two ECR2 beams, a 40 MeV helium and a 33 MeV carbon beam in the fall. For each run, the experiment lasted about a week and the source and cyclotron were stable for the duration of the experiment. The new beam line to the experiment worked well. However, the experimental requirement for a tiny beam spot with a moderate beam divergence at the experiment's target meant using very tight object slits which resulted in throwing away more than half of the extracted beam at the FC02 beam box. Furthermore, the momentum slits following the analyzing magnet were also narrowed to produce a clean, small beam spot, resulting in more beam losses. However, for the proton and deuteron beams there was enough beam current from the cyclotron to deliver a few nA to the experiment.

H- Ion Source Improvement

A 20 degree tilt has been added to the beam line below the H^- source. The tilt prevents dust from the filament from making its way through the extraction hole and to the cyclotron inflector. Previously a build up of dust would eventually cause an electrical short and the inflector would need to be pulled and cleaned. A bending magnet was added at the 20 degree bend (see Fig 1) to steer the H^- beam to the cyclotron inflector.

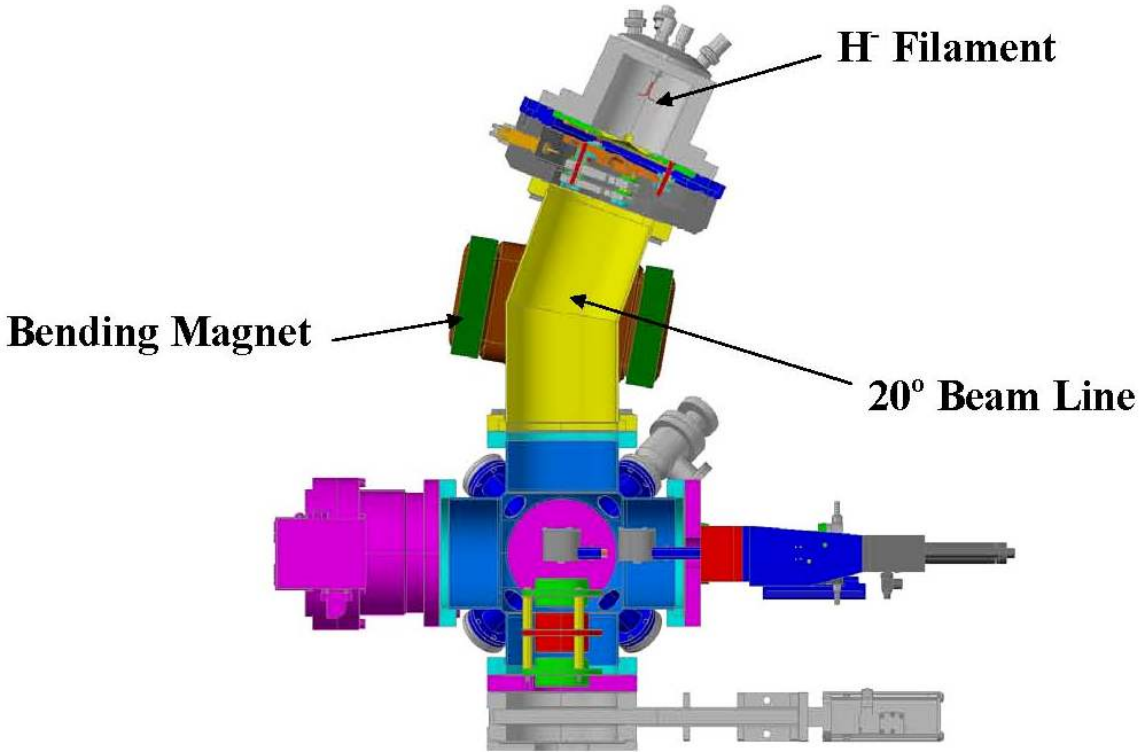

FIG. 2. A 20 degree tilt has been added to the beam line below the H^- source. The tilt prevents dust from the filament from shorting the cyclotron inflector. A bending magnet was added to steer the H^- beam to the cyclotron inflector.

13.7 AMeV40Ar Beam Development

Developing an intense 13.7 AMeV40Ar beam is important for the heavy ion guide program and we have worked on this beam from time to time throughout 2012. Initially the Ar beams ran as internal beams without extracting them because the required deflector voltage was higher than it could hold at that time. Using mainly $^{40}Ar^{14+}$, we sought to optimize the cyclotron tune for beam transmission and also to assess the vacuum attenuation for the argon beam (as compared to lighter ion beams such as ^{14}N or ^{16}O). Finally in December 2012, after spending a week of conditioning the deflector, we were able to sustain 88 kV on the deflector and extract the 13.7 AMeV $^{40}Ar^{14+}$ beam. We obtained 11 pnA on FC02 from 340pnA on ILC02, for a 3% throughput. Since a very similar charge-to-mass $^{14}N^{5+}$ beam at the same energy was obtained at 5% throughput, this comparison pointed out the importance of having a better cyclotron vacuum for running heavier beams. In addition to a better vacuum with the installation of cyropanels in the near future, we anticipate increased argon beam currents from the ECR2 ion source

using the two frequency heating (Fig. 3) and a better cooling on the plasma chamber. Also, changing to a spiral inflector and increasing the source voltage (and also in turn the inflector voltage) will probably be necessary to reach the 900 pnA intensity goal for this beam.

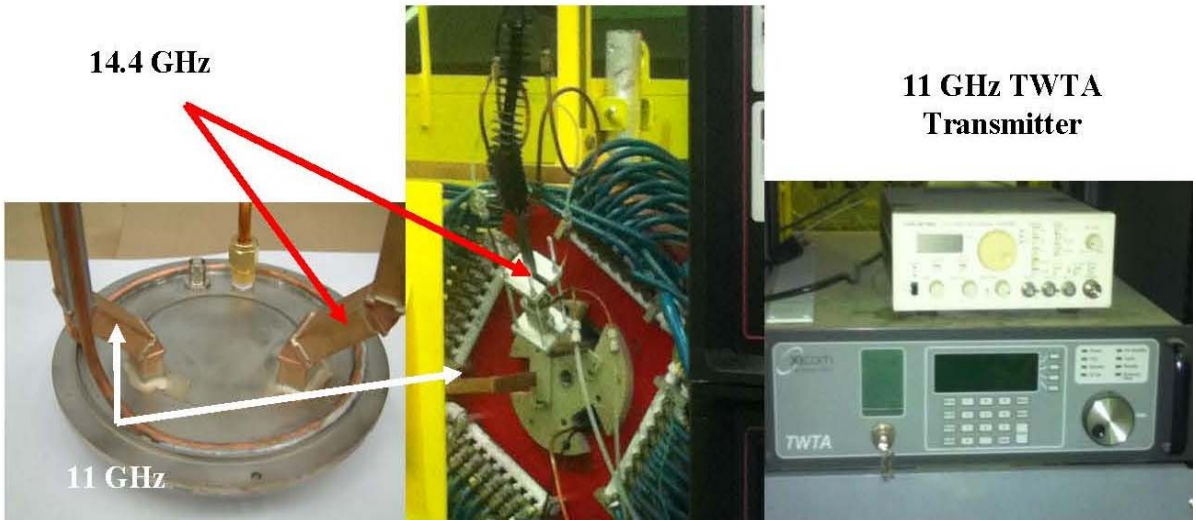

FIG. 3. Dual frequency heating system for ECR2. A new back plate has been built and installed to accept dual wave guides from both (11 GHz and 14.4 GHz) transmitters.

Third Harmonic Beams

Below 5.6 AMeV, the beams are accelerated in the third harmonic mode for the K150 cyclotron. We have worked to develop 2.5 to 5.5 AMeV for ^{12}C, ^{16}O, ^{20}Ne, and heavier ^{40}Ar, ^{45}Sc and ^{84}Kr beams. The throughput for the third harmonic beams has been poor, only 1%, as compared with 10-15% for the first harmonic beams. While we expected a smaller throughput for the 3rd harmonic beams because of a tighter RF acceptance and also a larger vacuum attenuation effects for slower beams, nevertheless the 1% throughput has been disappointing. There were several difficulties for running the 3rd harmonic beams. Initially, it was difficult just to keep the RF on, especially for the 15 MHz and higher frequency beams, but after conditioning the RF for long periods this problem has mostly dissipated. It did not help that a 3rd harmonic beam seems to need about 30% higher dee voltage than if it ran as a 1st harmonic beam. (This also means that for 3rd harmonic beams the number of turns in the cyclotron is 23% less than first harmonic beams, or about 250 to 300 turns.) Next, it was found that the beam tune was very sensitive to various cyclotron parameters such as the dee voltage and the main magnet and trim coil settings, much more so than the 1st harmonic beams. Often a small change of 1-2 A on a trimcoil was enough to destroy the beam tune. Despite not having the most efficient beam tune, several 3rd harmonic beams, such as 2.8 AMeV $^{12}C^{4+}$, 4.5 AMeV $^{20}Ne^{6+}$, and 5.5 AMeV $^{40}Ar^{11+}$, were delivered for experiments. The beam with the best throughput so far has been a 5.0 AMeV $^{16}O^{5+}$ beam, which achieved 3% (1.3 out of 45 μA), helped in part by the new grid on the inflector and optimized position of the inflector height in Mar. 2013. However, in tuning with $^{16}O^{4+}$ at the same energy a few days later, with the main magnet raised about 300 A above the $^{16}O^{5+}$ setting, the throughput for $^{16}O^{4+}$ did not match that of the $^{16}O^{5+}$ beam. This again

showed how difficult it is to tune the 3rd harmonic beams. But, we expect these 3rd harmonic beams will improve in the future with further experiences in beam tuning and improved cyclotron vacuum after the installation of the cryopanel.

CYDE and Beam Tuning

For a given beam, tuning the K150 cyclotron involves setting 18 parameters: the main and 17 trim coils. (The RF frequency is another parameter, but it is basically fixed by the energy of the beam.) These parameters are calculated with the help of the CYDE program. We had successes with CYDE solutions, but as it was mentioned in the last year's progress report, for some beams the solutions did not fully work. And without varying some trim coil values (from the original CYDE solution), especially the TC13, TC14 and TC15, some beams could not be accelerated out to the extraction radius. For some of those beams the adjustments to the TC14 and TC15 were substantial, as much as several hundred amps from the initial CYDE solution. Having to vary the trim coil values seemed to indicate some underlying problems with the field maps used by CYDE. CYDE references a set of old field maps of Berkeley's 88" cyclotron in its calculations, and while our cyclotron is a close copy of Berkeley's, it may not be surprising that the CYDE maps do not quite work for our cyclotron. To get a better understanding of the cyclotron field and to independently test the CYDE maps, the cyclotron was modeled with the TOSCA program. Fig. 4 shows a comparison of the CYDE maps with TOSCA calculations at 765, 1120, 1470, and 1840 A on the main coil (with all the trim coils turned off). The overall agreement is quite good,

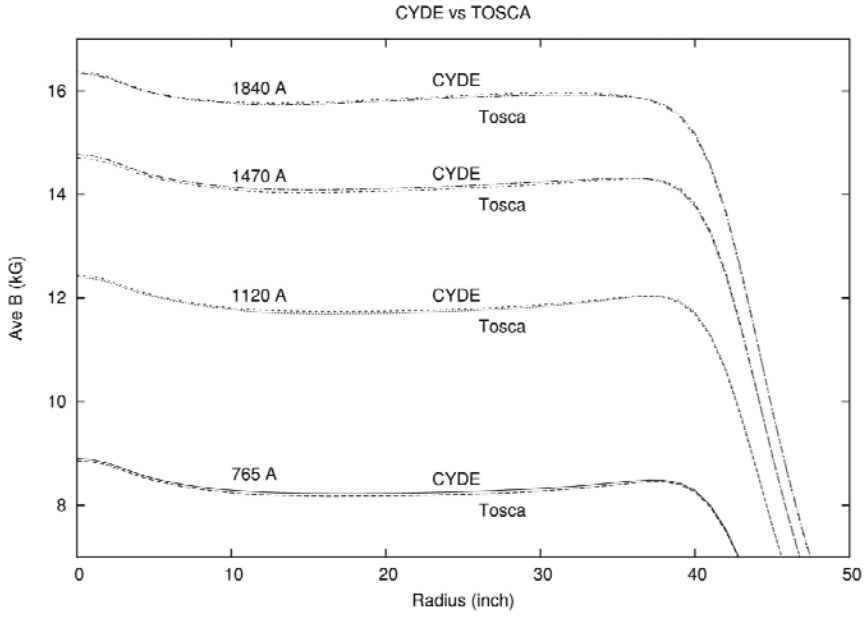

FIG. 4. Comparison of CYDE fields and TOSCA calculated fields at 765, 1120, 1470, and 1850 A on the main coil.

however upon a closer look, for example at 1120 A as shown in Fig. 5, especially around r=10 – 30", the TOSCA calculated field is about 40 gauss less than the CYDE. The absolute value of the TOSCA field is of secondary importance since the main magnet can always be tuned a few amps higher, however, the difference in the field profiles between the CYDE and TOSCA is significant. The actual TOSCA

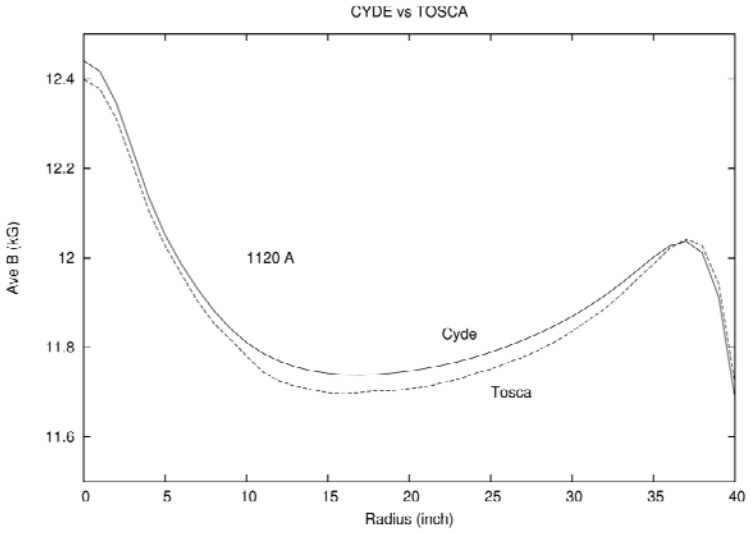

FIG. 5. CYDE has overestimated the field for the region from 10" to 30" by about 40 gauss as compared with TOSCA calculations.

calculated field was slightly rescaled from the original calculation (by 0.999) to get a better agreement with CYDE near 36" in Fig. 5. If we assume that the TOSCA calculations are true (or closer to the true cyclotron field than the CYDE maps), then the difference in the field from CYDE to TOSCA must be made up in order for the beams to be properly accelerated in the cyclotron, since CYDE calculations

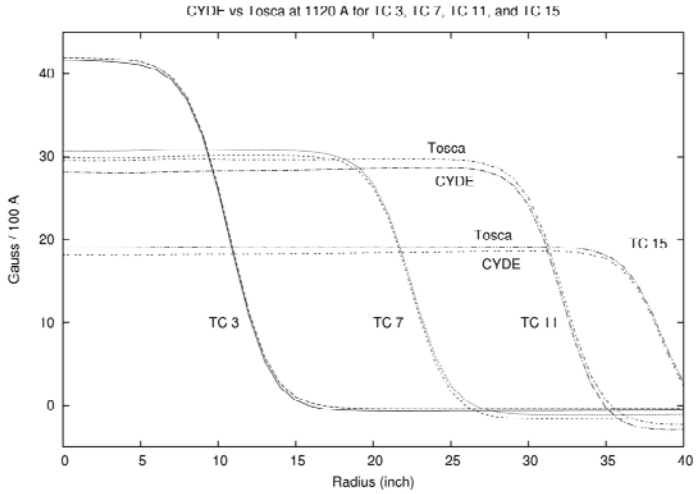

FIG. 6. Field profiles of several trim coils at 1120 A on the main magnet.

determine the necessary cyclotron field for the proper acceleration. The deficit in the CYDE field, about 40 gauss in r=10-30 for the 1120 A case, can be made up by using the trim coils. The field profiles of several trim coils are shown in Fig. 6. The trim coil fields were also modeled with TOSCA, and the differences between the TOSCA calculations and the CYDE maps for various trim coils were only a few gauss. The Trim Coil 13, which contributes about 18 gauss per 100 A (at 1120 A on the main magnet) and effective up 35", would be a good candidate to use to compensate for the CYDE field deficit. With 200 A on the Trim Coil 13 added to the TOSCA field, the overall agreement with CYDE is much better as shown in Fig. 7. Probably there are many other ways to make up for the CYDE field deficit using different groups of trim coils. In practice, we had some successes in tuning the beams using 100 to 200 A more positive on Trim Coil 14and about 50 A more positive on Trim Coil 7. The positive polarity refers to the field direction in the same direction as the main magnet (when accelerating the normal positive ion beams). Therefore running the TC 7 and 14 positive means that these trim coils add to the main coil field, which is the field correction that is predicted by the TOSCA analysis. Incidentally, running TC 13 instead of TC 14 was tried for a couple of beams and the beams did accelerate out to the extraction radius and were extracted to FC02, however using TC 14 gave slightly better results so far. Perhaps some combination of TC 13 and 14 might even work better in the future. However, at this time it is gratifying just to know the underlying reason for using an additional 200 A on TC 13 or 14.

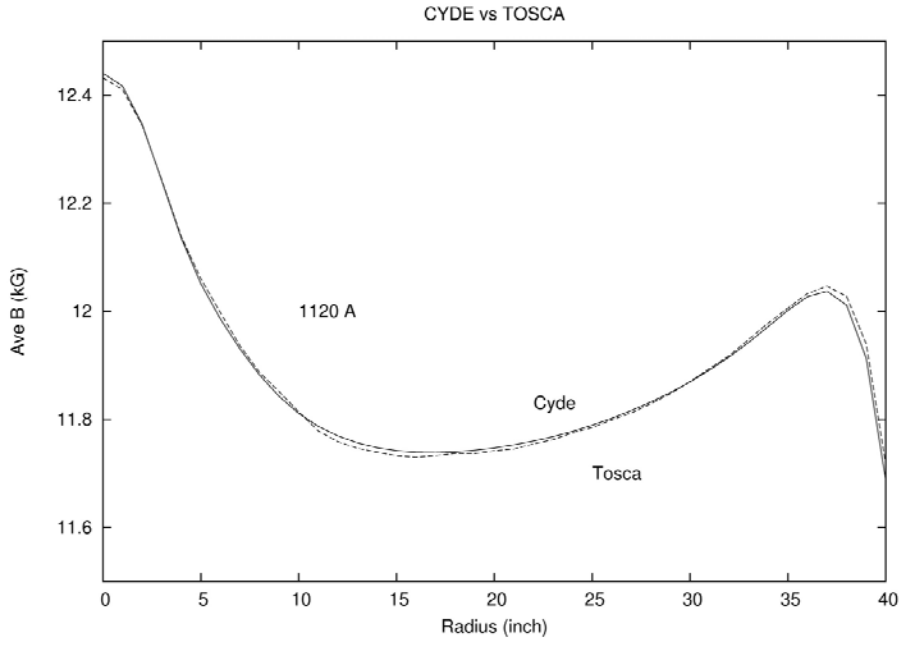

FIG. 7. Comparison of the CYDE field with the combined field of the TOSCA and 200 A on TC 13.

K150 Vacuum System

The dee tank will be equipped with one internal liquid nitrogen (LN2) cryogenic panel. As shown in Fig. 8, the panel will be placed as close to the central region of the cyclotron as possible where transmission losses from poor vacuum are the greatest. The panel system has been designed to accept liquid helium (LHe) as well. The high vacuum system will provide a vacuum pressure of low 10^{-7} torr for intense heavy ion beams.

In March 2009, a used CTI 1400 20 liters/sec LHe refrigeration system was obtained from HARC (Houston Area Research Center). After it is refurbished by the Cyclotron staff, this unit could be used to feed LHe or cold He gas to the cryopanel system of the K150 cyclotron. All internal pieces have been fabricated and the plan is to have the cryopanel installed and tested with LN2 by the end of June 2013. LHe or cold He gas will be added later in the project.

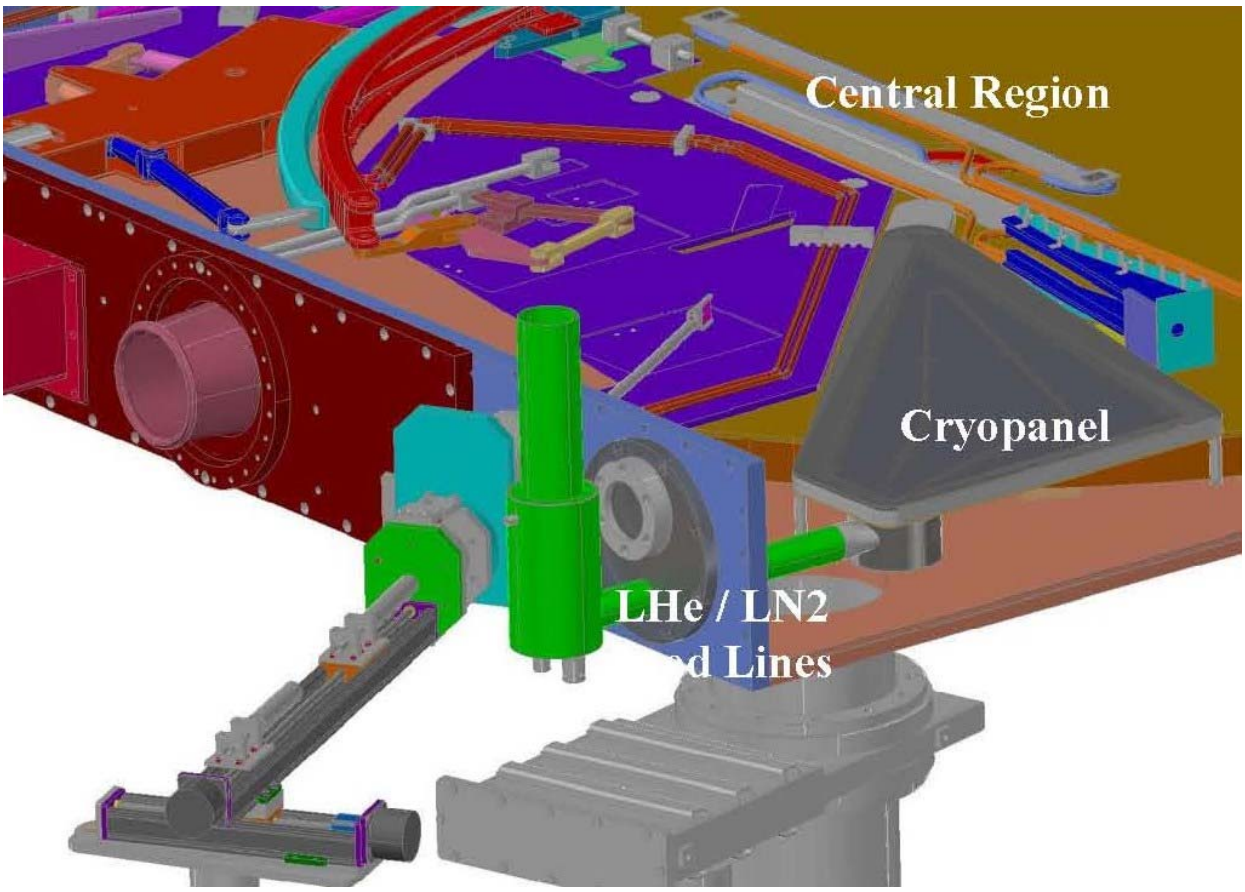

FIG. 8. Position of the LHe / LN2 cryopanel in the dee tank. The tip of the panel is placed close to the central region of the cyclotron where transmission losses from poor vacuum are the greatest.

Light Ion Guide

The tubes connecting the 3x tier roots blower system to the light ion guide chamber were installed (Fig 9) and the Light Ion Guide HV platform was tested up to 8 KV.

FIG. 9. The tubes connecting the 3x tier roots blower system to the light ion guide chamber have been installed and the Light Ion Guide HV platform was tested up to 8 KV.

The light ion guide gas cell and SPIG assembly were connected to the CB-ECR ion source as shown in Figure 10. Following the gas cell is a 1 meter long SPIG, then a 30 cm February 2013, the SPIG/Einzel transport system was tested and optimized with the ^{228}Th radioactive source positioned in the gas cell. The products from the ^{228}Th source were successfully transported from the gas cell and into the CB-ECR ion source with 99% transport efficiency. However due to the low intensity of the daughter products (20 pA), the daughter products were not charge bred and injected into the K500 cyclotron. Beam induced 1+ ions will be transported next and finally, radioactive ion products created from the gas cell.

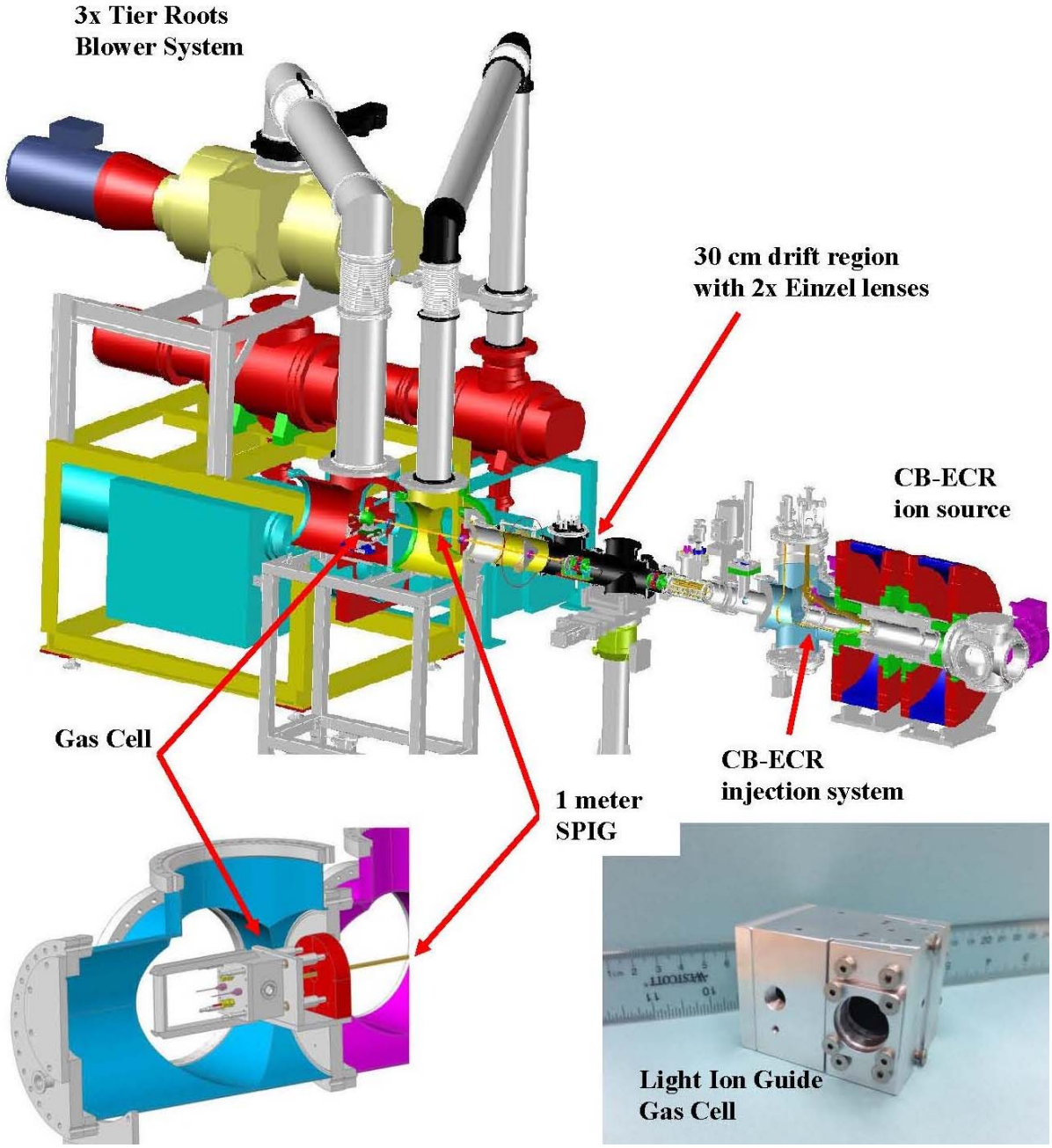

FIG. 10. Light ion guide system assembly. Following the gas cell is a 1 meter long SPIG, then a 30 cm drift region with two Einzel lenses before the injection system of the CB-ECR ion source.

Heavy Ion Guide

The Gas Catcher has been completely assembled including the Cone and the three Body sections (Fig 11). The vacuum box and support stand are under construction. The gas catcher will be moved to TAMU in June 2013 after the vacuum box and stand are completed (Fig 12). The chamber for the Branching System has been delivered and internal components are built (Fig 11). Beam optics components including Einzel lenses and X-Y steering elements are completed.

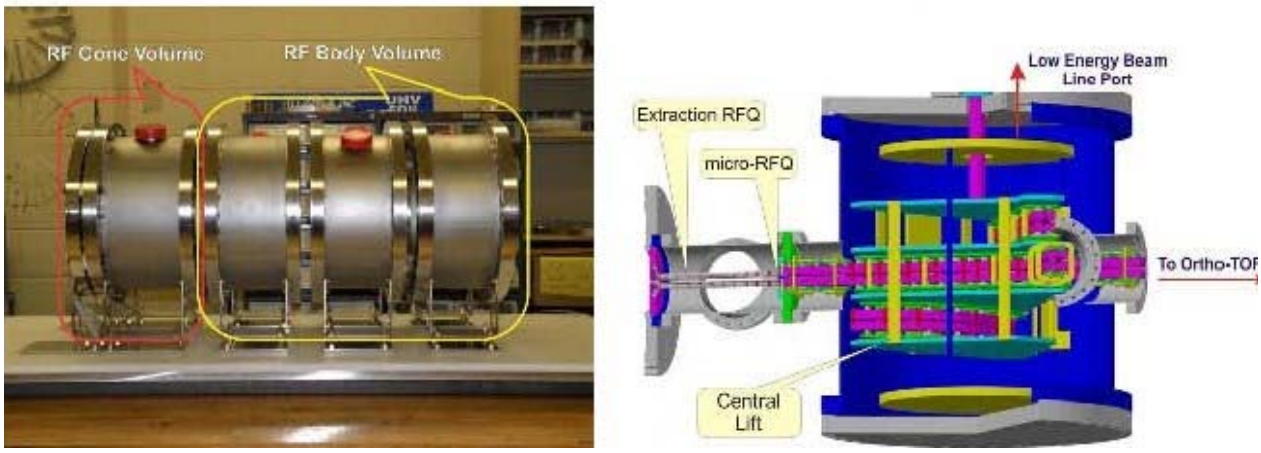

FIG. 11. Left: Gas catcher is complete and ready to be transported to TAMU. Right: Branching system chamber has been received and the internal components are built.

FIG. 12. Left: The vacuum box for the gas catcher is under construction and nearly finished. Right: The support stand is finished and ready for the vacuum box.

Big Sol Rebuild

Big Sol has been repaired, tested and is ready to be moved from Cave 2 over to the K150 Cyclotron vault on the heavy ion guide beam line. The problem of the frozen internal LN2 lines has been resolved. The solution involved rerouting the entry point of the LN2 feed to the body of the cryostat (Fig 13). To make the repair, a hole was cut in the side of the outer vessel of the chimney, lines cut and rerouted. The cryostat was filled again and LHe consumption was measure to be less than 2 liters per hour which is 5 times better than before the repair. Cryogens were flowed through the cryostat for two weeks to ensure that the repair was true.

FIG. 13. Left: Outer heat shield around body of Big Sol (note: the chimney is not installed in this picture). Right: LN2 is fed from above and originally looped around the chimney before branching off to the body. The repair redirected the feed directly to the body as shown by the white arrow.

CB-ECR Ion Source

In early fall of 2012, charge breeding of Rb was first demonstrated by the ion source. The breeding efficiency was measured to be low at ~2-5% and improvements were made to the injection scheme.

The first improvement involved adding a tube (Fig 14) at the entrance of the Einzel lens. With the tube in place, we observed a large improvement in the transport of injected ions through the plasma chamber (plasma not ignited). The tube helped to shield the ions from the non-symmetric electrical fields generated by the gas line and other pieces along the injection region.

The second improvement involved blocking the microwaves from the plasma chamber from back streaming through the injection hole and into the injection region. We observed a large improvement by adding a wire mesh over the injection hole of the plasma chamber. The mesh continued the electric field of the plasma chamber and deflected the microwaves from entering the injection region. A third improvement involved replacing the entrance microwave plug with another one, having a bigger opening (3/4"). The transport efficiency was found unchanged however we observed charge breeding for the first time after all three improvements were made.

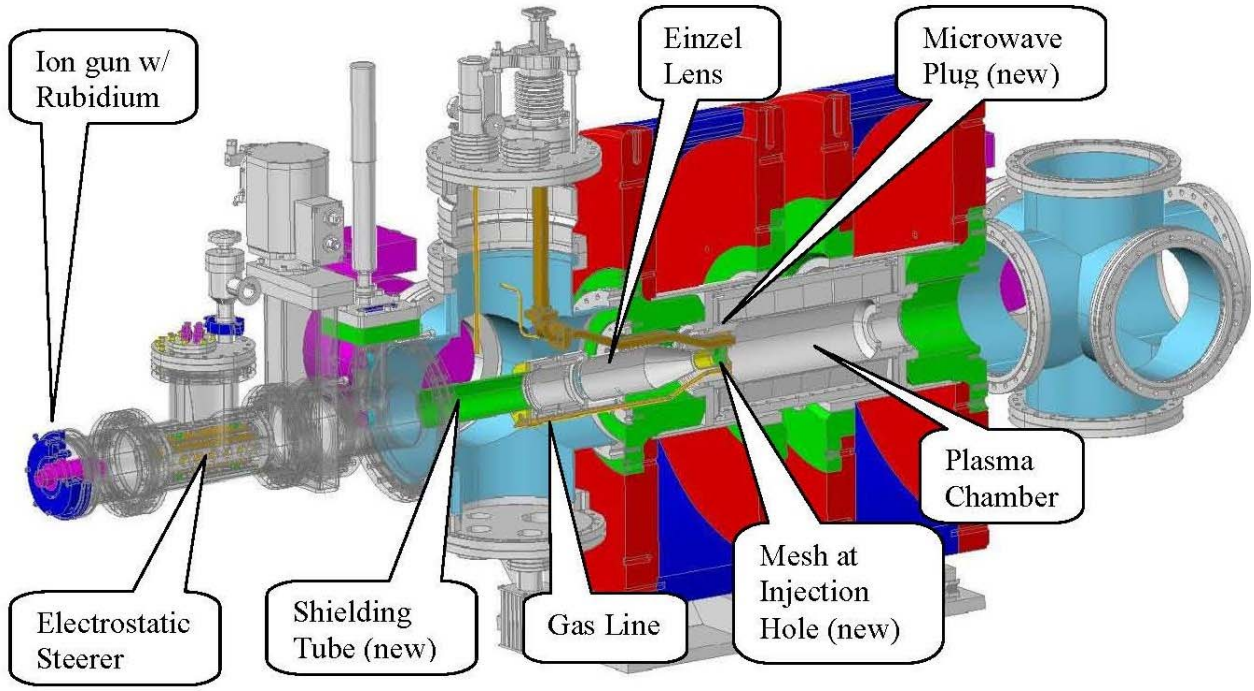

FIG. 14. View of the CB-ECR showing the new tube insert.

In December 2012, after further tuning we were able to find better operating conditions and the charge breeding effect was more pronounced. Charge breeding was also demonstrated with different 1+ sources including with Rb and Cs (Fig 15). One puzzling effect was that the breeding efficiency of Rb was found to be under 10% but was measured to be much higher for Cs at 80% or greater. It is possible that the Faraday cup at the entrance of the CB-ECR ion source was not measuring the current properly and will be studied further.

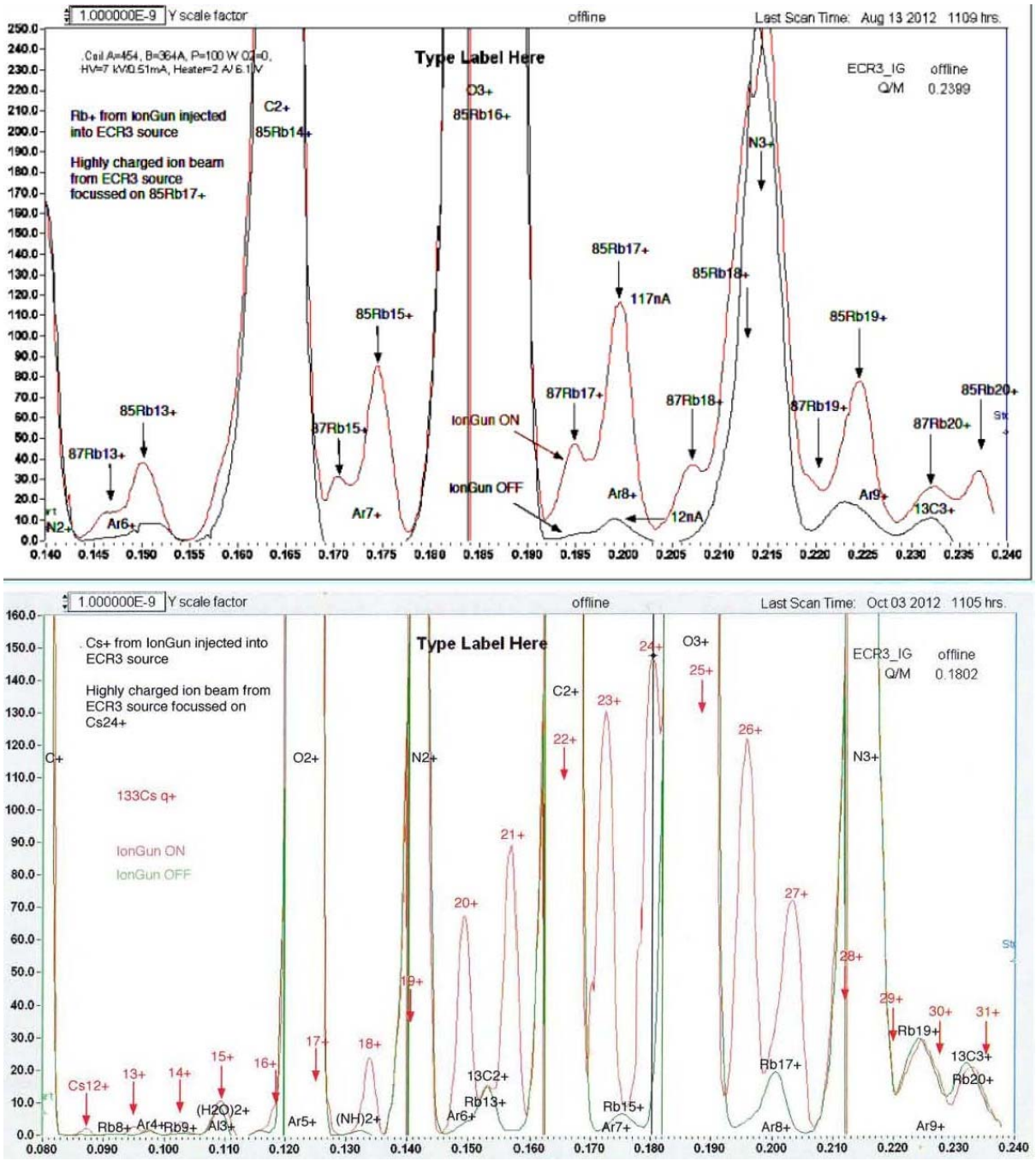

FIG. 15. Charge breeding analysis of Rb (above) and Cs (below) with the CB-ECR ion source. The total breeding efficiency of Rb was found to be <10%, which for Cs was found to be ~80%.

n+ Transport System

With the n+ transport system fully assembled, the computer control system was completed and the injection line was tested with the charge bred beams from the CB-ECR ion source then accelerated in

the K500 cyclotron and extracted. The throughput from the exit of the CB-ECR ion source to the exit of the K500 cyclotron was measured to be as high as 13.8% (Table I).

Table 1. Charge bred ions transported by the n+ transport system and accelerated by the K500 cyclotron. Throughput was measured to be as high as 13.8%.

Ion	Beam Energy (MeV/u)	Extracted Current from K500 (nA)	Throughput – from CB-ECR to K500 (%)
85Rb15+	10 MeV/u	4.0 nA	13.8 %
85Rb17+	15 MeV/u	6.4 nA	10.0 %
133Cs24+	10 MeV/u	14.0 nA	12.9 %

Progress on the charge breeding ECR ion source

G. Tabacaru, J. Arje, and D. P. May

The Charge Breeding ECR Ion Source (CBECR) is a key part in the Upgrade Project for the future re-acceleration of radioactive ion beams [1]. In the last year, the effort was concentrated to commission the CBECR and also to gain experience in tuning the injection beam line to the K500 cyclotron. The charge breeding is a complex process and theoretical works are not feasible to simulate and to describe in detail the process, so extensive experimental work is needed in order to achieve the final goal.

The ions to be charge breed, 1^+ charge state, were delivered by an ion gun from Heat Wave Labs [2] loaded initially with rubidium and afterwards, with cesium. The ion gun construction details can be found on the manufacturer website. Special attention was paid to the injection assembly from the ion gun into the CBECR. Downstream of the ion gun (see Fig. 1), an electrostatic steerer was installed in order to correct the ion gun misalignment and also a Faraday Cup Array was installed to measure the injected 1^+ ions current. There is no electrons suppression on this Faraday Cup, so no breeding efficiency can be inferred with reasonable uncertainty.

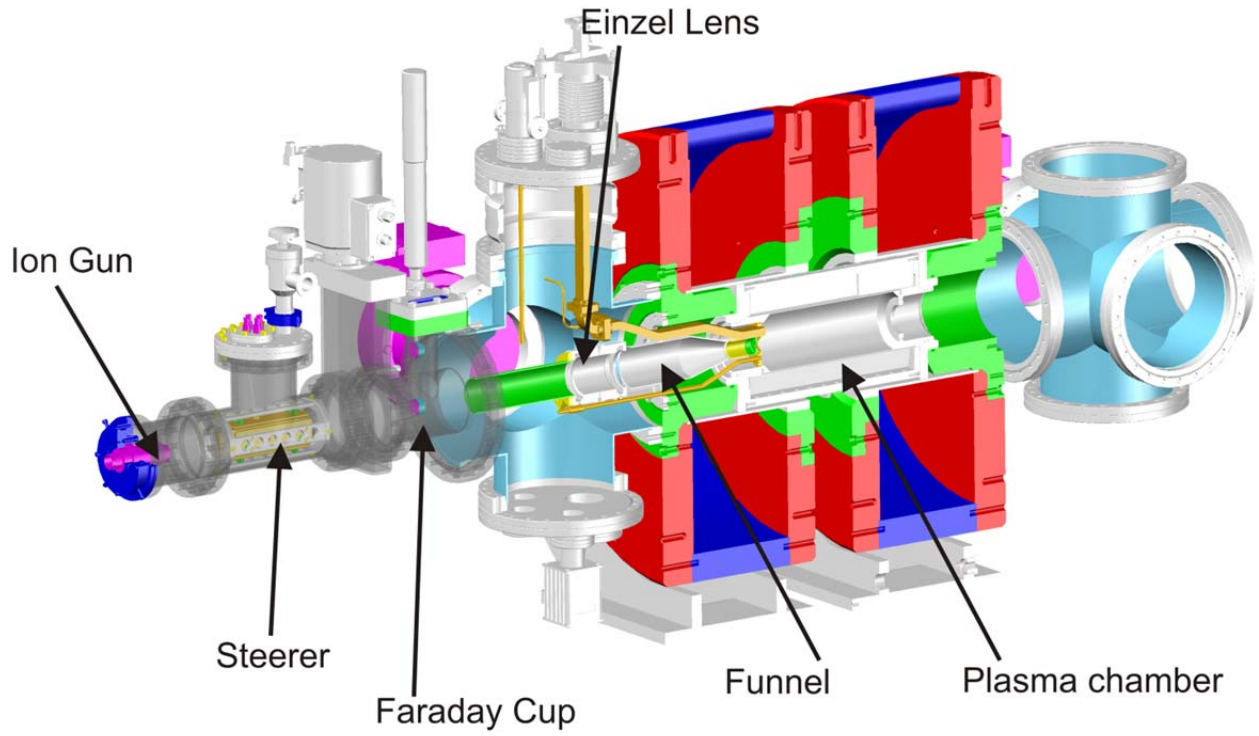

FIG. 1. Engineering drawing of the Charge Breeding ECR including the ion gun and the injection assembly.

The 1^+ ions from the ion gun have to overcome the ECRIS plasma potential in order to be trapped, thermalized and further ionized to achieve a higher charge state. Careful tuning of the injection elements is crucial and most of the effort was directed towards understanding and finding good settings to transport the 1^+ ions into the plasma chamber. Different charge state spectra were taken in various conditions: changing the microwave power transmitted, support gas load and injection settings. Initially, a computer program that monitors the analyzed current was used to follow variations of a specific charge state peak. Later, after finding robust signs of the breeding process, the usual charge state spectrum with the ion gun turned on and off was used to determine the strength of the process. Fig. 2 shows such a spectrum with the ion gun loaded with rubidium.

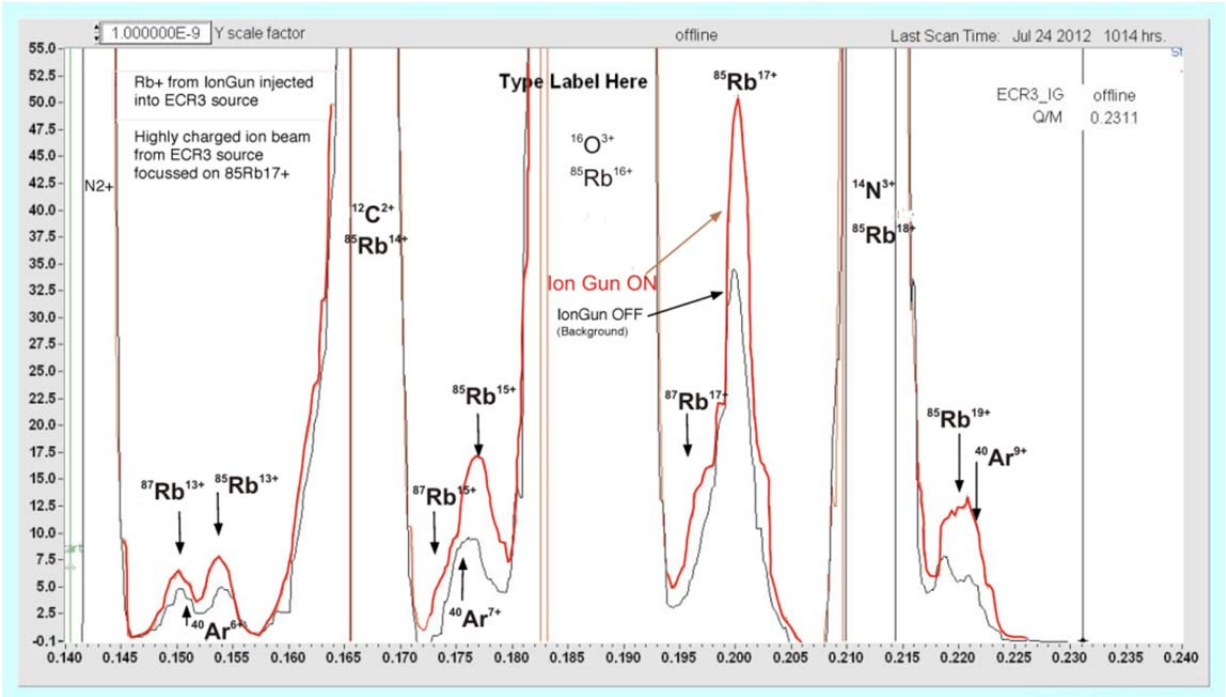

FIG. 2. Screenshot of the charge states spectrum showing the intensity variation of the $^{85}Rb^{17+}$ charge state when the ion gun was turned on or off.

When ion gun was loaded with cesium, and similar tests were performed showing a richer analyzed spectrum, and also a more efficient charge breeding process. Figure 3 represents a screenshot of the analyzed charge state spectrum with cesium used as the 1^+ ion source. It is noticed a multitude of higher charge states of cesium peaking at 24^+. These results are in agreement with the observation made by Vondrasek *et al.* [3].

The injected 1^+ ion current was not measured properly; consequently we cannot provide an efficiency figure for the charge breeding. Our tentative of efficiency measurements shows big discrepancy between rubidium and cesium breeding efficiency: from 0.5% for $^{85}Rb^{17+}$ charge state to 13.2% for $^{133}Cs^{24+}$ respectively.

Once the functioning of the CBECR was confirmed, we transported the new developed beams through the newly built injection beam line and accelerated with the K500 Cyclotron. The first

accelerated beam was $^{85}Rb^{15+}$ at the energy of 10 MeV/A using 8 kV CBECR extraction voltage. The new injection beam line transport efficiency was found to be excellent, and a current of 4.0 nA was measured at the cyclotron extraction, out of 29 nA analyzed $^{85}Rb^{15+}$ CBECR current. We also have accelerated $^{85}Rb^{17+}$ at the energy of 15 MeV/A and an extracted current of 6.4 nA, out of 64 nA analyzed $^{85}Rb^{17+}$CBECR current, was measured. $^{133}Cs^{24+}$ was accelerated also at the energy of 10 MeV/A and an extracted current of 14 nA was measured out of the Cyclotron for 108 nA analyzed $^{133}Cs^{24+}$ CBECR current. The average overall transport and acceleration efficiency was approximately 12 %. This exercise of accelerating the CBECR newly developed beams helped us also to debug and solve the inherent problems that appear to any commissioning of the new beam lines.

The CBECR is one of the key parts in the Upgrade Project and now it has demonstrated its functionality. The next step will be to couple the Light Ion Guide [4] to the Charge Breeding ECR and start the necessary tests to commission the two devices coupled together.

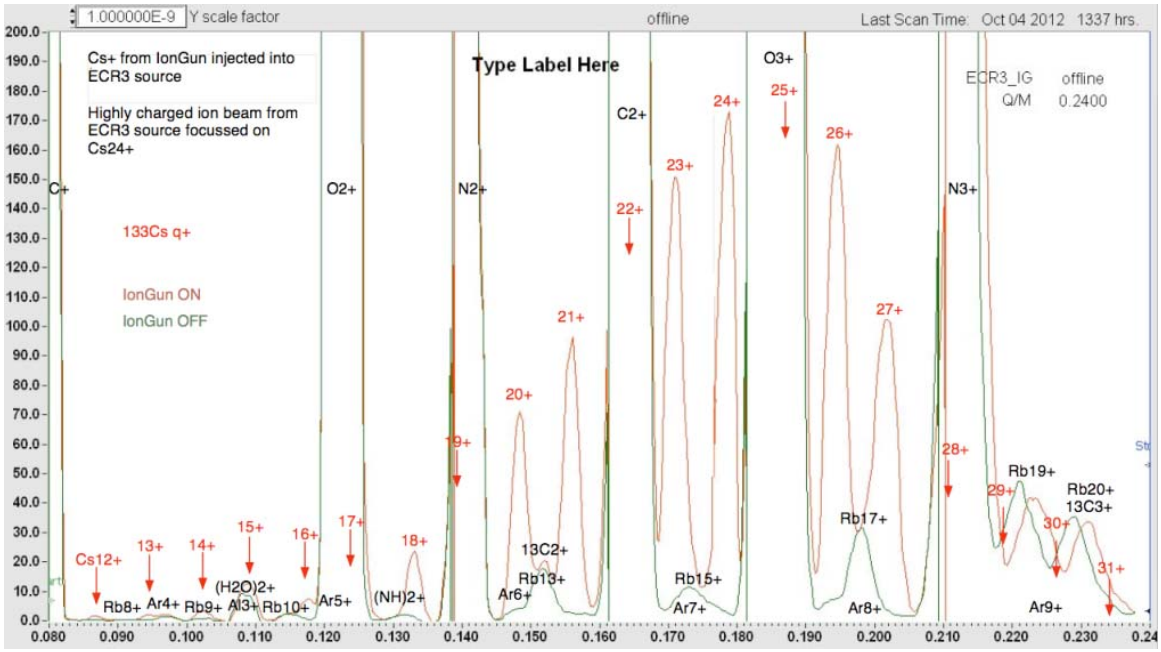

FIG. 3. Charge states analyzed spectrum with Cesium higher charge states pointed with red arrows.

[1] H.L. Clark *et al.*, *Progress in Research*, Cyclotron Institute, Texas A&M University (2011-2012), p.V-3;http://cyclotron.tamu.edu/2012%20Progress%20Report/5%20Superconducting%20Cyclotron%20and%20Instrumentation/V_6-15_ciup.pdf

[2] Heat Wave Labs, http://www.cathode.com/pdf/TB-171.pdf

[3] R. Vondrasek *et al.*, Proceedings of ECRIS2010, The 19th International Workshop on ECR Ion Sources, Grenoble, France, 2010; http://accelconf.web.cern.ch/AccelConf/ECRIS2010/papers/wecobk02.pdf

[4] G. Tabacaru, D. P. May, and J. Ärje, Proceedings of ECRIS2010, The 19th International Workshop on ECR Ion Sources, Grenoble, France, 2010; http://accelconf.web.cern.ch/AccelConf/ECRIS2010/papers/mopot010.pdf

Attenuation length in strip scintillators

Jonathan Button, William McGrew, Y.-W. Lui, D. H. Youngblood

I. Introduction

The ΔE-ΔE-E decay detector as described in [1] is composed of thin strip scintillators, which provide the ΔE signals, and of large block scintillators, which provide the E signals. An important characteristic of scintillators is the attenuation length λ of the light response, which is defined as the length for which the probability that a photon is not absorbed is 1/e. Due to the long and thin geometry of the strip scintillators (Saint Gobain BC408, dimensions 1mm x 1cm x 18cm), the attenuation length of the light response as quoted by Saint-Gobain (λ=210 cm) [2] is not appropriate because it is only valid for a bulk scintillator where the maximum distance from the connected PMT is small relative to the scintillator's height and thickness. A simulation of optical photon transport in the strip scintillators was used to make a more accurate estimate of the attenuation. The results of the simulation are then compared to analyzed data from a test run of the decay detector.

II. Calculated Attenuation Length

Of particular concern with the scintillator strips is the reduction of the light response due to photons which leave the scintillator when they strike a surface boundary of the material before entering the light guide. This was estimated by modeling the strip as a 3D rectangular volume (1 mm x 1 cm x 18 cm) in which photons are emitted randomly in position and momentum with an overall uniform distribution. The fraction of the emitted photons that reach the fiber optic cable is then obtained as a function of position along the strip.

When the photon strikes a boundary, if the angle of the photon trajectory relative to normal is greater than or equal to the critical angle (refractive index of 1.58) [2], then the photon reflects off the surface and remains inside the scintillator. For angles less than the critical angle, the reflection and transmission probabilities are calculated and then used to determine whether or not the photon remains inside the scintillator. The efficiency of the scintillator is determined by dividing the number of photons that arrive at the fiber optic end by the total number of photons generated. The efficiency is plotted with respect to initial position of the randomly generated photon from the end of the scintillator connected to the fiber optic bundle in Fig. 1. The simulated data were fit with a sum of two exponential decay curves ($y=a_1e^{-x/\lambda 1}+a_2e^{-x/\lambda 2}$). The first term is the transmission behavior for photons that travel directly to the end or have angles less than the critical angle measured with respect to normal of the refractive surface, effectively a "solid angle" for photons emitted which decreases rapidly with distance from the fiber optic connection. The attenuation length (λ_1 = 1.8 cm) for this mode of transmission is very short relative to the length of the scintillator. The second term is the transmission behavior for photons that are not incident on a surface or have angles greater than or equal to the critical angle when incident on a surface. The attenuation length (λ_2 = 104.3 cm) for this mode is much longer.

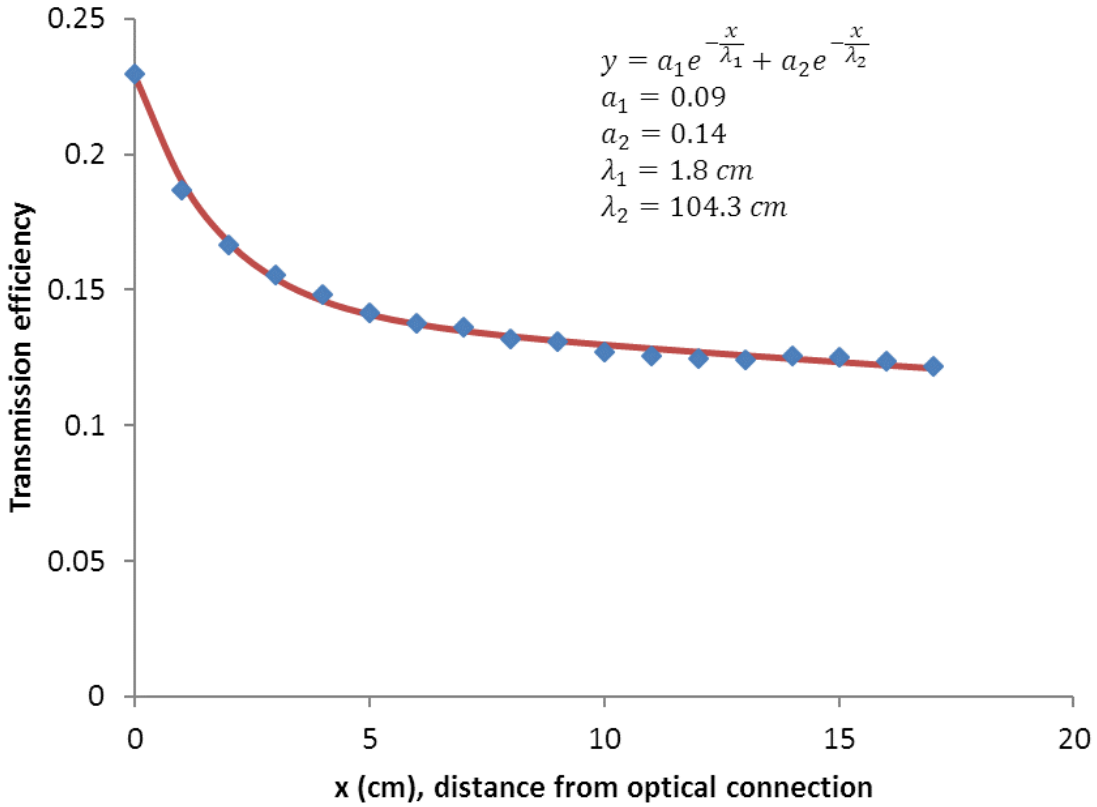

FIG. 1. Simulation result for the transmission efficiency of optical photons in a thin, strip scintillator (1cm x 1mm x 18 cm) with respect to the initial distance of the photon from the scintillator connection with its PMT.

III. Test Run Results

A test run of the completed decay detector was done using a beam of 30 MeV protons on a ^{12}C target. Overlapping segments of the vertically and horizontally aligned ΔE arrays form pixels which lie at some angle relative to the beam direction. In the array closest to the target, designated ΔE1, 13 scintillator strips are oriented vertically and are labeled V1 through V13, where V1 is the furthest left relative to the beam direction. V7 is centered above the beam path and is not of full-length. In the array ΔE2, 13 scintillator strips fill 12 horizontal rows labeled H1 through H12, where H1 is positioned at the top of the array. The H9 row is composed of 2 shorter length strips (H9L and H9R) located on the left and right of the beam path.

From the pixel geometry shown in Fig. 2, we know that the light response in the horizontal strips of the strip pairs which form the pixels should be the same (in the absence of the attenuation effect) at equal distances, left or right, from the center. This is because those pixels lie at equal angles with respect to the beam direction and will have the same energy deposited. The attenuation length in the individual

strips can then be measured by comparison of the light response from the symmetric pixel pairs about the detector center. This method has the advantage of not relying on estimates of the energy deposited.

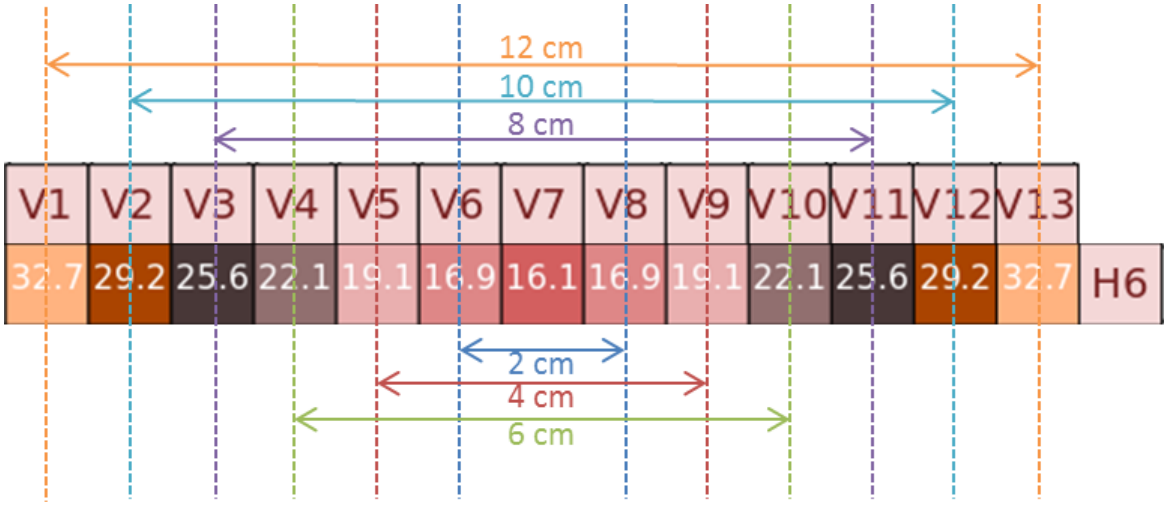

FIG. 2. Median distances between pixels that would have an equal light response in the absence of the attenuation. The value shown inside each pixel is the angle of that pixel relative to the beam direction.

The energy resolution in the 2D ΔE1-ΔE2 spectra is too large to distinguish the different energy protons (Fig. 3). However, examining the 2D ΔE1-ΔE2 spectra is advantageous for determining the attenuation length because of the smaller pitch between strip scintillators than between block scintillators.

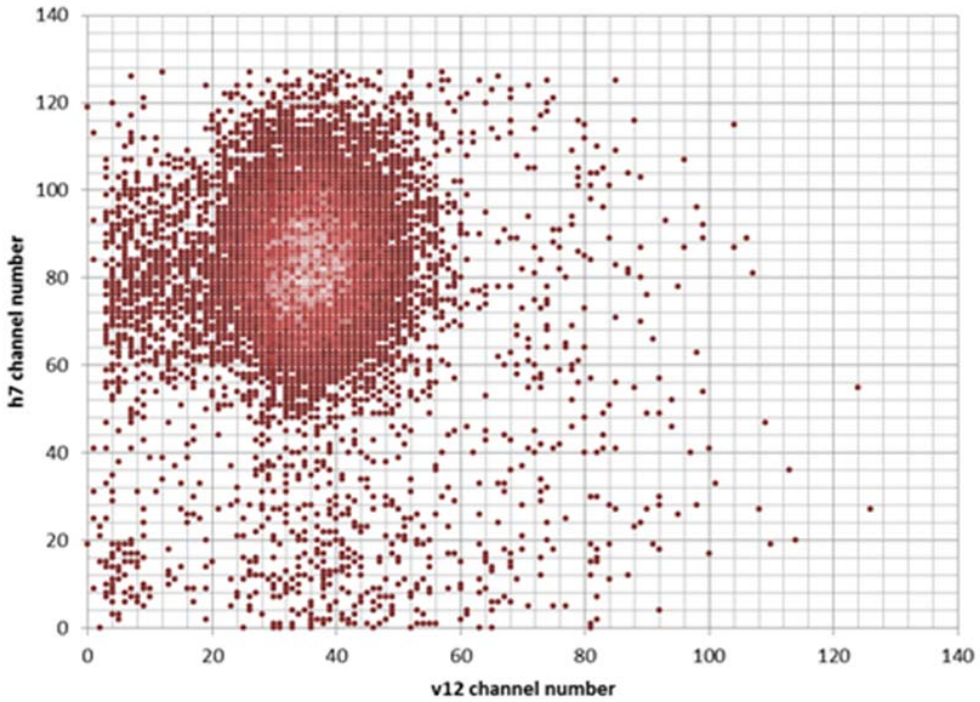

FIG. 3. An example ΔE1-ΔE2 2D-spectrum. The three peaks visible in the ΔE2-E 2D-spectra are not visible here due to the poorer energy resolution of the strip scintillators.

The ratio of the light response in the symmetric pixel pairs (relative light transmission = light response in the pixel further away from the optical connection / light response in the pixel closer to the optical connection) can be directly compared to the result from the simulation of the attenuation behavior (Fig. 1). The light response is taken to be the average peak position in the raw spectra and is shown in Fig. 4. The calculated ratios of the light responses are also shown in Fig. 4. The calculated ratios assume λ_1 = 1.8 cm and λ_2 =104.3 cm. Since none of the pixels are within 3 cm of the optical connection, the fits to the measured attenuation is not sensitive to the value of λ_1. They are shown for varying values of the distance from the optical connection to the pixel coincident with vertical strip V7 (which sits at the center of the vertical strip array). This distance is difficult to measure precisely because when the strips are wrapped and installed onto the frame, the position of the optical connection is hidden from view. Consequently, the distance between the center of the array and the optical connection for the horizontal strips used to calculate this attenuation length has a large uncertainty and is taken to be 10±1 cm. The

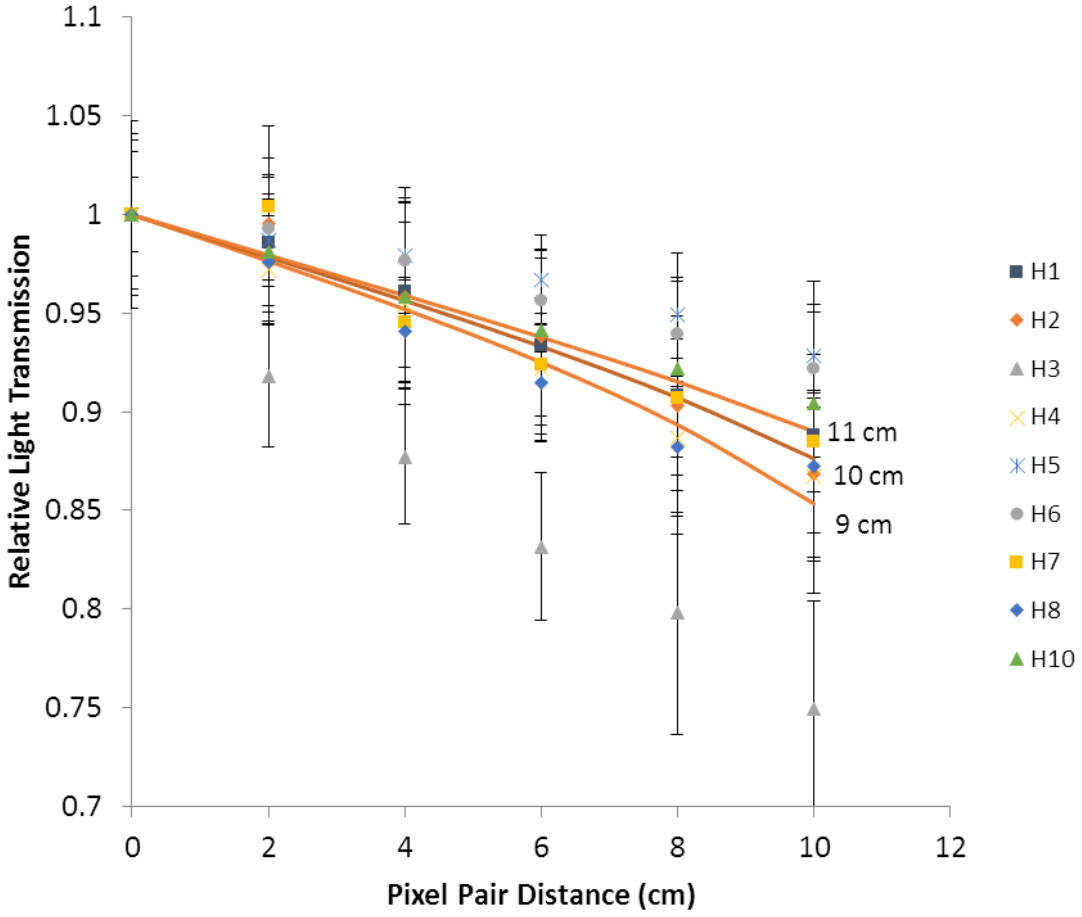

FIG. 4. Relative light transmission in horizontal strips vs. the distance between pixel pairs. The relative light transmission is the ratio of the light responses between the paired pixels. The pixel pair distance is described in Fig. 2. The plotted lines are the calculated values of the relative light transmission for varying distances (11 cm, 10 cm, and 9 cm) from the optical connection to the V7 strip.

measurement fits within the calculated range in all but three of the horizontal strips (H3, H5, and H6). In strip H3, the transmission efficiency decays faster than expected. The best fit to the data from strip H3 gives attenuation lengths of λ_1 = 1.8 cm and λ_2 = 36.4 cm. Damage to the scintillator strip is a possible cause of the shorter attenuation length λ_2. In strips H5 and H6, the observed attenuation length, λ_2 = 165 cm, is much longer than expected but λ_1 = 1.8 cm in these strips as well. Further tests should be done with these strips in order to understand the cause of the better than expected performance.

IV. Conclusion

The response by the ΔE1 and ΔE2 layers in coincidence was used to make a measurement of the attenuation length of the light response. Analysis of the attenuation behavior as a function of the distance between symmetric pixel pairs showed that the majority of the horizontal strips are working as expected. The attenuation behavior should be measured consistently in this manner in order to ensure that the strips are in good condition.

[1] J. Button, Master's Thesis, Texas A&M University, 2013.
[2] Saint-Gobain Ceramics & Plastics, Inc., Saint-Gobain Ceramics & Plastics, Inc. BC 400-404-408-412-416 Data Sheet, 2008), 2012.

Automatic degrader changer

M. Bencomo and J. C. Hardy

The purpose of this project is to design, build and install a remote controlled degrader changer for the tape transport system. The changer will allow a more efficient use of beam time by reducing the time it takes for a person to finely adjust the degrader thickness at the beginning of an experimental run. This changer consists of two thin wheels (0.0625 in) with radius 2.50 and 3.85 in. and with 3 and 8 slots, respectively, for different degrader thicknesses. These wheels will be rotated to different positions by two independent stepper motors using Arduino UNO microcontrollers interfaced with Processing software.

Arduino controllers are an open-source-based electronics with their own programming language based on Java, C and C++ [1]. These microcontrollers provide an efficient way to move the stepping motor to the required position with the precision of a fraction of degree, depending on the number of steps in the motor. Similarly, *Processing*, which is an open-source programming language for visual

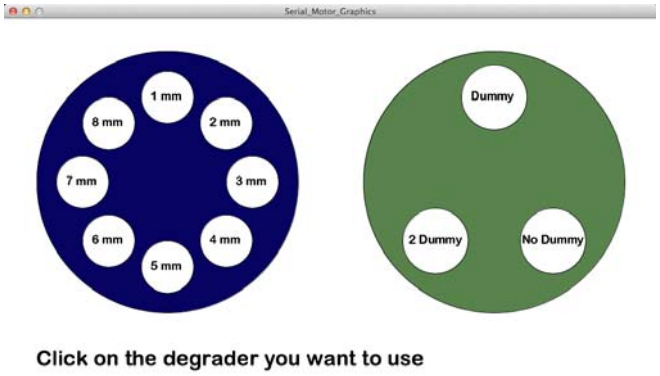

FIG. 1 Graphical user interface written with Processing.

FIG. 2. Arduino UNO microcontroller.

design, also based on Java and C, and developed at MIT Media Lab [2], provides the tools to create the interface for the controllers. So far, code for both the controllers and the interface (see Fig. 1) has been written and tested as well as the serial port communication between them. The Arduino microcontroller is shown in Fig. 2.

The experimental set up was not to be modified, which created some spatial restrictions that complicated the physical design. After several designs had been created and rejected, it was decided that the wheels would be separately supported and driven. Some supports and stands will have to be built to hold the stepper motors in place in order for the degrader slots to be in the correct position. All components will be made out of aluminum for strength and lightness. Currently, the design has been approved, all supports and wheels are being built, and the installation is expected to be completed by the end of May 2013.

The figures below show the different parts needed for this project. Everything in grey represents unmodified components of the experimental set-up; red shows the supports for the stepper motors, which

are themselves shown in black; green is for a minimally modified degrader stand and blue is the color of the wheels.

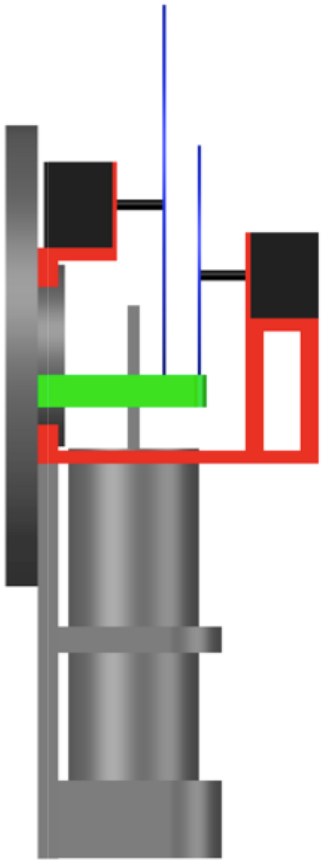

FIG. 3. Side view of degrader changer.

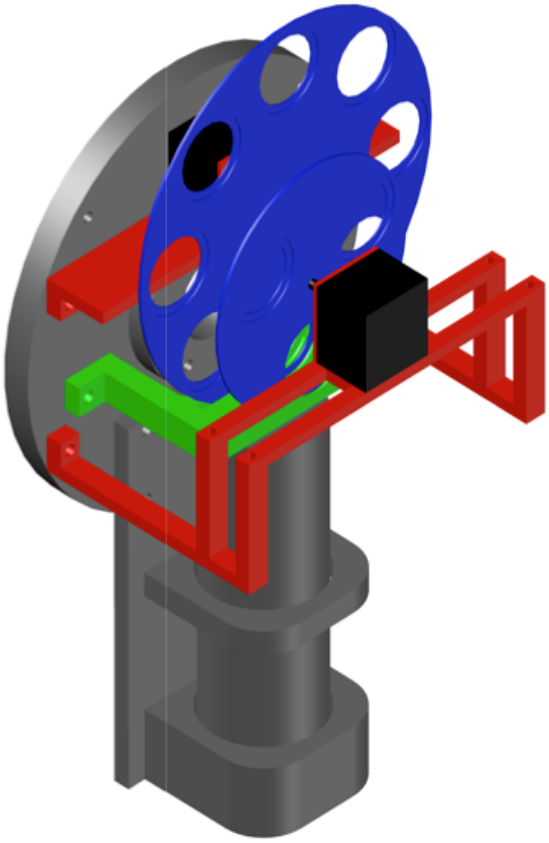

FIG. 4. Isometric view of degrader changer.

[1] http://arduino.cc
[2] http://processing.org

High-precision nuclear beta decay half-life measurement of $^{26}Al^{m}$ by a digital beta counting method

L. Chen, J. C. Hardy, M. Bencomo, V. Horvat, N. Nica, and H. I. Park

We have been developing a digital β-counting system over the past few years. Its principle and some preliminary test results were reported in last year's progress report [1]. In 2012-13 we have finished the data analysis of an on-line experiment in which the digital counting method was used to measure the $^{26}Al^{m}$ half-life. A detailed paper has been submitted recently for publication in Nuclear Instruments and Methods [2]. Here we report some details of the data analysis and the results of our on-line measurement of the $^{26}Al^{m}$ half-life.

By using pulse-shape analysis, we can now clearly distinguish a true β signal from a spurious one. Since we also record the time of arrival of each pulse, we have been able to examine time correlations between the two types of events. The measured time separation between successive events is plotted in Fig. 1, where the two panels illustrate the same data but are displayed with different time scales.

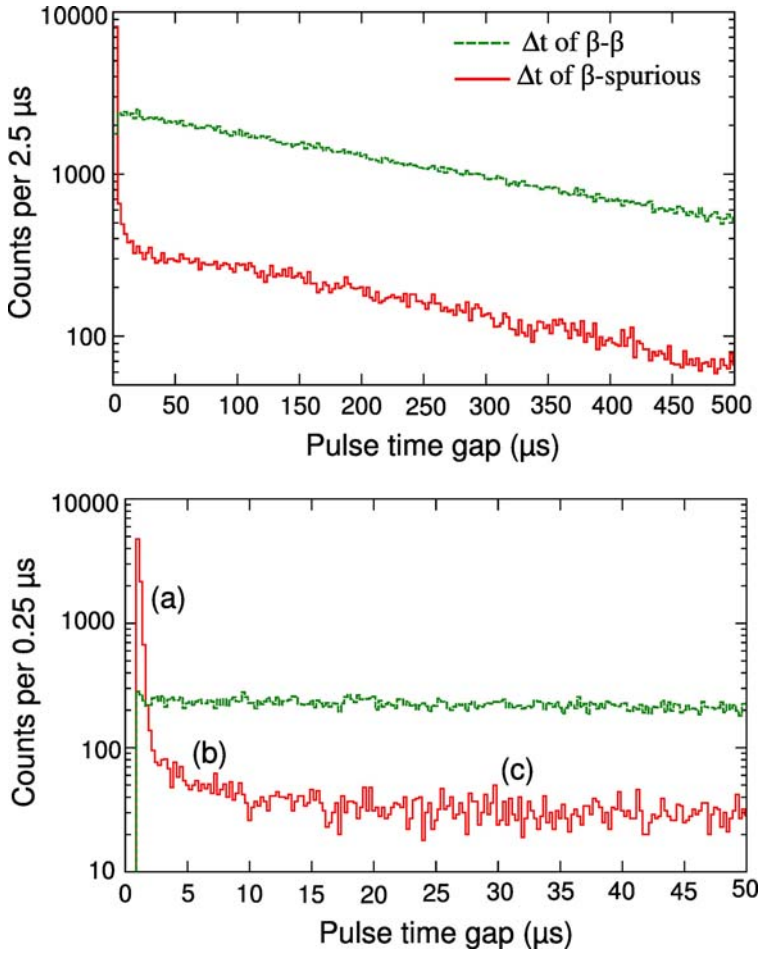

FIG. 1. The top panel plots the time-gap distribution of pulses over a period of 500 μs, measured with a 3 kBq β source at a detector bias of 2700 V. The bottom panel shows a zoomed-in plot of the same data to show the short-time details of the distribution.

The histograms identified as “β-β” give the distribution of time-gaps between two identified β's. The histograms identified as “β-spurious" give the distribution of time gaps that begin with an identified β event and end with a spurious pulse. In the bottom panel, the β-spurious histogram exhibits three different slopes, which are denoted as (a), (b) and (c). The first two correspond to fast spurious signals which appear within ~1 μs and ~10 μs, respectively, after a β signal. The third has a slope very similar to that of the β-β histogram. The results in Fig. 1 demonstrate that some spurious pulses are tightly time-correlated with a particular β signal: the events in the first 10 μs that contribute to the part of the histogram with slopes (a) and (b). However, the spurious events that constitute the remainder of the β-spurious plot, with slope (c), are probably not -- at least not within the time scale to which we are sensitive. Slope (c) is identical to the slope of the β-β histogram and reflects the fact that, after a β event has “started the clock", the appearance of a second β stops the clock, thus eliminating the possibility of a β-spurious correlation being recorded.

To characterize the performance of our digital counting system, we performed an on-line test experiment to measure the 6.345-s half-life of the superallowed β^+ emitter $^{26}Al^m$. The half-life of $^{26}Al^m$ has been measured before by a number of groups with consistent results [3,4,5] so it can serve as a good standard for test purposes.

The on-line measurement dead time for each event was 800 ns. To correct for lost events we followed the shadow window technique, which was introduced by Lynch in a recent measurement of the muon half-life [6]. This technique, schematically illustrated in Fig. 2, is a statistically correct method, which is also independent of the counting rate. After each recorded event, real or spurious, there is a dead-time during which real β events might be missed. We determine the possible loss for each event by placing a time-window with the same length as the dead-time at some predetermined time later (or earlier) in the same cycle. If the time between the observed event and this shadow window is much shorter than the decay half-life being measured, then the contents of the shadow window accurately reflect the loss due to the original dead-time. If the shadow window includes an event, then it too is partially dead and a second (shorter) shadow window to account for its dead time must be applied after a second delay. This process continues until no event is observed in the shadow window.

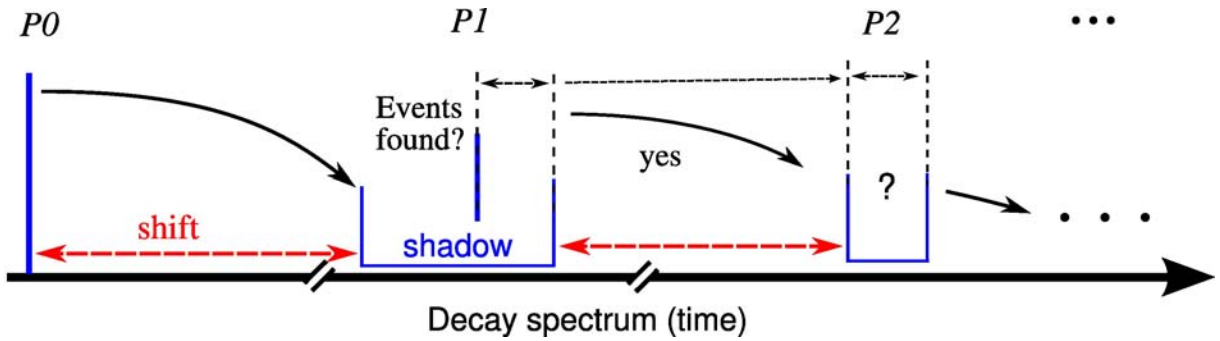

FIG. 2. A schematic illustration of the shadow window technique used to correct for dead time. P0 is the original pulse and P1 and P2 are events that may appear (or may not) in the first and second-order shadow window, respectively. The first order shadow window has the same length as that of the system dead time. The second-order window, if required, has a length equal to the part of the first-order window that is made dead by the appearance of P1. The process continues to a third-order window if P2 occurs, and so on.

In principle, to be reliable this method requires only that the delay time between the event and the shadow window be much shorter than the decay half-life; in reality, we found that the shadow window cannot be placed too near the original pulse on the down-stream side since there is a significant probability of a correlated β-spurious pair of events within a few hundred μs of one another (see Fig.1). We chose to avoid this problem by placing the shadow window 10 ms later than the original pulse to totally avoid this problem. That is corresponding to a 0.16% shift in terms of the half-life of $^{26}Al^{m}$. And in our analysis, we got consistent results when the shadow window was placed 50 μs in the up-stream side or 5 ms in the down-stream side.

After dead-time corrections had been made, we built a decay spectrum for each tape cycle. We then used the same fitting procedure as described in our previous papers (for example, Ref.[7]). We also artificially introduced into our software analysis a dead time after each event, which was significantly longer than the system's inherent 800 ns dead time. This way the software could also examine if any events appeared near the end of the imposed dead time and increase the shadow length in that case to incorporate the component of the inherent dead time that extended beyond the end of the imposed one. We reanalyzed our data a number of times with imposed dead times that ranged from 2 μs to 12 μs. The result is plotted in Fig. 3. The result we ultimately quote is from the analysis with an imposed dead time of 4 μs.

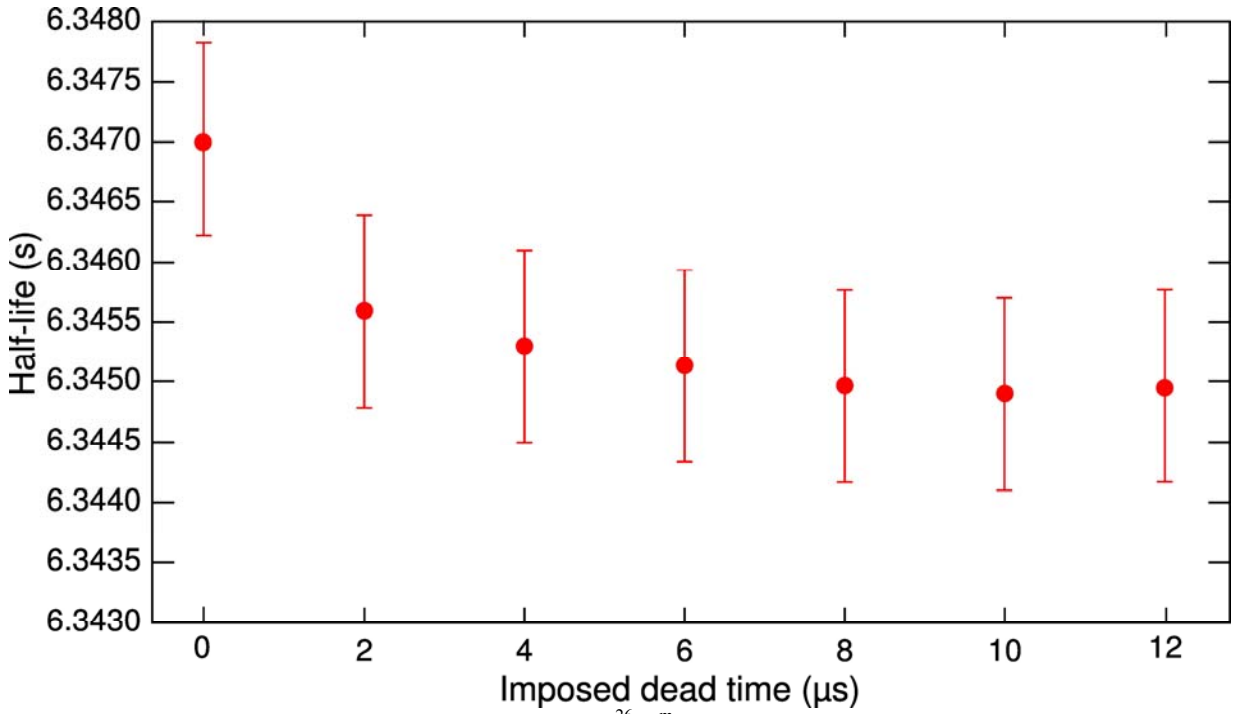

FIG. 3. Half lives obtained from the measured decay of $^{26}Al^{m}$ plotted as a function of the imposed dead time used in analysis. Note that the total dead time is equal to the imposed dead time or the inherent system dead time (800 ns), whichever is greater.

All spectra were fitted with the ROOT Minute2 package using the Maximum Likelihood method. Our fitting code was also tested with Monte Carlo generated decay data, in which there were 10^{9} events

with a decay half-life set to 6.34500 s. The half-life we obtained from fitting the simulated data was 6.34502(25) s, which successfully confirmed our fitting routines.

The evaluated half-lives of the 14 runs taken with 2650, 2700 and 2750 V detector bias are plotted in Fig. 4. Four runs with 2800 V bias, which is just above the plateau region, had significantly more spurious events and their overall analysis was not as satisfactory as it was for the other runs with lower bias voltages well within the plateau region, so we decided to eliminate them entirely. The average value of the results in Fig. 4 is 6345.30±0.90 ms.

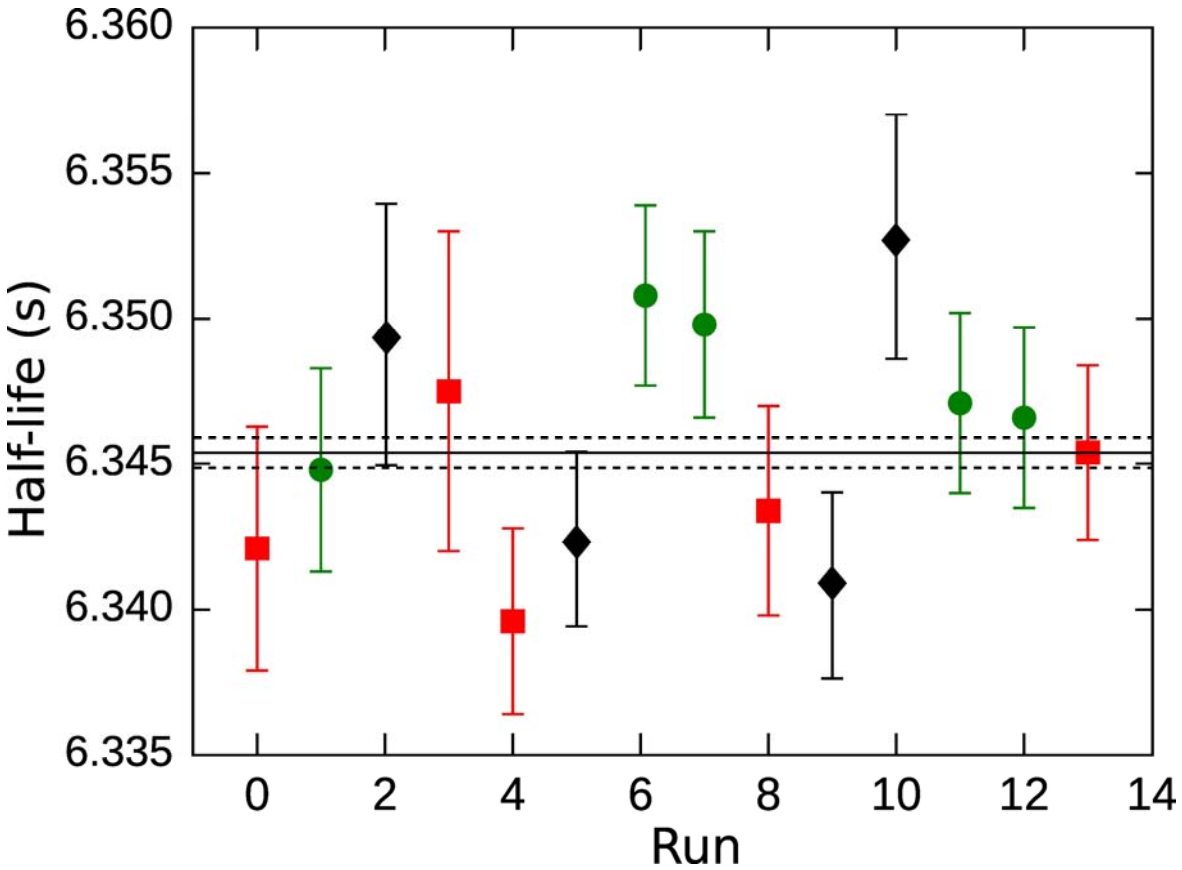

FIG. 4. The evaluated half-lives of 14 runs. The runs with bias 2650 V, 2700 V, 2750 V are represented by diamond, square, and circle, respectively.

In Fig. 5 we regroup the individual cycles according to their initial β-decay counting rate and obtain a half-life from each group. It is gratifying to see that there is no systematic dependence of the measured half-life on the experimental counting rate. All potential impurities identified at the MARS focal plane are stable isotopes so there is no need to incorporate any systematic uncertainty to our $^{26}Al^{m}$ half-life result to account for sample impurities. We therefore quote our final result for the $^{26}Al^{m}$ half-life to be 6345.30±0.90 ms, where the uncertainty is determined by counting statistics alone. This result is consistent with the 2009 published world average, 6345.0±1.9 ms [3], but has twice the precision. Our result also agrees with two measurements that have been published since 2009: 6346.54±0.46(stat)±0.60(syst) ms [4] and 6347.8±2.5 ms [5].

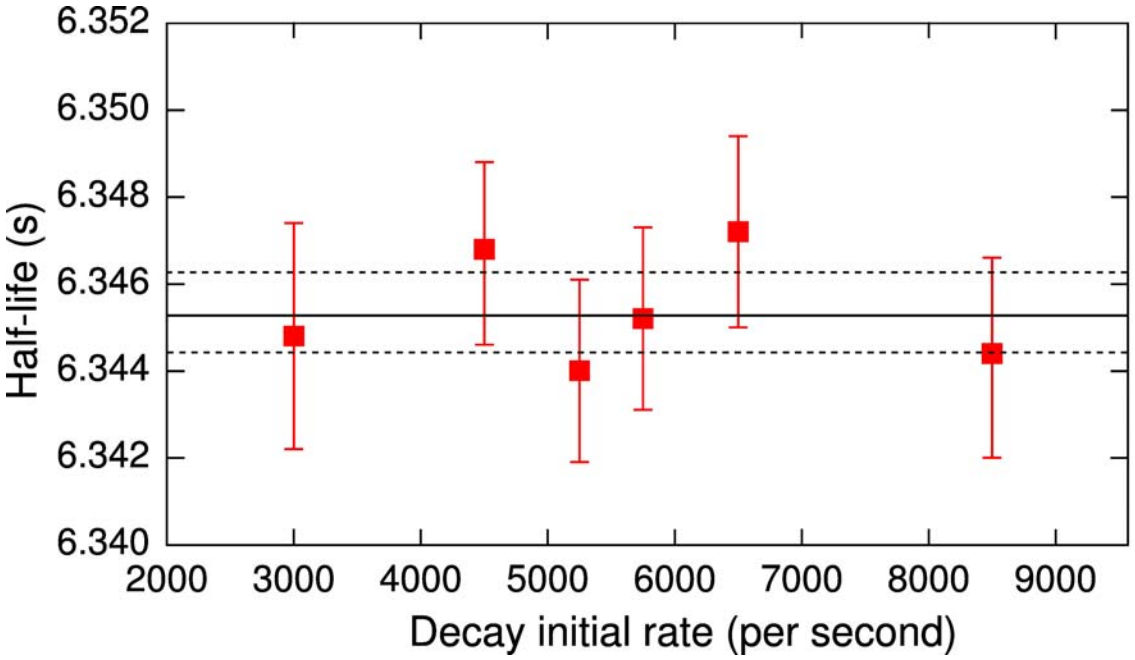

FIG. 5. The evaluated half-lives of as a function of initial decay rates. Cycles are regrouped in 6 groups according to their initial decay rate (in thousand per second): (2-4), (4-5), (5-5.5), (5.5-6), (6-7) and (7-10). The ranges for each group were chosen to include approximately equal numbers of events. The half-life results are plotted at the mid-point of each range.

[1] L. Chen and J.C. Hardy, *Progress in Research*, Cyclotron Institute, Texas A&M University (2011-2012), p. V-24.

[2] L. Chen, J C. Hardy, M. Bencomo, V. Horvat, N. Nica, and H.I. Park, Nucl, Instrum. Methods. Phys. Res. A. (submitted).

[3] J.C. Hardy and I.S. Towner, Phys. Rev. C **79**, 055502 (2009).

[4] P. Finlay, S. Ettenauer, G.C. Ball *et al.*, Phys. Rev. Lett. **106**, 032501 (2011).

[5] R.J. Scott, G.J. O'Keefe, M.N. Thompson and R.P. Rassool, Phys. Rev. C **84**, 024611 (2011).

[6] Kevin R. Lynch, Nucl. Phys. **B189**, 15 (2009).

[7] E. Iacob, J.C. Hardy *et al.*, Phys. Rev. C **82**, 035502 (2010).

Time-interval analysis of β decay

V. Horvat and J. C. Hardy

Work on the event analysis of β decay [1] continued and resulted in the development of a novel method of beta-decay time-interval analysis that produces highly accurate results for the half-life, decay rate, and background rate, regardless of the event rate, nature of the detection-system dead time, and/or extent of the dead time, while being conceptually simple, free of notable numerical challenges, fast and exact. The method applies when event arrival times are measured and recorded individually, which can be accomplished easily using existing electronic modules, such as time-to-digital converter (TDC) or waveform digitizer (WFD). These modules are controlled by means of a personal computer, using customized software developed in our lab.

This report describes the principles behind the *time-interval analysis method* and demonstrates its robustness based on an example involving simulated events.

The half-life of a β-decaying nuclide is determined from the known time-dependence of the event rate expected under ideal conditions (i.e., in the absence of the detection system's dead time), which is described by a function we denoted by ρ and call the *ideal rate function*. For example, in the case of a single-component decay in the presence of a constant background B,

$$\rho = A \exp(-\lambda t) + B \,, \tag{1}$$

where A is the initial ideal rate (at time $t = 0$) in the absence of background, and

$$\lambda = \ln(2) / T_{1/2} \tag{2}$$

is the nuclide-specific decay constant, which is related to the nuclide's half-life $T_{1/2}$. Here it is assumed that the system's detection efficiency does not depend on ρ.

The time-interval analysis method was derived based on Eqs. (9) and (10) of Ref. [1], which express the probability dp that an event occurring at time zero will be followed by the next event in the time interval [t , t + dt), provided that a known detection-system dead time t_d follows the event detected at time zero:

$$dp = \Theta(t - t_d) \exp[- \langle\rho\rangle_d (t - t_d)] \, \rho_t \, dt \,, \tag{3}$$

where

$$\langle \rho \rangle_d = \frac{1}{t - t_d} \int_{t_d}^{t} \rho(t') dt' \quad ; \tag{4}$$

ρ_t is the value of ρ at time t; and $\Theta(t - t_d)$ is the Heaviside (unit-step) function. The Heaviside function reflects the fact that the probability of detecting an event in the time interval [0, t_d) equals zero.

Consequently, dp on the left-hand side of Eq. (3) is also the probability of detecting an event in time interval [t, t + dt) following the detection of no events in the time interval [t_d, t). In fact, replacing t_d in Eqs. (3) and (4) with $t - t_l$, where t_l is the detection-system live time preceding the detection of the event at time t, yields

$$dp = \Theta(t_l) \exp[- <\rho>_l t_l] \rho_t \, dt \, , \tag{5}$$

where

$$< \rho >_l = \frac{1}{t_l} \int_{t-t_l}^{t} \rho(t')dt' \, . \tag{6}$$

The key element in the time-interval analysis method, which ensures that the method is exact (i.e., not involving any approximations in its concept), is to know t_d exactly. Unfortunately, in reality, the actual value of t_d cannot be determined exactly for each measured event. However, if the timing of each measured event is recorded, it is possible to impose, by means of software, a known fixed *extendable* dead time τ_e that follows each measured event. The measured (primary) events that are not eliminated by the imposed dead time can then be used to form a secondary event set. If τ_e is set to be equal to (or greater than) the largest actual dead time t_d in the original (primary) event set, then the actual dead time t_d, as well as the actual live time t_l, for each event in the secondary set can be determined exactly. Consequently, an exact analysis can be performed on the secondary event set, even though the nature and/or the extent of the detection-system dead time may not be known exactly for each event in the primary set.

To ensure that the dead time τ_e imposed on the events recorded in a real measurement is sufficiently large but not too large (to avoid removing too many events), analysis of the primary-event set must be performed several times, each time with a different value of τ_e. By plotting the results of the analyses as a function of τ_e, it should be straight-forward to determine the best value of τ_e (here denoted by τ_m), below which the results show a trend, and above which the results vary randomly. The extent of the random variations for $\tau_e > \tau_m$ must be smaller than those normally expected based on the number of events analyzed. This is because the secondary event sets obtained from the same primary event set by imposing different values of τ_e are not statistically independent.

The goal of data analysis is to determine the best estimates (or most-likely values) of the parameters of ρ and their uncertainties. In the time-interval analysis method, as applied to a single measurement of beta decay that started at time $t = 0$, this is accomplished by evaluating quantity Z, which is proportional to the probability of obtaining, in a repeated measurement under the same conditions, the actual time sequence of events that survived after the dead time τ_m had been imposed. Then

$$Z = \exp(-\int_{t_z}^{t_f} \rho dt) \prod_{i=1}^{N} (dp/dt)_i \, , \tag{7}$$

where

$$(dp/dt)_i = \Theta[t_l(i)]\exp[-\int_{t_i - t_l(i)}^{t_i} \rho(t')dt']\rho_i \quad ; \tag{8}$$

N is the total number of such events; t_i (i = 1, 2, …, N) is the instant when the i-th event occurred; $t_l(i)$ is the detection-system live time period *preceding* event i; t_f is the instant when the measurement ended; ρ_i is the value of the ideal event rate at time t_i; and

$$t_z = \min(t_f\ ,\ t_N + \tau_m)\ . \tag{9}$$

The exponential function in Eq. (7) represents the probability of measuring no events in the time interval (t_N , t_f).

Finally, the parameters of ρ [i.e., A, $T_{1/2}$, and B, if ρ is assumed to be given by Eqs.(1) and (2)] are varied iteratively in order to find the set of their most-likely values, which are taken to be those that maximize the value of Z. For practical reasons, this is done by minimizing the value of quantity E given by

$$E = -2\ln Z\ . \tag{10}$$

If several measurements are analyzed simultaneously so that, for example, a common value of $T_{1/2}$ can be determined, the parameters of ρ are varied iteratively in order to maximize the *product* of Z-values or to minimize the *sum* of E-values obtained for each measurement. The uncertainty of any parameter of ρ is obtained as the square root of the corresponding diagonal element of the inverse of the Hessian matrix of E.

Accuracy and statistical consistency of the results can be best assessed by applying the time-interval analysis method to simulated event sets that have been constructed based on imposed values for the parameters of ρ. The simulated event sets used to test the time-interval analysis method were made to mimic those obtained in the actual measurements of the ^{26m}Al half-life, which used the K-500 superconducting cyclotron, the Momentum Achromatic Recoil Separator, and the Precision On-Line Decay Facility at Texas A&M University [2]. Specifically, it was assumed that ρ is given by Eqs. (1) and (2), with B =1 s^{-1} and $T_{1/2}$ = 6.3452 s [3], while A ranged from 10^2 s^{-1} to 10^5 s^{-1}. The original sets of simulated events were made assuming that there is no dead time, but a dead time per event (τ_m) of up to 512 μs, as needed, was imposed on the data by the software before the beginning of the time-interval analysis. The total number of events in each primary set was about 60 million, which corresponds to a statistical precision slightly above 0.01%. The number of individual decay measurements in each simulated event set ranged from 66 at A = 10^5 s^{-1} to 57,693 at A = 10^2 s^{-1}. Each simulated measurement was assumed to last 125 s, which corresponds to about 20 half-lives.

In order to distinguish between the values of B, $T_{1/2}$, and A, on which the event simulation was based, and the corresponding values obtained in the analysis of the simulated event sets, lowercase symbols a, $t_{1/2}$, and b will be used for the latter.

To assess the meaningfulness and quality of results from the time-interval analysis method, a 500-channel decay spectrum was constructed for each simulated measurement, along with the corresponding spectrum of predicted values. These predicted values were obtained for each channel by integration of the most-likely ideal event rate ρ (as obtained in the analysis) over time, from the channel lower limit to the channel upper limit, while skipping the time intervals within the channel that were covered by the dead time. The corresponding channel contents of the individual spectra from the same set were then combined to construct a single spectrum in order to present statistically more meaningful results and to amplify and expose any systematic errors that might have occurred in the data analysis. An example of a spectrum and the results obtained this way are shown in Fig. 1.

Fig. 1 demonstrates that the time-interval analysis method produces accurate results, in particular

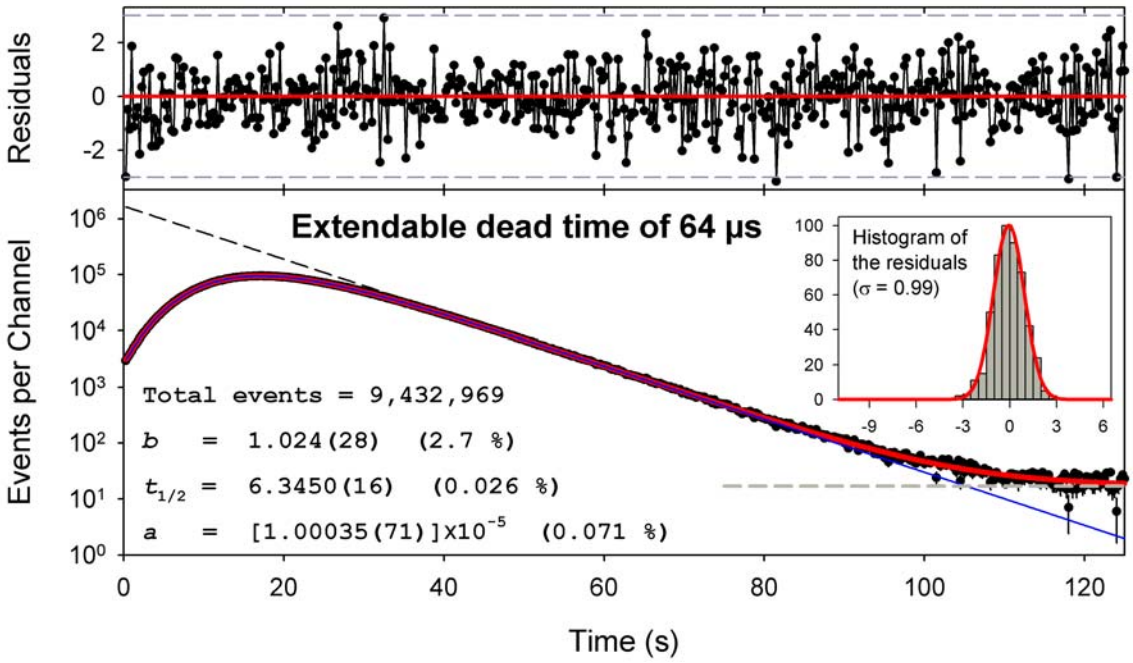

FIG. 1. Results of the time-interval analysis presented in the form of the combined decay spectrum and the corresponding spectrum of the residuals for the case of a simulated ideal event set obtained assuming $A = 10^5$ s^{-1}, $B = 1$ s^{-1}, and $T_{1/2} = 6.3452$ s, on which an extendable dead time of 64 μs was imposed. In the decay spectrum, the data points represent the number of events in each (0.25 s wide) channel, the thick solid (red) lines represent the expected values calculated based on the best estimates of the ideal rate parameters obtained in the analysis (and on the imposed dead time). Likewise, the thick dashed (gray) lines represent the background, while the thin solid (blue) lines represent the decay component. The thin dashed (black) lines represent the expected results under ideal conditions (i.e., no dead time). The residuals are shown as a function of time in a separate graph located above the corresponding graph of the decay spectrum, while their histograms are shown as inserts in the decay spectrum graph, using grey bars. Each histogram of the residuals was fitted by a Gaussian function. The best fit is shown by the solid (red) line and the best-fit standard deviation (σ) is indicated in the graph

for $t_{1/2}$, even in the case in which the decay spectrum is drastically distorted due to the presence of an *extendable* dead time. Note that the example shown in Fig. 1 is rather extreme and was chosen only to demonstrate the robustness of the time-interval analysis method.

[1] V. Horvat and J. C. Hardy, *Progress in Research*, Cyclotron Institute, Texas A&M University (2011-2012), p. V-28.
[2] http://cyclotron.tamu.edu/
[3] J.C. Hardy and I. S. Towner, Phys. Rev. C **79**, 055502 (2009).
[4] V. Horvat and J.C. Hardy, Nucl. Instrum. Methods Phys. Res. **A713**, 19 (2013).

Tests of the system to measure branching ratios

V. E. Iacob, H. I. Park and J. C. Hardy

Since we announced the last improvements in our branching-ratio setup [1] we have carried out a series of thorough tests. We present here results obtained in measurements performed on a β^+ source (^{22}Na) and in an on-line radioactive beam measurement (^{38}Ca). While in the case of the ^{22}Na source the average positron energy is about 220 keV (with the main branch end-point energy, E_{max}=546 keV), in the ^{38}Ca case the average positron energy is 2430 keV (with the main branch end-point energy, E_{max}=5590 keV).

Both experiments confirm the improvement of the data throughput obtained *via* a reduction in the number of "incomplete events", events that are identified by a β-γ coincidence trigger but are missing either the γ or the β energy signal, usually because it is below the corresponding spectrum cut-off energy. (Details about the event structure are given in [1].) Table I summarizes the results obtained in measurements, each lasting about one week. The relative losses are all below 0.1%, allowing for reliable data reduction at a precision of 0.1% or better, as required [2].

Table I. Experimental losses in β-γ coincidence events.

experiment	E_β induced losses	E_γ-induced losses
^{22}Na	0.04%	0.01%
^{38}Ca	<0.1%	<0.07%

The improved data transmission should not be confused with an improved absolute detection efficiency of the β and/or γ particles: The electronics processing the corresponding signals are still subject to detection thresholds that ultimately limit the absolute efficiency of the system. This is particularly important in the case of the efficiency of the β detector, which receives a spectrum that extends down to nearly zero energy, thus making the lowest energy events impossible to disentangle from noise. However, only the relative efficiency of the β detector is important in our branching-ratio measurements, so the cut-off effects caused by the electronic threshold in the β chain are relatively unimportant.

The last remark is particularly significant in the ^{22}Na source measurement: The source measurement is convenient as an off-line test, but it places a significant part of the emitted positrons below the detection threshold; this in turn makes the measurements more dependent on the value of the threshold used to remove noise contamination. Fig. 1 presents the energy release (ΔE) spectrum as measured with the ^{22}Na positron source, along with a Monte-Carlo generated spectrum from the EGSnrc [3] simulation code. While the shape of the simulated spectrum is a good match to the experimental one, it is obvious that a significant part of the real events were not analyzed by the setup as the β energy did not exceed the threshold.

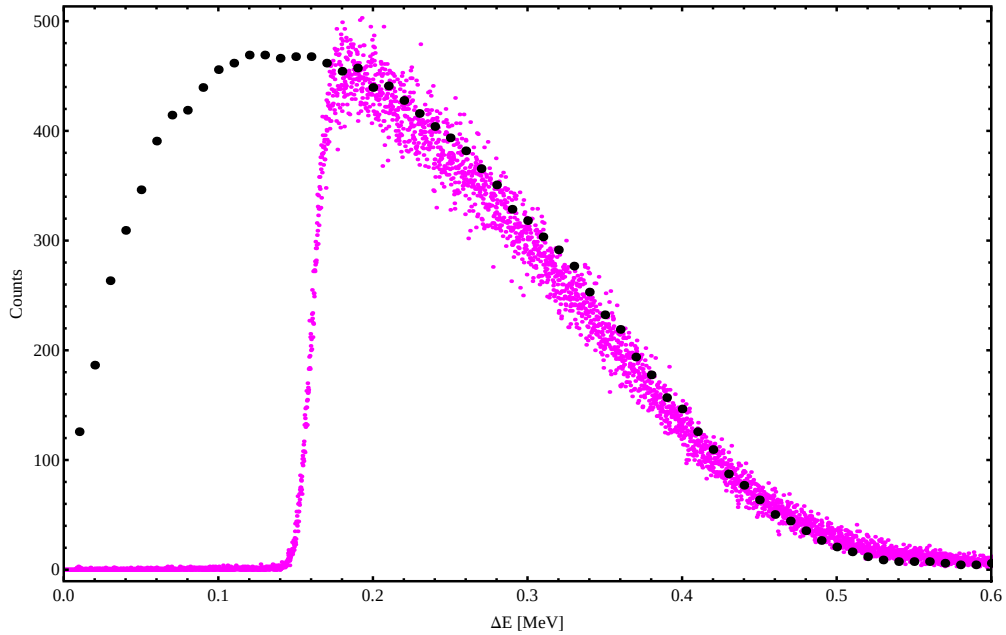

FIG. 1. Experimental ΔE spectra (tiny dots, purple) compared with Monte-Carlo generated spectra (large dots, black) for β^+ particles emitted by ^{22}Na.

This feature does not apply to the ^{38}Ca measurement. In this case the average positron energy is in the MeV region, and thus the majority of the positrons carry more energy than our 125 keV threshold. This is evident in Fig. 2, which presents a comparison of the experimental and Monte-Carlo-generated ΔE

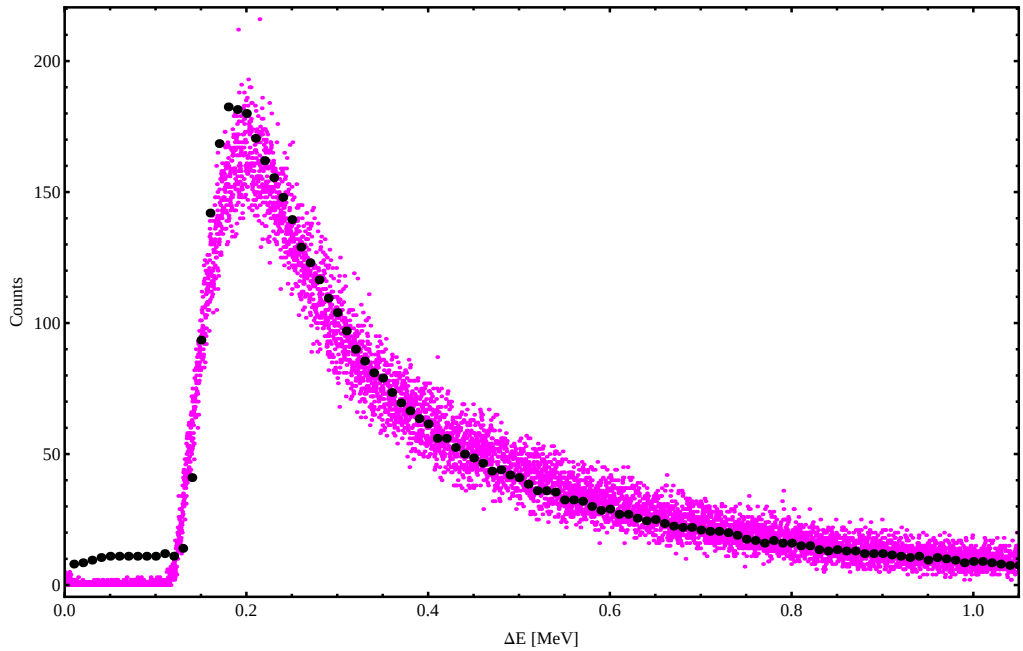

FIG. 2. Experimental ΔE spectra (tiny dots, purple) compared with Monte-Carlo generated spectra (large dots, black) for β^+ particles emitted by ^{38}Ca.

spectra for ^{38}Ca decay. A quantitative evaluation of the cut-off losses, based on the Monte Carlo simulation, is given in Table II.

Table II. Cut-off losses caused by the detection threshold.

experiment	Cut-off energy	Cut-off losses
^{22}Na	150 keV	38%
^{38}Ca	140 keV	3.5%

The improvements announced in [1] are further confirmed by the relative reduction of the "high" energy signals in the positron ΔE spectra: Indeed there was a dramatic reduction in the overlapping of genuine β signals with long tails originating from previous pulses. This explains the much better agreement between the Monte-Carlo-generated and experimental spectra, in the cases of both ^{22}Na and ^{38}Ca.

In conclusion – and most importantly for our application – the tests confirm the capability of our setup to generate reliable branching ratios at the 0.1% precision level required for superallowed *ft*-value measurements. Further details referring to the ^{38}Ca measurement are given in reference [2].

[1] V.E. Iacob, J.C. Hardy, and H.I. Park, *Progress in Research,* Cyclotron Institute, Texas A&M University (2011-2012), p. V-21

[2] H.I. Park, J.C. Hardy, V.E. Iacob, M. Bencomo, L. Chan, V. Horvat, N. Nica, B.T. Roeder, E. Simmons and R.E. Tribble, *Progress in Research,* Cyclotron Institute, Texas A&M University (2012-2013), p. I-11.

[3] I. Kawrakow, Med. Phys. **27**, 485 (2000); I. Kawrakow and D.W. O. Rogers, NRCC Report PIRS-701, NRC, Ottawa (2003); [http://www.nrccnrc.gc.ca/eng/solutions/advisory/ egsnrc_index.html].

TAMUTRAP facility annual report

R. S. Behling, Y. Boran, B. Fenker, M. Mehlman, D. Melconian and P. D. Shidling

The primary goal of the TAMUTRAP facility is to test the Standard Model for a possible admixture of a scalar (S) or tensor (T) type of interaction in T=2 superallowed beta-delayed proton decays. This information will be inferred from the shape of the proton energy spectrum. The main components of the facility are a Radio Frequency Quadrupole (RFQ) Paul trap used to cool and bunch the ions, and a measurement Penning trap system composed of two cylindrical Penning traps. Additional scientific goals for this system are mass measurements, lifetime measurements, ft-values, and providing a low-energy radioactive ion beam (RIB) for various other applications.

Over the past year, significant progress has been made toward the commissioning TAMUTRAP (Fig. 1). The geometry for the large, open-access Penning trap has been finalized and shown to be theoretically competitive with traps employed in other prominent facilities [1]. Critical systems such as the high voltage platform, power supplies, radio frequency (RF) voltage systems, and gas pressure controls for various beam line elements have been commissioned. Testing of several meters of beamline as well as the RFQ Paul trap used to bunch the incoming beam and lower emittance has begun with an offline ion source, and beam transmission through these elements has been confirmed. Additional beam optics have been fabricated and are currently being tested.

FIG. 1. The TAMUTRAP facility as of 4/16/13

One of the challenges in the design of the RFQ is efficiently matching the emittance of the incoming beam to the acceptance of the RFQ due to the need to decelerate it from 10-15 keV to a few tens of electron volts energy. This procedure is achieved by the injection optics, which consist of a ground tube and two cylindrical electrodes. The RFQ cooler and buncher must be floated to a potential slightly less than the beam energy in order to allow the rest of the beam line to remain at ground. In preparation for this, a high voltage platform capable of satisfying the voltage requirements has been built, and an

optical system for transmitting data to and from devices on the platform has been installed. The platform and communication system was tested and safety checked, and works as expected. Relying exclusively on electrostatic beam optics, there are many elements in the TAMUTRAP beam line that require the application of a precise voltage. Power supplies for these optics have been commissioned and tested, including multiple low and high voltage modules. In addition, the RFQ utilizes a high voltage RF signal to manipulate the incoming ion beam. An RF amplifier has been integrated into the RFQ electronics in such a manner that the RF signal will not damage any other power supplies or equipment. This entire circuit has been shown to provide the necessary voltage for proper functioning of the RFQ. Finally, cooling is achieved in the RFQ via interaction with a low pressure buffer gas, in this case ultra pure helium. To meet this requirement a PID system was installed in the beam line and tested for functionality. The vacuum outside the RFQ was designed to be maintained by differential pumping, the functioning of which was confirmed. The RFQ systems are shown in Fig. 2.

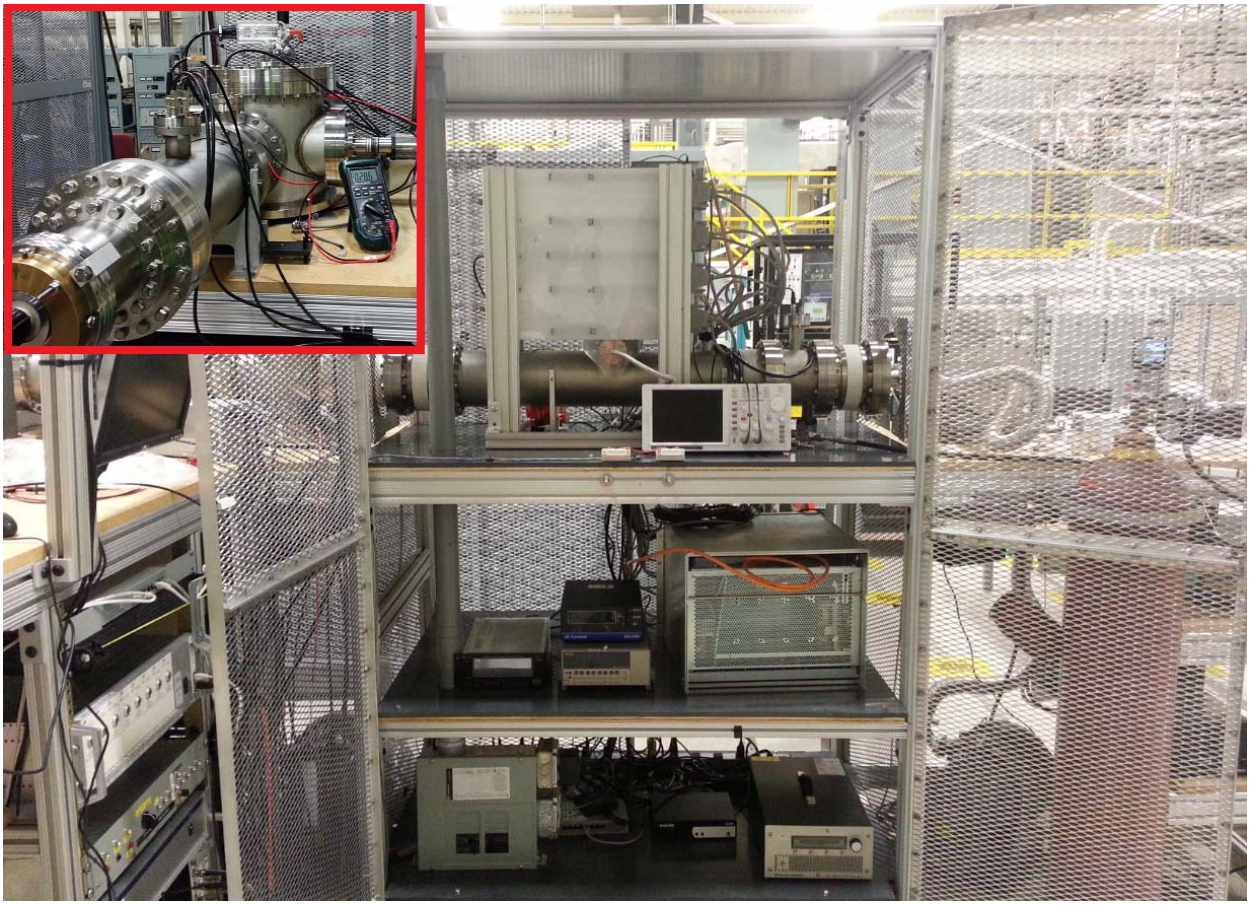

FIG. 2. The RFQ cooler and buncher and associated support systems with offline ion source (inset).

An in-house-designed ion gun employing a potassium ion source was developed for offline tests. After demonstrating beam properties useful for simulating the output of the heavy ion guide (HIG), including a low emittance when compared to commercially available ion gun designs and up to 1 μA maximum beam current, this ion gun was coupled to the assembled beam line. Subsequent testing has confirmed the function of various lenses, steerers, and injection electrodes by measuring beam current at periodically located Faraday cups connected to precision Keithley picoammeters. Such a method should

ultimately allow for an efficiency determination of the system. At this time, beam transport has been confirmed over several feet of beam line, and a relative efficiency of about 80% for the injection optics has been demonstrated for certain beam energies, though optimization of the injection optics is still ongoing.

Testing on the RFQ itself, coupled to the initial beam line and injection optics, has recently begun. After confirming the functionality of the necessary electronics and support systems (RF, drag potential, gas pressure, etc.), beam was injected into the RFQ and current was measured near the exit of the structure using a Faraday cup. The device has shown transmission of a low energy beam (from 40-120eV), with and without the presence of the Helium buffer gas. Further tests are currently being performed to determine the most favorable operating parameters for the device in order to maximize transport efficiency.

Concurrent with the testing of the beam line and RFQ, additional beam optics and equipment to be needed later in the assembly of the facility were being fabricated and assembled. The beam optics on this list include the spherical deflector needed to bend the beam ninety degrees, a prototype cylindrical deflector (Fig. 3) that could be used for the same purpose (upcoming testing will indicate if its performance is satisfactory), and a pulsing cavity used to lower the beam energy for loading into the measurement trap. The cylindrical deflector is the first of these elements to be completed, and is currently awaiting testing.

FIG. 3. The cylindrical ninety degree deflector currently awaiting testing.

In addition to this hardware, TAMUTRAP will also ultimately require precision timed voltage switching for certain beam elements. For this application, a National Instruments FPGA and Behlke high voltage, ultrafast switches have been purchased. Control systems for these devices are now in the works.

The immediate outlook for the TAMUTRAP facility involves initially completing the efficiency tests on the RFQ and injection optics. After that, additional sections of the beam line will be installed and tested, including the fast switching elements mentioned above. Once the efficiency of these sections has been determined, an emittance test utilizing position sensitive multi-channel plate (MCP) detectors will be performed, indicating what quality beam can be expected for feeding the measurement trap. It is expected that significant progress toward these milestones will be made in the upcoming year.

[1] R.S. Behling *et al.*, *Progress in Research*, Cyclotron Institute, Texas A&M University (2012-2013), p. I-22.

Upgrade plan for the Oxford detector

A. Spiridon, R. Chyzh, M. Dag, M. McCleskey, and R. E. Tribble

The Oxford detector is one of the two focal plane detectors of the Multipole-Dipole-Multipole (MDM) spectrometer. It is used to identify particles and measure their positions along the dispersive x-direction. Using raytrace reconstruction we can determine the scattering angle at the target as a function of the angle of the particle path in the detector.

It has been used primarily to study scattering and transfer reactions involving nuclei with A≤26. However at higher masses, we are having significant difficulties in particle identification and realized that in order to study nuclei above this range we would need to improve the existing setup.

In the simplest terms, the Oxford detector is an ionization chamber with a plastic scintillator at the back. Four resistive wires working in avalanche conditions allow for position determination at four different depths in the detector and therefore permit raytrace reconstruction. A detailed description can be found in ref [1]. **Error! Reference source not found.** shows a schematic side view of the detector and its components.

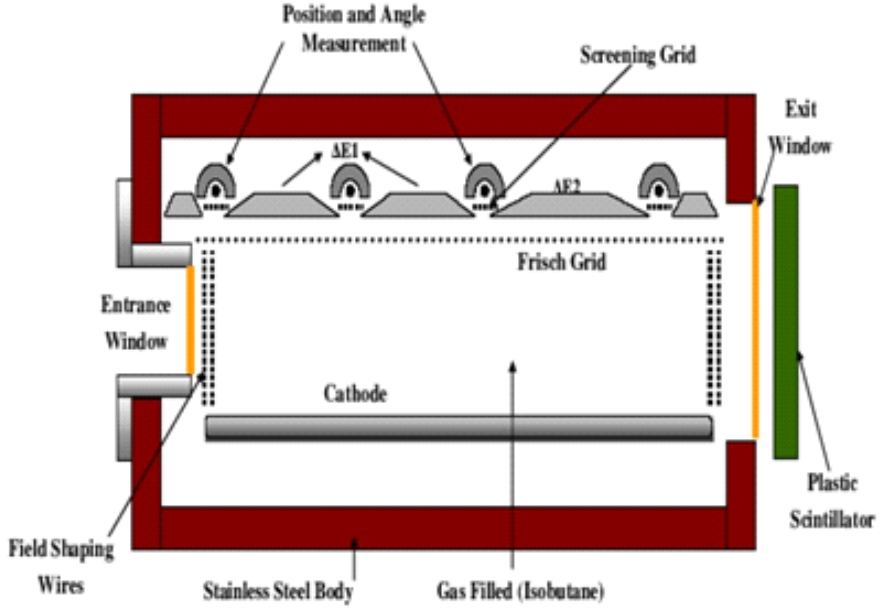

FIG. 1. Schematic of the Oxford detector.

Identification of the ions is done by the usual ΔE-E method: a plot of the energy that particles lose as they pass through the ionization chamber versus the residual energy left when they stop in the scintillator. These are the parameters we seek to detect with better resolution at this time.

Energy lost in the ionization gas is measured by the three anode plates at the top that can be seen in the figure above. Currently, with only the first two plates connected to produce a signal we call ΔE1, we obtain a reasonable energy resolution. The third plate, ΔE2, gives a signal that is too noisy to be of

any use. We propose to improve this by introducing Micromegas (see ref [2] for description). These micro-mesh structures have been used in AstroBox [3], a detector system built specially for low noise and used to detect very low-energy protons from beta-delayed proton emitters. However, this different detection setup used in the MARS beam line has been shown to give also very good energy resolution with the incoming energetic ions of the beam. In a first step, we will temporarily affix the Micromegas over the ΔE2 anode and test how well this works with the usual Oxford settings, particularly the gas pressure. If the results are positive we would then proceed by replacing all the anode plates with the micro-mesh structures and test again. A challenge we see here is how well these micromegas will work at the low pressures we use (p=50 torr), as they were used at above 1 atm in AstroBox.

Regarding the residual energy, we are looking to improve this by replacing the plastic scintillator with a different detection material. We see two possibilities for this.

The first is to use Si pads to cover the back of the Oxford detector (8.1cm x33.6 cm). However the size of the area raises the issue of how to cover it given current production costs and availability. At the moment, we expect we might need two rows of Si pads (6 pads in each row, with the size of a quadratic form detector of 5.6 cm and a dead area ~1 cm wide). The thickness of a Si pad is roughly 400 μm with an energy resolution for α-particles of 5.5 MeV of 1.2%. As we have not yet decided on the optimum size of each pad and number that we need, we ordered two small α-detectors (diameter of 2.5 cm) for testing and expect them to arrive soon.

The second possibility to improve residual energy detection would be to add another volume of gas at a higher pressure (~ 800 torr) then in the first space and stop the particles there. The setup would be similar to the recently developed AstroBox detector [3], which we know to have much better resolution than the scintillator.

Our aim is to complete and test the first step by the end of summer 2013.

[1] D. H. Youngblood, Y.-W. Lui, H. L. Clark, P. Oliver, G. Simler, and Nucl. Instrum. Methods Phys. Res. A**361**, 359 (1995); M. McCleskey, Ph.D Dissertation, Texas A&M University, 2011.

[2] Y. Giomataris *et al.*, Nucl. Instrum. Methods Phys. Res. **A376**, 29 (1996).

[3] E. Pollacco et al., Nucl. Instrum. Methods Phys. Res. (accepted).

A reliable, low-cost automated LN_2 filling system for the STARLiTe clover array

M. McCleskey

The STARLiTe (**S**ilicon **T**elescope **A**rray for **R**eactions **Li**vermore National Lab **Te**xas A&M) consists of segmented annular silicon detectors surrounded by a HPGe clover array in close geometry (see Ref. 1). These HPGe clover detectors are cooled with liquid nitrogen and, when biased, the dewars containing the liquid nitrogen for each detector must be refilled at 12 hour intervals. With up to six detectors in the array, this amounts to approximately 1 hour of beam time lost per day for manual filling, which over the course of a 1 week experiment amounts to the equivalent of a lost 8 hour shift. Given the value of beam time, such downtime should be minimized.

In response to this need, a system has been designed at Texas A&M Cyclotron Institute (TAMU-CI) for this purpose. It consists of a programmable micro controller interfaced with a six channel relay array for powering six independent cryogenic solenoid valves attached to a common manifold fed by a large LN_2 dewar (see Fig. 1). The microcontroller is an Ardunio Pro Mini which is based on the (ATmega328). This microcontroller was chosen for its ease of use (it is C programmable through a TTL serial connection using open source software), compact form factor (0.7” x 1.3”) and low cost (around $20). A relay driver IC (ULN2003) was used to interface the TTL digital output of the microcontroller to 12V relays. These relays switch the 120VAC power to the cryogenic solenoid valves that control the flow of LN_2 to the clover detector dewars.

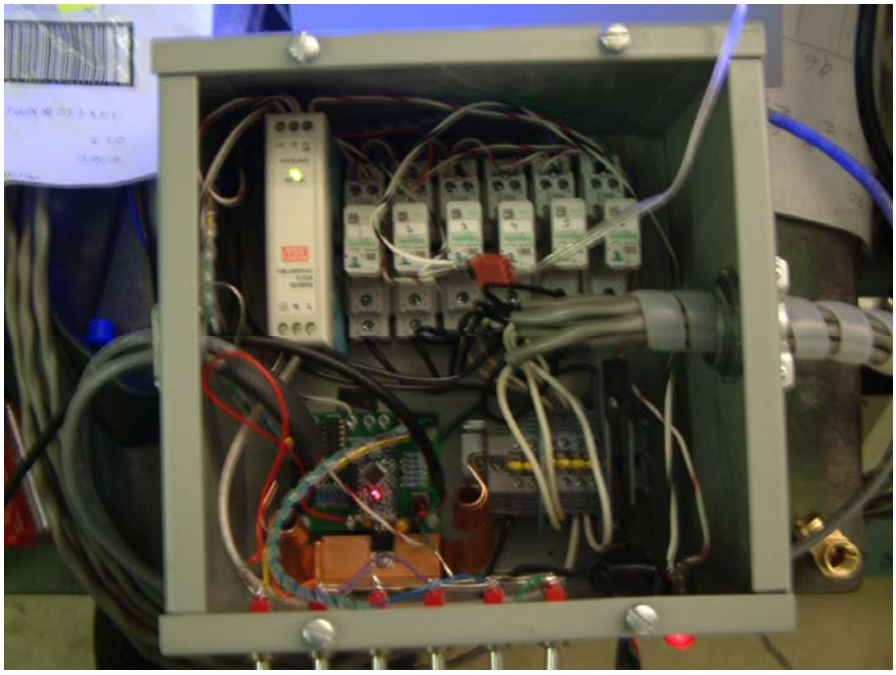

FIG. 1. LN2 system. Microcontroller is seen in the bottom left and the relays are in the upper right.

The Arduino Pro Mini has 8 analog inputs of which 6 are used for monitoring the temperature in the exhaust line of each clover in order to detect the presence of LN_2. The 12 digital I/O pins (excluding those used for the TTL serial communication) are split between the aforementioned relay control outputs and inputs for an array of switches that allow the user to initiate a fill (either one that must be manually turned off by the user or one terminated by liquid sensed in the exhaust line).

A low cost Intel Atom-based computer is used to monitor the fill cycles of the clover dewars. A Python script was written which handles the communication with the autofill system as well as provides an easy to use graphical user interface (Fig 2) to display information on the fill cycles and to accept user commands. While the computer is used to monitor the fill cycles, the autofill system does not require a connection to the computer to operate and will continue running as long as it is powered. In the event of a power loss, the autofill system will start a new fill cycle once power is restored and resume filling at the previously set interval (typically 12 hours) thereafter. The monitor computer is also used to send alerts via SMS in the event of a fill cycle not finishing in a reasonable amount of time, which could be indicative of an empty LN_2 dewar. A second script was written to allow remote users to check on the system via an SSH session.

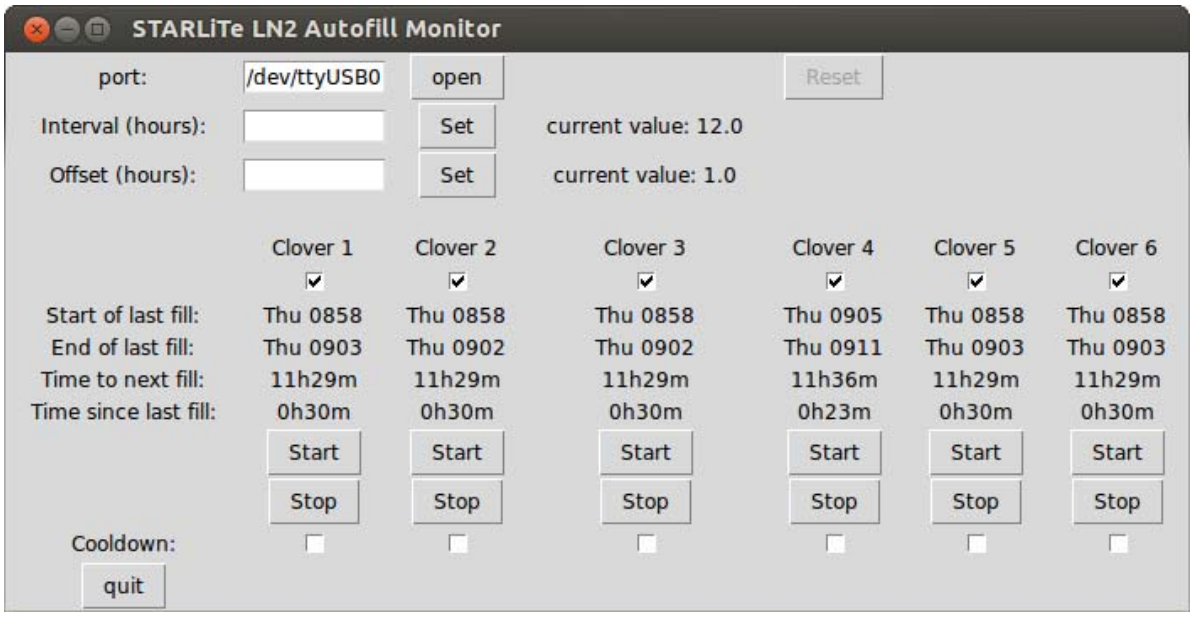

FIG. 2. Control/monitor GUI.

The exhaust line LN_2 sensors are PT-100 RTD probes connected to a voltage divider circuit that keeps a small current (about 20mA) flowing through the sensor. The purpose of this current is to provide a small amount of heat input to the sensor that must be overcome by direct contact with liquid nitrogen as opposed to the cold gaseous nitrogen that is present during the fill cycle before the clover dewar is full. A delay and a requirement for a continued LN_2 temp reading was also implemented to ensure that a brief splash of LN_2 is not sufficient to terminate the fill. In practice this has proven effective.

In summary, a reliable, low cost automatic LN_2 fill system has been designed and built at TAMU-CI for use with the STARLiTe clover detector array.

[1]. S.R. Lesher *et al.*, Nucl. Instrum. Methods Phys. Res. **A621**, 286 (2010).

Detector tests for SAMURAI silicon tracker

A. Saastamoinen, M. McCleskey, B. T. Roeder, L. Trache, R. E. Tribble,
L. G. Sobotka,[1] J. Elison,[1] J. C. Blackmon,[2] C. Rasco,[2] M. Kurokawa,[3] H. Baba,[3]
H. Otsu,[3] K. Yoneda,[3] and J. Zenihiro[3]
[1] *Washington University, St. Louis, Missouri,*
[2] *Louisiana State University, New Orleans, Louisiana,*
[3] *RIKEN Nishina Center, Wako, Saitama, Japan*

This report summarizes briefly the in-beam detector and electronics test for the SAMURAI Si tracker project performed at the NIRS-HIMAC facility (Heavy-Ion Medical Accelerator in Chiba, Japanese National Institute for Radiological Sciences). The aim of the experiment was to study the responses of a double-sided silicon strip detector (Micron TTT2, 300 μm) and a single sided silicon strip detector (Hamamatsu GLAST, 300 μm) with associated electronics in conditions as close as possible to the ones in the upcoming experiments with SAMURAI spectrometer [1] at RIBF facility in RIKEN.

The beam time consisted of a total of 5 shifts with different beams and goals:

- ^{12}C at 400 MeV/u for setting up and checking the system performance.
- ^{56}Fe at 400 MeV/u to produce a cocktail of secondary beams with A/Z = 2 to check linearity and response of the system with wide range of energy deposits. This provides also the energy calibration (access to external sources was limited to a single ^{241}Am source).
- ^{1}H at 150 MeV/u to see if system can detect high energy protons (low energy deposit in thin Si).
- ^{40}Ar at 290 MeV/u to determine possible effects from δ-rays.
- ^{84}Kr at 400 MeV/u to determine possible effects from δ-rays and to see responses from ions closer to A = 100 region at this energy range.

We prepared a high quality vacuum system that could be connected directly to the HIMAC beam lines (standard procedure is to have setup separated by an air gap to ensure safety of the medical facility). This allowed us to be sure to not have any background δ-rays from beam-line windows and thus have conditions as close as possible to those at RIBF. The vacuum requirements, mostly pumping time to reach low enough pressure, limited the amount of possible detector configurations that could be tested.

For TTT detector we used the internal charge-sensitive amplifier (CSA) of the HINP16C chips [2]. The CSAs were run with high gain (0-70 MeV range) for all the beams, except for ^{84}Kr, for which we had to switch to low gain (0 – 350 MeV range). For the GLAST detector we had a 64 channel external dual gain charge-sensitive preamplifier (DGCSP), designed and manufactured at RIKEN, which had simultaneous high and low gain and this was read out with the HINP16C chips in external amplifier configuration.

This was the first time that our readout system (TABS) with two motherboards (total of 512 channels) was run in online conditions and it was found to perform as expected from offline tests. This was also the first time that the system was operated through the RIKEN data acquisition software [3]. Development of the analysis codes for the future setup is still on going process with aim to integrate the Si tracker code to the full SAMURAI setup.

Both detectors and electronics chains were found to be linear over the ranges of energy deposits used. Fig. 1 illustrates A/Z = 2 cocktail from ^{56}Fe fragmentation as observed with TTT2 detector and high-gain of HINP internal CSA.

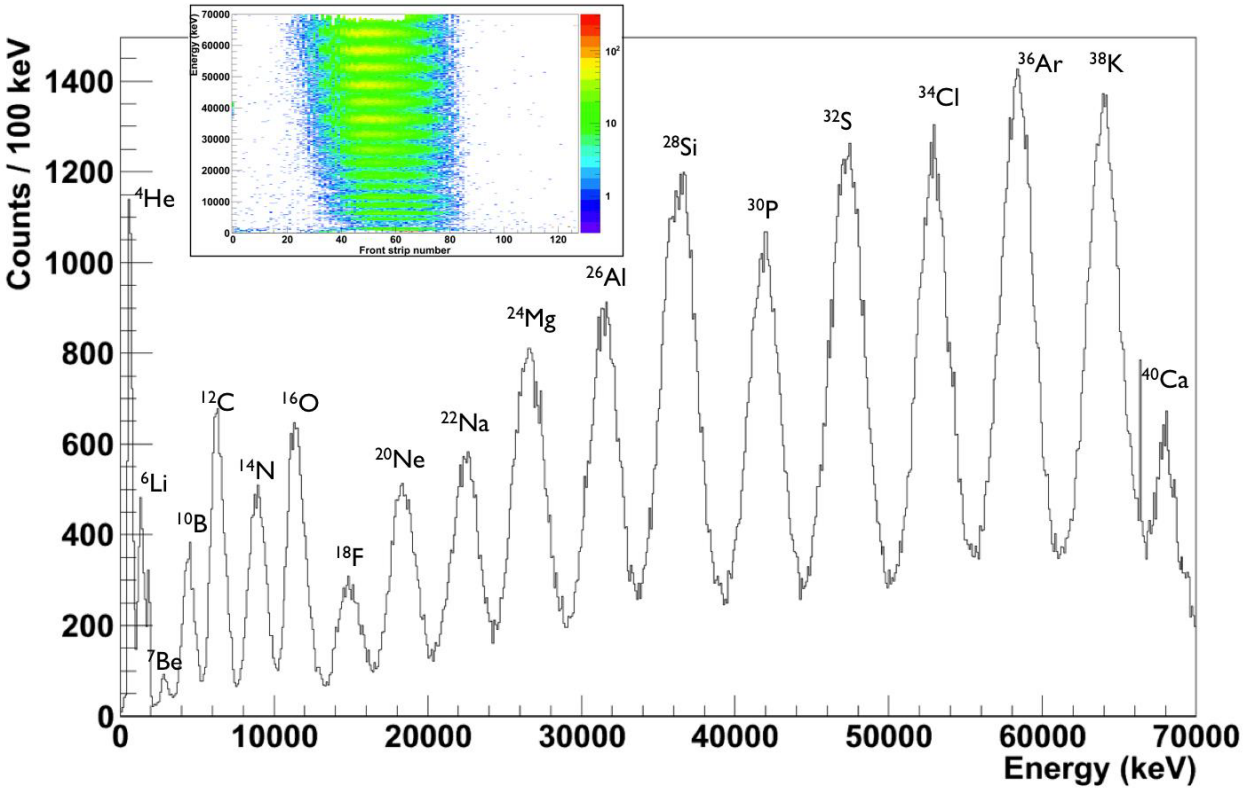

FIG. 1. Energy deposits of A/Z = 2 cocktail from ^{56}Fe fragmentation at 400 MeV/u with TTT2 detector front (junction) side. Inset shows the distribution along different strips.

We observed only a small fraction of the protons with the TTT2 and HINP CSAs. This is not entirely unexpected with the internal CSA of HINP chips as the ~300 keV energy deposit from 150 MeV protons is just at the detection threshold. The few candidates for protons are shown in Fig. 2 with noise like events removed by requiring that $|E_{front} - E_{back}| < 100$ keV and that multiplicity of the event is one on both sides. Notably there are only about 3000 counts in the peak, out of over 800 000 events in total. The external RIKEN CSA did yield also only circumstantial evidence about protons as the electronics thresholds were rather high in most of the channels. As a future improvement, the response for high energy protons will be improved by increasing the thickness of the detector from 300 μm to 500 μm and with an upgrade to the HINP chips, lowering the thresholds about factor of two. The combination of higher energy deposit and lower thresholds should yield a good response from high energy protons. The new detectors and improved HINP chips are to be tested in fall 2013.

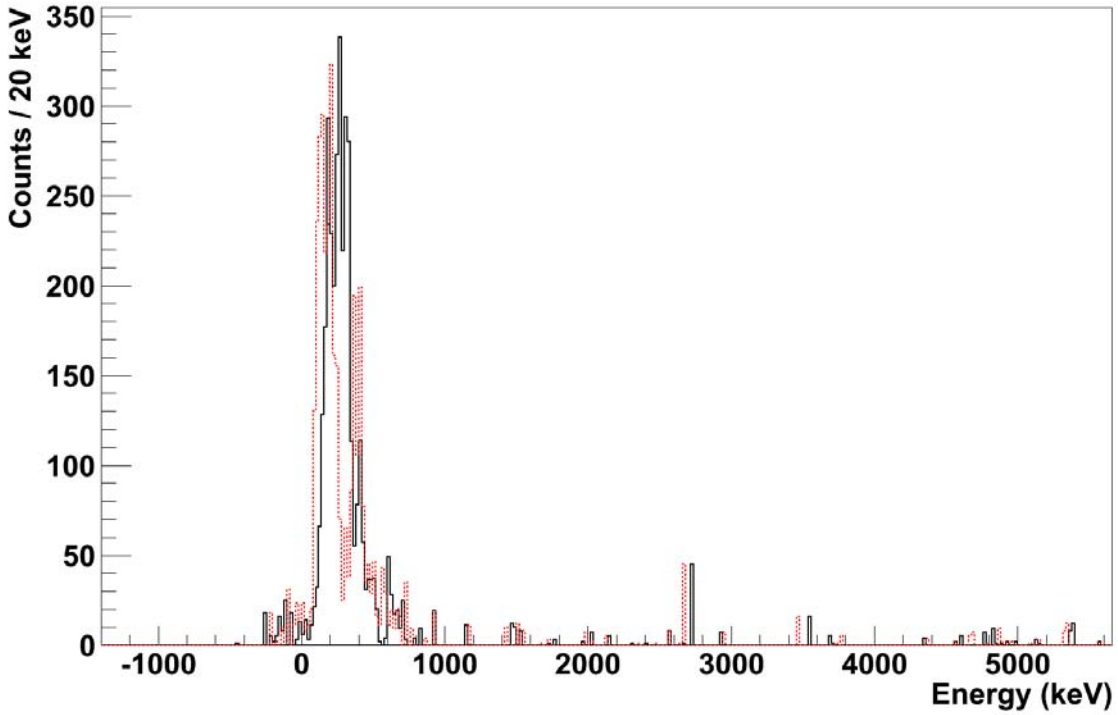

FIG. 2. Most probable candidates as 150 MeV protons as observed with TTT2 detector. The spectrum from front (junction) side is in solid black line and the spectrum from back (ohmic) side is in dashed red line.

To test production of δ-rays we had a set of Pb and Al foils (to simulate a production target and another Si detector at larger distance, respectively) <100 cm upstream in the beam line before the GLAST detector. The TTT detector was located <50 cm behind the GLAST detector. With the present setup, at these distances, we did not observe any significant amount of δ-rays. This is an encouraging result if the final configuration of the SAMURAI setup is built in similar distances and utilizes double-sided strip detectors. Unfortunately the time available did not allow us to test two detectors at a few cm distance to have a measurement in configuration similar to two single-sided detectors (which would be the configuration if two GLAST detectors are combined as position sensitive detector). We have also designed and built a permanent magnet setup that can suppress electrons up to few MeV (as tested with ^{90}Sr source). This magnet fits easily inside normal beam line pipe and can be used if δ-rays are found to be problematic in future.

[1] Y. Shimizu *et al.*, J. Phys.: Conf. Ser. **312**, 052022 (2011).
[2] G. Engel *et al.*, Nucl. Instrum. and Meth. in Phys. Res. A **652**, 462 (2011).
[3] H. Baba *et al.*, Nucl. Instrum. and Meth. in Phys. Res. A **616**, 65 (2010).

Status of STARLiTe beamline at Texas A&M Cyclotron Institute

J. T. Burke, R. Casperson, M. McCleskey and the STARLiTe collaboration

The STAR LiTe collaboration consists of more than 55 researchers, post-docs, graduate and undergraduate students from five different countries and multiple national laboratories and universities. Work on the installation of the STARS (Silicon Telescope Array for Reaction Studies) and the LiBerACE (Livermore-Berkeley array for collaborative experiments) [1] at TAMU-CI was completed in March of 2012 and the commissioning run of 243Am(p,t)241Am for the study of the 240Am(n,f) reaction via the surrogate method was completed in April of 2012 [2]. Since that time an additional 8 experiments have been performed by 6 different groups representing over 1100 hours of beamtime. Analysis of these experiments is ongoing and results are expected to begin to be published in the coming months.

Experiments performed this past year:

- ^{174}Yb(p,d)^{173}Yb* to measure benchmark ^{173}Yb(n,g) case for surrogate reaction
- ^{239}Pu(p,d)^{238}Pu*, ^{239}Pu(p,t)^{237}Pu* to measure ^{236,237}Pu(n,g) cross sections using the surrogate technique
- ^{95}Mo(d,pg)^{96}Mo*, ^{95}Mo(d,p)^{96}Mo to measure ^{95}Mo(n,g) cross sections using the surrogate technique
- ^{89}Y(p,d)88Y*, ^{89}Y(p,t)^{87}Y to measure ^{87}Y(n,g) cross sections using the surrogate technique
- ^{54}Fe(^{12}C,p) for nuclear structure and model testing
- ^{24}Mg(^{4}He,^{4}He)^{24}Mg* as a surrogate for the astrophysical ^{12}C + ^{12}C reaction
- ^{175}Lu(p,d)^{174}Lu* to determine ^{173}Lu(n,g) cross section using the surrogate technique
- ^{152}Sm(p,d)^{153}Sm* and ^{154}Sm(p,d)^{155}Sm*

[1] S.R. Lesher *et al.*, Nucl. Instrum. Methods Phys. Res. **A621**, 286 (2010).

[2] M. McCleskey *et al.*, *Progress in Research*, Cyclotron Institute, Texas A&M University (2011-2012) p. V-58.

SECTION V

PUBLICATIONS

PAPERS PUBLISHED
April 1, 2012 – March 31, 2013

Beta particles, J.C. Hardy, McGraw-Hill Encyclopedia of Science and Technology, eleventh edition (2012).

Do radioactive half-lives vary with the earth-to-sun distance? J.C. Hardy, J.R. Goodwin and V.E. Iacob, Appl. Radiat. and Isot. **70**, 1931 (2012).

Ernest Rutherford and the origins of nuclear physics, J.C. Hardy, Phys. in Canada **68**, 21 (2012).

Superallowed 0^+-to-0^+ beta decay from T_z = -1 *sd*-shell nuclei, J. C. Hardy and I.S. Towner, J. Phys.: Conf. Ser. **387**, 012006 (2012).

Superallowed nuclear beta decay: precision measurements for basic physics, J.C. Hardy
Carpathian Summer School of Physics 2012, edited by L. Trache, and P.G Isar, AIP Conference Proceedings **1498**, 106 (2012).

Time-interval analysis of beta decay, V. Horvat and J.C. Hardy, Nucl. Instrum. Methods Phys. Res. **A713**, 19 (2013).

New results on mass measurements of stored neutron-rich nuclides in the element range from Pt to U with the FRS-ESR facility at 360-400 Mev/u, L. Chen *et al*. Nucl. Phys. **A882**, 71 (2012).

Direct observation of long-lived isomers in ^{212}Bi, L. Chen *et al*. Phys. Rev. Lett. **110**, 122502 (2013).

Nuclear Data Sheets for A = 37, J. Cameron, J. Chen, B. Singh, and N. Nica, Nucl. Data Sheets **113**, 365 (2012).

Nuclear Data Sheets for A = 34, N. Nica and B. Singh, Nucl. Data Sheets **113**, 365 (2012).

Nuclear Data Sheets for A = 77, B. Singh and N. Nica, Nucl. Data Sheets **113**, 365 (2012).

Implantation-decay station for low-energy β-delayed proton measurements, M. McCleskey, L. Trache, A. Saastamoinen, A. Banu, E. Simmons, B. Roeder, G. Tabacaru, R.E. Tribble, T. Davinson, P.J. Woods, J. Aysto, Nucl. Instrum. Methods Phys. Res. **A700**, 124 (2013).

One-proton breakup of ^{24}Si and the ^{23}Al(p,γ)^{24}Si reaction in type I X-ray bursts, A Banu, F. Carstoiu, N.L. Achouri, W.N. Catford, M. Chartier, B. Fern*a*ndez-Dom*i*nguez, M. Horoi, B. Laurent, N.A. Orr, S. Paschalis, N. Patterson, B. Piertras, B.T. Roeder, P. Roussel-Chomaz, S. Thomas, L. Trache, R.E. Tribble, Phys. Rev. C **86**, 015806 (2012).

β–Delayed proton-decay study of ^{20}Mg and its implication for the ^{19}Ne(p,γ)^{20}Na breakout reaction in X-ray bursts, J.P. Wallace, P.J. Woods, G. Lotay, A. Alharbi, A. Banu, H.M. David, T. Davinson, M. McCleskey, B.T. Roeder, E. Simmons, A. Spiridon, L. Trache, R.E. Tribble, Phys. Lett. B **673**, 183 (2012).

Total and partial photoneutron cross sections for Pb isotopes, T. Kondo, H. Utsunomiya**,** S. Goriely, I. Daoutidis, C. Iwamoto, H. Akimune, A. Okamoto, T. Yamagata, M. Kamata, O. Itoh, H. Toyokawa, Y.-W. Lui, H. Harada, F. Kitatani, S. Hilaire, and A.J. Koning, Phys. Rev. C **86,** 014316 (2012).

Separation of pygmy dipole and M1 resonances in ^{90}Zr by a high-resolution inelastic proton scattering near 0°, C. Iwamoto, H. Utsunomiya, A. Tamii, H. Akimune, H. Nakada, T. shima, T. Yamagata, T. Kawabata, Y. Fujita, H. Matsubara, Y. Shimbara, M. Nagashima, T. Suzuki, H. Fujita, M. Sakuda, T. Mori, T. Izumi, A. Okamoto, T. Kondo, B. Bilgier, H.C. Kozer, Y.-W. Lui, and K. Hatanaka, Phys. Rev. Lett. **108**, 262501 (2012).

Precision measurement of the neutron beta-decay asymmetry, M.P. Mendenhall, D. Melconian *et al.*, Phys. Rev. C **87**, 032501(R) (2013).

Design of a unique open-geometry cyclindrical Penning trap, M. Mehlman, P.D. Shidling, R.S. Behling, L.G. Clark, B. Fenker and D. Melconian, Nucl. Instrum. Methods Phys. Res. **A712**, 9, (2013).

Performance of the Los Alamos National Laboratory spallation- driven solid-deuterium ultra-cold neutron source, A. Saunders, D. Melconian *et al.*, Rev. Sci. Instrum. **84**, 013304 (2013).

Measurement of the neutron β-asymmetry parameter A_0 with ultracold neutrons, B. Plaster D. Melconian, *et al.*, Phys. Rev. C **86**, 055501 (2012).

Decay studies for neutrino physics: electron capture decays of ^{100}Tc and ^{116}In, A. García, D. Melconian *et al.*, Hyperfine Interact. (2012).

γ-ray constraints on the properties of unbound ^{32}Cl levels, C. Wrede, D. Melconian *et al.*, Phys. Rev. C **86**, 047305 (2012).

Atomic parity non-conservation in Francium: the FrPNC experiment at Triumf, S. Aubin, D. Melconian *et al.*, Nuovo Cimento C **35**, 85 (2012).

Suppression of the centrifugal barrier effects in the off-energy-shell neutron + ^{17}O interaction, M. Gulino, C. Spitaleri, X.D. Tang, G.L.Guardo, L. Lamia, S. Cherubini, B. Bucher, V. Burjan, M.

Couder, P. Davies,R. deBoer, X. Fang, V.Z. Goldberg, Z. Hons, V. Kroha, L. Lamm, M. LaCognata, C. Li, C. Ma, J. Mrazek, A.M. Mukhamedzhanov, M. Notani, S. O'Brien, R.G. Pizzone, G.G. Rapisarda, D. Roberson, M.L. Sergi, W. Tan, I.J. Thompson, and M. Wiescher, Phys. Rev. C **87**, 012801 (2013).

Status of the ACCULINNA-2 project at FLNR, A.S. Fomichev, G.M. Ter-Akopian, A.A. Bezbakh, V. Chudoba, A.V. Daniel, M.S. Golovkov, A.V. Gorshkov,V.A. Gorshkov, L.V. Grigorenko, G. Kaminski, S.A. Krupko, Y.Ts. Oganessian, Y.L. Parfenova, S.I. Sidorchuk, A.A. Korsheninnikov, V.Z. Goldberg, M. Pfutzner, I.G. Mukha, H. Simon, O.B. Tarasov, N.K. Timofeyuk, and M.V. Zhukov, J. Phys.: Conf. Ser. **337**, 012025 (2012).

Resonance scattering to study exotic nuclei at the limits of stability, V.Z. Goldberg, B.T. Roeder, G.V. Rogachev, G.G. Chubarian, E.D. Johnson, C. Fu, A.A. Alharbi, M.L. Avila, A. Banu, M. McCleskey, J.P. Mitchell, E. Simmons, G. Tabacaru, L. Trache, and R.E. Tribble, J. Phys.: Conf. Ser. **337**, 012008 (2012).

Level structure of ^{10}C, V.Z. Goldberg and G.V. Rogachev, Phys.Rev. C **86**, 044314 (2012).

Clustering in non-self-conjugate nuclei, G.V. Rogachev, M. Avila, S. Cherubini, V.Z. Goldberg, M. Gulino, E.D. Johnson, A.N. Kuchera, M. LaCognata, L. Lamia, S. Romano, L.E. Miller, R.G. Pizzone, G.G. Rapisarda, M.L. Sergi, C. Spitaleri, R.E. Tribble, W.H. Trzaska, and A. Tumino, Prog. Theor. Phys.(Kyoto), Suppl. **196**, 184 (2012).

Distance calculation methods used in linearization for particle identification in multi-detector arrays, L. W. May, Z. Kohley, S. Wuenschel, A. B. McIntosh, G.A. Souliotis, and S.J. Yennello, AIP Conf. Proc. **1525**, 616 (2013).

Sensitivity of intermediate mass fragment flows to the symmetry energy, Z. Kohley, M. Colonna, A. Bonasera, L.W. May, S. Wuenschel, M. Di Toro, S. Galanopoulos, K. Hagel, M. Mehlman, W.B. Smith, G.A. Souliotis, S.N. Soisson, B.C. Stein, R. Tripathi, S.J. Yennello, and M. Zielinska-Pfabe, Phys. Rev. C, **85**, 064605 (2012).

Constraints on the symmetry energy and neutron skins from experiments and theory, M. B. Tsang, J. R. Stone, F. Camera, P. Danielewicz, S. Gandolfi, K. Hebeler, C. J. Horowitz, Jenny Lee, W. G. Lynch, Z. Kohley, R. Lemmon, P. Möller, T. Murakami, S. Riordan, X. Roca-Maza, F. Sammarruca, A. W. Steiner, I. Vidaña, and S. J. Yennello, Phys. Rev. C **86**, 015803 (2012).

Multifragmentation of reconstructed quasi-projectiles in the mass region A □ 30, S.N. Soisson, A. Botvina, G.A. Souliotis, B.C. Stein, L. Heilborn A.L. Keksis, Z. Kohley, L.W. May, D.V. Shetty, S. Wuenschel and S.J. Yennello, J. Phys. G., **39** 115104 (2012).

Asymmetry dependence of the nuclear caloric curve, A.B. McIntosh , A. Bonasera, P. Cammarata, K.

Hagel, L. Heilborn, Z. Kohley, J. Mabiala, L.W. May, P. Marini, A. Raphelt, G.A. Souliotis, S. Wuenschel, A. Zarrella, and S.J. Yennello, Phys. Lett. B **719**, 337 (2013).

Systematic study of the symmetry energy within the approach of the statistical multifragmentation model, P. Marini, A. Bonasera, G. A. Souliotis, P. Cammarata, S. Wuenschel, R. Tripathi, Z. Kohley, K. Hagel, L. Heilborn, J. Mabiala, L. W. May, A. B. McIntosh, and S. J. Yennello, Phys. Rev. C **87**, 024603 (2013).

Experimental determination of the quasi-projectile mass with measured neutrons, P. Marini, A. Zarrella, A. Bonasera, G. Bonasera, P. Cammarata, L. Heilborn, Z. Kohley, J. Mabiala, L.W. May, A.B. McIntosh, A. Raphelt, G.A. Souliotis, and S.J. Yennello, Nucl. Instrum. Methods Phys. Rev., **A707**, 80 (2013).

Using light charged particles to probe the asymmetry dependence of the nuclear caloric curve, A.B. McIntosh, A. Bonasera, Z. Kohley, P.J. Cammarata, K. Hagel, L. Heilborn, J. Mabiala, L.W. May, P. Marini, A. Raphelt, G.A. Souliotis, S. Wuenschel, A. Zarrella, and S.J. Yennello, Phys. Rev. C **87**, 034617 (2013).

Investigation of the nuclear phase transition using the Landau free-energy approach, J. Mabiala, A. Bonasera, H. Zheng, A.B. McIntosh, L.W. May, P. Cammarata, Z. Kohley, K. Hagel, L. Heilborn, A. Raphelt, G.A. Souliotis, A. Zarrella, and S.J. Yennello, Phys. Rev. C **87**, 017603 (2013).

Correlations with projectile-like fragments and emission order of light charged particles, Z. Kohley, A. Bonasera, S. Galanopoulos, K. Hagel, L.W. May, A.B. McIntosh, B.C. Stein, G.A. Souliotis, R. Tripathi, S. Wuenschel, and S.J. Yennello, Phys. Rev. C **86**, 044605 (2012).

The nuclear matter symmetry energy at $0.03 \leq \rho/\rho_0 \leq 0.2$, R. Wada, K. Hagel, L. Qin, J.B. Natowitz, Y.G. Ma, G. Roepke, S. Shlomo, A. Bonasera, S. Typel, Z. Chen, M. Huang, J. Wang, H. Zheng, S. Kowalski, C. Bottosso, M. Barbui, M.R.D. Rodrigues, K. Schmidt, D. Fabris, M. Lunardon, S. Moretto, G. Nebbia, S. Pesente, V. Rizzi, G. Viesti, M. Cinausero, G. Prete, T. Keutgen, Y. El Masri, and Z. Majka, Phys. Rev. C **85**, 064618 (2012).

Laboratory Tests of Low Density Astrophysical Nuclear Equations of State, L. Qin, K. Hagel, R. Wada, J.B. Natowitz, S. Shlomo, A. Bonasera, G. Röpke, S. Typel, Z. Chen, M. Huang, J. Wang, H. Zheng, S. Kowalski, M. Barbui, M.R.D. Rodrigues, K. Schmidt, D. Fabris, M. Lunardon, S. Moretto, G. Nebbia, S. Pesente, V. Rizzi, G. Viesti, M. Cinausero, G. Prete, T. Keutgen, Y. El Masri, Z. Majka, and Y.G. Ma, Phys. Rev. Lett. **108**, 172701 (2012).

In-medium phenomena in low density nuclear matter, K. Hagel, R. Wada, L. Qin, J.B. Natowitz, S. Shlomo, A. Bonasera, H. Zheng, C. Bottosso, M. Barbui, M.R.D. Rodrigues, K. Schmidt, G. Röpke, S.

Typel, Z. Chen, M. Huang, J. Wang, S. Kowalski, D. Fabris, M. Lunardon, S. Moretto, G. Nebbia, S. Pesente, V. Rizzi, G. Viesti, M. Cinausero, G. Prete, T. Keutgen, Y. El Masri, and Z. Majka, J. Phys.: Conference Series **420**, 012086 (2013).

Average neutron detection efficiency for DEMON detectors, S. Zhang, W. Lin, M.R.D. Rodrigues, M. Huang, R. Wada, X. Liu, M. Zhao, Z. Jin, Z. Chen, T. Keutgen, S. Kowalski, K. Hagel, M. Barbui, A. Bonasera, C. Bottosso, T. Materna, J.B. Natowitz, L. Qin, P.K. Sahu, K.J. Schmidt, *et al.*,Nucl. Instrum. Methods Phys. Res. **A709**, 68 (2013).

Study on fragments emission in the Ni-64+Ni-64 reaction at 40 AMeV, Kun Yang, Xiguang Cao, Fudong Shi *et al.*, Plasma Sci & Tech **14**, 386 (2012)

Temperature measurements of cluster fusion plasmas using D-He-3 or CD4-He-3 mixtures on the Texas Petawatt, Woosuk Bang, Marina Barbui, Aldo Bonasera *et al.*, Conference on Lasers and Electro-Optics (CLEO), San Jose, California 2012

Experimental signals of a nuclear liquid-gas phase transition, J. Mabiala, A. Bonasera, H. Zheng, A.B. McIntosh, Z. Kohley, P. Cammarata, K. Hagel, L. Heilborn, L.W. May, A. Raphelt, G.A. Souliotis, A. Zarrella, and S.J. Yennello, J. Phys.: Conference Series **420**, 012110 (2013).

Particle-particle correlation functions as an experimental probe of the nuclear asymmetry energy, L. Heilborn, H. Zheng, A. Bonasera, A.B. McIntosh, P.J. Cammarata, J. Mabiala, L.W. Larray, A. Raphelt, G.A. Souliotis, A. Zarella, and S.J. Yennello, J. Phys.: Conference Series **420**, 012111 (2013).

Asymmetry dependence of the nuclear caloric curve, A.B. McIntosh, A. Bonasera, P.Cammarata, K. Hagel, L. Heilborn, Z. Kohley, J. Mabiala, L.W. May, P. Marini, A.Raphelt, G.A. Souliotis, S. Wuenschel, A. Zarrella, S.J. Yennello, J. Phys.: Conf. Ser. **420**, 012085 (2013).

Temperature measurements in low excitation energy reactions to probe a possible phase transition, A. Raphelt, G.A. Souliotis, P.J. Cammarata, L. Heilborn, J. Mabiala, L. J. Phys.: Conf. Ser. **420**, 012109 (2013).

Symmetry energy effects on reaction break-up mechanisms near the Fermi energy, P.J. Cammarata, A.B. McIntosh, M. Colonna, L.W. May, L. Heilborn, J. Mabiala, A. Raphelt, A. Zarrella and S.J. Yennello, J. Phys.: Conf. Ser. **420**, 012113 (2013).

Equation of state effects on nucleon transport, L.W. May, P. Cammarata, L. Heilborn, Z. Kohley, J. Mabiala, A.B. McIntosh, A. Raphelt, A. Zarrella, and S.J. Yennello, J. Phys.: Conf. Ser. **420**, 012112 (2013).

Source-specific neutron detection efficiencies of the TAMU neutron ball, A. Zarrella, P. Marini, A.B. McIntosh, P. Cammarata, L. Heilborn, J. Mabiala, L.W. May, A. Raphelt, and S.J. Yennello, J. Phys.: Conf. Ser. **420**, 012164 (2013).

The ASY-EOS experiment at GSI: investigating the symmetry energy at supra-saturation densities, P Russotto *et al*. J. Phys.: Conf. Ser. **420**, 012092 (2013).

Isotopic yields as a probe of the symmetry energy: dealing with the secondary decay effects, P. Marini *et al*, J. Phys.: Conf. Ser. **420**, 012096 (2013).

Prospects for the discovery of the next new element: influence of projectiles with Z > 20, C. M. Folden III, D. A. Mayorov, T. A. Werke, M. C. Alfonso, M. E. Bennett, and M. J. DeVanzo, J. Phys. Conf. Ser. **420**, 012007 (2013).

Updated evidence of the Trojan horse particle invariance for the ^{2}H(*d*,*p*)^{3}H reaction, R. G. Pizzone, C. Spitaleri, C.A. Bertulani, A.M. Mukhamedzhanov, L. Blokhintsev, M. La Cognata, L. Lamia, A. Rinollo, R. Spartá, and A. Tumino, Phys. Rev. C **87**, 025805 (2013).

Suppression of the centrifugal barrier effects in the off-energy-shell neutron+17O interaction, M. Gulino, C. Spitaleri, X.D. Tang, G.L. Guardo, L. Lamia, S. Cherubini, B. Bucher, V. Burjan, M. Couder, P. Davies, R. deBoer, X. Fang, V.Z. Goldberg, Z. Hons, V. Kroha, L. Lamm, M. La Cognata, C. Li, C. Ma, J. Mrazek, A.M. Mukhamedzhanov, M. Notani, S. O'Brien, R.G. Pizzone, G.G. Rapisarda, D. Roberson, M.L. Sergi, W. Tan, I.J. Thompson, and M. Wiescher, Phys. Rev. C **87**, 012801(R) (2013).

Measurement of the 3 keV resonance in the reaction 13C(alpha,n)16O of importance in the s-proces, M. La Cognata, C. Spitaleri, O. Trippella, G.G. Kiss, G.V. Rogachev, A.M. Mukhamedzhanov, M. Avila, G.L. Guardo, E. Koshchiy, A. Kuchera, L. Lamia, S.M.R. Puglia, S. Romano, D. Santiago, and R. Sparta, Phys. Rev. Lett. **109**, 232701 (2012).

Electron- and photon-impact atomic ionisation, I. Bray**,** D.V. Fursa, A.S. Kadyrov, A.T. Stelbovics, A.S. Kheifets, and A.M. Mukhamedzhanov, Phys. Rep., **520**, 135 (2012).

Coulomb renormalization and ratio of proton and neutron asymptotic normalization coefficients for mirror nuclei, A.M. Mukhamedzhanov, Phys. Rev. C **86**, 044615 (2012).

Generalized Faddeev equations in the Alt-Grassberger-Sandhas form for deuteron stripping with explicit inclusion of target excitations and Coulomb interaction, A.M. Mukhamedzhanov, V. Eremenko, and A.I. Sattarov, Phys. Rev. C **86**, 034001 (2012).

Nuclear astrophysics from view point of few-body problems, A. Tumino, C. Spitaleri, C. Bertulani A. Mukhamedzhanov, Few-Body Systems 0, 1 (2012).

Effects of hadronic potentials on elliptic flows in relativistic heavy ion collisions, J. Xu, L.W. Chen, C.M. Ko, and Z.W. Lin, Phys. Rev. C **85**, 041901(R) (2012).

Charmonium production from nonequilibrium charm and anticharm quarks in quark-gluon plasma, T. Song, K.C. Han, and C.M. Ko, Phys. Rev. C **85**, 054905, 1 (2012).

Contributions of hyperon-hyperon scattering to subthreshold cascade production in heavy ion collisions, F. Li, L.W. Chen, C.M. Ko, and S.H. Lee, Phys. Rev. C **85**, 1 (2012).

Effects of initial fluctuations on bottomonia suppression in relativistic heavy-ion collisions, T. Song, K.C. Han, C.M. Ko, Nucl. Phys. **A897**, 141 (2012).

Dilepton production in proton-proton and Pb+Pb collisions at $s_{NN}^{1/2}$=2.76 TeV, O. Linnyk, W. Cassing, J. Manninen, E.L. Bratkovskaya, P.B. Gossiaux, J. Aichelin, T. Song, and C.M. Ko, Phys. Rev. C **87**, 014905 (2013).

Quarkonia formation time in quark-gluon plasma, T. Soong, C.M. Ko, S.H. Lee, Phys. Rev. C **87**, 034910 (2013).

Resonances from AMPT, C.M. Ko, Proceedings of Hadronic Resonances Production in Heavy Ion Collisions and Elementary Collisions, Austin, Texas, March 5-5, 2012, edited by A. Badala and C. Markert, Eur. Phys. J.: Web of Conferences **36**, 00014 (2012).

Dileptons from SIS to LHC energies, E.L. Bratkovskaya, O. Lynnk, V.P. Konchakovski, W. Cassing, V. Ozvenchuk, J. Manninen, Proceeding of 28th Winter Workshop on Nuclear Dynamics, Dorado, del Mar, Puerto Rico, April 7-14, 2012, edited by C. Pruneau and R. Bellwied, J, Phys. Conf. Ser. **389**, 012016 (2012).

Subthreshold cascade production in heavy ion collisions, F. Li, L.W. Chen, C.M. Ko, and S.H. Lee, Proceedings of 11th International Conference on Nucleus-Nucleus Collisions, San Antonio, Texas (May 2012), J. Phys.: Conf. ser. **420**, 012015 (2013).

Event-by-event bottomonia suppression in relativistic heavy-ion collisions, T. Song, K. Han, and C.M. Ko, Proceedings of 11th International Conference on Nucleus-Nucleus Collisions, San Antonio, Texas, May 27 - June 1, 2012, J. Phys.: Conf. ser. **420**, 012023 (2013).

Effects of initial fluctuations on jet quenching, H. Zhang, T. Song, and C.M. Ko, Proceedings of 11th International Conference on Nucleus-Nucleus Collisions, San Antonio, Texas, May 27 - June 1, 2012, J. Phys.: Conf. ser. **420**, 012043 (2013).

Jet fragmentation via recombination of parton showers, K. Han, R. Fries, C.M. Ko, Proceedings of 11th International Conference on Nucleus-Nucleus Collisions, San Antonio, Texas, May 27 - June 1, 2012, J. Phys.: Conf. ser. **420**, 012044: 1- 4 (2013).

Quarkonia production in relativistic heavy-ion collisions, C.M. Ko, K. Han, and T. Song, Proceedings of International Conference on Heavy Ion Collisions in the LHC Era, Qui Nhon, Vietnam, July 15-21, 2012, J. Phys.: Conf. ser. **422**, 012006 (2013).

Higher order corrections to density and temperature of fermions from quantum fluctuations, H. Zheng, A. Bonasera, Phys. Rev. C, **86**, 027602 (2012).

Density and temperature of bosons from quantum fluctuations, H. Zheng, G. Giuliani, and A. Bonasera, Nucl. Phys. **A892**, 43 (2012).

On the expansion and fate of the universe, A. Bonasera, J. Mod. Physics, **3**, 1722 (2012).

Heavy-quark diffusion and hadronization in quark-gluon plasma, M. He, R.J. Fries, and R. Rapp, Phys. Rev. C **86**, 014903 (2012).

Sum rule analysis of vector and axial-vector spectral functions with excited states in vacuum, P. Hohler, and R. Rapp, Nucl. Phys. **A892**, 58 (2012).

A T-matrix calculation for in-medium heavy-quark gluon scattering, K. Huggins, and R. Rapp, Nucl. Phys. **A896**, 24 (2012).

D_s meson as quantitative probe of diffusion and hadronization in nuclear collisions, M. He, R.J. Fries, and R. Rapp, Phys. Rev. Lett. **110**, 112301 (2013).

Evaluating chiral symmetry restoration through the use of sum rules, P.M. Hohler and R. Rapp, Eur. Phys. J. Web Conf. **36**, 00012 (2012).

Update on chiral symmetry restoration in the context of dilepton data, R. Rapp, J. Phys. Conf. Ser. **420**, 012017 (2013).

Equation of state of symmetric and asymmetric nuclear matter at various densities and temperatures, S. Shlomo, European Physical Society – 24th Nuclear Physics Conference "Nuclear Physics In Astrophysics V (NPA5)", J. Phys.: Confer. Ser. **337**, 012014 (2012).

Modern energy density functional and the current status of the equation of state of nuclear matter, S. Shlomo, Carpathian Summer School of Physics-2012 (CSSP12), AIP Conference Proceedings **1498**, 115 (2012).

Giant resonances in ^{40}Ca and ^{48}Ca, M. R. Anders, S. Shlomo, T. Sil, D.H. Youngblood, Y-W. Lui, and Krishichayan, Phys. Rev. C **86**, 024303 (2013).

Giant resonances in ^{40}Ca and ^{48}Ca, M.R. Anders and S. Shlomo, 11th International Conference on Nucleus-Nucleus Collisions (NN2012), J. Phys. Conf. Series **420**, 012051 (2013).

Jet-tagged back-scattering photons for quark gluon plasma tomography, Rainer J. Fries, Somnath De and Dinesh K. Srivastava, Nucl. Phys. **A904**, 569 (2013).

Predictions for p+Pb collisions at $\sqrt{s_{NN}}$ = 5 TeV, Javier L. Albacete *et al.*,Int. J. Mod. Phys. E **22**, 1330007 (2013).

Global flow of glasma in high energy nuclear collisions, Guangyao Chen and Rainer J. Fries, Phys. Lett. B **723**, 417 (2013).

Precision muon decay measurements and improved constraints on the weak interaction, A. Hillairet, R. Bayes, J.F. Bueno, Yu.I. Davydov, P. Depommier, W. Faszer, C.A. Gagliardi, A. Gaponenko, D.R. Gill, A. Grossheim, P. Gumplinger, M.D. Hasinoff, R.S. Henderson, J. Hu, D.D. Koetke, R.P. MacDonald, G.M. Marshall, E.L. Mathie, R.E. Mischke, K. Olchanski, A. Olin, R. Openshaw, J.-M. Poutissou, R. Poutissou, V. Selivanov, G. Sheffer, B. Shin, T.D.S. Stanislaus, R. Tacik, and R.E. Tribble (TWIST Collaboration), Phys. Rev. D **85**, 092013 (2012).

Single spin asymmetry A_N in polarized proton-proton elastic scattering at $\sqrt{s}$ =200 GeV, STAR Collaboration (L. Adamczyk *et al.*), Phys. Lett. B **719**, 62 (2013).

Anomalous centrality evolution of two-particle angular correlations from Au-Au collisions at $\sqrt{s_{NN}}$ = 62 and 200 GeV, STAR Collaboration (G. Agakishiev *et al.*), Phys. Rev. C **86**, 064902 (2012).

Inclusive charged hadron elliptic flow in Au + Au collisions at $\sqrt{s_{NN}}$ = 7.7 - 39 GeV, STAR Collaboration (L. Adamczyk *et al.*), Phys. Rev. C **86**, 054908 (2012).

Measurement of Direct Photons in Au+Au Collisions at $\sqrt{s_{NN}}$ =200 GeV, PHENIX Collaboration (S. Afanasiev *et al.*), Phys. Rev. Lett. **109**, 152302 (2012).

Measurements of D^0 and D^* Production in p+p Collisions at $\sqrt{s}$ =200 GeV, STAR Collaboration (L. Adamczyk *et al.*), Phys. Rev. D **86**, 072013 (2012).

Transverse single-spin asymmetry and cross-section for π^0 and η mesons at large feynman-x in polarized p+p collisions at $\sqrt{s}$ =200 GeV, STAR Collaboration (L. Adamczyk *et al.*), Phys. Rev. D **86**, 051101 (2012).

Longitudinal and transverse spin asymmetries for inclusive jet production at mid-rapidity in polarized p+p collisions at s √ =200 GeV, STAR Collaboration (L. Adamczyk *et al.*), Phys.Rev. D **86**, 032006 (2012).

Di-electron spectrum at mid-rapidity in p+p collisions at $\sqrt{s_{NN}}$ =200 GeV, STAR Collaboration (L. Adamczyk *et al.*), Phys. Rev. C **86**, 024906 (2012).

Nuclear modification factor for open-heavy-flavor production at forward rapidity in Cu+Cu collisions at $\sqrt{s_{NN}}$ =200 GeV, PHENIX Collaboration (A. Adare *et al.*), Phys. Rev. C **86**, 024909 (2012).

Energy and system-size dependence of two- and four-particle v2 measurements in heavy-ion collisions at RHIC and their implications on flow fluctuations and nonflow, STAR Collaboration (G. Agakishiev *et al.*), Phys. Rev. C **86**, 014904 (2012).

Directed flow of identified particles in Au + Au collisions at $\sqrt{s_{NN}}$ =200 GeV at RHIC, STAR Collaboration (L. Adamczyk *et al.*), Phys. Rev. Lett. **108**, 202301 (2012).

Measurement of the W→ev and Z/γ ∗ →e + e − production cross sections at mid-rapidity in proton-proton collisions at s √s = 500 GeV, STAR Collaboration (L. Adamczyk *et al.*), Phys. Rev. D **85**, 092010 (2012).

SECTION VI

APPENDIX

TALKS PRESENTED
April 1, 2012 – March 31, 2013

Low energy nuclear physics facilities in the US and opportunities for collaboration, **R.E. Tribble**, **Invited Talk**, US-Korea Workshop on International Cooperation on Particle, Nuclear and Astrophysics Research, South Korea (April, 2012).

The state of affairs of present and future nucleus-nucleus collision science, **R.E. Tribble**, **Invited Key-note Talk**, the NN2012 International Conference in San Antonio, Texas (May 2012).

Asymptotic normalization coefficients as an indirect technique for nuclear astrophysics, **R.E. Tribble**, **Invited Presentation**, the Carpathian Summer School, Sinaia, Romania (July, 2012).

Interim report from the nuclear science advisory subcommittee on implementing the 2007 long range plan, **R.E. Tribble**, Nuclear Science Advisory Committee Meeting, Washington, D.C. (September 2012).

Stable beam reaction rates by indirect techniques, **R.E. Tribble**, **Invited Presentation**, the Nuclear Astrophysics, Town Meeting in Detroit, Michigan (October 2012).

Implementing the NSAC 2007 long range plan, **R.E. Tribble**, report to NSAC, January, 2013.

Measurement of V_{ud} with $0^+ \rightarrow 0^+$ nuclear beta decays, **J.C. Hardy, Invited Talk**, 11th International Conference on the Intersections of Particle and Nuclear Physics, St. Petersburg, Florida (May 2012).

Superallowed nuclear beta decay: precision measurements for basic physics, **J.C. Hardy, Invited Talk**, Carpathian Summer School of Physics 2012, Sinaia, Romania (June 2012).

Beta decay: a window on fundamental symmetries (parts 1, 2, and 3), **J.C. Hardy, Invited lectures (3)**, Ecole Joliot Curie, Frejus, France (September 2012).

Ernest Rutherford and the origins of nuclear physics, **J.C. Hardy, Colloquium**, University of North Carolina, Chapel Hill, North Carolina (November 2012).

Experimental aspects in the precise superallowed nuclear beta-decay measurements, **V.E. Iacob, Invited Talk**, Carpathian Summer School of Physics 2012, Sinaia, Romania (June 2012).

Probing fundamental physics with precision superallowed beta-decay experiments, **L. Chen, Seminar**, University of Tennessee, Knoxville, Tennessee (May 2012).

High-precision measurements of the superallowed beta decays of ^{38}Ca and ^{46}V, **H.I. Park, Seminar**, Center for Experimental Nuclear Physics and Astrophysics, University of Washington, Seattle, Washington (November 2012).

New ICC precision measurements in ^{119}Sn, **N. Nica** U.S. Nuclear Data Program annual meeting, Brookhaven National Lab, Upton, New York (November 2012).

$^{119}Sn^m$ – a difficult experimental case to test internal-conversion theory, **N. Nica**, 20th meeting of the Nuclear Structure and Decay Date network, Kuwait (January 2013).

Further test of internal-conversion theory with a measurement in $^{119}Sn^{m}$, **N. Nica**, International Conference on Nuclear Data for Science and Technology, New York City, New York (March 2013).

Measurement of branching ratios in the β decay of ^{38}Ca, **H.I. Park**, J.C. Hardy, V.E. Iacob, M. Bencomo, L. Chen, J. Goodwin, V. Horvat, N. Nica, B. Roeder, L. Trache and R.E. Tribble, APS Meeting, Atlanta, Georgia (March 2012).

The giant monopole resonance, nuclear matter incompressibility and symmetry energy, **Y.-W. Lui**, **Colloquium**, Shanghai Jiao Tung University, Shanghai, China (April 2012).

The systematic of giant monopole resonance and the implications for nuclear matter incompressibility, **Y.-W. Lui**, **Colloquium**, Shanghai Institute of Applied Physics (SINAP), Shanghai, China (April 2012).

Giant monopole resonance – experiment, **Y. –W. Lui, Invited Lectures (5)**, Institute of Modern Physics (IMP) & Heavy Ion Research Facility in Lanzhou (HIRFL), Lanzhou, China (Sept. 2012).

Systematics of giant monopole resonance and recent studies, **Y.-W. Lui**, **Invited Talk**, Conference in Collective Motions in Nuclei under Extreme conditions (COMEX4), Hayama, Kanagawa, Japan (October 2012)

α-cluster states in N≠Z nuclei, **V.Z. Goldberg, Invited Talk,** Conference in Nuclear dynamics and structure'12, Opatija, Croatia (July 2012).

Unusual states in light nuclei, **V.Z. Goldberg, Invited Talk,** Conference in Fundamental Problems of Nuclear Physics, Atomic Power Engineering and Nuclear Technologies, Voronezh, Russia (June, 2012).

Exciting examples of unusual nuclear structure in light nuclei, **V.Z. Goldberg**,**Seminar**, Lomonosov Moscow State University, Moscow, Russia (July 2012).

Nuclear structure problems to investigate at ACCULINNA, **V.Z. Goldberg**, **Seminar**, JINR. FLNR. Dubna, Russia (August 2012).

The RHIC spin program: achievements and future opportunities, **C.A. Gagliardi, Invited Talk**, (on behalf of the RHIC Spin Collaboration), APS Div. Nucl. Phys., Mini-Town Meeting on RHIC Physics, Newport Beach, California (October 2012).

What makes the proton spin? **C.A. Gagliardi, Invited Talk**, DOE Office of Science Graduate Fellows Ann. Meet., Brookhaven National Laboratory, Upton, New York (July 2012).

Recent results from RHIC, **C.A. Gagliardi, Invited Plenary**, 11th Int. Conf. Nucl.-Nucl. Coll. (NN2012), San Antonio, Texas (May 2012).

Measurement of the $d(^{26}Al^{m},p)^{27}Al$ reaction for nuclear astrophysics, **B.T. Roeder**, **Invited Talk**, M. McCleskey, L. Trache, V.Z. Goldberg, V.E. Iacob, E. Simmons, A. Spiridon, R.E. Tribble, M. Gulino, M. LaCognata, R.G. Pizzone, G.G. Rapisarda, R. Sparta, C. Spitaleri, T. Davinson, G. Lotay, P.J. Woods, XXXV ReuniÃ£o de Trabalho sobre FÃsica Nuclear no Brasil, Maresias, Brasil (September 2012).

AstroBox - a new detection system for very low-energy protons from Î²-delayed p-decay, **Alexandra Spiridon**, Carpathian Summer School of Physics 2012: exotic nuclei and nuclear/particle astrophysics (IV), Sinaia, Romania (July 2012).

Gluon polarization and jet production at STAR, **P. Djawotho, Invited Talk**, (for the STAR Collaboration), 3rd Workshop QCD Struct. Nucl. (QCD-N'12), Bilbao, Spain (October 2012).

Forward two-particle correlations and asymmetries from polarized p+p at $\sqrt{s}$ = 200 GeV at STAR, **J.L. Drachenberg, Seminar**, Physics Department, Valparaiso University, Valparaiso, Indiana (May 2012).

Forward two-particle correlations and asymmetries from polarized p+p at $\sqrt{s}$ = 200 GeV at STAR, **J.L. Drachenberg, Seminar**, Physics Department, University of Texas, Austin, Texas (May 2012).

Transverse spin effects and graduate school musings, **J.L. Drachenberg, Seminar**, Physics Department, Abilene Christian University, Abilene, Texas (April 2012).

Probing high-temperature QCD matter, **S. Mioduszewski**, **Colloquium**, Florida Atlantic University, Boca Raton, Florida (April 2012).

Long-range pseudo-rapidity correlations at high p_T in $\sqrt{s_{NN}}$ = 200 GeV Au+Au, **Martin Codrington**, **Seminar**, University of Texas, Austin, Texas (May 2012).

TAMU-TRAP facility for weak interaction physics, **P. Shidling**, **Invited Talk**, DAE Symposium on Nuclear Physics, Delhi University, New Delhi, India (Dec. 2012).

The state of the art for extracting V_{ud} from nuclear β decay, **D. Melconian**, **Invited Talk**, 7th International Workshop on the CKM Unitarity Trangle, Cincinnati, Ohio (Sept. 2012).

^{37}K beta asymmetry, **R.S. Behling**, **Invited Progress Report**, ISAC Science Forum, TRIUMF, Vancouver, British Columbia (Dec. 2012).

Precise lifetime measurements of T=1/2 nuclei, **P. Shidling**, DAE Symposium on Nuclear Physics, Delhi University, New Delhi, India (Dec. 2012).

SAMURAI TPC: a time projection chamber to study the nuclear symmetry energy at RIKEN-RIBF with rare isotope beams, **A.B. McIntosh**, **Invited Talk**, International Workshop of Nuclear Symmetry Energy and Reaction Mechanism (ASY-EOS 2012), Siracusa, Sicily, Italy (September 2012).

Increasing opportunities through negotiation and communication skills, **A.B. McIntosh**, **Invited Talk**, AAPT meeting, Philadelphia (July 2012).

Asymmetry dependence of the nuclear caloric curve, **A.B. McIntosh**, **Invited Talk**, 11th International Conference on Nucleus-Nucleus Collisions, San Antonio (May 2012)

Nuclear & radiochemistry at Texas A&M University: Assuring a future U.S. based nuclear and radiochemistry expertise, **Sherry Yennello, Invited Talk,** Public Briefing, National Academy of Science, Washington , DC (May 2012).

Using heavy ion collisions as a probe of the nuclear equation of state, **Sherry Yennello, Invited Talk,** Carpathian Summer School of Physics 2012, Romania

Asymmetry dependence of the nuclear caloric curve, **Sherry Yennello, Invited Talk,** Workshop on Nuclear Symmetry Energy at Medium Energies (ASY-EOS), Siracusa, Italy (September 2012).

Stellar secrets: earth-bound insights to elements through heavy-ion reactions, **Sherry Yennello, Invited Talk,** Ethel Ashworth-Tsutsui Memorial Lecture And Awards Ceremony, College Station, Texas (November 2012).

SAMURAI TPC: A time projection chamber to study the nuclear symmetry energy at RIKEN-RIBF with rare isotope beams, **A.B. McIntosh**, APS Division of Nuclear Physics, Newport Beach, California (October 2012).

Asymmetry dependence of nuclear temperatures and densities, **A.B. McIntosh**,, A. Bonasera , Z. Kohley , S. Galanopoulos , K. Hagel , L.W. May , P. Marini , D.V. Shetty , W.B. Smith , S.N. Soisson , G.A. Souliotis , B.C. Stein , R. Tripathi , S. Wuenschel , S.J. Yennello, APS Division of Nuclear Physics, Newport Beach, California (October 2012).

Distance calculation methods used in linearization for particle identification in multi-detector arrays, **L.W. May**, 22nd International Conference on the Application of Accelerators in Research and Industry **(**CAARI 2012) Fort Worth, Texas (August 2012).

Production of nuclides near the N = 126 shell using projectiles with Z > 20, **Charles M. Folden III**, APS April Meeting, Denver, Colorado, April 13, 2013

Prospects for the discovery of the next new element and chemical studies of the heaviest elements, **Charles M. Folden III**, **Invited Talk**, Texas A&M University Department of Chemistry Seminar, College Station, Texas (September 2012).

Heavy element chemistry at Texas A&M University - from off-Line to on-Line, **Megan E. Bennett**, 11th Workshop on a Recoil Separator for Superheavy Element Chemistry, Darmstadt, Germany (September 2012).

Development of a gas stopper for heavy elements chemistry at Texas A&M University, **Marisa C. Alfonso**, 11th Workshop on a Recoil Separator for Superheavy Element Chemistry, Darmstadt, Germany (September 14, 2012).

Heavy element chemistry at Texas A&M University - from off-line to on-line, **Megan E. Bennett**, International Nuclear Target Development Society Conference, Mainz, Germany (August 2012).

Heavy element chemistry at TAMU: from off-line to on-line, **Megan E. Bennett** (presented by Charles M. Folden III), 244th American Chemical Society National Meeting, Philadelphia, Pennsylvania (August 19, 2012).

Prospects for the discovery of the next new element, **Charles M. Folden III**, 244th American Chemical Society National Meeting, Philadelphia, Pennsylvania (August 19, 2012).

Prospects for the discovery of the next new element, **Charles M. Folden III**, **Invited Talk**, 11th International Conference on Nucleus-Nucleus Collisions, San Antonio, Texas (May 31, 2012).

Production of radon and thorium isotopes near N = 126 shell in ^{48}Ca and ^{54}Cr induced fusion reactions on ^{162}Dy, **Dmitriy A. Mayorov**, 11th International Conference on Nucleus-Nucleus Collisions, San Antonio, Texas (May 29, 2012).

Production of radon and thorium isotopes near N=126 shell closure in ^{48}Ca and ^{54}Cr induced fusion reactions on ^{162}Dy, **Dmitriy A. Mayorov**, APS April Meeting, Atlanta, Georgia (April 2012).

What information can be extracted from transfer reaction? **A.M. Mukhamedzhanov**, **Invited Talk**, International Workshop on Understanding spectroscopic factors, Institute of Extreme Matter, Darmstadt Technical University and GSI, Darmstadt, Germany (April 2012).

Generalized Faddeev equations for the deuteron stripping including the target excitations and Coulomb interaction, **A.M. Mukhamedzhanov**, DOE panel, Department of Energy, Germantown, Maryland, (September 2012).

Advancing the theory of deuteron stripping populating bound states and resonances, **A.M. Mukhamedzhanov**, DOE panel, Department of Energy, Germantown, Maryland, (September 2012).

Advancing the theory of deuteron stripping reactions populating bound states and resonances and application for nuclear astrophysics, **A.M. Mukhamedzhanov**, **Invited Talk**, 3rd International Symposium on Frontiers in Nuclear Physics, Bejhang University, Beijing, China (November 2012).

Toward a complete description of heavy-flavor transport in medium, **M. He, Invited talk**, STAR Muon-Telescope-Detector Workshop, Tsinghua University, Beijing, China (April 2012).

Heavy quarks and quarkonia in hot matter, **R. Rapp, Invited Lecture**, The Berkeley School of Collective Dynamics in High-Energy Collisions, Lawrence Berkeley National Laboratory, Berkeley, California (May 2012).

Toward a complete description of heavy-flavor transport in medium, **M. He**, 5th Int. Conf. on Hard and Electromagnetic Probes of High-Energy Nuclear Collisions, Cagliari, Italy (May 2012).

Update on search for chiral symmetry restoration in heavy-ion collisions, **R. Rapp, Invited Talk**, 11th Int. Conf. on Nucleus-Nucleus Collisions (NN2012), San Antonio, Texas (May 2012).

Theoretical perspective on electromagnaetic radiation at RHIC, **R. Rapp, Invited Talk**, 2012 Annual AGS & RHIC User's Meeting, Brookhaven National Laboratory, Upton, New York (June 2012).

Heavy flavor in medium, **R. Rapp, Invited Lectures (3)**, 2012 JET Collaboration Summer School, McGill University, Montreal, Canada(June 2012).

Comprehensive analysis of in-medium quarkonia at SPS, RHIC and LHC, **R. Rapp**, 23rd Int. Conf. on Ultrarelativistic Nucleus-Nucleus Collisions (Quark Matter 2012), Washington DC (August 2012).

Thermal electromagnetic radiation in heavy-ion collisions, **R. Rapp, Invited Lecture**, 34th Int. School of Nuclear Physics on "Probing the Extremes of Nuclear Matter with Heavy Ions", Erice, Italy (September 2012).

Theory of thermal dileptons, **R. Rapp, Invited Talk**, Symposium on "Hot Topics in Hot Matter" in Honor or I. Tserruya's 70th birthday, Weizmann Institute, Rehovot, Israel (October 2012).

Nonperturbative heavy-flavor diffusion and hadronization in a hydrodynamics description of heavy-ion collisions, **M. He, Invited Talk**, 5th Int. Workshop on Heavy-Quark Production in Heavy-Ion Collisions, Utrecht University, Netherlands (November 2012).

Thermal dileptons, **R. Rapp, Invited Talk**, Thermal Radiation Workshop, Brookhaven National Laboratory, Upton, New York (December 2012).

Connection between dilepton data and chiral symmetry restoration, **P. Hohler, Invited Talk**, Thermal Radiation Workshop, Brookhaven National Laboratory, Upton, New York (December 2012).

Electromagnetic radition and heavy flavor in heavy-ion collisions, **R. Rapp, Invited Talk**, EMMI Workshop on Persepctives and Challenges for Future Experiments in Heavy-Ion Collisions, GSI Darmsstadt, Germany (February 2013).

Dilepton production in heavy-ion collisions, **R. Rapp, Invited Talk**, 8th Int. Workshop on Critical Point and Onset on Deconfinement, Napa, California (March 2013).

Update on search for chiral symmetry restoration in heavy-ion collisions, **R. Rapp, Invited Heavy-Ion Forum Seminar**, CERN, Geneva, Switzerland (March 2012).

Chiral symmetry restoration in heavy-ion collisions, **R. Rapp, Invited High-Energy/Nuclear Physics Seminar**, Rice University, Houston, Texas (June 2012).

Anisotropic flows in HIC, **C.M. Ko, Invited Talk**, Symposium on Cosmo, Cancer, Criticality and Chromoplasmology, Seattle, Washington (May 2012).

Dihadron correlations in AMPT, **C.M. Ko, Invited Talk,** Workshop on the Ridge Correlation in High-Energy Collisions at RHIC and LHC, Seattle, Washington (May 2012).

Probing the nuclear symmetry energy with rare isotope beams, **C.M. Ko, Invited Talk,** Workshop on Rare Isotope Physics Theory, Daejean, Korea (May 2012).

Why particles and antiparticles flow differently?, **C.M. Ko, Invited Talk**, Symposium on Contemporary Subatomic Physics, Montreal, Canada (June 2012).

Effects of hadronic mean-field potentials on elliptic flows in HIC, **C.M. Ko, Invited Talk**, Second International Symposium on Non-Equilibrium Dynamics, Heraklion, Greece (June 2012).

Anisotropic flows and dihadron correlations in AMPT, **C.M. Ko, Invited Talk,** Workshop on Initial State Fluctuations and Final State Correlations in Heavy-Ion Collisions, Trento, Italy (July 2012).

Quarkonia production in relativistic heavy ion collisions, **C.M. Ko, Invited Talk,** Conference on Heavy Ion Collisions in the LHC Era, Qui Nhon, Vietnam (July 2012).

Mean-field effects on elliptic flow in relativistic heavy ion collisions, **C.M. Ko, Invited Talk,** Bertsch Symposium on Nuclear Physics, Seattle, Washington (September 2012).

Elliptic flow of baryon-rich matter, **C.M. Ko, Invited Talk**, The International Workshop on Nuclear Dynamics in Heavy-Ion Collisions, Shenzhen, China (December 2012).

Event-by-event bottomonia suppression in relativistic heavy-ion collisions, **T. Song,** 11th International Conference on Nucleus-Nucleus Collisions, San Antonio, Texas (May 2012).

Subthrehold cascade production in heavy ion collisions, **F. Li,** 11th International Conference on Nucleus-Nucleus Collisions, San Antonio, Texas (May 2012).

Patonic mean-field effects on elliptic flows, **T. Song, Invited Talk**, 4th Asian Triangle Heavy Ion Conference, Pusan, Korea (November 2012).

Density and temperature of fermions from quantum fluctuations, **H. Zheng**, A. Bonasera, 11th international conference on nucleus-nucleus collisions (NN2012), San Antonio, Texas (May 2012).

Density and temperature of fermions and bosons from quantum fluctuations, **H. Zheng**, **Invited Talk**, G. Giuliani, and A. Bonasera, International Workshop on Nuclear Dynamics in Heavy-Ion Collisions (IWND12), Shenzhen, China (December 2012).

Energy density functional for nuclei and the current status of the equation of state of nuclear matter, **S. Shlomo**, **Invited Talk**, Conference on Beauty in Physics: Theory And Experiment, in Honor of Franco Iachello, on The Occasion of his 70th Birthday, Hacienda, Cocoyoc, Mexico, (May 2012).

Modern Energy density Functional And The Current Status of The Equation of state of Nuclear Matter, **S. Shlomo, Invited Talk**, Carpathian Summer School of Physics-2012 (CSSP12), Sinaia, Romania (June 2012).

Modern energy density functional for properties of finite nuclei and the nuclear matter, **S. Shlomo**, **Invited Talk**, The 4th International Conference on Current Problems in Nuclear Physics And atomic Energy (NPAE2012), Kiev, Ukraine (September 2012).

Determining modern energy density functional for nuclei and the status of the equation of state of Nuclear matter, **S. Shlomo**, **Invited Talk**, Department of Physics, Texas A&M University at Commerce, Texas (February 2013).

Giant resonances in ^{40}Ca and ^{48}Ca, **M.R. Anders**, **Invited Talk**, 11th International Conference on Nucleus- Nucleus Collisions (NN2012), San Antonio, Texas (May 2012).

Giant resonances in ^{40}Ca and ^{48}Ca, **M.R. Anders**, Joint Fall Meeting of the Texas Section of APS, AAPT and Zone 13 of the SPS, (October 2012)

Quark recombination, **Rainer J. Fries**, **Invited Talk**, Workshop Cosmos, Cancer, Criticality and Chromoplasmology, Seattle, Washington (May 2012).

Jet-triggered back-scattering photons for QGP tomography, **Rainer J. Fries**, 5th International Conference on Hard and Electromagnetic Probes of High-Energy Nuclear Collisions (Hard Probes 2012), Cagliari, Italy (May 2012).

Flowing gluon fields, **Rainer J. Fries**, **Invited Talk**, Symposium on Contemporary Subatomic Physics (SCSP 2012), McGill University, Montreal, Quebec (June 2012).

Jet-triggered back-scattering photons for QGP tomography, **Rainer J. Fries**, Quark Matter 2012, Washington DC (August 2012).

Toward a comprehensive description of heavy flavor dynamics, **Rainer J. Fries**, **Invited Talk**, KMI Workshop QGP 2012, Kobayashi-Maskawa Institute, Nagoya, Japan, (September 2012)

Open heavy flavor probes in strongly interacting nuclear matter, **Rainer J. Fries**, **Invited Talk**, 8th Workshop on High-P_T Physics at LHC, Wuhan, China (October 2012)

Introduction to heavy ion collisions, **Rainer J. Fries**, **Invited Lectures** (Series of six lectures), SERC School, VECC Kolkata, India, (January 2013).

Non-perturbative heavy-flavor transport at RHIC and LHC, **Min He**, 5th International Conference on Hard and Electromagnetic Probes of High-Energy Nuclear Collisions (Hard Probes 2012), Cagliari, Italy (May 2012).

Initial conditions with flow from a McLerran Venugopalan model with transverse dynamics, **Guangyao Chen**, Hot Quarks 2012, Guanica Puerto Rico (October 2012).

Jet-tagged back-scattering photons in heavy-ion collisions, **Somnath De**, 8th Workshop on High-P_T Physics at LHC, Wuhan, China (October 2012).

Dileptons and photons from the hadronization process, **Guangyao Chen**, RBRC Workshop on Thermal Radiation, Brookhaven National Laboratory, Upton, New York (December 2012).

RESEARCH PERSONNEL AND ENGINEERING STAFF

April 1, 2012 - March 31, 2013

Faculty and Research Group Leaders

Aldo Bonasera, Senior Scientist
Charles M. Folden III, Assist. Prof. of Nuclear Chemistry
Rainer Fries, Assist. Professor of Physics
Carl A. Gagliardi, Professor of Physics
John C. Hardy, Professor of Physics
Che Ming Ko, Professor of Physics
Dan Melconian, Assist. Professor of Physics
Saskia Mioduszewski, Assist. Prof. of Physics
J. B. Natowitz, Professor of Chemistry, Bright Chair
Ralf Rapp Associate Professor of Physics
Shalom Shlomo, Senior Scientist
Robert E. Tribble, Professor of Physics, Director
Sherry J. Yennello, Professor of Chemistry
Dave H. Youngblood, Professor of Physics
Akram M. Zhanov, Senior Scientist

Research Staff

Juha Arje, Research Scientist- From 4/1/2012
Marina Barbui, Assist. Research Scientist
Henry Clark, Accelerator Physicist (50%)
Grigor Chubaryan, Research Scientist
Vladilen Goldberg, Research Scientist
John C. Hagel, Research Scientist (50%)
Vladimir Horvat, Research Scientist (50%)
Victor Iacob, Associate Research Scientist
Yiu-Wing Lui, Research Scientist
Ninel Nica, Associate Research Scientist
George Souliotis, Associate Research Scientist
Livius Trache, Research Scientist – To 12/31/12
Meiko Uesaka, Research Scientist – To 6/30/12

Visiting Scientists

Ian Towner – From 6/18/12 To 8/31/12

Accelerator Physics and Radiation Line Staff

Joseph Brinkley, Research Associate
Lixin Chen, Research Associate – From 3/1/13
Henry Clark, Accelerator Physicist (50%)
Vladimir Horvat, Research Scientist (50%)
Bruce Hyman, Research Associate
George Kim, Accelerator Physicist
Don May, Accelerator Physicist
Brian Roeder, Accelerator Physicist
Gabriel Tabacaru, Accelerator Physicist

Computer Systems Staff

Robert Burch, Jr., Lead Microcomputer/LAN Administrator
John C. Hagel, Research Scientist (50%)

Engineering Staff

Greg Derrig - Retired
Robert Olsen, Senior Mechanical Engineer

Postdoctoral Research Associates

Megan Bennett – To 10/15/12
Lixin Chen – To 2/28/2013
Pibero Djawotho
Vasily Eremenko
Gianluca Giuliani
Ahmed Hamed – To 8/31/12
Min He – To 8/31/12
Paul Hohler
Eun-Joo Kim - From 1/5/13
Yunpeng Liu – From 1/2/13
Matthew McCleskey
Alan McIntosh
Mirganka Mondal
Hyo-In Park
Rosario Pizzone – To 5/12/12
Antti Saastamoinen
Katarzyna Schmidt - To 9/30/12
Praveen Shidling
Taesoo Song
Sara Wuenschel – From 1/1/13
Yi Xu – From 9/28/12

STUDENTS

April 1, 2012 - March 31, 2013

Graduate Students

Mason Anders
Marisa Alfonso
Matteo Barbarino
Richard Spence Behling
Miguel Bencomo – From 6/1/11
Jonathan Button
Paul Cammarata – From 6/1/11
Zilong Chang – From 6/1/11
Matthew Cervantes – To 8/15/12
Roman Chyzh
Guangyao Chen
Martin Codrington – To 5/12/12
Murat Dag – From 9/1/12
James Drachenberg – To 5/15/12
Benjamin Fenker
John Goodwin – To 12/15/12
Kyong Choi Han
Lauren Heilborn
Kyle Higgins – To 7/11/12
Nathan Holt
Liaoyuan Huo - To 11/15/12
Feng Li
Larry May
Demitri Mayarov
Michael Mehlman
Andrew Raphelt
Steven Rose – From 1/16/13
Ellen Simmons
Alexandra Spiridon
Sidharth Somanathan
Tyler Werke
Andrew Zarrella – From 6/1/12
Hua Zheng

Undergraduates and Student Technicians

Nicolas Blando – From 5/14/12
Giacoma Bonasera – To 1/24/13
Lindsay Bryce – From 1/10/13
Matthew Chapman – From 1/15/13
Haley Demos – From 9/14/12
Kathrine Galvin – To 2/21/13
Leslie Galvan – From 1/29/13
Zachary Gastony
Hunter Gould – From 9/20/12
Mathew Johnson – To 1/11/13
Hanyu Li – From 10/16/12

ORGANIZATIONAL CHART - CYCLOTRON INSTITUTE

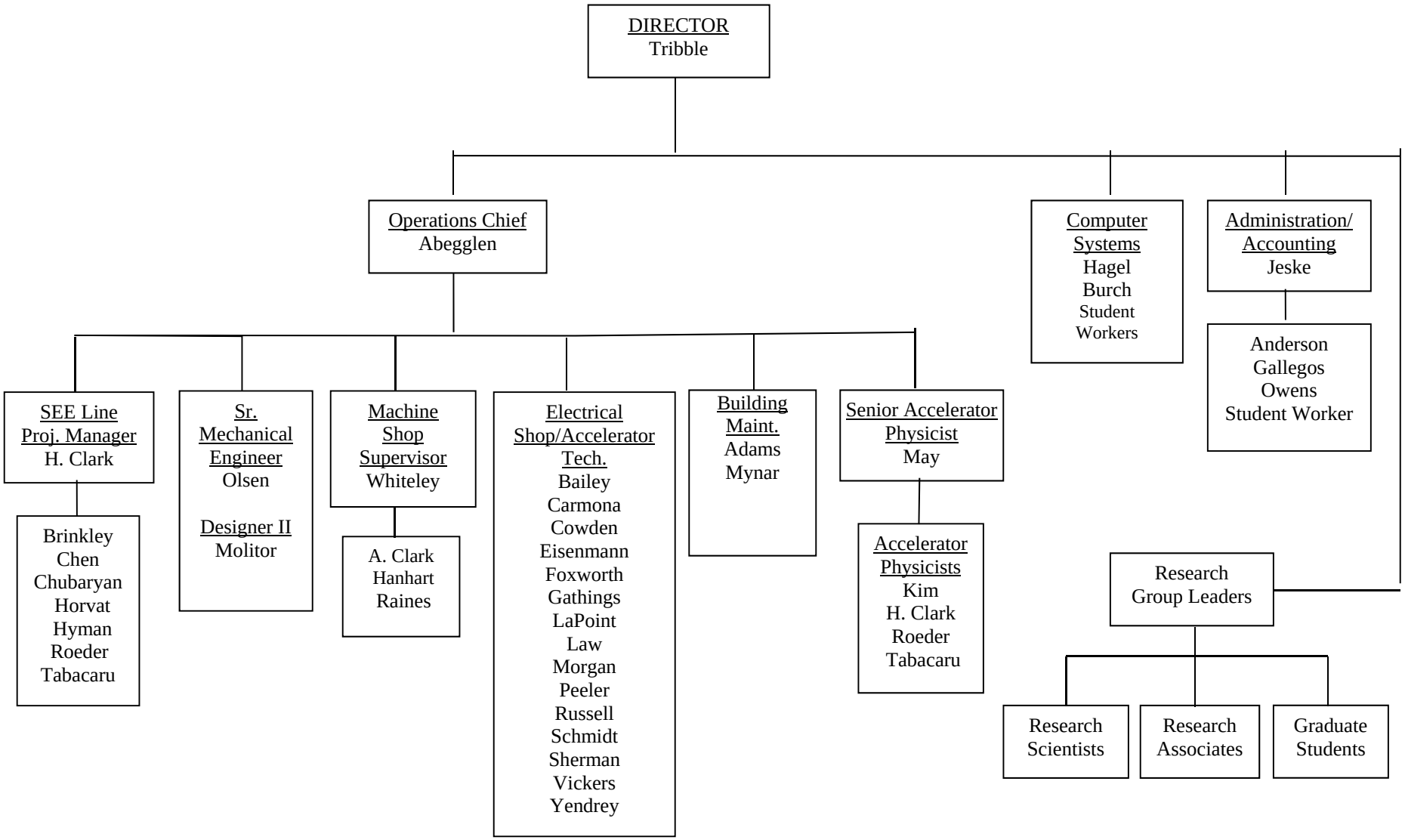

STUDENTS WHO RECEIVED GRADUATE DEGREES
FROM THESIS WORK CONDUCTED
AT
THE CYCLOTRON INSTITUTE

April 1, 2012 – March 31, 2013

Name	Year	Thesis Title	Advisor	Present Position
Mike Mehlman	2012	*Design of TAMUTRAP and Testing of RFQ Pressure Control System*	D. Melconian	Continue to Ph. D. degree
John Goodwin	2012	*Can Environmental Factors affect Half-Life in Beta Decay? An Analysis*	J. C. Hardy	N.A.
Martin Cordrington	2012	*Lon- Range Rapidity at High pT in sqrt(s) = 200 GeV Au+Au Collision with STAR*	S. Mioduszewski	N.A.
James Lucus Drachenberg	2012	*Forward Di-Hadron Asymmetries from p + p at sqrt(s)=200GeV at STAR*	C. A. Gagliardi	N.A.
Matthew C. Cervantes	2012	*Heavy Quarkonium Production at sqrt(s_{NN}) = 200 GeV*	S. Mioduszewski	Post. Doc. at Cyclotron Institute, Texas A&M university
Kyle Huggins	2012	*A T-Matrix Approach to Heavy Quark Interaction with Thermal Gluons in a Quark Gluon Plasma*	Ralf Rapp	N.A.

INSTITUTE COLLOQUIA AND SEMINARS
April 1, 2012-March 31, 2013

2012

April 24	Dr. Antti Saastamoninen, University of Jyvaskyla and Cyclotron Institute, Texas A&M University, College Station, Texas	*Beta-Decay Studies for Nova Nucleosynthesis*
May 10	Professor Helmut Satz, Fakultaet fuer Physik, Universitaet Bielefeld, Bielefeld, Germany	*Quark Confinement and Hadrosythesis*
May 14	Dr. Daniel Abriola, Internaltional Atomic Energy Agrncy, Vienna, Austria	*LAEA's Research Coordinated Project (CRP) on Beta-Delayed Neutron Emission*
May 15	Dr. Dan Bardayan, Oak Ridge National Laboratory, Oak Ridge, Tennessee	*New Instruments and Recent Results in the Study of Transfer Reactions at HRIBF*
May 22	Professor Olaf Scholten, KVI, University of Groningen, Netherlands	*The Approximation in IBA; Old Mass Xe and Te*
May 24	Professor Wenqing Shen, NSFC and Shanghai Institute of Applied Physics, Chinese Acacemy of Science	*National Science Foundation of China and Development of Chinese Nuclear Physics*
June 5	Professor Gerd Roepke, Institute of Physics, University of Rostock, Rostock, Germany	*Four-Particle (Alpha Like) Correlations in Nuclear Systems*
July 27	Dr. Yongseok Oh, Department of Physics, Kyungpook National University, Daegu, Korea	*High Spin Resonances in Hardon Reactions*
August 9	Professor H. Sakai, RIKEN, Wako, Japan	*New Result from RIKEN RIBF*
August 22	Dr. Dai-Mei Zhou, Institute of Particle Physics, Central China Normal University, Wuhan, China	*Comparative Study for Non-Statistical Fluctuation of Net Proton, Baryon, and Charge Multiplicities*
August 22	Dr. Yun Cheng, Institute of Particle Physics, Central China Normal University, Wuhan, China	*Hydrodynamical and Transport Model for Ultra-Relativistic Heavy Ion Reactions*

August 27	Dr. Ken Moody, Chemical Sciences Division, Lawrence Livermore National Laboratory, Livermore, California	*Forensic Radiochemistry*
October 17	Professor Mark Raizen, Physics Department, University of Texas, Austin, Texas	*Magnetically Activated and Guided Isotope Separation*
November 12	Professor K. A. Gridnev, St. Petersburg State University, St. Petersburg, Russia	*Extreme Neutron Rich Sector of the Nuclear Chart: New Horizons!*
November 20	Dr. Livius Trache, National Institute for Physics and Nuclear Engineering, Bucharest-Magurele, Romania	*Current and Future Nuclear Physics Research at IFIN-HH Bucharest, Romania*
December 4	Dr. Michael Youngs, NSCL Michigan Station University, East-Lansing, Michigan	*Measuring the Density Dependence of the Symmetry Energy through Emitted Tritons and ^{3}He*
December 11	Dr. Xinfeng Chen, Department of Chemistry, Washington University in St. Louis, St. Louis, Missouri	*Nuclear g Factor Measurement with Recoil-into-Vacuum Method*

2013

January 22	Professor Gerd Roepke, Institute of Physics, University of Rostock, Rostock, Germany	*Cluster in Nuclear Systems – Equation of State and Nuclear Structure*
January 23	Professor N. Auerbach, School of Physics and Astronomy, Tel Aviv University, Tel Aviv, Israel	*Electric Dipole Moments in Nuclei and Atoms; Test of Time Reversal Symmetry*
January 25	Professor N. Auerbach, School of Physics and Astronomy, Tel Aviv University, Tel Aviv, Israel	*The Shear Viscosity to Entropy Density Ratio in Nuclei*
February 20	Dr. Paolo Avogadro, Texas A&M Universit at Commerce, Commerce, Texas	*QRPA Study of Giant Monopole Resonances*